

Multi-physics modeling of VVERs with high fidelity high-resolution codes

Présentée le 25 mai 2022

Faculté des sciences de base
Laboratoire de physique des réacteurs et de comportement des systèmes
Programme doctoral en énergie

pour l'obtention du grade de Docteur ès Sciences

par

Marianna PAPADIONYSIOU

Acceptée sur proposition du jury

Prof. D. Dujic, président du jury
Prof. A. Pautz, M. Hursin, directeurs de thèse
Prof. H. G. Joo, rapporteur
Prof. M. Avramova, rapporteuse
Prof. A. Manera, rapporteuse

“Ἀρχάς εἶναι τῶν ὅλων ἀτόμους καὶ κενόν, τὰ δ’ ἄλλα πάντα νενομίσθαι”

*The atoms and the vacuum are the beginning of everything, the rest are
constructs of the mind*

Δημόκριτος, 470 - 430 B.C., Ancient Greek Philosopher & Scientist

“Hexagons are the Bestagons”

CGP Grey, Dates Unknown, American Youtuber

Acknowledgements

This thesis summarizes the work of 4 years, over which I had the opportunity to collect a number of experiences that will accompany me forever. I learnt many things through this PhD, not only concerning nuclear engineering, that make me appreciate the time I dedicated to this project, more than the title it carries with it. Besides the scientific outcome, I know that I am a better person now than I was 4 years ago, as a new researcher and as a more mature human being, through the trials and joys of this work.

Firstly and above all, I want to thank Mathieu Hursin for his continuous support and participation in this work. He is a precious mentor and a brilliant scientist. If at some point in my career I reach a level of knowledge comparable to his, I will consider myself successful. My thanks also go to Prof. Andreas Pautz and Hakim Ferroukhi who offered me the opportunity to work in PSI in a project that excited me so much. I thank also Alexander Vasiliev and the whole Core behavior group and LRT for their help and support of my work. Prof. Han Gyu Joo hosted me in SNU and enabled me to work with nTF on site, which allowed my research to reach the level at which it is presented here. His support and openness for collaboration were vital for the completion of the thesis. From SNU many thanks also go to all the students of SNURPL, especially Seungug Jae, Jaejin Lee, Namjae Choi and Seongchan Kim, who helped me and taught me many things. I am very grateful to Prof. Maria Avramova and the CTF team for their support. She was always available to provide guidance, which proved crucial more than once. Finally, I received major support by Marc Serrabou Caubet, who was always there to help me with Merlin6 and my complicated code systems. Many things would be much more difficult if he was less present.

On a personal note, I must thank my family and friends for always supporting me to achieve the best I can in all aspects of my life. Mom & Dad thank you for pushing me to become who I am. I would not have made it without you. To my sister, my brother, Maria, my grandmother, my uncle and his family I love you and I miss you. From Greece, Yota, Katerina, Melina and Evdoxia, your presence and strength is an inspiration for me to move forward. I admire you and I am proud to be your friend. From my university back home, Giorgos, Stratos, Trifonas, Dimitris, Alex and Nikos, I feel if one of us makes it then we all succeed. I am happy

to have “grown up” with you and I look forward for what is to come. From Switzerland, Ahmed, Emeline, Fanny, Petra, Lubomir, Petros and Simone, we started a trip together and I would do it all over again. Thank you for being part of my life and often a light in the darkness. Special tokens of gratitude I owe to Dionysis. He was the one that informed me about the Nuclear master in Switzerland and encouraged me to apply to what ended up being the beginning of the rest of my life. You were there always to help me any way you could, my precious friend. Last but not least, I give many thanks to my partner Jarmo. Thank you for your patience and your kind heart and for being present to experience this with me. I love you and I cherish you.

Abstract

The calculations performed for the design and operation of a Nuclear Power Plant (NPP) are a key factor for its safety analyses. The standard for the computational analysis of NPPs is the so called conventional approach, which relies on coarse mesh diffusion for the neutronic solver and 1D channels for the T/H solver. The recent evolution of computing clusters allows the use of a novel approach, with codes performing first-principle based multi-physics simulations with high-resolution of the calculated parameters. Due to their computational cost, these methods can only be used as an audit tool of the conventional approach. In recent years, the nuclear industry has moved towards the establishment of Best Estimate Plus Uncertainty safety limits. The novel approach is a step forward to that direction. At the same time, VVER technology is expanding, with new reactors being built worldwide. However, there is currently no multi-physics tool available for sub-pin VVER steady state and cycle analysis. A clear need exists for more refined simulation tools capable of handling hexagonal geometries.

The goal of this PhD is the development of a novel computational scheme based on the 3D sub-pin neutron transport code nTRACER-FAST (nTF), coupled to the sub-channel code COBRA-TF (CTF) for VVER full core steady state and cycle analysis. The coupling of a neutronic code with sub-pin resolution to a sub-channel T/H solver, as well as the use of CTF for full core VVER sub-channel analysis are one of the main novelties of this work, to the extent of the writer's knowledge. In this thesis, nTF is verified & validated for VVER 3D core standalone neutronic calculations against data published in international benchmarks. The internal sub-pin coupling of nTF to CTF for hexagonal geometries is fully developed on the course of this study. A double domain decomposition scheme that allows both codes to be executed in parallel is designed. The multi-physics core solver is verified for steady state simulations. nTF/CTF is also compared with nTF using a simplified 1D T/H solver, proving that to achieve accurate predictions, computational tools of different fidelity should not be mixed. Finally, nTF/CTF is developed for 3D full core cycle analysis. The coupled code system is validated with experimental data, achieving the target accuracy set for industrial use. The capability of the solver for sub-pin predictions throughout the depletion cycle is demonstrated.

A conventional computational route for VVER analysis, built with CASMO5-VVER as a lattice code for the nodal neutronic solver PARCS, is also established. The use of PARCS with CASMO5-VVER is another novelty of the present work. CASMO5-VVER/PARCS is verified and validated for VVER standalone neutronic and multi-physics steady state simulations and cycle analysis. The modeling options that optimize the use of the code system and the generation of CASMO5-VVER cross-sections for PARCS are described.

The comparison of the novel and conventional computational routes demonstrates the accuracy enhancement enabled by the high-resolution core solver, during steady state and depletion calculations. The work performed during this thesis also showed that the nTF/CTF computational requirements are manageable for VVER cycle analysis, when a state-of-the-art computing cluster is used. This illustrates that such high fidelity, high-resolution computational scheme can be used as an audit tool for the conventional route.

Keywords: Multi-physics, high-resolution, VVER, cycle analysis, nTRACER, COBRA-TF, CASMO5-VVER, PARCS

Résumé

La conception et l'exploitation d'une centrale nucléaire (CN) nécessitent un grand nombre de simulations pour leurs analyses de sûreté. La norme pour la modélisation des CNs est l'approche dite conventionnelle, qui repose sur un calcul de diffusion à maillage grossier pour le solveur neutronique et sur une description 1D des éléments du réacteur pour le solveur T/H. L'évolution récente des clusters de calcul permet l'utilisation d'une nouvelle approche, avec des codes effectuant des simulations multi-physiques basées sur une approche mécanistique avec une haute résolution des paramètres calculés. En raison de leur coût de calcul, ces méthodes ne peuvent être utilisées que comme un outil d'audit de l'approche conventionnelle. Ces dernières années, l'industrie nucléaire s'est orientée vers l'établissement de limites de sécurité de type "Best Estimate Plus Uncertainty". Cette nouvelle approche constitue un pas dans cette direction. En le même temps, la technologie VVER se développe, avec la construction de nouveaux réacteurs dans le monde entier. Cependant, il n'existe actuellement aucun outil de calcul couplé à haute résolution pour l'analyse du cycle des VVERs, un besoin évident que la présente thèse s'entend à combler.

L'objectif de cette thèse est donc le développement d'un nouveau schéma de calcul basé sur le code de transport hétérogène en 3D, nTRACER-FAST (nTF), couplé au code sous-canal COBRA-TF (CTF) pour l'analyse de l'état stationnaire et du cycle d'un cœur complet de VVER. Le couplage d'un code neutronique à résolution fine (les variations internes au crayon sont calculées) à un solveur T/H capable de résolution équivalente; ainsi que leur application à la modélisation d'un cœur complet de VVER durant un cycle sont les principales nouveautés de ce travail. Dans cette thèse, nTF est vérifié et validé pour des calculs de neutronique pure pour un cœur de VVER, à l'aide de données publiées dans des benchmarks internationaux, utilisées comme référence. Le couplage interne de haute résolution entre nTF et CTF pour les géométries hexagonales est entièrement développé au cours de ce travail. Sa vérification est réalisée avec succès par comparaison à un schéma de calcul de référence. Enfin, un modèle nTF/CTF est développé pour l'analyse d'un cycle complet d'un cœur de VVER. La comparaison à des données expérimentales permet de démontrer que la précision voulue pour

une utilisation industrielle est atteinte. La capacité du solveur à modéliser les variations fines de puissance tout au long du cycle est démontrée.

Une voie de calcul conventionnelle pour l'analyse d'un VVER, construite avec CASMO5-VVER comme code de réseau et PARCS comme code de cœur, est également établie. L'utilisation de PARCS avec CASMO5-VVER est une autre nouveauté du présent travail. La méthode est vérifiée et validée pour des simulations neutroniques pures, ainsi que pour des simulations couplées de cycle, d'un cœur de VVER.

La comparaison des deux approches de calcul permet de quantifier les améliorations en termes de précision permises par le solveur de haute résolution. Le travail effectué au cours de cette thèse a également montré que les exigences en termes de coûts de calcul de nTF/CTF sont gérables pour des analyses de cycle de VVER, lorsqu'un cluster de calcul de pointe est utilisé. Ceci illustre le fait qu'un tel schéma de calcul à haute-fidélité et haute résolution peut être utilisé comme un outil d'audit pour la voie conventionnelle.

Table of Contents

Acknowledgements.....	iv
Abstract.....	vii
Résumé.....	ix
Table of Contents.....	xii
List of Figures.....	xvi
List of Tables.....	xxiii
Introduction.....	1
Chapter 1 Background & Motivation.....	6
1.1 Research Motivation.....	6
1.2 Previous work on the area of VVER simulation tools.....	9
1.3 Research goals.....	13
Chapter 2 Theory.....	18
2.1 Objective.....	18
2.2 High Performance Computing and available computing clusters.....	19
2.3 nTRACER – Fast.....	22
2.3.1 Cross-section generation.....	22
2.3.2 Planar MOC on hexagonal geometry.....	23
2.3.3 3D CMFD Formulation.....	26
2.3.4 1D Axial Solver.....	28
2.3.5 Parallelization.....	29
2.3.6 Cycle depletion.....	30
2.3.7 Simplified T/H solver.....	30
2.4 COBRA-TF.....	31
2.4.1 Conservation Equations.....	31
2.4.2 CTF Computational grid and discretized conservation equations.....	33
2.4.3 Numerical solution.....	34
2.4.4 Conductor Models.....	35
2.5 Codes for conventional VVER analysis.....	37

2.5.1	Parametrization of few group macroscopic cross-sections.....	38
2.5.2	CASMO5-VVER.....	39
2.5.3	GenPMAXS.....	41
2.5.4	PARCS.....	42
2.6	Codes for verification of the LRT solvers.....	43
2.6.1	Serpent2.....	43
2.6.2	SUBCHANFLOW.....	44
2.7	Benchmarks for verification and validation & target accuracy.....	44
2.7.1	NURESIM-SP1 V1000-2D benchmark.....	45
2.7.2	X2 benchmark.....	46
2.7.3	Target accuracy.....	50
Chapter 3	Neutronics Standalone Calculations for the Hot Zero Power State	52
3.1	Objective	52
3.2	Neutronic analysis with the novel approach	53
3.2.1	nTF vs Serpent2 for simple VVER configurations	54
3.2.2	Verification with a 2D full core model with a heavy reflector.....	58
3.2.3	Verification with a 3D full core model and validation with experimental data	67
3.3	Neutronic analysis with the conventional approach.....	82
3.3.1	Verification of PARCS with 2D full core models.....	82
3.3.2	Verification of CASMO5-VVER for 2D geometries	84
3.3.3	Verification of the CASMO5-VVER/PARCS code system with a real 3D VVER-1000 core model	88
3.4	Major outcomes of the work presented in this chapter	92
Chapter 4	Multi-Physics Analysis of the Hot Full Power State	94
4.1	Objective	94
4.2	Development of the nTF/CTF core solver	96
4.2.1	Internal coupling scheme.....	97
4.2.2	Domain Decomposition.....	99
4.2.3	CTF pre-processor for hexagonal geometries in nTF.....	102
4.2.4	Introduction of the CTF fuel pin temperature profile to the coupled code system	103
4.2.5	Parallelization	105
4.2.6	Capabilities and coupled compilation of the nTF and CTF versions used for the LRT multi-physics core solver.....	107
4.3	Comparison of the nTF/CTF core solver with the Serpent2/SUBCHANFLOW high-resolution multi-physics code system	109

4.3.1 Study of basic functions of the coupled code systems for HFP calculations	109
4.3.2 VVER full core comparison	114
4.4 Comparison of the nTF/CTF core solver with the nTF/1D-TH multi-physics tool	123
4.4.1 Mini-core models.....	123
4.4.2 VVER-1000 full core comparison.....	127
4.5 Multi-physics analysis with the conventional approach	132
4.6 Major Outcomes of the work presented in this chapter	133
Chapter 5 Multi-Physics Depletion Analysis.....	136
5.1 Objective	136
5.2 Cycle analysis with nTF/CTF	138
5.2.1 Assessment of the nTRACER depletion solver with Serpent2	138
5.2.2 nTF/CTF cycle analysis scheme.....	141
5.2.3 The LRT core solver X2 model for cycle analysis.....	146
5.2.4 Comparison of the nTF/CTF cycle analysis with experimental data	149
5.3 Cycle analysis with CASMO5-VVER/PARCS	157
5.3.1 CASMO5-VVER case matrix for cycle analysis	157
5.3.2 Comparison of the CASMO5-VVER/PARCS cycle analysis with experimental data	158
5.4 Comparison of the novel and conventional LRT solver for VVER-1000 cycle analysis	162
5.5 Major Outcomes of the work presented in this chapter	166
Conclusions & Future Work	168
Appendix.....	174
Bibliography	177
Curriculum Vitae	191

List of Figures

Figure 1.1. Illustration of the effect of the BEPU approach on the safety margins (left) and possible power uprate (right) [3].....	7
Figure 1.2. VERA calculation tools diagram [50]	12
Figure 2.1. A socket or NUMA and the structure of an HPC machine built with NUMAs [76]	19
Figure 2.2. Workflow of a series of parallel tasks (left), and OpenMP and MPI operative scheme [5].....	20
Figure 2.3. MOC domain decomposition [82].....	24
Figure 2.4. nTF MOC calculation scheme.....	25
Figure 2.5. Pincell mesh of MOC and CMFD for an hexagonal assembly	28
Figure 2.6. Scalar (top, left) axial momentum (top, right) and transverse momentum (down) computational mesh of CTF.....	34
Figure 2.7. Meshing of the fuel rod, where j is the axial discretization, k the azimuthal segments and i the radial mesh cells with thermal resistances R	36
Figure 2.8. Flowchart of CASMO5/PARCS code system.....	37
Figure 2.9. Example of depletion trees and branches for a case matrix	39
Figure 2.10. Left: The unrodded symmetric fresh fuel loading of exercise V1000-2D-C1. Right: Technical drawing of the heavy reflector of the VVER-1000 core as specified in the benchmark [96].....	45
Figure 2.11. Fuel designs, core layout and Serpent2 model of the heavy reflector for the X2 benchmark.....	47
Figure 2.12. Axial layout of the Serpent2 fuel pin model	47
Figure 2.13. Positions of the control rod banks in $1/3^{\text{rd}}$ of the reactor core, together with the “stuck” rod	48
Figure 2.14. Power history and boron letdown curve for the 1st cycle of X2.....	49
Figure 3.1. Eigenvalue difference of nTF vs Serpent2 for 2D pincells of different enrichment	55
Figure 3.2. Pin layout of X2 fuel assembly 13AU (left) and 390GO (right).....	57

Figure 3.3. Relative pin power difference of nTF vs Serpent2 for the X2 fuel assembly 13AU (left) and 390GO (right).....	57
Figure 3.4 (<i>Fig. 2.10</i>) Left: The symmetric fresh fuel loading of exercise V1000-2D-C1-tr. Right: Technical drawing of the heavy reflector of the VVER-1000 core as specified in the benchmark.....	59
Figure 3.5. Left: A reflector section corresponding to one assembly, as specified in the benchmark specifications. Right: nTF model II of the same assembly with homogeneous pincells for the water gap.....	60
Figure 3.6. Relative assembly power difference and eigenvalue difference between nTF and Serpent2 for the case with a simplified [model I] (left) and a refined [model II] (right) reflector model in nTF.....	61
Figure 3.7. Normalized power for the VVER-1000 core as calculated by Serpent2.....	62
Figure 3.8. Relative pin power difference between nTF and Serpent2 for the case with a simplified [model I] (left) and a refined [model II] (right) reflector model in nTF.....	63
Figure 3.9. Exact geometry (top left) and nTF model III (top right) of the reflector water gap. nTF model II (bottom) with homogeneous pincells for the water gap.....	64
Figure 3.10. Relative pin power difference between nTF and Serpent2 for the case with a semi-explicitly modeled reflector water gap in nTF [model III].....	65
Figure 3.11. Relative pin power difference between nTF and Serpent2 for the case with a semi-explicitly modeled reflector water gap in nTF [model III] and P2 anisotropic scattering approximation.....	66
Figure 3.12. (<i>Fig. 2.11</i>) Fuel designs, core layout and Serpent2 model of the heavy reflector for the X2 benchmark.....	68
Figure 3.13. Serpent2 reference X2 model details [98] and corresponding nTF approximations.....	71
Figure 3.14. Relative pin power difference between nTF and Serpent2 (left) and axial relative power profile of both codes (right). All approximations are used in nTF.....	74
Figure 3.15. Relative pin power difference between the nTF HZP final X2 model and Serpent2.....	76
Figure 3.16. Relative assembly power difference between nTF and Serpent2 vs core height and relative difference of the axial power profile at the same level.....	77
Figure 3.17. Relative pin power difference between the nTF HZP final X2 model with P2 anisotropic scattering and Serpent2.....	78
Figure 3.18. (<i>Fig. 2.13</i>) Positions of the control rod banks in the reactor core.....	79

Figure 3.19. S-curve and differential rod worth for CR #10	80
Figure 3.20. Reflector models used for two-group cross-section generation with Serpent2 [108]	83
Figure 3.21. Relative difference of the assembly power map calculated by Serpent2/PARCS vs the Serpent2 reference solution for exercise V1000-2D-C1 [108]	84
Figure 3.22. Radial layouts of Rostov-2 assemblies [102]	85
Figure 3.23. Eigenvalue comparison between CASMO5-VVER and Serpent2 for rodded and unrodded assemblies with P0 and P3 scattering treatment [102]	85
Figure 3.24. Two-group cross-section comparison of CASMO5-VVER vs Serpent2 [102] ..	86
Figure 3.25. Rostov-2 core layout and CASMO5-VVER reflector model [102]	87
Figure 3.26. Relative difference of the normalized pin power as calculated by CASMO5-VVER with P0, P3 and P5 scattering treatment vs Serpent2.....	87
Figure 3.27. Heavy reflector assembly model (REFLE3) in Serpent2 (left) and CASMO5- VVER (right)	89
Figure 3.28. Relative difference of the assembly power and difference in BC between CASMO5-VVER/PARCS and the X2 reference solution for model (A) without corner stiffeners, (B) with corner stiffeners and (C) with the CASMO5 critical spectrum correction	90
Figure 4.1. Structure of the nTRACER/CTF & of the nTF/CTF coupled code system	98
Figure 4.2. Internal coupling scheme for the nTF/CTF multi-physics core solver.....	99
Figure 4.3. Domain Decomposition in nTF and CTF and superimposition of the meshes ...	100
Figure 4.4. Numbering scheme of computational cells for a hexagonal geometry mini-core in nTF (top) and CTF (bottom)	101
Figure 4.5. Radial discretization of the fuel pin in nTF_1D-TH and CTF for the fuel conduction solver.....	103
Figure 4.6. Double domain decomposition parallelization scheme of nTF/CTF	105
Figure 4.7. Eigenvalue difference of nTF vs Serpent2 as a function of moderator density (a) and eigenvalue of the same codes as a function of fuel temperature (b) for a 3.6% w/o pincell	110
Figure 4.8. Relative pin power difference of nTF vs Serpent2 for the X2 fuel assembly 13AU (left) and 390GO (right) for HFP.....	111
Figure 4.9. Fuel thermal conductivity defined by CTF and SCF as a function of temperature	113

Figure 4.10. Zircaloy specific heat capacity (left) and thermal conductivity (right) defined by CTF and SCF as a function of temperature	113
Figure 4.11. Relative pin power difference between nTF/CTF and Serpent2/SCF for the X2 HFP state.....	115
Figure 4.12. Axial relative power profile and its relative difference between nTF/CTF and Serpent2/SCF for the X2 HFP state	115
Figure 4.13. Relative assembly power difference between nTF/CTF and Serpent2/SCF vs core height and relative difference of the axial power profile at the same level	116
Figure 4.14. Axial relative power profile of both codes and absolute coolant temperature difference between nTF/CTF and Serpent2/SCF as a function of height.....	118
Figure 4.15. Typical radial temperature distribution in a LWR fuel rod measured experimentally [120].....	118
Figure 4.16. Absolute coolant temperature difference and absolute fuel Doppler temperature difference (top) and relative axial power difference and absolute fuel Doppler temperature difference (bottom) between nTF/CTF and Serpent2/SCF as a function of height.....	119
Figure 4.17. Location of the selected pin in the core (left). Absolute center and surface temperature difference between nTF/CTF and Serpent2/SCF for the selected pin (right)....	120
Figure 4.18. Axial relative power profile its relative difference between nTF/CTF and Serpent2/SCF for the X2 HFP state with SCF & CTF material properties	121
Figure 4.19. Axial Doppler temperature profile and its absolute difference between nTF/CTF and Serpent2/SCF for the X2 HFP state with SCF & CTF material properties	121
Figure 4.20. Relative difference of the axial power profile, $[(Pow_{nTF/1D-TH} - Pow_{nTF/CTF}) / Pow_{nTF/1D-TH}]$, between nTF/CTF and nTF/1D-TH for <i>Case 0 & Case 4</i>	126
Figure 4.21. Absolute difference of the coolant temperature, $[Cool.Tem_{nTF/1D-TH} - Cool.Tem_{nTF/CTF}]$, between nTF/CTF and nTF/1D-TH for <i>Case 0 & Case 4</i>	126
Figure 4.22. Relative difference of the pin power profile, $[(Pow_{nTF/1D-TH} - Pow_{nTF/CTF}) / Pow_{nTF/1D-TH}]$, between nTF/CTF and nTF/1D-TH for <i>Case 0 & Case 4</i>	126
Figure 4.23. Absolute difference of the pin-wise coolant temperature at the mid-height of the mini-core, $[Cool.Tem_{nTF/1D-TH} - Cool.Tem_{nTF/CTF}]$, between nTF/CTF and nTF/1D-TH for <i>Case 4</i>	127
Figure 4.24. Temperature profile of a pincell calculated by CTF and the nTF fuel conduction model, starting with the same fuel gap temperature	127
Figure 4.25. Relative pin power difference between nTF/CTF and nTF/1D-TH for the X2 HFP state	128

Figure 4.26. Axial relative power profile and its relative difference between nTF/CTF and nTF/1D-TH for the X2 HFP state	129
Figure 4.27. Relative assembly power difference between nTF/CTF and nTF/1D-TH vs core height and relative difference of the axial power profile at the same level.	130
Figure 4.28. Axial relative power profile of both codes as a function of height and absolute coolant temperature difference between nTF/CTF and nTF/1D-TH.	131
Figure 4.29. Absolute coolant temperature difference and absolute volume-averaged fuel temperature difference between nTF/CTF and nTF/1D-TH as a function of height.	131
Figure 4.30. Relative difference of the assembly power and difference in BC between the CASMO5-VVER/PARCS X2 model with corner stiffeners and the reference solution for the HFP (left) and HZP (right) case.	133
Figure 5.1. Eigenvalue difference (a) and relative difference of the number density of U-235 (b), Pu-241 (c), Xe-135 (d) and Sm-149 (e) between nTRACER and Serpent2 as a function of BU	141
Figure 5.2. Eigenvalue difference and relative difference of the number density of important isotopes for the 2.2% pin between nTRACER and Serpent2 as a function of BU	141
Figure 5.3. nTF/CTF depletion calculation scheme for BU step k	143
Figure 5.4. Data stored in the nTF restart file for a moderator FXR and a fuel FXR.	145
Figure 5.5. Real CR geometry (left) and nTF model (right).....	146
Figure 5.6. Measured and Simplified power history for the 1 st cycle of X2 as a function of Effective Power Days (EFPDs)	147
Figure 5.7. Axial power profile with and without the 1D MOC axial solver for X2 HZP 1/6 th core and relative difference.....	149
Figure 5.8. nTF/CTF relative pin power maps for the X2 BOC, MOC & EOC.....	151
Figure 5.9. nTF/CTF calculated and measured boron curve for the 1 st X2 cycle. The difference of the calculation vs the measurement is also presented.....	152
Figure 5.10. Measured and simplified power history for the 1 st cycle of X2 as a function of EFPDs. The difference of the calculation vs the measurement is also presented.....	152
Figure 5.11. Comparison of the nTF/CTF assembly power vs experimental and reconstructed data for the three measurement points (1 st : 29.8 EFPDs, 2 nd : 90.8 EFPDs & 3 rd : 208.7 EFPDs)	155
Figure 5.12. Sub-pin power profiles of selected pins at mid-core height for the three measurement points (1 st : 29.8 EFPDs, 2 nd : 90.8 EFPDs & 3 rd : 208.7 EFPDs).....	156

Figure 5.13. Boron letdown curve for the 1st cycle of X2 measured and calculated by CASMO5-VVER/PARCS with the UM case-matrix as a function of BU. The difference of the calculation vs the measurement is also presented..... 159

Figure 5.14. Comparison of the CASMO5-VVER/PARCS assembly power vs experimental and reconstructed data for the three measurement points (1st: 29.8 EFPDs, 2nd: 90.8 EFPDs & 3rd: 208.7 EFPDs)..... 161

Figure 5.15. Boron letdown curve measured and calculated by nTF/CTF and CASMO5-VVER/PARCS with the absolute difference as a function of EFPDs 163

Figure 5.16. Axial offset measured and calculated by nTF/CTF and CASMO5-VVER/PARCS as a function of EFPDs 164

List of Tables

Table 2.1. Technical features of the different computational environments used in this study	21
Table 2.2 Structure of the history trees and operating conditions of the branches for the case-matrix used in this thesis. TMO: moderator temperature, H: history	39
Table 2.3. Operational conditions for all HZP simulated states of the X2 core	48
Table 2.4. Exposure and power level of the three measurement points in the 1st cycle of X249	
Table 2.5 Target accuracy for all parameters used for verification & validation in this study	50
Table 3.1. Pin power and eigenvalue difference of nTF vs Serpent2 for the X2 3D core.....	78
Table 3.2. Temperature reactivity coefficients simulated and experimentally measured.....	80
Table 3.3. Eigenvalue difference of nTF from Serpent2 for the 2D assembly model of CR bank #10.....	81
Table 3.4. Experimentally measured and calculated SCRAM worth	82
Table 3.5. Pin power and eigenvalue difference of CASMO5-VVER vs Serpent2 for 2D Rostov-2.....	87
Table 3.6. Assembly power, axial profile and boron concentration difference of CASMO5-VVER/PARCS vs Serpent2 for the X2 3D full core models A, B and C.....	91
Table 4.1. Modules used for the compilation of nTF/CTF in LCLRS and Merlin6.....	107
Table 5.1. Operating conditions of the simplified cycle history simulated by nTF/CTF and the calculated boron concentration	150
Table 5.2. Operating conditions of the three measurement points	154
Table 5.3. Maximum relative difference and RMS of nTF/CTF vs experimental and reconstructed data for the three measurement points.....	154
Table 5.4 (<i>see Table 2.2</i>). Structure of the history trees and operating conditions of the branches used in the UM case-matrix. TMO: moderator temperature, TF: fuel temperature, H: history	158
Table 5.5. Maximum relative difference and RMS of CASMO5-VVER/PARCS vs experimental and reconstructed data for the three measurement points	160
Table 5.6. Maximum relative difference and RMS of nTF/CTF and CASMO5-VVER/PARCS vs experimental and reconstructed data for the three measurement points	164

Table 5.7. Computational time requirement of the LRT solvers for the simulation of the 1st X2 cycle 165

Introduction

The thesis is organized in five chapters that describe the motivation, methodology and outcomes of this study. Chapters 1 & 2 present the background, research goals and theory of the project, whereas Chapters 3 to 5 are dedicated to the results of the work performed during the course of the PhD. Chapters 3 to 5 have the same structure: they start with a description of their specific objectives as well as the role of those objectives towards the goals of the thesis. Specific questions and issues that arose in the course of the project are also developed. Once the objectives are set, the relevant work performed to achieve these objectives is detailed. This refers to the programming tasks, like modifications on the codes, and necessary sensitivity analyses, like optimization of the modeling options. All approximations made during the course of this work are identified and their possible impact is discussed or, optimally, quantified. Finally, the results are presented and discussed. The accuracy of the solution is assessed according to pre-defined criteria and the sources of discrepancies are investigated. Bottlenecks that can cause discrepancies in the next steps of the thesis, as well as, areas that require improvement are identified. At the end of the thesis, all the conclusions drawn in the various chapters, are summarized and the achievements of the PhD are put in perspective of the defined research goals. Future work and improvement of the computational routes are also discussed.

Chapter 1 begins with the research motivation of this thesis. The Water-Water Energetic Reactor (VVER) is a pressurized light water reactor with a hexagonal fuel lattice. The standard for the computational analysis of light water reactors is the so called conventional approach, which relies on coarse mesh diffusion for the neutronic solver and 1D channels for the T/H solver. The recent evolution of computing clusters allows the use of a novel approach, with computational tools performing first-principle based multi-physics simulations with high-resolution of the calculated parameters. In this chapter, the evolution of the computational tools employed for VVER safety analysis over the years is presented in detail, pinpointing the most popular codes and benchmarks that contributed to their development. The more advanced state of high-resolution high fidelity multi-physics solvers for Cartesian geometries is illustrated and compared to the tools currently used for high fidelity VVER analysis. The capabilities of the available novel solvers that can handle hexagonal geometries are also discussed, setting the

stage for the work performed during the PhD. The goal of this work is the development of a novel computational scheme based on the 3D sub-pin neutron transport code nTRACER-FAST (nTF), coupled to the sub-channel T/H code COBRA-TF (CTF) for VVER full core steady state and cycle analysis. A conventional computational route for VVER analysis, built with CASMO5-VVER as a lattice code for the nodal neutronic solver PARCS, is also established. The selection of these specific codes for the development of the novel and conventional core solvers is also discussed in this chapter.

Chapter 2 presents the computational tools involved in this study. The architecture of the clusters where all calculations are performed is briefly described, together with the parallelization techniques employed by the novel codes used in the thesis. Their methodology is presented in detail, with focus on specific functions or modeling options that prove important for this work. The solvers of the conventional computational route are also introduced, together with the method used to generate cross-section libraries for cycle analysis. In addition, the two benchmarks employed for the verification and validation (V&V) of the novel and conventional coupled code system, NURESIM-SP1 V1000-2D-C1-tr and X2, are presented in this chapter together with the codes used to produce a reference solution. The performance of the novel and conventional solvers is evaluated according to a set of pre-defined criteria, targeting specific levels of accuracy for a set of parameters, which is also presented in this chapter.

Chapter 3 focuses on standalone neutronic calculations with the solvers of both computational routes. The performance of nTF is assessed for Hot Zero Power (HZP) conditions with pincell and single assembly models against a Monte Carlo solution produced with the code Serpent2. The NURESIM-SP1 benchmark is used to verify nTF for 2D full core calculations, but, most importantly, to optimize the modeling of the VVER heavy reflector for high-resolution analysis. Several levels of approximations are introduced and their impact on the accuracy of nTF is quantified. With the optimal heavy reflector model, a V&V analysis of the nTF 3D core model of the X2 benchmark is carried out for the HZP conditions. Together with the description of the nTF X2 model, all necessary approximations and a mesh convergence study of nTF are presented. Different modeling options are studied for the corner stiffeners and anisotropic scattering in nTF, resulting to the optimized nTF X2 3D full core model, which is the basis for all full core calculations of this thesis. An existing Monte Carlo reference solution is used for verification purposes. nTF is also validated with experimental data of the X2 benchmark. Moving to the conventional route, PARCS and CASMO5-VVER are verified separately. PARCS is used to reproduce the NURESIM-SP1 benchmark with cross-

sections generated by Serpent2. CASMO5-VVER on the other hand is verified versus Serpent2 with pincell and single assembly models in terms of reactivity, two group constants and power distribution. The treatment of anisotropic scattering is also studied with CASMO5-VVER 2D full core models. In addition, the method of modeling the heavy reflector with the CASMO5-VVER/PARCS code system is discussed. It must be pointed out that a large portion of the conventional route verification has been carried out during a semester project and an internship I helped supervising. Finally, CASMO5-VVER is used to generate cross-sections for the PARCS model of the X2 benchmark. The coarse mesh solution is compared with the reference benchmark computational results in HZP conditions, testing different modeling options for the corner stiffeners and the leakage correction in CASMO5-VVER.

Chapter 4 is dedicated to multi-physics steady state calculations with the novel and conventional core solvers. The biggest part of this PhD was focused on the coupling of CTF to nTF for full core VVER analysis. The internal coupling scheme is described in detail together with all necessary modifications and the development of both the neutronic and thermal-hydraulic (T/H) solvers. This includes the introduction of matching mesh numbering schemes, according to the superposition of the CTF spatial discretization on the nTF mesh. In addition, a pre-processor for the creation of CTF inputs for hexagonal geometries is established within nTF and described in this chapter. The calculation of fuel pin radial temperature profiles (azimuthally averaged) by CTF and their transfer to nTF is also presented. Finally, the double parallelization scheme, employed for the execution of the internally coupled code system is described. The nTF cross-section library is assessed using Serpent2 in Hot Full Power (HFP) conditions. The novel core solver is employed for the calculation of the X2 HFP steady state. nTF/CTF is verified for the X2 HFP model against an available Serpent2/SUBCHANFLOW reference solution. The comparison includes power distributions and temperature profiles for the full core model and a selected pin. The effect of specific modeling options like the material properties used by the T/H codes and the method that applies fuel temperature feedback to the neutronic code are analyzed. In addition, the nTF/CTF coupled code system is compared with nTF and its embedded simplified T/H solver. The comparison begins with simplified models (mini-core) to establish the impact of major differences between the calculations schemes (e.g. cross-flow). Subsequently, the two multi-physics solvers (nTF/CTF vs nTF/1D-TH) are compared for the 3D full core VVER model. All discrepancies are discussed in the light of the simplified models' study conclusions. Finally, X2 HFP is also modeled with the conventional computational route using the internal simplified T/H solver of PARCS. The results (boron

concentration, axial and assembly power profiles) are also compared to the Serpent2/SUBCHANFLOW solution.

Chapter 5 reports on the expansion of both computational routes from steady state calculations to reactor cycle analysis. The depletion library of nTF is evaluated vs Serpent2. The nTF/CTF depletion analysis scheme is presented in detail, together with all necessary modifications on both codes to achieve such kind of calculation. These include the execution of CTF for multiple state-point calculations with a single initialization process, the production of restart files and the expansion of the nTF control rod module to hexagonal geometries. The large computational cost of the reactor cycle calculations requires further improvement of the X2 nTF and CTF models, especially with respect to the computational mesh. The impact of the modifications is quantified. Additional approximations are also introduced and, where applicable, marked as areas for future improvement. nTF/CTF is validated, using a simplified power history, with the X2 1st cycle boron let-down curve and measured power maps at specific burnup steps of the cycle. The evolution of the pin power distribution with exposure is discussed together with sub-pin power profiles of a selection of fuel pins. CASMO5-VVER/PARCS is also validated for the 1st cycle of X2, but with the detailed power history. The generation of the suitable CASMO5-VVER cross-section matrix for PARCS is discussed. Finally, the two routes (conventional and high-resolution) are compared in terms of accuracy and computational costs for the cycle calculation.

At the end of the thesis, all conclusions drawn from Chapters 3-5 are summarized in the “Conclusion & Future Work” section. The achievements of this PhD are discussed in reference to the research goals set in Chapter 1, but also for their scientific value in general. Finally, actions to improve the novel and the conventional core solver are suggested for the continuation of this study.

Chapter 1

Background & Motivation

«Αί μοῦσαι κατοικοῦσιν ἐν ταῖς ψυχαῖς τῶν φιλοπόνων»

1.1 Research Motivation

The ultimate goal of a Nuclear Power Plant (NPP) is to produce electricity with an efficient, financially competitive, but most importantly, safe manner. To that aim, modeling is key for many aspects of a NPP life cycle, from design to licensing, construction, operation and decommissioning. Verified and validated multi-physics and multiscale computational tools are necessary in order to reproduce the complex phenomena, taking place in a reactor and predict the evolution of the relevant parameters. The safe operation of a NPP is inherently connected with the accurate prediction of its core behavior. The conventional approach for the neutronic analysis of the reactor core consists of the pre-calculation of the necessary neutronic parameters, on a subset of the geometry, while using a detailed description of the space and energy variables (first step). Then, a separate code (second step) uses said parameters to perform simplified (diffusion or low order transport) neutron balance calculations in a much coarser space and energy discretization at the full core level. It is referred to as the “two-step approach”. The neutronic codes are coupled to thermal-hydraulic (T/H) solvers of similar resolution, capable of assembly-wise analysis of the core, at best, and coarse mesh modeling of the Reactor Pressure Vessel (RPV). The approximations involved in this type of analysis are a contributing factor to the establishment of conservative operational limits for NPPs [1]. Currently, the nuclear industry is re-evaluating this approach. The alternative is based on the calculation of the best estimated value of those parameters, complemented with uncertainty limits (BEPU) [2] (see Fig. 1.1).

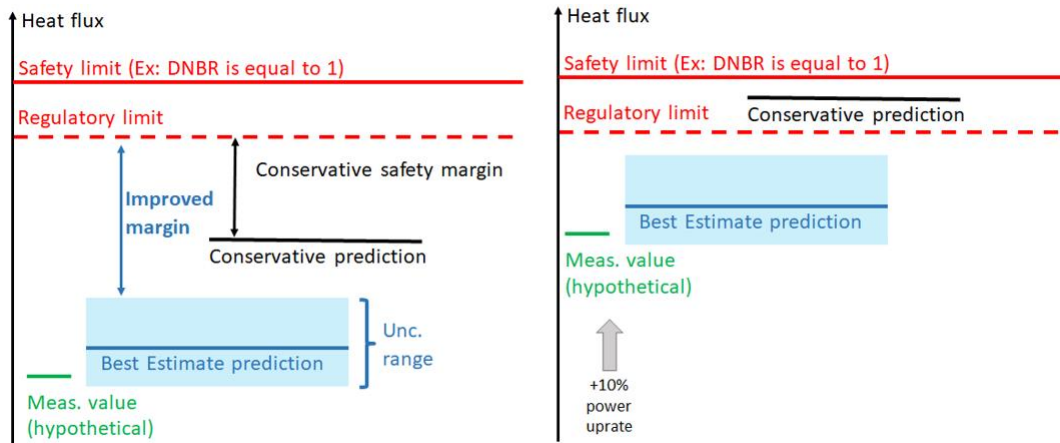


Figure 1.1. Illustration of the effect of the BEPU approach on the safety margins (left) and possible power uprate (right) [3]

In recent years, the evolution of computing power and computational techniques lead to the development of codes capable of multi-physics simulations of high-resolution models. The novel approach aims at pin level, or optimally sub-pin level, neutronic calculations, using cross-sections generated on the fly and sub-channel codes with heat conduction analysis at the sub-pin level (fuel rods meshed radially, azimuthally and axially). Novel solvers allow for more tightly coupled and more first-principles-based modeling with higher accuracy. These high fidelity high-resolution codes aim at the prediction of safety parameters, like the fuel temperature, on a local scale, simulating local heterogeneities (e.g. local CRUD formation) and their consequences, which are approximated or excluded in coarse mesh calculations. The production of information with few approximations on a local scale provides a detailed representation of the core behavior, revealing problematic regions, which can be sources of fuel rod failure [4], and should in principle allow a more accurate estimation of the operational conditions in the core. Hence, the use of high fidelity high-resolution computational tools can help remove some of the conservatism and reduce the safety margins while guaranteeing the same level of safety. Reducing the safety margins would require design and operation analyses with tools of high fidelity and resolution (e.g. sub-pin flux profile as input in fuel behavior codes). The computational cost of such calculations is significant, larger than the cost of the conventional approach, and requires large computing clusters [5]. Despite the ongoing growth of computational environments, high fidelity methods are not suitable yet for routine production calculations. However, they can be used as an audit tool for the conventional approach, to enhance its prediction capabilities through a better understanding of its source of biases. The use of high-resolution core solvers, by facilitating the establishment of a larger safety margin (= margin to acceptance criteria, Fig. 1.1) through the BEPU approach and

providing predictions that can monitor local phenomena, will result in more efficient and flexible use of the fuel and of the reactor [6]. The novel approach can be used to tackle important issues for achieving power uprates, lifetime extension, and higher fuel burn-up while ensuring that fuel performance and safety are optimized for the existing reactors and to improve the design and safety of the new reactors. This is crucial for the future of Nuclear Energy, since the current energy policies demand more competitive electricity prices and load following systems available for different applications [7].

Currently, the water-water energetic reactor (VVER) technology is under expansion, including new projects in emerging nuclear countries but also in established ones such as Finland. The VVER is a type of Light Water Reactor (LWR) originally developed in Russia. It is a pressurized water reactor (PWR), initially designed by OKB Gidropress before the 1970s. There has been continuous development of VVERs, resulting in a series of models with increasing power outputs. The most common designs are the VVER-440, the VVER-1000 and the VVER-1200, which evolved to VVER-TOI. The VVER-440 is a six cooling loops model, whereas the other two are limited to four cooling loops. The main distinguishing feature of the VVER from other PWRs is the use of hexagonal fuel assemblies. Other important differences are the presence of horizontal steam generators, the absence of bottom penetrations in the pressure vessel and the use of high capacity pressurizers, to ensure a large coolant inventory. In comparison to other Russian reactor types (e.g. RBMK), VVERs use an inherently safer approach, e.g. water moderation instead of graphite, including four safety barriers, the fuel pellet, the cladding, the RPV and the reactor containment. Therefore, a number of countries, mostly in Europe (e.g. Hungary, Czech Republic, Finland, Russia), but also in Asia (e.g. China, Iran, India) are operating or constructing VVER installations.

The status of VVERs worldwide has led to the evolution of computational tools and methods that can treat hexagonal geometry, in order to simulate and analyze the reactor core. However, at the time of writing, there is only one high-resolution core solver available for VVER multi-physics cycle analysis, based on a Monte Carlo code coupled to a sub-channel code and a fuel thermo-mechanics solver [8]. This code system cannot be used as a regular audit tool due to its large computational requirements [6]. More importantly, the coupled code system does not have the capabilities for sub-pin analysis, limiting its predictions to pin-by-pin calculations. Monte-Carlo codes cannot obtain statistically converged estimates of the power distribution within the fuel pellet in a practical amount of time, requiring T/H feedback with a single fuel temperature per pin and not a profile, which increases the uncertainty range of the

calculated safety parameters. Considering the abundance of VVER installations all over the world and their current expansion plans in Europe, there is a clear need for the development of refined multi-physics simulation tools capable of providing high fidelity high-resolution VVER full core analysis.

1.2 Previous work on the area of VVER simulation tools

The use of coarse mesh methods for the prediction of the neutronic behavior of the LWRs was established already since the 1970s [9]. These so-called nodal methods rely on solving the neutron diffusion equation or low-order transport on homogenized assemblies, axially meshed. Typical examples are KIKO-3D from KFKI Budapest [10], DYN3D from Rossendorf [11] and HEXTRAN from VTT Finland [12]. The cross-sections for the homogenized volumes are pre-calculated by separate 2D lattice codes using transport or stochastic methods. The energy discretization in the core wide solution is usually limited to two groups. Validated lattice codes widely used for VVER analysis are HELIOS [13] and EXCEL [14]. Nodal methods have evolved through the years. As research aimed at the constant improvement of the simulation tools used for the reactor core, new methods were developed to solve the diffusion equation on hexagonal geometry. The few group diffusion code TRIPHEX employed a finer meshing calculation technique of the large hexagonal homogenized assembly by dividing it into $6n^2$ triangular meshes, where 'n' is the number of equal divisions on a side of the hexagon [15]. ANDES, a multi-group diffusion code, used the Analytic Coarse Mesh Finite Difference method (ACMFD) on 6 triangular nodes for each axial layer of the homogenized assembly [16]. The diffusion code ACNECH applied higher order polynomials on the nodal expansion method [17]. At the same time, codes that can do diffusion on the homogeneous pin level were developed and verified for VVERs. HEXPIN [18] could perform few-groups neutron diffusion calculations for the homogenized pin, with data provided by the lattice code EXCEL on the 2D VVER core. Nodal methods remain the first choice for reactor safety analysis. Even at the countries of origin of the VVER, the majority of 3D full core calculations are still performed by nodal diffusion solvers at the assembly level or at the pin level. C-PORCA is a nodal diffusion code used extensively at Paks in Hungary [19]. The KASKAD 2007 software [20] is developed by Kurchatov Institut and includes a 3D coarse mesh (BIPR-8A) [21] and a 2D pin-by-pin diffusion solver (PERMAKA).

The coupling of nodal codes to T/H solvers is also a well-established approach. The conventional T/H solvers are capable of two-phase flow calculations in assembly sized

channels with several axial layers. The energy deposition in the core through fission is determined by the neutronic solver and taken into account in the T/H solver by one or more heat structures per assembly, up to one per fuel rod. Typical examples of T/H system codes used for VVER analysis are ATHLET [22], CATHARE [23], SMABRE [12] and RELAP [24]. The Kozloduy-6 benchmark [25]–[27] had a major impact on the evolution of computational tools for VVERs. This benchmark established several of the coupled code systems used for VVER analysis today and is still employed for the validation of conventional solvers [28]–[30]. Typical examples are DYN3D/ATHLET, PARCS/TRACE, BIPR8/ATHLET, COBAYA/COBRA. Several methods of coupling were tested (internal, external, parallel), especially for DYN3D/ATHLET [22], in order to improve the efficiency and accuracy of the simulations and, in later years, parallel processing of core solvers through platforms on the premise of the same benchmark was performed as well [31]. The major outcome of the benchmark was the identification of the coolant mixing in the reactor vessel as an unresolved issue in the analysis of complex plant transients with reactivity insertion. This benchmark was crucial for the development of T/H solvers [32], which were not adequate at the time to capture the phenomena occurring at the lower, upper plenum and the downcomer. Currently, the plant system is modeled by 1D components and the RPV is built either with several 1D parallel channels interconnected with cross-flow (quasi-3D, ATHLET) or as a 3D volume radially and axially meshed (3D, TRACE [28]). This method of RPV modeling succeeds in capturing the 3D coolant mixing phenomena occurring in the lower plenum and the downcomer [28], [33]. Due to the impact of V1000CT, the OECD/NEA benchmark team launched a new benchmark for coupled 3D code systems, Kalinin-3 [34], designed in a great extent to test the issues that emerged from the Kozloduy-6 benchmark. The initial calculation schemes used to simulate Kalinin-3 included 3D nodal neutronic simulations of the core, one T/H channel per assembly and finer meshing of the RPV.

In contradiction to VVER analysis, the evolution of simulation tools for Cartesian geometry to high-resolution high fidelity solvers has been an integral part of nuclear research for the last decades. The progress in high performance computing (HPC) and the introduction of large state-of-the-art computing clusters motivated the development of novel multi-physics code systems as part of several large projects. The SALOME platform (2006-2015) was created on the premise of the NURESAFE project [35], [36] by 22 European organizations. It incorporates higher fidelity methods, innovative computational fluid dynamics, and fuel modeling codes. The MCSAFE project (2017-2020) aimed to make the Monte Carlo based

standalone and coupled code systems (advanced depletion, time-dependent Monte Carlo methods and algorithms for massively parallel simulations) suitable numerical tools for core design, safety analysis and industry applications of LWRs [37]. The Consortium for Advanced Simulation of LWRs (CASL) [38], [39] and the Nuclear Energy Advanced Modeling and Simulation (NEAMS) [40], [41] program, originally sponsored by the US Department of Energy, now merged into a joint modeling and simulation workbench. The workbench aims at the development of novel solvers to simulate every aspect of the reactor and to facilitate multiscale multi-physics safety analysis (including production tools and high fidelity tools) and design of LWRs. The state-of-the-art novel simulation tools, developed in the framework of the above projects or independently, for the analysis of LWRs are based on the following principles. Monte Carlo codes are coupled with T/H solvers, most commonly to provide reference multi-physics solutions. Deterministic neutronic solvers perform multi-group transport calculations over the whole core. The novel T/H solvers are based on sub-channel, porous media or Computational Fluid Dynamics (CFD) methods. The coupling of the codes is employed on the local scale of pin/sub-channel, optimally taking into account sub-pin heterogeneity. HPC methods are required due to the large computational costs of those multi-physics simulations. Uncertainty and sensitivity analysis methods are integrated in the development of multi-physics methods. An example of a novel high fidelity, high-resolution code system is VERA [42] (see Fig. 1.2). The platform was developed by CASL and can be considered one of the most advanced PWR 3D core simulators worldwide [6]. VERA is also expanding to BWRs [43]. Another example of a high-resolution deterministic neutronic solver, developed by SNU, independently of the above projects, is nTRACER [44]. nTRACER is capable of sub-pin predictions for steady state, transient and cycle analysis [45], [46], [47]. The code has been also coupled with the sub-channel codes MATRA [44], COBRA-TF [48] and ESCOT [49] for multi-physics high fidelity analysis.

Virtual Environment for Reactor Applications (VERA)

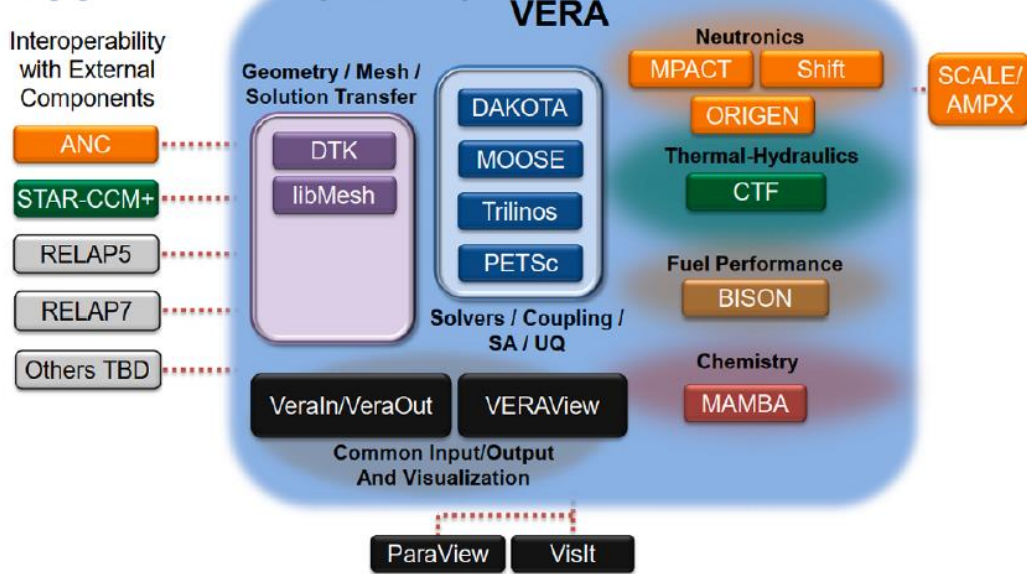


Figure 1.2. VERA calculation tools diagram [50]

Worldwide, the evolution of high-resolution tools for VVERs is ongoing, however, in a significantly slower pace than for Cartesian geometry. In order to solve a whole-core eigenvalue problem, COMET, capable of 3D VVER analysis [51], divides the core into a series of local fixed-source transport problems, each one of which is defined over a coarse mesh. It uses Monte Carlo methods to solve the series of fixed-source problems and to produce response functions, which then are used to determine the solution of the original problem (iterative process). Concerning deterministic neutronic solvers, several lattice codes can perform 2D full core VVER calculations (e.g. CASMO5-VVER [52]). However, Monte Carlo codes are the preferred method for high-resolution neutronic analysis of VVERs [53]. MCNP5 has recently been validated standalone for steady state simulations of a VVER-1200 [54]. It has also been used in the past to provide neutronic feedback (uncoupled) for the sub-channel T/H analysis of the Bushehr Nuclear Power Plant (BNPP) core by COBRA-EN [55]. On the other hand, full core high-resolution T/H analysis is more common. A full core VVER sub-channel model was developed and coupled with the KARATE-1200 code system [56] in the Hungarian Academy of Sciences. The system code ATHLET is used also with pin-wise meshing [57], [58]. The T/H module of KORSAR/GP, developed in Gidopress, is now capable of full core pin-by-pin simulations (several parallel channels with cross-flow) [59]. VIPRE-01 is a sub-channel code developed in the Czech experimental NPP UJV Rez for full core VVER analysis [60]. The

multi-physics core solver of COBAYA3/SUBCHANFLOW was validated with the Kalinin-3 benchmark [61] for 3D neutronic nodal calculations and sub-channel T/H analysis.

One of the reasons for the rarity of novel multi-physics simulation tools that can handle hexagonal geometry is the lack of high-resolution benchmarks to validate such solvers. In recent years this is changing, as can be reflected by the new specifications of two VVER-1000 benchmarks, X2 [62] and Rostov-2 [63]. X2 involves steady state, cycle and transient analysis, whereas Rostov-2 is focused on reactivity compensation through boron dilution and its associated stepwise insertion of a control rod cluster. Both benchmarks aim at the verification and validation of high-resolution multi-physics solvers for VVER analysis. The international projects, mentioned in the previous paragraph, that were established for the development of novel solvers, included coupled code systems for VVER analysis as well. However, all of them, except Serpent2/SUBCHANFLOW, did not involve high-resolution full core analysis both with the neutronic and the T/H solver. Serpent2 has been used for the 3D full core pin-by-pin analysis of VVERs standalone [62], and coupled to SUBCHANFLOW [64]. The most evolved pin-by-pin high fidelity solver for VVER steady state and cycle analysis is Serpent2/SUBCHANFLOW/TRANSURANUS [8], which was developed on the framework of the MCSAFE project.

1.3 Research goals

There are very few novel simulation tools available for VVER safety analysis in comparison to the options for Cartesian geometry. The state-of-the-art multi-physics core solvers are combining Monte Carlo codes with sub-channel T/H calculations [8], [65]. It was mentioned in section 1.1 that these coupled code systems are too computationally expensive to be used even as an auxiliary audit tool, especially for cycle analysis. In addition, due to their cost, they are not capable of sub-pin predictions, which are necessary for the accurate modeling of the local conditions in a VVER and the establishment of the BEPU approach for safety analysis. To broaden the portfolio of LWR related competences at the Nuclear Energy and Safety department (NES) of Paul Scherrer Institut, the Laboratory for Reactor Physics and T/Hs (LRT) launched an internal project, aimed at developing capabilities for VVER safety analyses. This thesis is the first step in this project. The desired outcome of this work is the development of both a novel and a conventional computational route for VVER steady state and cycle analyses, together with the assessment of the differences between the two calculation routes.

The novel computational scheme is based on the deterministic direct whole core neutron transport code nTRACER-Fast (nTF), developed at Seoul National University (SNU) [44], capable of 3D sub-pin transport calculations in hexagonal geometries. The code was initially envisioned as a Fast reactor simulator, where hexagonal lattices are typical. Moreover, the solver has been used by SNU, together with the nTRACER LWR library, for VVER calculations [66], [67]. In the course of this study, nTF has been coupled to the sub-channel T/H code COBRA-TF (CTF), which is developed in North Carolina State University (NCSU) and other institutes, to create the novel VVER core solver. The hexagonal capability for nTRACER was built in only recently by SNU [67] and requires further verification and validation, especially for 3D geometries. nTRACER is a continuously evolving sub-pin transport solver (2D/1D scheme), incorporating a variety of methods (e.g. different axial solvers, GPU & CPU parallelization) and modeling options (e.g. control rods, Xe dynamics) that ensure efficiency and accuracy for LWR modeling. nTRACER includes a coupling interface for T/H solvers and is developed with a hybrid parallelization scheme. The Reactor Physics Laboratory of SNU (SNURPL) is in close collaboration with LRT, where nTRACER has been used regularly for high-resolution high fidelity PWR analysis [5], [46]. As it was mentioned in the previous section, CTF has been verified for 3D VVER full core calculations on a coarse mesh [29] and for high-resolution hexagonal assembly analysis [68]. The sub-channel code uses a two-fluid modeling approach with three separate, independent flow fields. CTF includes a wide range of T/H models to ensure accurate LWR safety analysis. The capabilities of CTF exceed the requirements of this study. As a pressurized reactor, VVER experiences single-phase upward flow, except on transients. Since the core behavior is dominated by neutronic phenomena for steady state and cycle analysis, a solver based on more empirical correlations and less computationally expensive (e.g. SUBCHANFLOW) would have been adequate and easier to use. However, one of the goals of the LRT VVER project is to develop the high-resolution computational tool also for transient calculations. Thus, CTF is a much more suitable choice for the novel VVER solver, even though transient analysis is not part of this study. A CFD code is not considered for the coupling, since its computational cost is larger than the requirements of CTF. In addition, nTRACER and CTF have been coupled before, for steady state calculations in Cartesian geometry [69], which reduces the effort for the coupling to nTF. Finally, LRT has been focused solely on CTF as a sub-channel code for LWR high-resolution analysis [70]. In this thesis nTF/CTF is referred to as the novel LRT core solver.

The goal of this work is the verification and validation (V&V) of the high-resolution capabilities for standalone neutronic calculations, multi-physics steady state and depletion cycle analysis. The completion of such an objective required a thorough code verification of nTF, since the hexagonal solver is relatively new and in VVER normal operation the neutronic phenomena are the key factor for core behavior. For the same reason, the full core VVER CTF models are built and optimized only to provide T/H feedback to nTF. The T/H code did not undergo a standalone verification in the framework of the PhD, since CTF has been used more extensively for hexagonal geometries and the thesis does not include transient analysis; also, due to lack of time. However, the coupling and parallelization of both codes for hexagonal geometries and VVER analysis has been done within this PhD. Besides V&V, the objective of this study is the identification of bottlenecks and sources of discrepancies in the coupled code system and the quantification of their effect on the solution. The coupling of a neutronic code with sub-pin resolution to a sub-channel T/H solver, as well as the use of CTF and nTF, for 3D full core VVER high-resolution analysis are, to the extent of the writer's knowledge, a novel concept.

The conventional route is based on the code PARCS [71], a state-of-the-art 3D nodal reactor core simulator developed at the University of Michigan (UM), which solves the steady state and time-dependent multi-group neutron diffusion or low-order neutron transport equation in Cartesian or hexagonal geometries. PARCS has been validated for whole core VVER safety analysis [72], [73]. In general, PARCS is used coupled to system codes; however, it also includes a simplified T/H solver to provide feedback. At this stage of the VVER LRT project, PARCS is not coupled to a system code, since there is not transient analysis. PARCS also employs an external executable, GenPMAXS, to generate the appropriate cross-section library from the outcome of different lattice codes. In this work, the lattice code is CASMO5-VVER [52]. CASMO is developed by Studsvik Scandpower, solving the multi-group transport equation on 2D assembly or full core geometry based on the Method of Characteristics (MOC). CASMO and PARCS are used regularly in LRT for safety analyses on Cartesian geometry, independently or together [74]. Nonetheless, the module treating hexagonal geometry in CASMO is relatively new, thus further verification is required. In this thesis, CASMO5-VVER/PARCS is also referred to as the conventional LRT core solver. Besides the novel coupled code system, a V&V exercise is also carried out for the conventional computational route for standalone neutronic calculations, multi-physics steady state and depletion cycle analysis. CASMO5-VVER and PARCS are verified separately before they are employed

together to compute the same benchmarks as the novel solver. The impact of the simplified T/H solver on the coarse mesh neutronic solution is also discussed. The use of CASMO5-VVER with PARCS for full core VVER analysis has never been attempted before, to the extent of the writer's knowledge, thus the optimization of all relevant models, including the modeling options used for the generation of an accurate cross-section library by GenPMAXS, is a major outcome of this study. The goal is to provide LRT with a conventional core solver, using the standard two-steps approach (cross-sections generated by 2D assembly models, not full core model), which is capable of steady state and cycle analysis. The development of both a novel and a conventional computational route in parallel allows a better understanding of the corresponding methodology and the approximations involved in either approach. The two routes are compared in terms of accuracy on the coarse mesh solution. More importantly, the conventional solver is used as a measure of comparison for the capabilities and computational requirements of the novel approach. The thesis aims at introducing nTF/CTF, which can provide sub-pin predictions, as an audit tool for design and production calculations. The conclusions drawn from the study for the advantages and limitations of the high-resolution core solver will aid the improvement and subsequent establishment of such tools for VVER analysis.

Chapter 2

Theory

«Μηδέν εἶναι μῆτε τέχνης ἄνευ μελέτης μῆτε μελέτην ἄνευ τέχνης»

2.1 Objective

This chapter introduces the reader to the computational methods used in this study for the analysis of VVERs. The capabilities and methodology of the sub-pin 3D high-resolution neutronic code nTF and of the thermal-hydraulic (T/H) sub-channel code CTF are presented in detail. The conventional nodal code PARCS, together with the associated cross-section library generator GenPMAXS and the lattice code CASMO5-VVER are also described. Moreover, particular attention is given to specific features or functions of these codes that play an important role in the outcome of the study. The Monte Carlo code Serpent2 and the T/H solver SUBCHANFLOW are used in this thesis for the assessment and verification of the novel and conventional LRT core solvers. Their methodologies are also discussed in this chapter, especially to highlight similarities and differences with respect to the computational methods used by the LRT solvers. As it is explained in Chapter 1, high-resolution simulations of full core models are impossible without the use of computing clusters. Before presenting the capabilities of the code systems that are part of this study, the concept of computational parallelization, or High Performance Computing (HPC), is discussed together with the relevant techniques employed by the high-resolution solvers. In addition, the clusters used for the VVER analysis in this thesis are described briefly, focusing on their computational capacity. Finally, the verification and validation of the LRT core solvers is based on specific benchmarks of VVER NPPs, which are also introduced.

2.2 High Performance Computing and available computing clusters

The definition of HPC is “*High Performance Computing most generally refers to the practice of aggregating computing power in a way that delivers much higher performance than one could get out of a typical desktop computer or workstation in order to solve large problems in science, engineering, or business*” [75]. In computer engineering, each group of cores that is connected physically to the same memory banks, accessing the data with the same speed, is contained by a “socket” (see Fig. 2.1). Usually, a machine used for HPC may contain several sockets with their individual memory banks. However, all cores can access the memory banks on which they are not connected (e.g. through a hyper-transport bus), with a time penalty. Normally, only one socket is directly connected with the other components of the machine (e.g. graphics card). The remaining sockets exchange data with the rest of the machine or with other machines (when in cluster formation) through the connecting socket, resulting in latencies. When this structure is applied the sockets are called NUMAs (Non-Uniform Memory Access). A computing cluster is usually a collection of machines (computing nodes), built with NUMAs that communicate with specific protocols. The inter-node communication in a cluster experiences higher latencies than the communication between NUMAs in the same node.

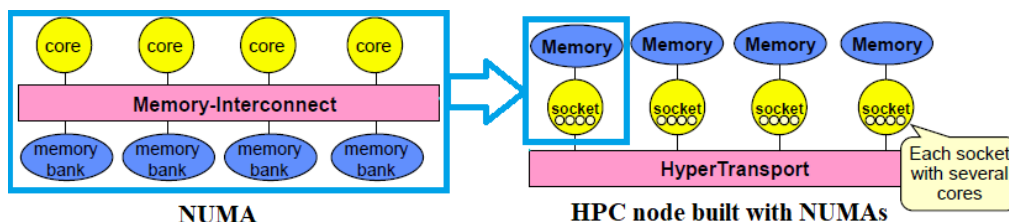


Figure 2.1. A socket or NUMA and the structure of an HPC machine built with NUMAs [76]

Specifically for computational tools in nuclear engineering, HPC is employed for the division of a specific code function to sub-programs (tasks or threads), which are executed simultaneously (in parallel) by different cores, sockets in the same computer, or computing nodes in a cluster. The objective is to split the calculation and send the parts to as many individual processors as possible in order to decrease the calculation time. Dedicated interface specifications need to be used for the parallelization of nuclear solvers, which are compiled and connected to the executables as libraries. The ones employed by the codes used in this thesis are the Message-Passing Interface (MPI) library and the Open Multi-Processing (OpenMP) application programming interface. With MPI parallelization, the total memory engaged for the calculation is distributed among the different “MPI tasks”, which do not have

direct access to the memory of other tasks. Each task runs a sub-program of the code, typically the same for each task, for which the variables have the same name but different memory locations that are private to the task. The contents of the variables can be communicated among MPI tasks via special send & receive routines (message passing). This parallelization method is optimally used for functions of the code that can be individually executed without inter-communication (see Fig. 2.2), like for the decomposition of a 3D core in several 2D planes where the transport equation is solved separately. The MPI tasks can subsequently return all flux information to a “master” task through send routines, where the 2D solutions are coupled by a 1D solver for the 3rd direction (see Fig. 2.2). OpenMP is a standard programming model for shared memory parallel programming. The focus is to parallelize calculation loops with independent iterations. Each OpenMP “thread” is executing exactly the same algorithm, but for different values of the parameters, which are stored in the same location (vectors or matrices) (see Fig. 2.2). An example is the calculation of the cross-sections for each fuel pin of a 2D neutronic model. The fuel pin material composition and temperature needed for the calculation is stored in the same location for all pins and it does not affect the cross-sections of other pins. When the loop is finished the main thread continues the execution of the algorithm (see Fig. 2.2). In general, a code used in nuclear engineering can employ either parallelization technique according to its needs or combine the two; what is called “hybrid” parallelization. In the latter case, the code is subdivided to sub-programs executed by different MPI tasks and for each sub-program OpenMP is used when entering loops with independent iterations.

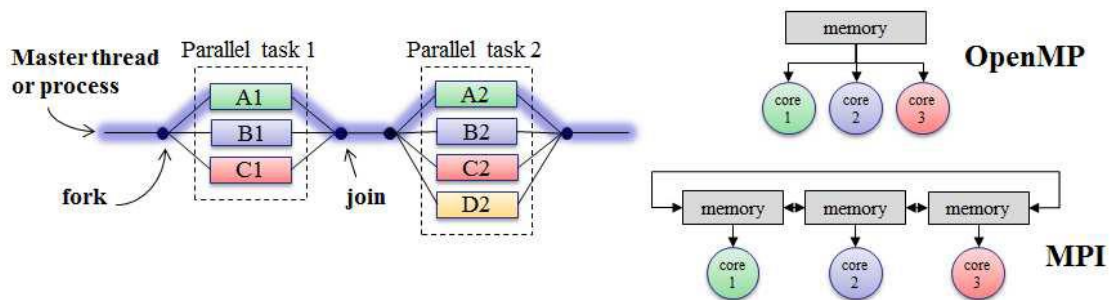


Figure 2.2. Workflow of a series of parallel tasks (left), and OpenMP and MPI operative scheme [5]

The optimal use of the parallelization techniques depends on the architecture of the cluster where the calculation takes place. The MPI parallelization can be applied to any of the structures described in the beginning of this section. This means that different MPI tasks can be distributed among the cores of a socket or the NUMAs of a cluster (one NUMA or one computing node = one task), since shared memory is not necessary. On the other hand, OpenMP threads can be assigned only inside a computing node, since the memory must be

shared. When hybrid parallelization can be applied in a cluster, the optimal use of resources would be succeeded by assigning one MPI to each socket and distribute the OpenMP threads among the cores of the socket. Thus, the required communication time is minimized.

In this work, the terms Wall time and CPU time are used to describe the computational time of parallel calculations. Wall time refers to the actual time required to do the calculations, whereas CPU time is the time needed by 1 CPU [$CPU\ time = Wall\ time \times CPUs$]. During the course of this study, three different computational environments are used. The LCLRS machines are a group of individual LINUX computers that belong to LRT. The machines are not inter-connected and each one includes two sockets. Both parallelization specifications can be applied to the LCLRS machines, separately or together. An MPI task can be assigned to a single or several cores and OpenMP threads can be distributed the same way. The Swiss National Supercomputer Center, or CSCS, operates high-performance computing systems as a service facility for a diverse range of purposes – from high-resolution simulations to the analysis of complex data. Several clusters are owned by CSCS and one of them, Piz Daint, is used in this study. Piz Daint is built with physical nodes of two NUMAs each with varying memory. The workload manager that connects the nodes and distributes the calculation according to the requirements of the user is the software SLURM. Besides CSCS where specific memory and time limitations are applied, the bulk of this work is performed in the PSI HPC cluster Merlin6. This cluster has a similar structure with Piz Daint; however, the memory available per node is significantly larger and calculations’ wall-time can be extended to more than 24 hrs. The features of the three computational environments used in this study are summarized in Table 2.1. It must be pointed out that in LCLRS the user is allocated the memory that corresponds to the number of cores requested, whereas in CSCS or Merlin6 a user can engage the whole memory capacity of a node even if using only a portion of the cores. All computational environments are used according to the size of the intended calculation and the availability of the corresponding code in the computational environment. LCLRS and Merlin6 are built with the exact same LINUX architecture and the same auxiliary modules (e.g. compilers, MPI libraries) exist in both systems.

Computational environment	# Physical Nodes	NUMAs per physical node	Cores per socket	Memory per node (GB)
LCLRS	1	2	14	264
CSCS	1813	2	18	64 or 128
Merlin6	72	2	22	320

Table 2.1. Technical features of the different computational environments used in this study

2.3 nTRACER – Fast

nTF is a direct deterministic transport code capable of 3D sub-pin resolution [44]. The code solves the neutron transport equation considering a heterogeneous description of the reactor geometry with a 2D/1D scheme and 3D acceleration. nTF employs the planar (2D) Method of Characteristics (MOC) based on 3D Coarse Mesh Finite Differences (CMFD) formulation. The full core solution is obtained by repeated alternating calculations of planar MOC, with a hexagon-based modular ray-tracing scheme, and 3D CMFD problems. For the hexagonal core, the CMFD scheme is formulated to apply to an unstructured geometry, in order to be used on the polygon cells of the hexagon-based mesh [77]. The CMFD relations for the axial current, which are needed to form a 3D CMFD problem, are obtained by 1D axial solvers. The radial and axial solutions are then coupled by the transverse leakage terms to form a 3D problem. Nodal diffusion and the 1D SP3 source expansion nodal method (SENM) have been used in the past for the axial direction, however the latest version of nTF incorporates a 1D MOC axial solver, to increase the accuracy and improve the stability of the code [78]. The convergence of the solution is determined by three user-defined convergence criteria for the eigenvalue, the fission source and the residual.

2.3.1 Cross-section generation

nTF is using the nTRACER cross-section library, which is based on ENDF/B.VII.0. The library is built with a 47 energy group structure (HELLIOS [79]) and provides the necessary cross-sections and neutronic data to solve the Boltzmann and Bateman equations. The default approximation in nTRACER and nTF for the scattering anisotropy of neutrons (see Section 2.3.2.2) is to assume isotropic scattering (P0) and use transport-corrected total cross-sections (inflow correction) [80]. During the calculation, the cross-sections are generated on the fly with the subgroup method. In the subgroup method, the resonances in a single broad energy group are represented by a set of discrete cross-section levels and the corresponding energy widths, defined to preserve the area of the resonances. The cross-section levels and energy widths are denoted as the subgroup level and the subgroup weight. With this representation of the resonances, the integrated reaction rate in the group can be approximated by a summation of the subgroup levels, multiplied with the corresponding flux and weighted with the subgroup weight. To incorporate the region dependent leakage into the self-shielded flux the subgroup fixed source problem is solved (SGFSP). This method is valid when the temperature of the region is uniform. However, nTF employs temperature profiles in the fuel and cladding to

perform sub-pin analysis. To tackle this issue the number density adjustment scheme [44] is applied on the effective cross-sections. Resonance interferences due to the presence of other nuclides are treated with the use of the Resonance Interference Factors library [81]. In the nTRACER library, 16 energy groups span the resonance range, 7 subgroup levels are considered in each group and 55 isotopes have resonance information in the nTRACER library, which means that 6160 SGFSPs must be solved to complete the resonance treatment. To accelerate the cross-section generation by reducing the number of the solved problems the Macro Level Grid (MLG) method is used [80]. In addition, to take into account shadowing effects of the neighboring pins the Equivalent Dancoff Cell (EDC) method is used, which reduces the size of the SGFSP problem [80]. Neglecting the angular dependence of the total cross-section in the resonance energy range can yield biases in the self-shielding calculation and lead to significant reactivity errors. nTF employs spectral superhomogenization (SPH) factors [80] to the total cross-section before each MOC calculation in order to preserve the angle dependent total reaction rates in the resonance energy groups. After the MOC calculation, the SPH factors are used to correct also the resulting flux. The SPH factors are tabulated in a separate library file.

2.3.2 Planar MOC on hexagonal geometry

The 3D Boltzmann transport equation discretized in energy can be given as the following, with the group index omitted:

$$\left(\Omega_x \frac{\partial}{\partial x} + \Omega_y \frac{\partial}{\partial y} + \Omega_z \frac{\partial}{\partial z}\right) \varphi(x, y, z, \hat{\Omega}) + \Sigma_t(x, y, z) \varphi(x, y, z, \hat{\Omega}) = Q(x, y, z, \hat{\Omega}) \quad (2.1)$$

where φ is the angular flux, Σ_t the total cross-section and Q the anisotropic source. The transport equation for a discretized angle m can be integrated over the axial direction on a plane designated by plane index k as follows:

$$\left(\Omega_x^m \frac{\partial}{\partial x} + \Omega_y^m \frac{\partial}{\partial y}\right) \bar{\varphi}_m^k(x, y) + \Sigma_t^k \bar{\varphi}_m^k(x, y) = \bar{Q}_m^k(x, y) - L_{z,m}^k(x, y) \quad (2.2)$$

where $\bar{\varphi}_m^k$ and \bar{Q}_m^k are the axially averaged angular flux and the source while the axial leakage source is defined as:

$$L_{z,m}^k(x, y) = \frac{\Omega_z^m}{h_z} \left(\varphi_m^{T,k}(x, y) - \varphi_m^{B,k}(x, y) \right) \quad (2.3)$$

with $\varphi_m^{T,k}$ and $\varphi_m^{B,k}$ being the angular fluxes at the top and bottom of the plane and h_z the thickness of the plane. If the magnitude and the angular dependence (approximated as isotropic) of the axial leakage is known for each plane, then the 3D transport problem is

converted into a set of planar fixed source problems, coupled with the axial leakage term. Then, the planar problems can be solved independently by a 2D MOC calculation scheme.

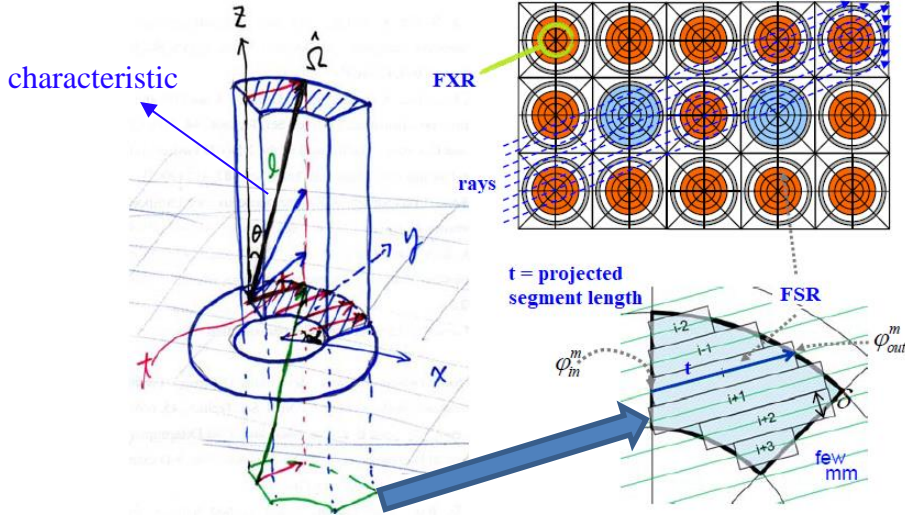


Figure 2.3. MOC domain decomposition [82]

For MOC, the problem domain is decomposed as illustrated in Fig. 2.3. Each material area is subdivided in smaller regions where the cross-sections and the source is considered constant. The regions of constant cross-sections are called Fixed cross-sections Regions (FXRs) and the regions of constant source are called Fixed Source Regions (FSRs). Each FXR contains multiple FSRs. In order to reduce equation 2.2 to an Ordinary Differential Equation that can be solved analytically the problem domain is traced with characteristic lines or “rays” of multiple directions. These rays further subdivide each FSR in small regions associated to a segment of which the ray is the central axis (see Fig. 2.3). The solution of the Boltzmann equation along a characteristic s can be expressed as follows:

$$\frac{d\varphi(s)}{ds} + \Sigma_t\varphi(s) = Q \xrightarrow{\text{Integrating Factor}} \varphi(s) = \varphi_{in}e^{-\Sigma_t s} + \frac{Q}{\Sigma_t}(1 - e^{-\Sigma_t s}) \quad (2.4)$$

where $\varphi(0) = \varphi_{in}$, the incoming angular flux. Solving equation 2.4 for segment i (see Fig. 2.3), (“ray tracing”), gives the outgoing angular flux, the average angular flux and the scalar flux:

$$\varphi_{out}^m = \varphi_{in}^m e^{-\Sigma_t l} + \frac{Q_m}{\Sigma_t} (1 - e^{-\Sigma_t l}) \quad (2.5a)$$

$$\bar{\varphi}_m = \frac{Q_m}{\Sigma_t} - \frac{\varphi_{out}^m - \varphi_{in}^m}{\Sigma_t l} \quad (2.5b)$$

$$\phi = \sum_m \omega_m \bar{\varphi}_m \quad (2.5c)$$

where $l = t/\sin\theta$ is the real length of the segment (see Fig. 2.3) and ω_m the weighting factor for the ray. The larger the number and directions of rays crossing a FSR the more accurate the

solution will be. In MOC codes, this can be controlled by defining the value of ray spacing (the distance between rays of the same direction) and the number of polar and azimuthal angles the rays should cover. Each ray crosses the whole problem domain and the different directions are created by reflecting each ray at the outer boundary of the domain in a different angle. In nTF, the MOC rays are defined according to the hexagonal-assembly based modular ray-tracing scheme [77]. This scheme defines the basic rays for a unit geometry, such as the fuel assembly in hexagonal geometry, and then constructs the full core ray by path linking. It provides large savings not only in terms of memory for storing the segment lengths and the region indices along the neutron path, but also in terms of the computing time for the path analysis. After the MOC calculation, the flux within each energy group is averaged over the whole FSR and used by the code for the next steps of the 2D/1D scheme. The fact that nTF calculates the flux spectrum and relative power of each FSR, constitutes the code capable of sub-pin safety analysis.

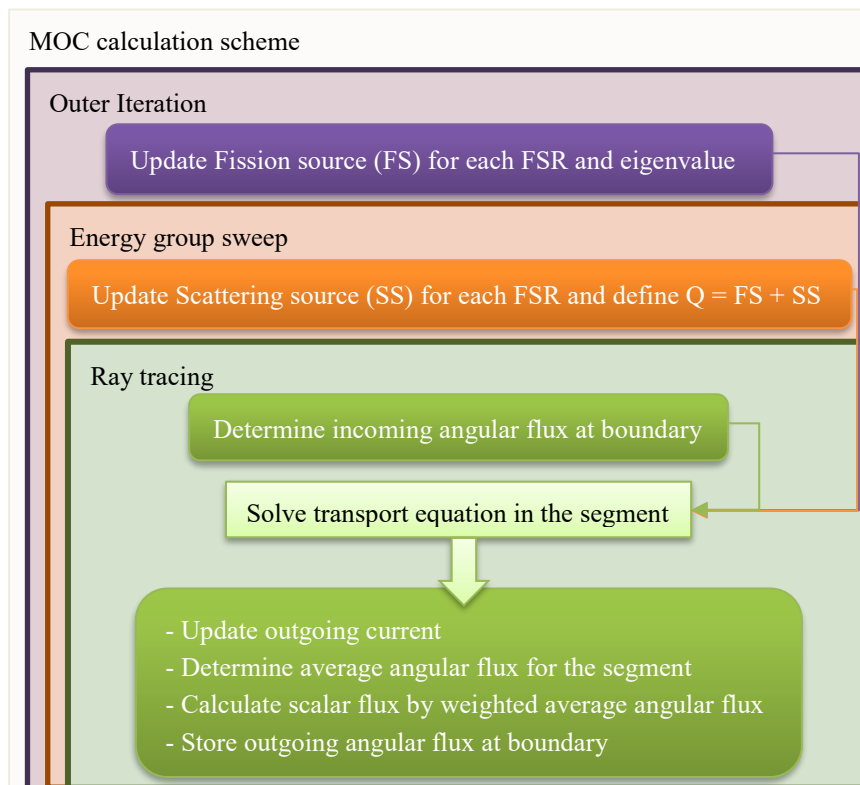


Figure 2.4. nTF MOC calculation scheme

2.3.2.1 Node major and Group major calculation schemes

The MOC calculation algorithm is illustrated in Fig. 2.4. In nTF, two different versions of this algorithm are available and both of them are used in this study. With the group major (GM) calculation scheme the energy groups ray tracing is sequential. The node major (NM) calculation scheme allows the ray tracing of all energy groups to happen in parallel (OpenMP).

NM requires the source term and total cross-section to be stored for all segments and all energy groups simultaneously, which results in high memory requirements, much higher than GM that only needs the parameters of the specific energy group for the ray tracing. However, the computational time of NM is significantly lower.

2.3.2.2 Pn approximation of the scattering source

The scattering source of neutrons of a specific energy E and angle $\widehat{\Omega}$ in a segment can be written as follows:

$$Q_s(x, y, E, \widehat{\Omega}) = \int_{4\pi} d^2\widehat{\Omega}' \int_0^\infty dE' \Sigma_s(x, y, E \leftarrow E', \widehat{\Omega} \leftarrow \widehat{\Omega}') \varphi(x, y, E', \widehat{\Omega}') \quad (2.6)$$

where E' and $\widehat{\Omega}'$ are the original neutron energy and angle before scattering occurred, φ is the flux of neutrons with E' and $\widehat{\Omega}'$ and Σ_s is the cross-section for neutrons with E' and $\widehat{\Omega}'$ to be scattered to energy E and angle $\widehat{\Omega}$. Equation 2.6 can be expanded with spherical harmonics (Pn) of which the n^{th} order scattering source is expressed with Legendre polynomials. In a reactor the scattering of neutrons, especially on light nuclei, is anisotropic. However, to reduce the computational cost of a calculation, nTF is normally using the 0^{th} order of the scattering source, which is equivalent to isotropic scattering, with transport correction of the total cross-section to recover some of the anisotropy. In order to treat more accurately the scattering source, nTF gives the option of describing the scattering source through a P2 approximation [83]. Nonetheless, higher order expansions of the Legendre polynomials require higher order angular moments of the flux, increasing the memory requirements and computational time of the calculation significantly.

2.3.3 3D CMFD Formulation

The 2D/1D scheme is internally coupled by the 3D CMFD acceleration technique. The flux calculated by the planar MOC is used to homogenize the cross-sections in a pin, conserving the volumetric reaction rate for each node. CMFD calculates the 3D distribution of the homogenized pin scalar flux and the eigenvalue. The axial nodal calculations are performed periodically during the CMFD outer iteration with the radial transverse leakage updated from the previous step's CMFD solution. The axial solver calculates the axial leakage source, which is then fed to the subsequent MOC calculation. CMFD also provides an initial guess of the fission source to the subsequent planar MOC calculation to accelerate its convergence. The CMFD formulation is based on the 3D diffusion equation for the whole core, which can be discretized in energy and space as follows:

$$\nabla \cdot \vec{J}(\vec{r}, E) + \Sigma_t(\vec{r}, E)\varphi(\vec{r}, E) = Q(\vec{r}, E) \rightarrow \sum_{is} \frac{J_{is,i}^g}{h_{is,i}} + \Sigma_{t,i}^g \varphi_i^g = Q_i^g \quad (2.7)$$

where \vec{J} is the neutron current, i is the homogenized pin node index, is is the index of the surface of node i , $h_{is,i}$ is the perpendicular length from the center of the node to surface is , and $J_{is,i}^g$ is the net current from the surface is of node i for group g . For hexagonal geometry, the homogenized pins have irregular shapes (see Fig. 2.5). Thus, the CMFD formulation must be applied on unstructured nodes. In this case, the length $h_{is,i}$ is the distance from the gravitational center of the unstructured node i to the center of the surface is . Employing an approximation of the finite difference method to Fick's law [84] and omitting the group index, the net current in surface is for the unstructured node i is:

$$J_{is,i} = -D_i \frac{\varphi_{is,i} - \varphi_i}{h_{is,i}} \quad (2.8)$$

where $\varphi_{is,i}$ is the surface flux of surface is for the unstructured node i and D_i is the diffusion coefficient of node i . Due to flux and current continuity, $\varphi_{is,i} = \varphi_{is,i+1}$ and $J_{is,i} = J_{is,i+1}$, the net current can be written as:

$$J_{is,i} = -\tilde{D}_{is,i}(\varphi_{i+1} - \varphi_i) \quad \text{with} \quad \tilde{D}_{is,i} = \frac{2D_i D_{i+1}}{h_{is,i} D_{i+1} + h_{is,i+1} D_i} \quad (2.9)$$

where $i + 1$ is the node on the other side of the surface is and $\tilde{D}_{is,i}$ is flux difference-to-current conversion factor. In order to preserve the surface currents calculated by the planar MOC a correction term must be added to equation 2.9:

$$J_{is,i} = -\tilde{D}_{is,i}(\varphi_{i+1} - \varphi_i) - \hat{D}_{is,i}(\varphi_{i+1} + \varphi_i) \quad \text{with} \quad \hat{D}_{is,i} = \frac{-J_{is,i,MOC} - \tilde{D}_{is,i}(\varphi_{i+1,MOC} - \varphi_{i,MOC})}{\varphi_{i+1,MOC} + \varphi_{i,MOC}} \quad (2.10)$$

where $J_{is,i,MOC}$ and $\varphi_{i,MOC}$ are the net current and node average flux calculated by the planar MOC and $\hat{D}_{is,i}$ is the current correction coefficient. The CMFD relations for axial current are obtained by the embedded 1D axial solver. With equation 2.10 and the homogenized pin cross-sections from the MOC calculation the 3D CMFD problem is constructed. The CMFD convergence is determined based on relative residual reduction; the iteration exits when the residual is reduced below 10% of the initial value. Since the MOC and axial nodal problems are formed for given axial and radial transverse leakage information, several iterations are required between CMFD, MOC and the axial solver. The CMFD can be further accelerated by performing some iterations with the energy discretization collapsed in 2, 4 or 8 groups.

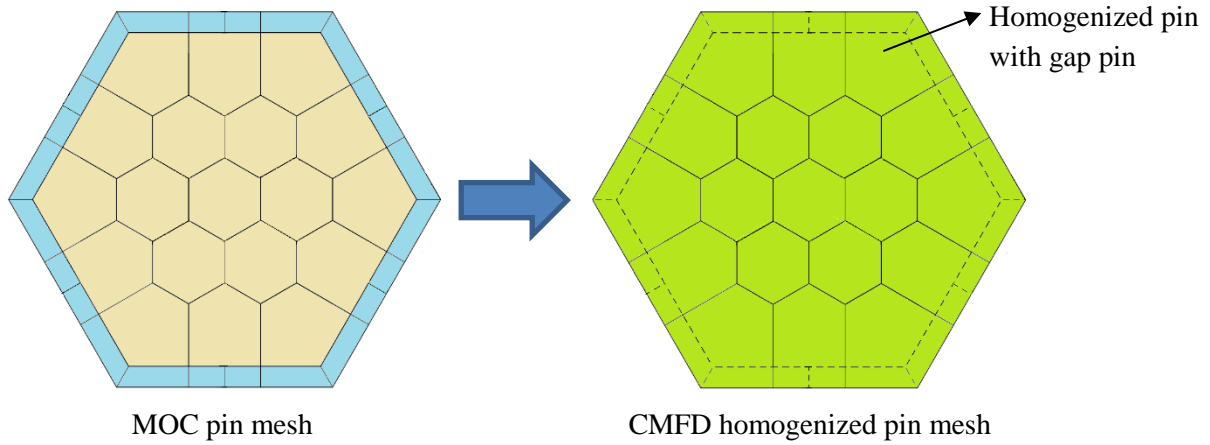


Figure 2.5. Pincell mesh of MOC and CMFD for an hexagonal assembly

2.3.4 1D Axial Solver

The latest versions of nTRACER and nTF are using a 1D MOC solver for the axial direction [78]. The 1D MOC solver is applied to each homogenized pin, defined for CMFD. The step characteristics (SC) scheme is employed. SC has a benefit over other options, such as linear source. It can ensure a positive solution as far as the source term remains positive (see Section 2.3.4.1). Equation 2.4 is solved for the axial direction, where the source (Q) refers to the fission source, the scattering source and the transverse leakage, coupling the 1D solution to the 2D calculation. For the angular discretization, the Gauss-Legendre (GL) quadrature with five points is used. Not so many angles are necessary since the equation is applied to the homogeneous pin. SC must be applied on a fine mesh to ensure accuracy. Thus, a sub-grid structure is introduced axially, dividing the plane into layers of 0.5 cm. In order to correspond to the sub-grid structure, the axial shape of the sources is reconstructed inside each pin with the use of a flux form function f determined by the previous axial sweep:

$$f_i = \frac{\phi_i}{\phi_I} = \frac{H_I \phi_i}{\sum_{i \in I} \phi_i h_i} \quad (2.11)$$

where I and i are the coarse and fine mesh indices and H and h the coarse and fine mesh thickness. The radial transverse leakage term, calculated during the 3D CMFD iteration is provided by the coarse mesh and considered isotropic. The shape of the transverse leakage within the CMFD coarse mesh is described by a quadratic polynomial. This polynomial is then integrated for each sub-layer to form a piecewise constant distribution. The 1D MOC problem requires several sweeps over the entire pin, thus an appropriate parallelization scheme is necessary. The plane-wise domain decomposition applied for 2D MOC is also used for the axial solver. The intra-node solution of the piece-wise 1D MOC problems is parallelized with OpenMP, which is applied radially. The plane boundary angular fluxes are communicated

amongst nodes with the MPI protocol. The data of all energy groups are transferred together, thus the axial solver has non-negligible memory requirements.

2.3.4.1 Instability in the 2D/1D scheme

The 2D/1D scheme can become unstable. The CMFD acceleration can start diverging during the calculation due to the use of axial nodes that are too thick or too thin, the occurrence of negative fluxes and the unphysical currents introduced by the high-order polynomial expansion techniques employed axially to capture the spatial variation of flux (SP3) [78],[85]. Usually the 2D MOC and 3D CMFD planes are set consistent, and they provide transverse leakages to the 1D axial solver. However, the 2D MOC planes are often too thick to resolve properly the axial shape of flux, and this leads to inaccurate and unphysical transverse leakages of the 1D axial solver. The occurrences of negative fluxes are often due to the introduction of transverse leakage and the transport correction. In the cells where no fission source exists (e.g. reflector), the transverse leakage can make the total source negative. This is more common in the axial solution than in the radial solution. For the transport correction, the weighted sum of the first moment components of the scattering matrix is subtracted from the self-scattering cross-section, making the self-scattering terms often negative for light nuclei such as hydrogen. This can result in negative total sources, especially in the fast groups. In nTF, with the use of the 1D MOC solver with SC, the SP3 solver is replaced by the sub-grid scheme, which can suppress severe axial flux variations. Additional measures are introduced, like Leakage splitting, P_L method, and limited transport correction, to improve the stability of the calculation (see [78] for details and naming conventions). These measures can affect the accuracy of the solution and the computational requirements, thus they are selectively applied to the non-fuel regions such that their impacts are minimized. Another method to deal with instabilities is to subdivide the thick CMFD planes in subplanes [86], however this option is not available for nTF.

2.3.5 Parallelization

In order to perform practical full core nTF calculations, the developers adopted a hybrid parallelization scheme using both OpenMP and MPI. For this, a proper domain decomposition of the problem is necessary. The spatial domain of the core is separated in several axial layers; usually 16 to 24 is good practice. Each 2D axial layer can only be associated to one separate MPI process. Thus, the computational size of the problem is defined by the number of axial layers. Their solution is achieved by parallelizing the different tasks with multiple threads using

the OpenMP libraries. The hybrid model is a shared memory model. The performance of nTF can be highly affected by the presence of NUMAs [5]. The optimal choice in this case is to bind the MPI processes (one or more) fully to separate NUMAs. The number of processes that can be associated to a NUMA depends of course on the available memory of the node. nTF has extensive memory requirements, particularly for large physical systems, which may result in the use of the memory of several NUMAs for one MPI task, even though the program is executed by the cores of a single NUMA, causing performance penalties.

2.3.6 Cycle depletion

For depletion calculations, nTF is using the nTRACER depletion library and a simplified predictor-corrector scheme described below. The Bateman equation is solved with the flux at the beginning of the burnup (BU) step (predictor). The Krylov subspace method is used by default, nonetheless the Chebyshev Rational Approximation method (CRAM) is also available. In the simplified predictor-corrector scheme, the new material composition and cross-sections are used to perform a state-point neutronic calculation and predict the flux. The new flux is used to recalculate the material composition of the BU step (corrector). The results of the predictor and the corrector steps are averaged to produce the material composition at the end of the BU step. In the typical predictor-corrector scheme with linear interpolation a second state-point neutronic calculation would take place with the averaged material composition. In the simplified approach, the transport calculation after the corrector step is omitted resulting in drastic reduction (near half) of the calculation time. The typical predictor-corrector is also available in nTRACER. The nTRACER depletion solver has been extended to hexagonal geometries for use with nTF (Chapter 5) during the course of the PhD.

2.3.7 Simplified T/H solver

nTRACER includes a T/H feedback module which employs a simplified 1D T/H solver based on energy and mass balance principles. For each pin the following equation is solved on every axial subdivision:

$$Q_{th} = \dot{m}c_p(T_{out} - T_{in}) \quad (2.12)$$

where Q_{th} is the thermal power produced by that pin for the specific axial node, \dot{m} is the mass flow rate, c_p is the specific heat capacity and T_{out}, T_{in} the outlet and inlet temperature of the node. Given that the thermal power is known by the neutronic calculation, T_{out} is calculated for each node and it is averaged with T_{in} to provide the node temperature and relevant coolant

properties. The temperature distribution within the fuel rod is obtained by solving a 1D radial heat conduction problem (axial heat conduction is neglected). The conduction equation is solved in the cladding for the inner cladding temperature and the average. The gap thermal conductivity is used to calculate the fuel surface temperature. The fuel region is subdivided in equispaced rings, the number of which is defined by the user. The fuel conduction equation is solved, taking into account the pin power profile of the rings:

$$T(r_1) = T(r_2) + \frac{Q_{th} \cdot ring_power(\%)}{4\pi k} \quad (2.13)$$

where $T(r_1)$ is the temperature at the inner surface of the ring, $T(r_2)$ is the temperature at the outer surface of the ring, $ring_power(\%)$ is the percentage of the pin thermal power produced in the ring and k is the fuel thermal conductivity. More details for this solver are provided in Chapter 4. The 1D T/H module is extended to hexagonal geometries for use with nTF in the course of this study.

2.4 COBRA-TF

CTF [87] is a T/H simulation code designed for Light Water Reactor (LWR) vessel and core analysis. As a sub-channel code, CTF models the detailed intra-assembly flow and sub-pin heat conduction, resulting in sub-pin T/H calculations. The CTF T/H analysis is carried out in an array of parallel channels delimited by fuel rods and open gaps, and divided into axial intervals. The volumes bounded by axial planes and channel lateral borders make up the 3D computational mesh (control volumes) where the flow differential equations are solved. CTF uses a two-fluid three-field modeling approach. To obtain T/H parameters such as pressure gradient and fuel rod temperature in each control volume, one needs to couple continuity, energy and pressure equations. CTF is parallelized with the MPI standard using radial domain decomposition. Each MPI task is assigned a group of channels (e.g. an assembly or several assemblies). CTF requires information from neighboring control volumes to form the conservation equations in a computational cell. When grouping channels for each MPI task, minimizing the number of gaps connecting channels in separate MPI tasks reduces the communication time between tasks.

2.4.1 Conservation Equations

CTF employs a two-fluid model approach with three separate fluid fields, continuous liquid, liquid droplets, and vapor. Each of the three fields is modeled with its own set of conservation equations for mass and momentum. The continuous liquid and the liquid droplets

are considered in thermal equilibrium, thus are described by a common energy equation. In CTF gravity (g) is assumed to be the only body force of the coolant and pressure (P) is considered the same for all phases. It must be pointed out that since this is a study of PWRs, where a single coolant phase occurs outside of accident scenarios, this section focuses on the equations and phenomena corresponding to the continuous liquid phase. The generalized conservation equation of mass for the continuous liquid for a computational cell is the following:

$$\frac{\partial(a_l \rho_l)}{\partial t} + \nabla \cdot (a_l \rho_l \vec{V}_l) = L_l + M_l^T \quad (2.14)$$

On the left-hand side, the first term is the change of mass with time and the second term is the advection of mass in or out of the computational cell (\vec{V}_l is the continuous liquid velocity field). On the right-hand side, the term L_l represents the mass transfer into or out of the continuous liquid phase, which normally for a PWR should be zero. The final term of the equation is the mass transfer in the computational cell due to turbulent mixing. Since CTF assumes axially-dominated sub-channel flow, only a simple turbulent diffusion model is used to calculate turbulent transfer through sub-channel gaps. Turbulent mixing only occurs in the lateral direction. The momentum conservation equation of the continuous liquid can be given as:

$$\begin{aligned} & \frac{\partial(a_l \rho_l \vec{V}_l)}{\partial t} + \frac{\partial(a_l \rho_l v_x \vec{V}_l)}{\partial x} + \frac{\partial(a_l \rho_l v_y \vec{V}_l)}{\partial y} + \frac{\partial(a_l \rho_l v_z \vec{V}_l)}{\partial z} \\ & = a_l \rho_l \vec{g} - a_l \nabla P + \nabla \cdot [a_l (\boldsymbol{\tau}_l^{ij} + \mathbf{T}_l^{ij})] + \vec{M}_l^L + \vec{M}_l^d + \vec{M}_l^T \end{aligned} \quad (2.15)$$

The terms of the left hand side of the equation are the change of momentum with time and the advection of momentum in the computational cell. On the right hand side there is the gravitational force, the pressure force, the viscous and turbulent shear stress due to turbulent mixing. The viscous shear stress can be expanded into wall-fluid and fluid-fluid components. The turbulent shear stress and the liquid-liquid shear stress are not modeled in CTF, thus are not included in the following equations. \vec{M}_l^L is the momentum change due to phase change, which in this case should be zero. \vec{M}_l^d corresponds to the drag forces between interfaces, which should also be eliminated for single phase fluid. \vec{M}_l^T is the axial momentum source due to turbulent mixing. The energy conservation equation is:

$$\frac{\partial(a_l \rho_l h_l)}{\partial t} + \nabla \cdot (a_l \rho_l h_l \vec{V}_l) = -\nabla \cdot [a_l (\vec{Q}_l + \vec{q}_l^T)] + \Gamma_l h_l^i + q_{wl}''' + a_l \frac{\partial P}{\partial t} \quad (2.16)$$

The left hand side represents the energy change due to time and advection. The right hand side terms are in order: the heat conduction in the fluid, which is not modeled in CTF so \vec{Q} is zero, the turbulence heat flux, the energy transfer due to phase change, which is also zero for

PWRs during normal operation, the volumetric wall heat transfer and the pressure work term. CTF assumes that there is no volumetric heat generation occurring in the fluid, that radiative heat transfer only occurs between solid surfaces and that internal dissipation is negligible.

2.4.2 CTF Computational grid and discretized conservation equations

CTF employs a staggered mesh (two different meshes applied together - see Fig. 2.6) for the solution of the conservation equations to increase numerical stability and accuracy [88]. In a fuel rod bundle, the T/H channels are defined as the space between the fuel rods or between the fuel rods and the boundary of the calculation domain (see Fig. 2.6). These channels are subdivided into axial intervals of varying height forming the calculation control volumes or sub-channels. When cross-flow is possible through the lateral border of the sub-channels, this border must be defined by the user as a gap. In the CTF models used in this work, all channel borders are defined as gaps, unless specified otherwise, allowing cross-flow. The computational grid created by the lateral borders of channels and the axial intervals is the scalar mesh, used to define scalar variables (e.g. P, fluid properties). Two secondary meshes are defined; the axial momentum mesh and the transverse momentum mesh, where the velocity field is calculated (see Fig. 2.6). A transverse momentum cell is created for each scalar cell in channels that are defined to have gaps. With the staggered mesh, all scalar quantities are calculated for the center of the control volumes defined by the model geometry and the velocity field is defined at the surfaces of those volumes (see Fig. 2.6). The information for the geometry of the model and the connections between channels is provided by the user. The CTF models of this thesis are built with a uniform radial discretization over the height of the model.

Unless the input requires the solution of the equations in Cartesian coordinates, CTF expands the finite difference form of the conservation equations in sub-channel coordinates. The sub-channel approach is a simplified coordinate system that only considers two flow directions, axial flow and lateral flow, thus resulting in one less momentum equation for each field. Lateral flow enters a sub-channel through the gaps connecting it with other sub-channels (cross-flow). In the discretized form of the conservation equation, if a gap is not defined between two sub-channels then there is no advection term across that border for energy, mass or momentum transfer (no cross-flow). The lateral flow is not described with a set of fixed coordinates; instead, it represents the terms of the equations corresponding to any orthogonal direction to the vertical axis. Thus, it has no direction once it leaves a gap. This assumption is

valid for axially-dominated flow since there is little cross-flow and, subsequently, small transfer of momentum across sub-channels.

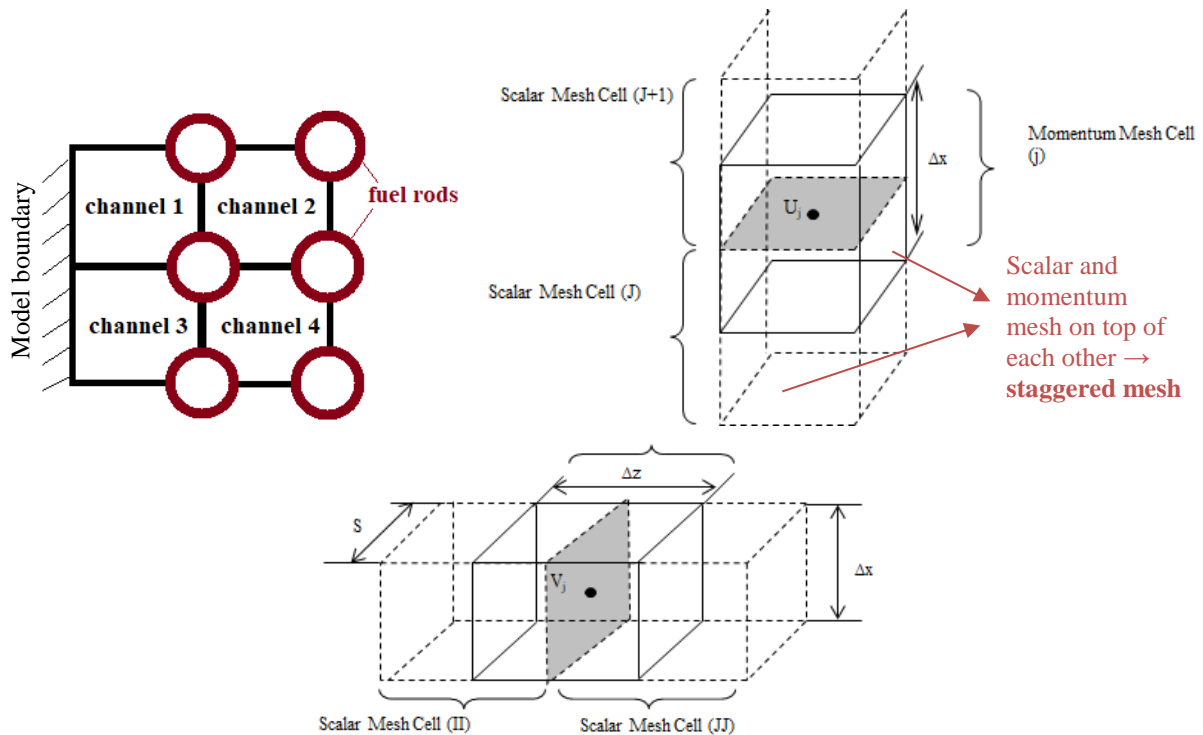


Figure 2.6. Scalar (top, left) axial momentum (top, right) and transverse momentum (down) computational mesh of CTF

2.4.3 Numerical solution

The conservation equations are solved simultaneously over the computational grid using the Semi-Implicit Method for Pressure-Linked Equations (SIMPLE). The steps of the algorithm taken from [88] are:

1. Use an initial guess for the pressure field, P^* . CTF is employing a user-defined reference pressure to define the pressure field, accounting for hydrostatic forces.
2. Solve the momentum equations for fluid velocity. First the transverse momentum equations and then the axial momentum equations are solved for the mass flow rates of the current time step.
3. Use the continuity equations to solve the pressure field correction, P' . This step forms the “inner” iteration. The continuity and energy equations form a system of equations over the computational grid that must be solved simultaneously such that they all equal zero, and mass and energy is conserved. For large models this can be a very large matrix to solve. These equations are functions of the computational cell pressure, but also of the pressure of the

neighboring cells; another reason why they need to be solved simultaneously. However, the number of unknowns is larger than the number of equations, which leads to the formation of the pressure matrix for the scalar mesh. The pressure matrix contains one pressure equation for each cell with the total number of unknown pressures equaling the total number of scalar mesh cells.

4. Calculate the corrected pressure field, $P = P' + P^*$. The remaining scalar quantities are also calculated with the corrected pressure.
5. Calculate the corrected velocity field using the corrected pressure field.
6. Solve the remaining discretized equations that influence the flow field (e.g. fuel rod heat transfer).

The above algorithm forms the “outer iteration” of CTF, which is repeated until the solution is converged for each time-step. For steady state calculations, CTF forms a pseudo-steady state problem, where the time terms still exist in all conservation equations. CTF solves the pseudo-steady state as a transient, and at every time-step it evaluates a set of simulation convergence criteria to determine if the solution has become steady.

2.4.4 Conductor Models

Besides the high-resolution calculation of fluid properties, CTF contains specific capabilities for modeling solid components such as heated and unheated conductors, also in high-resolution. The CTF rod models can be used to define solid or hollow nuclear fuel rods (active) and cylindrical structures with no internal heat sources like the guide tubes (passive). For active rods, CTF uses a finite difference form of the heat conduction equation, which is formulated using the heat balance approach [89]. The general conduction equation for a solid mesh cell is:

$$\frac{d}{dt} \int_V \rho C_p VT = \oint_A \vec{n}_k Q_k dA + \int_V Q''' dV + \oint_A Q_s dA \quad (2.17)$$

The left hand side of the equation gives the evolution of temperature T with time, where C_p is the specific heat and ρ is the material density. The first term of the right hand side is a surface integral that accounts for axial and lateral energy conduction. The second term represents the volumetric energy generation inside the solid mesh cell and finally the last term accounts for the convective heat transfer to and from the surrounding fluid. The source term is zero for unheated conductors. For fuel rods, the volumetric heat generation from fission is defined by the user for each solid mesh cell.

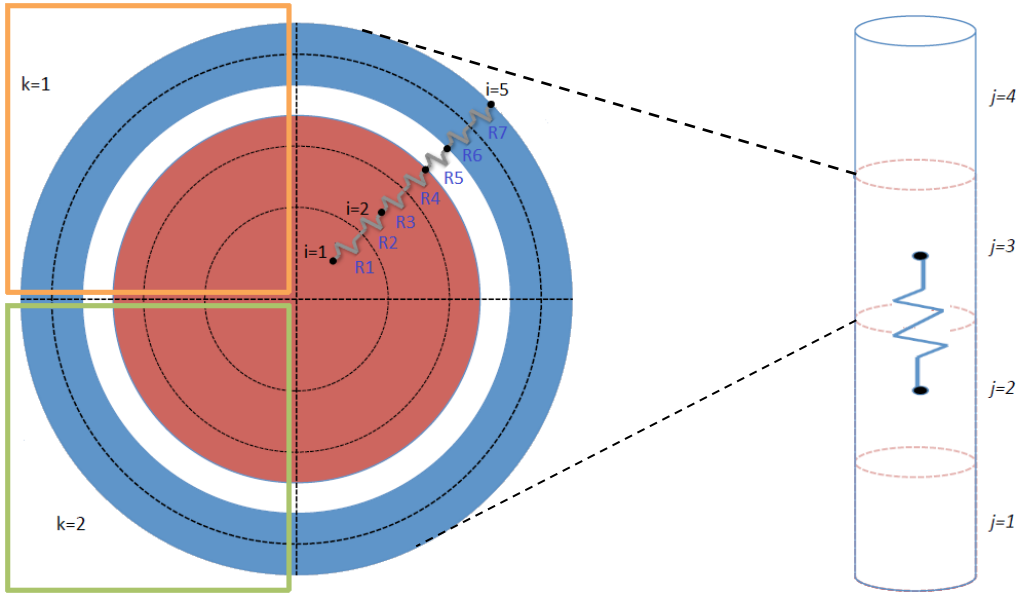


Figure 2.7. Meshing of the fuel rod, where j is the axial discretization, k the azimuthal segments and i the radial mesh cells with thermal resistances R .

In CTF, the fuel rods are discretized into solid mesh cells or control volumes according to [89]. The rod is divided into axial segments matching the axial discretization of the neighboring sub-channels. Each cell is discretized in azimuthal segments that follow the sub-channel-rod connection. This means that each sub-channel is connected to one azimuthal segment of a rod (e.g. in Fig. 2.6 each rod would be discretized in 4 azimuthal segments). The fuel rod is discretized also radially with equispaced rings, except the outer surface node that has half the thickness of the others (see Fig. 2.7). The number of radial mesh cells for the fuel is defined by the user; however, the cladding is divided by default in two regions and the fuel gap is one region. The calculation nodes, where the fuel conduction equation (2.18) is solved, are defined by CTF (see Fig. 2.7). Nodes inside the fuel pellet will always be in the center of the mesh cell volume for internal mesh cells. However, the fuel pellet surface cell has its node on the surface of the fuel pellet. The two cladding mesh cells will have their nodes on the opposite surfaces of the clad. The temperature is not calculated in the gap region. For unheated tubes the user can define as many radial segments as desired and the nodes are in the center of the volume mesh cells. The thermal conductivity k_{ab} in the lateral and axial direction is determined with the concept of thermal resistances (see Fig. 2.7):

$$Q_{a \rightarrow b} = k_{ab}(T_b - T_a) \quad (2.18)$$

$$\text{where } k_{ab} = \frac{1}{R_{a \rightarrow \text{boundary}} + R_{\text{boundary} \rightarrow b}} \quad (2.19)$$

This meshing allows the calculation of local temperature dependent material properties and also local variations on the heat transfer resistance and heat generation. The CTF rod solution algorithm works by looping over each rod, then each axial layer of the rod, then each azimuthal segment at that layer. For a single segment, CTF then loops over each radial node and sets up the terms that will form the equation for that node. The rod conduction solution is implicit in only the radial direction; azimuthal and axial conduction terms are added to the conduction equations explicitly.

2.5 Codes for conventional VVER analysis

As it was mentioned in the introduction, the conventional coupled code system of LRT is built with CASMO5-VVER as the lattice code and PARCS as the core simulator. GenPMAXS is an auxiliary tool to process the output of lattice codes and built the few group cross-section libraries for PARCS. The establishment of the conventional LRT solver is a less complicated task than the development of the novel coupled code system. The relevant codes are used in standalone mode and are designed to model hexagonal geometries. Thus, there is no need for modifications on their source. The main challenge concerning the conventional LRT core solver arises from the fact that the lattice code, CASMO5-VVER, used for cross-section generation, has been released only recently and required independent verification. Of special importance is the generation of the PARCS library from the CASMO output, which must follow a format that can be processed correctly by GenPMAXS. Fig. 2.8 illustrates the calculation scheme of the conventional code system.

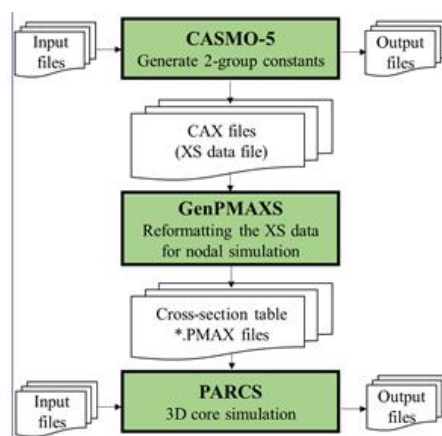


Figure 2.8. Flowchart of CASMO5/PARCS code system

2.5.1 Parametrization of few group macroscopic cross-sections

The cross-sections and other neutronic parameters for nodal calculations are generated by the lattice code. Each assembly configuration (fuel or reflector) with different structure or material composition requires a lattice calculation. For PWRs the operating conditions that affect the cross-section generation are the position of the control rod (CR), the moderator density (DM), the boron concentration (BC) and the fuel temperature (TF). These are defined as state variables. During steady state, the operating conditions for the core simulation are fixed. Thus, a single set of cross-sections and neutronic data, corresponding to the specific operating conditions, needs to be generated for each assembly. For transient or depletion analysis the operating conditions of the core are not fixed or known a priori throughout the calculation, which requires a number of state-points to reach the end of cycle, or the end of the transient. For these simulations, the lattice codes must produce several sets of cross-sections, which correspond to different values of the state variables defined by a “case-matrix”. The term “case-matrix” refers to all the different combinations of operating conditions for which neutronic data are generated. The whole of the neutronic data sets (or “points”) comprise the cross-section library. The nodal code uses the neutronic data that correspond to the operating conditions of the currently simulated state-point, or, most commonly, interpolates between two points in the library to match the operating conditions of the state-point. Normally, a specific set of conditions is selected as the “reference” state. The lattice code is depleting each assembly in the reference state, storing macroscopic cross-sections and neutronic parameters for each burnup step. At each burnup step, the code is also calculating the difference of the cross-sections (in the form of partial derivatives) if the value of the state variables would change to a different combination of operating conditions at that moment of the cycle. The collection of partial derivatives are called “branches”. The reference case together with the branches is defined as a “tree” (see Fig. 2.9). When it comes to depletion analysis, besides the state variables that are affecting the neutron balance, the previous state of the core, or “history”, is also important. A case-matrix should include several trees with varying reference operating conditions, in order to ensure the nodal code can use the neutronic data that correspond to its current state, with the correct history. Fig. 2.9 presents an example of two different trees. Table 2.2 presents the structure of the history trees and the operating conditions of the branches of the case-matrix used for the generation of cross-sections in this work. The branches cross-sections are calculated for the exposures listed on the table.

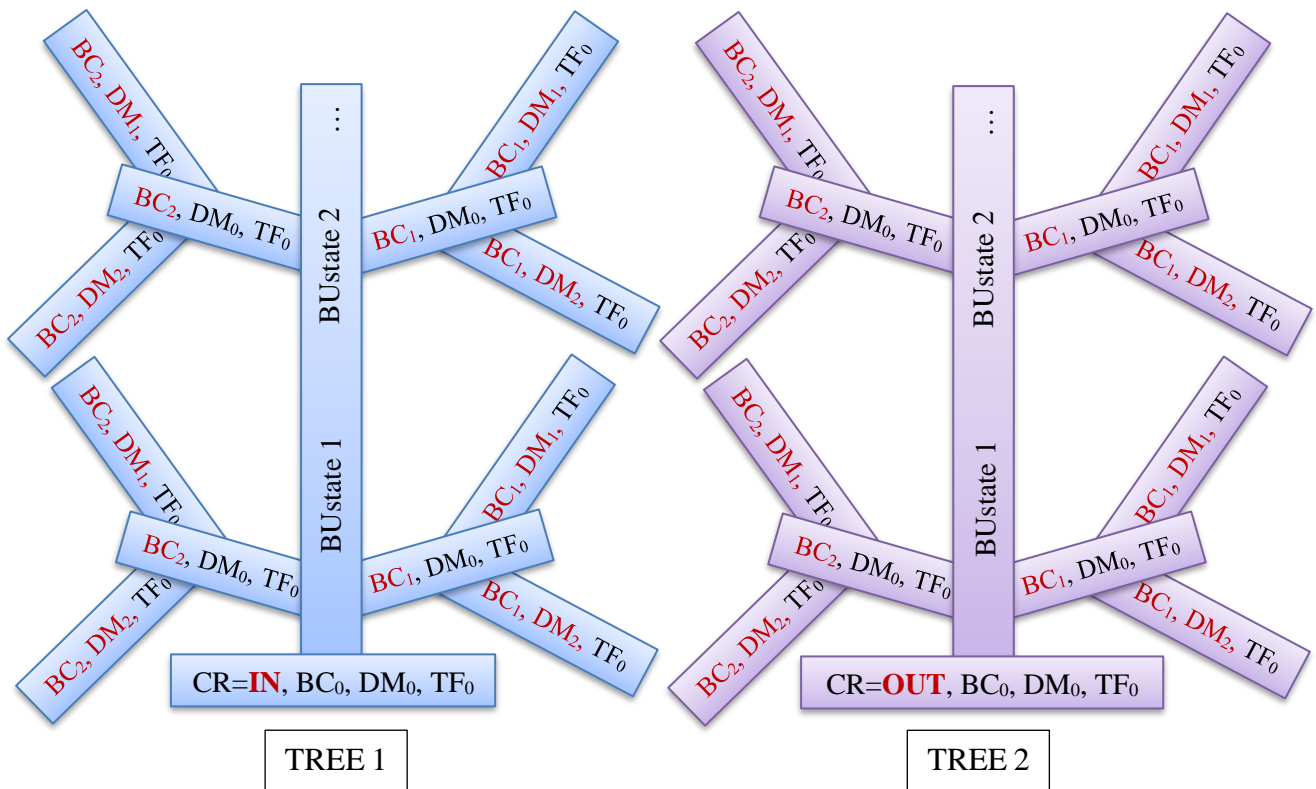


Figure 2.9. Example of depletion trees and branches for a case matrix

Tree #	History tree				Branches			
	HCR	HTMO	HBC	HTF	CR	TMO	BC	TF
1	OUT	580	500	900	OUT	580	0.01	541
2	OUT	540	500	900	IN	600	500	900
3	OUT	620	500	900	540	620	2000	1800
4	OUT	580	0.01	900	560			
5	OUT	580	2000	900	Exposure (MWd/kg): 0.0, 0.1, 0.5, 1, 2, 4, 6, 8, 10, 11, 15, 20, 25, 30, 40			
6	IN	580	500	900				

Table 2.2 Structure of the history trees and operating conditions of the branches for the case-matrix used in this thesis. TMO: moderator temperature, H: history

2.5.2 CASMO5-VVER

CASMO5 is a multi-group 2D transport lattice code for burnup calculations on BWR and PWR configurations. CASMO5-VVER [52] is the extension of the code to hexagonal geometries for VVERs. The code can simulate cylindrical fuel rod bundles of varying composition in a hexagonal pitch array with allowance for water gaps and corner stiffeners in the regions separating fuel assemblies. Reflector/baffle calculations must be performed with CASMO5, not the hexagonal module, unless simulating a 2D full core model. Nuclear data for CASMO5 is collected in a library containing microscopic cross-sections in 586 energy groups. The effective cross-sections in the resonance energy region are calculated with the Equivalence

Theory. The “shadowing” effect between different pins is taken into account through the use of Dancoff factors calculated by CASMO5. Subsequently, the effective cross-sections are used in a series of 1D collision probability micro-group pincell calculations to obtain the detailed neutron flux in 586 energy groups. The goal is to generate the appropriate spectrum for each material region of the lattice, which is then used for the energy condensation of the cross-sections to 19 or 35 groups. The data generated in the previous steps constitute the input to the 2D MOC transport calculation. CASMO5 uses pre-determined ray spacing and azimuthal angles (0.05 cm & 72 angles) based on extensive testing to achieve high accuracy. The transport equation is solved with a Linear Source approximation to the MOC, which is available for both Transport-Corrected P0 isotropic and full anisotropic scattering treatments. For the hexagonal geometry the code employs appropriate quadrature sets for the MOC and the Coarse Mesh Non-linear Diffusion acceleration. In the depletion calculation, a predictor-corrector approach with linear interpolation at the end of the step is used (the material composition at the end of step is defined by averaging the results of the predictor and the corrector). The default depletion methodology uses a CRAM based solver.

2.5.2.1 Critical Spectrum

Single assembly lattice calculations for cross-section generation are typically performed under the assumption of zero leakage boundary conditions. Thus, the homogenized cross-sections are obtained by collapsing the multi-group neutronic parameters with an infinite lattice flux spectrum. In a real system, where leakage is present, the infinite lattice spectrum is inaccurate. To account for that, CASMO5 adjusts the flux with a critical buckling calculation, changing the infinite lattice spectrum to one corresponding to a critical spectrum. However, CASMO5 assumes that the buckling is independent of energy. According to the CASMO5 manual: *“Often in reactor applications, the energy-independent leakage assumption is not accurate, since the leakage does not affect each of the multi-group data in the same way. The effect of leakage on the homogenized cross-section is much larger for two-groups compared to few (4 or more) groups.”* The reason for this discrepancy is that as the energy of the neutrons increases, the mean free path becomes larger, allowing higher leakage probability. Thus, an energy independent buckling cannot adjust the spectrum accurately to capture leakage appropriately, which is reflected in the generated cross-sections. This issue has been recognized by the developers of CASMO5/SIMULATE3 and corrected by doing the leakage correction in SIMULATE3 using ad-hoc modifications of the down-scatter, fast absorption, fast fission

cross-sections and fast diffusion coefficients [90]. In this study the leakage correction is tested also with PARCS in lack of a better alternative.

2.5.3 GenPMAXS

The Purdue Macroscopic cross-section (PMAXS) is a specific file format, established by the PARCS developing team. PMAXS files store all cross-sections and neutronic parameters generated by lattice codes with a specific structure that can be processed by PARCS. One PMAXS file catalogues the neutronic data for one type of assembly (fuel or reflector). Normally, PMAXS files include the principal macroscopic cross-sections, the microscopic cross-sections of Xe/Sm, the group-wise form functions with several different branch states for the appropriate fuel burnup states, and all of the appropriate kinetics data. PMAXS provides all of the data necessary to perform core simulation for steady-state, transient applications and cycle depletion. The GenPMAXS program (Generation of the Purdue Macroscopic XS set) is developed to process the output of different lattice codes and generate the PMAXS files for the PARCS calculation. Currently, PARCS employs a macroscopic depletion method in which the microscopic cross-sections and the fuel number densities are not tracked individually during core depletion. Only the macroscopic cross-sections are determined by the depletion module with burnup and history indices. In PMAXS, the macroscopic cross-sections are tabulated as a function of the state variables, such as the control rod position (CR), burnup and the history variables. All these are called independent variables. The neutronic parameters used in PARCS are constructed with the assumption of a linear superposition of the partial cross-sections (branches) on a base reference state. The case-matrix used by the lattice code must fulfill some requirements for GenPMAXS to process the data correctly. A reference state is specified in the GenPMAXS input. GenPMAXS expects that all trees are based on that reference state with alterations of one state variable at the time. The branches for each tree are categorized according a predefined sequence of state variables, independently of their position on the lattice code tree. For PWRs this sequence is CR, DM, BC, TF. Each branch is stored in the PMAXS file according to the first state variable of the sequence that changed from the reference state or from any branch state previously stored by this process. That variable characterizes the branch. The branches have reference values for all state variables after the branch variable (see Fig. 2.9). This means that a branch cannot be used if two state variables are changed simultaneously from the previous branch or reference state. For example, if the reference state is CR=IN, DM=0.72, BC=500, TF=900 GenPMAXS cannot use the branch CR=OUT,

DM=0.69, BC=500, TF=900 if the branch CR=OUT, DM=0.72, BC=500, TF=900 is not calculated by the lattice code. GenPMAXS can only be executed in serial mode.

2.5.4 PARCS

The conventional LRT core solver is based on the code PARCS, a state-of-the-art three-dimensional nodal reactor core simulator developed at University of Michigan, which solves the steady state and time-dependent multi-group neutron diffusion or low-order neutron transport equation in Cartesian or hexagonal geometries [71]. To model reactors with hexagonal geometries (e.g. VVER), PARCS is using a multi-group nodal diffusion kernel based on the Triangle-based Polynomial Expansion Nodal (TPEN) method [91]. This kernel consists of flux calculations for a hexoctahedron assembly node, through two coupled transverse-integrated neutron diffusion equations, one for the radial and one for the axial direction. The radial equation is solved by dividing the hexagonal surface into six triangles and calculating the flux in each triangle through a 2D polynomial expansion of the 3rd order. On the other hand, the axial equation is solved by the nodal expansion method (NEM), which requires the moments of the radial leakage up to the second order. The 0th and the directional moments of the axial leakage are also required by the TPEN solver. Continuity of the surface currents and corner point fluxes is used for the calculation of the coefficients of the polynomials, together with the first and second order moments of the flux. In the TPEN, the source is approximated by a 2D polynomial of the second order, defined to preserve the spatial dependency of the source. The coupled TPEN kernel is resulting in a linear system, which provides two-group node-average fluxes as well as two-group interface currents. The solution is accelerated with the PARCS Coarse Mesh Finite Differences (CMFD) formulation, which is applied on the full core. The cross-section library for nodal codes like PARCS must be generated separately by a lattice code and processed by the library generator GenPMAXS. All parameters produced by PARCS (e.g. power) belong to the global scale. PARCS can produce results of higher resolution with pin power reconstruction functions, provided by the lattice code. However, this functionality is not available yet for hexagonal geometries. During depletion calculations, for each burnup step the power in each fuel node is used to calculate the new burnup of the node, and the assembly cross-sections' derivatives and other neutronics parameters are computed at the new burnup using the PMAXS file, generated by GenPMAXS, for the corresponding nodal exposure. PARCS includes a 1D simplified mass/energy solver, which can be used for simple single phase calculations. This solver is generally adequate for

steady-state eigenvalue calculations, criticality searches, cycle depletion calculations, PWR and VVER analysis, where the pressure boundary remains intact and the fluid conditions remain single phase. Typical PARCS full core calculations are fast enough that no HPC is required; thus it is executed in serial.

2.6 Codes for verification of the LRT solvers

A big part of this study is based on code-to-code comparison for the assessment of the capabilities and accuracy of the LRT core solvers. Serpent2 and SUBCHANFLOW have been used before as a multi-physics coupled code system for the safety analysis of VVERs [8], [64]. Serpent2 and SUBCHANFLOW are selected for the verification of the LRT core solvers since the available benchmarks' high-resolution reference solutions are produced by this code system. However, Serpent2 is available in LRT, allowing the verification of the neutronic codes in detail before comparing full core results. SUBCHANFLOW is not available, but close communication with the corresponding benchmark team allowed modifications on the relevant models used for the comparison with the LRT core solvers, where necessary.

2.6.1 Serpent2

Serpent2 is a multi-purpose three-dimensional continuous-energy Monte Carlo particle transport code, developed at VTT Technical Research Centre of Finland, Ltd. As a Monte Carlo code, Serpent2 can explicitly represent the phenomena occurring in the reactor core without the biases induced by the discretization of the mathematical models. Thus, it is commonly used for the verification of deterministic transport codes, as well as the generation of few group cross-sections among other uses. A large number of particle histories must be completed to achieve acceptable statistical uncertainties, resulting in large computational costs. Serpent2 deals with particle transport through a combination of conventional surface-tracking and the Woodcock delta-tracking method [92]. The code reads continuous-energy nuclear cross-sections from ACE format data libraries. In this study, Serpent2 is used with ENDF.VII.0. The code is written in standard ANSI-C language. For depletion calculations, Serpent2 employs a variety of predictor-corrector methods with different accuracy and computational requirements. In this study, the constant extrapolation with linear interpolation is used (full predictor-corrector see Section 2.3.6). The depletion methodology involves a CRAM-based solver. Serpent2 can run in parallel in computer clusters and multi-core workstations. The hybrid shared memory parallelization technique of MPI and OpenMP is used. It must be noted

that all Monte Carlo codes have high memory requirements, Serpent2 in particular. One gigabyte of RAM should be sufficient for one burnup step, but a minimum of 3 GB is recommended for full cycle calculations [93].

2.6.2 SUBCHANFLOW

SUBCHANFLOW (SCF) [94] is a high-resolution sub-channel code developed by Karlsruhe Institute of Technology (KIT). It is originally based on the legacy sub-channel codes COBRA-IV-I and COBRA-EN. Instead of describing two-phase flow by simulating the processes on a microscale basis (e.g., separate conservation equations for liquid droplets, films or vapor bubbles), SCF employs empirical correlations for pressure drop, heat transfer coefficients, void generation, etc., collected over the last decades. In addition, user-defined empirical correlations can be implemented. The code is using a three-equation two-phase flow model that is a mixture equation for mass, momentum, and energy balance. The constitutive relations are expressed as mixture equations for wall friction and wall heat flux, as well as a slip velocity relation. SCF can simulate both rectangular and hexagonal rod bundles and full core models. A sub-channel is divided into several axial mesh volumes. Transport of mass, momentum, and energy is possible along the axial direction and between the neighboring channels (lateral direction, cross-flow) in a simplified manner. The fuel rod or heater rod surface temperatures are calculated depending on power release and cladding-to-coolant heat transfer. For each axial layer, the rod is divided into a number of radial rings to solve the heat conduction equation in the radial direction by a finite volume method. Axial heat conduction can be accounted for in transients. For steady-state calculations, SCF performs a quasi-static simulation. SCF is not using any HPC methods, thus it must be executed in serial.

2.7 Benchmarks for verification and validation & target accuracy

The verification and validation of the LRT coupled code systems is performed with international benchmarks, which focus on the high-resolution modeling and analysis of VVERs. This thesis is based on the study of the VVER-1000, as the benchmarks available to LRT, including suitable data for the verification of high-resolution codes, concern this reactor type. The fuel elements and core are larger than its predecessor the VVER-440, but the same in size with the latest VVER models (1200 & TOI). Both benchmarks presented in this section can be reproduced by high-resolution and conventional coupled code systems. They provide data for code-to-code comparison and experimental validation. In addition, the modeling

requirements and intricacy of geometry structure are changing from the 2D benchmark to the 3D full core, allowing the assessment of the solvers while gradually approaching the complexity of a real VVER-1000. In this study, the performance of the LRT coupled code systems in reproducing the international benchmarks is evaluated according to a pre-defined set of criteria, targeting specific levels of accuracy for a set of parameters.

2.7.1 NURESIM-SP1 V1000-2D benchmark

Exercises V1000-2D-C1/2/3 are part of the SP1 Core Physics work packages within the European project NURESIM [95], where PSI previously participated for the PWR analyses. These exercises involve 2D static core calculations with zero axial buckling for nodal solvers. Each exercise refers to different loadings at Hot Zero Power (HZP) and includes unrodded, partially rodded and fully rodded configurations. Two-group diffusion solutions are provided for homogenized assemblies for each case, together with homogenized collapsed two-group diffusion parameters for each assembly. These parameters include homogenized diffusion coefficients, cross-sections and discontinuity factors for fuel and reflector assemblies. The core loading map for exercise V1000-2D-C1 is presented in Fig. 2.10.

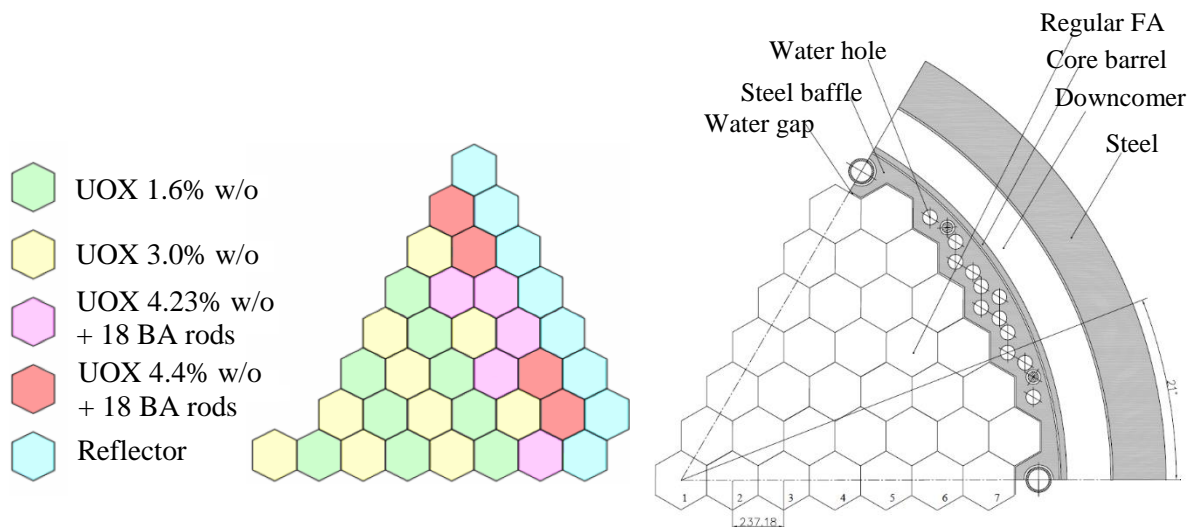


Figure 2.10. Left: The unrodded symmetric fresh fuel loading of exercise V1000-2D-C1. Right: Technical drawing of the heavy reflector of the VVER-1000 core as specified in the benchmark [96]

V1000-2D-C1-tr is also part of the SP1 Core Physics work packages within NURESIM [96]. It is an extension of exercise V1000-2D-C1 for testing heterogeneous transport solvers. The benchmark includes the detailed geometry and material data for the unrodded and fully rodded HZP states of a full-size 2D VVER-1000 core with a heavy reflector. The core is 1/6 symmetric and the structures surrounding the fuel assemblies (steel buffer, core barrel, etc.) are

specified in detail up to the inner radius of the reactor pressure vessel. A 1/6th core sector and the corresponding heavy reflector are presented in Fig. 2.10. The considered core loading consists of fresh UOX and UOX+B assemblies with CrB2 burnable absorber rods. The absorber rods are inserted in the guide tubes of the selected assemblies. The spacer grids are modeled as a homogenized mixture with the moderator surrounding the assemblies. There are no corner stiffeners in the active core. The provided data correspond to HZP conditions with boric acid concentration in the moderator of 6.0 g/kg.

2.7.2 X2 benchmark

The X2 benchmark is based on the VVER-1000 operational data of the second unit of the Khmelnytsky NPP located in Ukraine. The aim of the X2 benchmark [97] is to develop a VVER-1000 data platform for the verification and validation of reactor simulation tools. In addition to experimental plant data, such as reactivity coefficients, Monte Carlo reference numerical solutions are used to provide quantities not directly available from measurements (e.g. pin power). X2 consists of three stages including HZP experiments, cycle depletion and several transients, which occurred at the unit during the first cycles of operation. An effort to revise the X2 benchmark was initiated with an updated and refined publication of the HZP experiments [98]. The new benchmark specifications include detailed geometry models of the active core and the heavy reflector, as well as updated material compositions for the critical state (HZP) and corresponding operational data. A description of the HZP start-up tests together with the relevant experimental data, like temperature reactivity coefficients, SCRAM worth and worth of specific rod banks, are also part of the revised specifications. Finally, the power distribution at the assembly and the pin level is provided for code verification. The calculated reference solution is produced by the Monte Carlo code Serpent2.

Fig. 2.11 presents the layout for the fresh core and the structure of the heavy reflector as depicted in the benchmark specifications. The fuel assembly distribution is 60° rotationally symmetric and the reflector is 30° symmetric. The groove region (see Fig. 2.11, right) at the edge of the core basket, which is cylindrical with horizontal grooves, is not modeled explicitly, but as a homogeneous mixture of coolant and steel, the material composition of which is specified in the benchmark. Fig. 2.12 depicts the axial layout of a fuel pin in the Serpent2 model. The pin is modeled explicitly, from the lowerplug at the bottom of the fuel to the upper plenum. The spacer grids are simulated as rings around the cladding, with the same axial

thickness as the actual spacers. The axial reflectors are simulated as four homogenized regions of steel and moderator and the corner stiffeners are modeled explicitly.

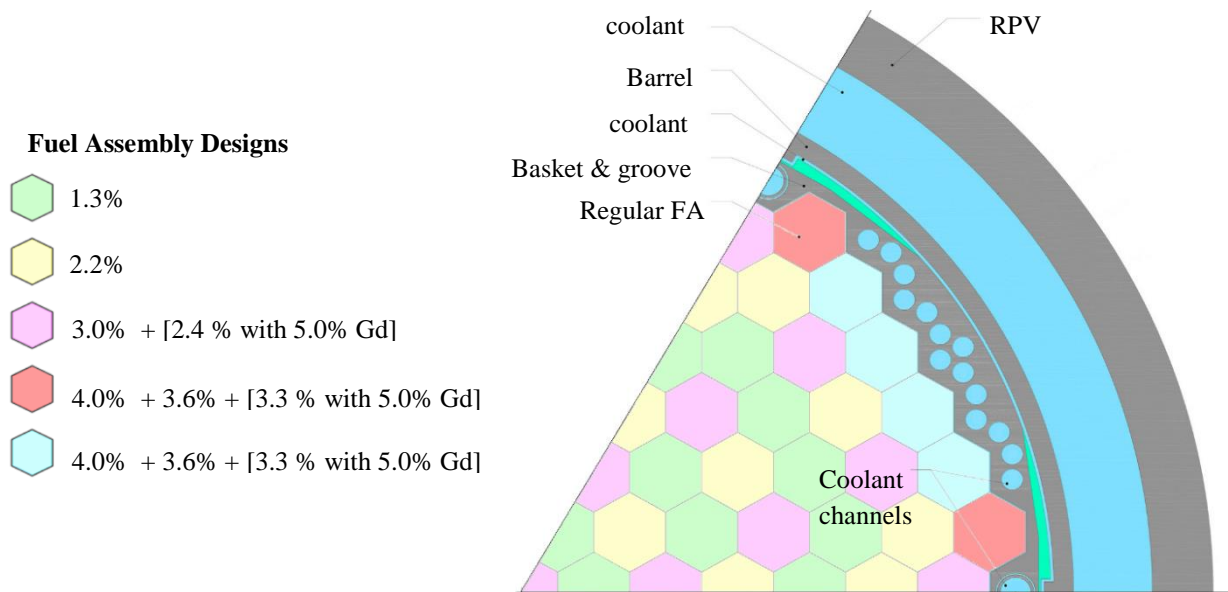


Figure 2.11. Fuel designs, core layout and Serpent2 model of the heavy reflector for the X2 benchmark

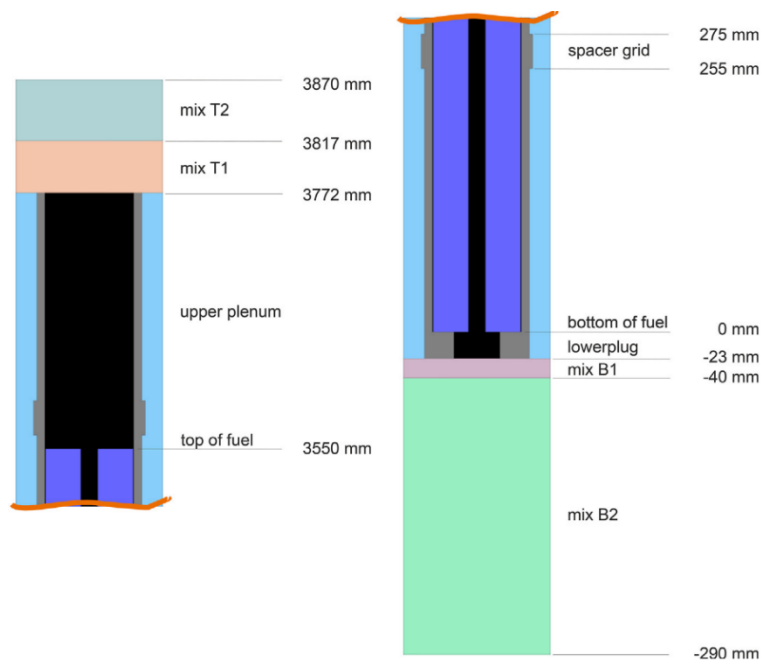


Figure 2.12. Axial layout of the Serpent2 fuel pin model

The measurements of temperature reactivity coefficients (TRC) were conducted at zero-burnup state (no fission product poisoning, no Xe-135, no Sm-149) with variant coolant temperature (T_{in}). The experiment was repeated for two different values (TRC1 & TRC2) of boron concentration (CB) and with control rods in banks 1 to 6 fully withdrawn ($H = 100\%$).

Control rod movements in banks 7 to 10 compensated the reactivity insertion, caused by the coolant temperature change. The SCRAM worth start-up tests included two steps. First, from the nearly critical state all control rods, except the chosen “stuck” cluster (see Fig. 2.13), were fully inserted. The SCRAM with stuck rod was measured. Secondly, the “stuck” rod was dropped down and the full SCRAM worth was measured. The coolant temperature and boric acid concentration remained practically unchanged during the SCRAM test. Finally, the integral and differential worth of control rod bank #10 was measured with steps’ length of 4%–7%, starting from fully inserted (0%). The core inlet coolant temperature and the pressure above the core were kept stable during the measurements. Table 2.3 lists the operational conditions, including control rod positions, for all reactor states studied in the benchmark. Fig. 2.13 presents the position of the control rod banks in the core, which are distributed with 120° rotational symmetry. The “stuck” rod is also depicted in Fig. 2.13.

State #	description	CB (g/kg)	T _{in} (°C)	H10 (%)	H9 (%)	H8 (%)	H7 (%)	H1-6 (%)	H_stuck (%)
1	criticality	6.9	281.0	76	100	100	100	100	100
2	TRC1, point 1	7.05	276.4	76	100	100	100	100	100
3	TRC1, point 2	7.05	280.6	76	100	100	100	100	100
4	TRC2, point 1	5.7	275.7	0	0	31	80	100	100
5	TRC2, point 2	5.7	280.2	0	0	31	80	100	100
6	Before SCRAM	6.9	280.5	75	100	100	100	100	100
7	SCRAM with stuck rod	6.9	280.5	0	0	0	0	0	100
8	Full SCRAM	6.9	280.5	0	0	0	0	0	0

Table 2.3. Operational conditions for all HZP simulated states of the X2 core

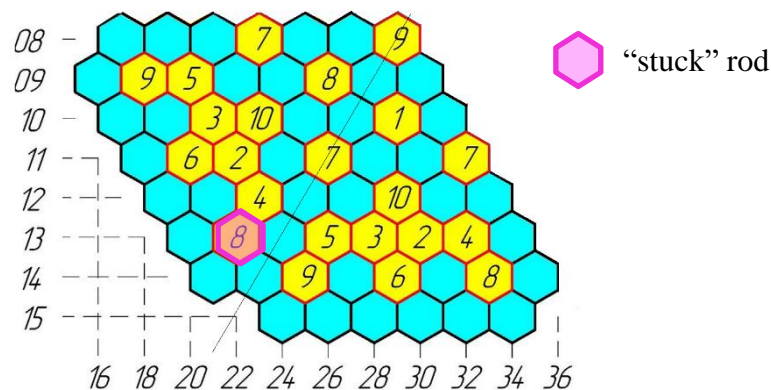


Figure 2.13. Positions of the control rod banks in 1/3rd of the reactor core, together with the “stuck” rod

There is not yet a revision of the benchmark for other reactor states besides HZP, where experimental data and reference solutions are provided together with detailed models for high-

resolution solvers. However, LRT is in contact with the benchmark team, which provided all relevant information for the study presented in this thesis. The Hot Full Power (HFP) steady state corresponds to an inlet temperature of 287 °C with an exit pressure of 15.7 MPa. The nominal power of the reactor is 3000 MW. The same fresh fuel configuration presented in Fig. 2.11 is loaded in the core for HFP and for the first depletion cycle of X2. The corresponding power history together with the boron letdown curve is illustrated in Fig. 2.14. Both curves begin at 4.51 EFPDs, not at the actual beginning of the cycle. This means that in a cycle calculation the power from 0 EFPDs until 4.51 EFPDs is assumed steady and equal to the power at 4.51 EFPDs. If this is not corresponding to the actual power history of X2, it could cause discrepancies in the results, however not significant ones. Axial offset measurements are also provided for the whole cycle. The benchmark team provided LRT also with assembly power maps for three exposure states at different points in the cycle. The data consist of SPND readings at several locations in the active core and reconstructed power profiles, based on the experimental readings. There is not any measurement uncertainty associated with the experimental data, just a general requirement that the in-core monitoring system measures power distribution within 5% accuracy. There is no specific information as to how this requirement is applied. The time, exposure and power of the three state-points are presented in Table 2.4.

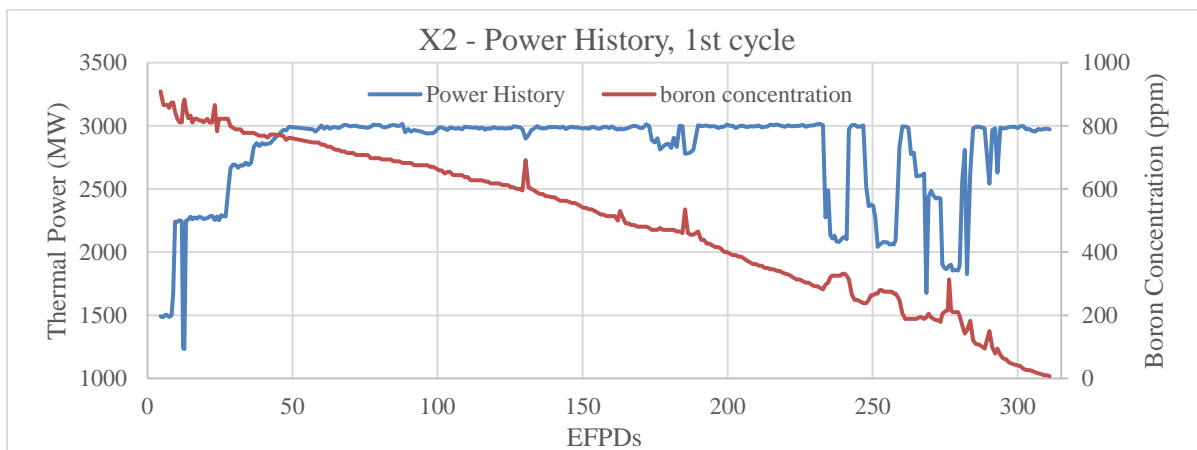


Figure 2.14. Power history and boron letdown curve for the 1st cycle of X2

Measurement point #	EFPDs	Days	Th. Power (MW)
1 st	29.8	45.86	2667
2 nd	90.80	108.14	2976
3 rd	208.7	227.41	3000

Table 2.4. Exposure and power level of the three measurement points in the 1st cycle of X2

2.7.3 Target accuracy

The performance of the LRT coupled code systems is evaluated according to desired accuracy criteria that are specified for the verification and validation of computational tools for PWR analysis. The criteria are different if the codes are used standalone or if multi-physics simulations are considered. In addition, the target accuracy is changing according to the reactor state that is simulated (HZP, HFP or cycle depletion). The criteria presented in this section are based on information found in literature for code-to-code comparison (verification), in [99], or comparison to measurements during normal operation, in [100]. Table 2.5 summarizes the accuracy criteria used in this study. It must be pointed out that if validation is performed with experimental data that are accompanied by uncertainties, these are used for the evaluation of the computational tools. Finally, for HFP power distribution the criteria employed for comparison are the same as for HZP. According to [99] a different set of criteria should be used, because the HZP criteria can be too strict for multi-physics simulations.

Eigenvalue for pin, assembly and core calculations	Boron Concentration for core calculations			
	HZP		HFP & cycle	
	RMS	Max	RMS	Max
200 pcm	25 ppm	50 ppm	32 ppm	100 ppm

Pin & Assembly Power distribution		2D Assembly	2D Core	3D Core
HZP	RMS	1.0%	1.5%	2.0%
	Max	1.5%	2.5%	3.0%
Cycle	RMS	-	-	1.5%
	Max	-	-	5.0%

Control Rod Worth & SCRAM Worth	Axial Offset RMS - Cycle
10%	1.2%

Table 2.5 Target accuracy for all parameters used for verification & validation in this study

Chapter 3

Neutronics Standalone Calculations for the Hot Zero Power State

«Αρχή ήμισυ παντός»

3.1 Objective

The first step in order to develop a multi-physics code system is to verify and validate the neutronic code. As it is mentioned in Chapter 1, CTF has been verified for VVER analysis, whereas nTF is a relatively new computational tool. Moreover, as it was discussed in sections 1.3 and 2.4, a VVER is a pressurized water reactor, where single-phase fluid is transferring heat, experiencing mostly upwards flow with little inter-assembly mixing. The possibility for two-phase flow or, in general, strong thermal-hydraulic (T/H) feedback effects exists only in accident conditions, which are not considered in this thesis. Thus, the behavior of the core is dominated by the neutronic phenomena.

Besides verification and validation, the purpose of the standalone analysis is to discover the weak points of the neutronic code, before introducing the effect of the T/H code and the depletion library. It will allow distinguishing the different sources of discrepancy in the calculations and optimize the use of the solver (e.g. computational mesh). The optimal way to perform this kind of study is the use of fresh Hot Zero Power (HZP) benchmarks; the material composition and temperature are fixed throughout the model, there is no need for T/H feedbacks. The factors which determine the outcome of the calculation are the accuracy of the geometry description, the XS libraries and finally the computational methods used. Thus, it must also be determined, at this stage, if any modifications on the neutronic code are necessary to allow for better application of the computational methods or improved modeling of the core.

In order to achieve the desired level of accuracy, the neutronic code should be able to model explicitly all the geometric features of the reactor which have an impact on key parameters, or reproduce their effect with modeling techniques. For the conventional neutronic analysis, the effect of local perturbations is handled through the coarse mesh neutronic parameters (cross-sections and discontinuity factors) determined by the lattice code. The local values of the neutron flux or power can be reconstructed by response functions, which also take into account the local geometry of the core [101]. Ideally, in high-resolution codes the core geometry would be modeled explicitly in full detail. Monte Carlo codes have such capabilities. However, deterministic codes, like nTRACER or CASMO, are often limited in terms of geometry description, due to the discretization schemes involved in the solution of the transport equation. Therefore, case specific modeling approximations are necessary, together with corresponding numerical techniques (e.g. methods to increase stability) to allow the effective modeling of real reactor cores. Moreover, complex geometries often result in computationally expensive calculations, because they require finer meshing. The goal of high-resolution deterministic codes is the simulation of the reactor core with enough details and a reduced number of approximations to ensure the accurate prediction of local and global key parameters, as well as cost-effective calculations. At this stage of the analysis, one can quantify the effect of the different structural features and decide how to model them (e.g. use of homogenized regions or of an explicit representation), optimizing the accuracy of the calculation vs the resources required and extending the capabilities of the solver if necessary.

The neutronic codes used in this work are in different levels of development and validation for the VVER analysis. As it was mentioned in Chapter 1, PARCS has been extensively used for whole core VVER analysis, so that nTF requires a much more detailed study of its new hexagonal modeling capabilities before use in a validation exercise. Likewise, the CASMO5-VVER module was a recent addition to the version available at LRT. As a result, even though such work has probably been done by Studsvik, an assessment of its performance is also desirable. Finally, CASMO5-VVER has never been used together with PARCS, so dedicated verification exercises are required before validation.

3.2 Neutronic analysis with the novel approach

As a first step, in order to examine thoroughly the performance of the novel neutronic code, a sensitivity study is realized which includes the comparison of nTF deterministic

calculations with the Monte Carlo code Serpent2, for simple VVER configurations. Subsequently, nTF is verified with the 2D full core HZP NURESIM-SP1 benchmark [96]. Different options for the modeling of the heavy reflector are examined. Finally, the study moves to the 3D full core X2 benchmark, where the performance of the code is verified against Serpent2 and validated against experimental data in HZP state. The aim of this work is to study the capacity of nTF to simulate the behavior of a real VVER-1000 core, with the introduction of approximations where necessary (e.g. for “problematic” structures). The modeling and computational capabilities of the solver need to be extended where the impact of those approximations on global and local parameters is preventing the solution from reaching the target accuracy.

3.2.1 nTF vs Serpent2 for simple VVER configurations

The goal of this study is to analyze separately the various models required to simulate successfully elements of the VVER core with a deterministic code. The cross-examination is performed for a range of models, from pincells to 3D fuel assemblies with Gd pins, increasing gradually the complexity of the problem. Each step aims at the evaluation of different nTF features, which could be sources of discrepancies. Several 2D pincell models of different enrichment (with and without Gd) are cross-compared in order to assess the nTRACER library, e.g. resonance self-shielding methods. Pincell models are appropriate for this purpose since they are less affected by heterogeneous transport. The nTRACER library is built by SNU and it is based on ENDF/B-VII.0. A consistent nuclear data library is used by Serpent2. The effect of heterogeneous transport is studied with the simulation of 2D VVER-1000 assemblies with reflective boundary conditions. One assembly model contains pins of the same low enrichment whereas the other assembly presents strong radial heterogeneity through the use of Gd pins and fuel pins of different enrichment. The same assemblies are also modeled in 3D, with top & bottom reflectors, to determine the effect of the 1D MOC axial solver and void boundary conditions.

3.2.1.1 Pincell models

The 2D pincell models of different enrichment correspond to the fuel compositions described in the X2 benchmark. Fig. 3.1 presents the eigenvalue difference of nTF vs Serpent2, $[\text{keff}_{\text{Serpent2}} - \text{keff}_{\text{nTF}}]$, for different enriched states with Gd and without, with P0 transport corrected and P2 scattering treatment (see Section 2.3.2.2). The coolant density is set at 0.7629 g/cc, including 1207 ppm of natural Boron (X2 critical state). The temperature of all

elements is set at 600 K, and not 554.15 K, which corresponds to the X2 critical state, to avoid the interpolation of the Serpent2 $S(\alpha, \beta)$ thermal scattering tabulated data for the moderator. The Monte Carlo uncertainty for all Serpent2 calculations is less than 5 pcm (3,000 active batches and 40 inactive batches of 40,000 histories each). All fuel pins are modeled with 7 radial subdivisions in nTF except for Gd pins that are modeled with 10.

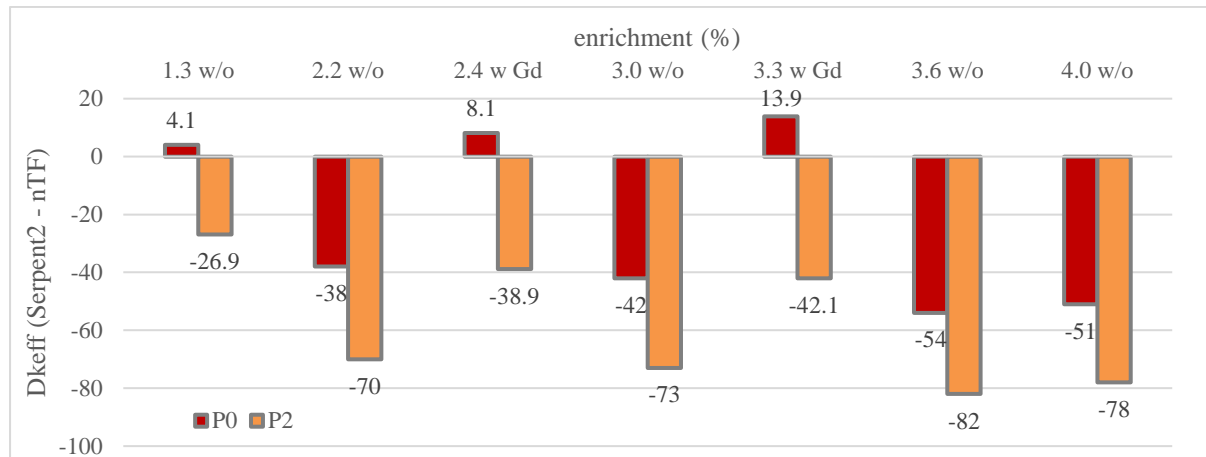


Figure 3.1. Eigenvalue difference of nTF vs Serpent2 for 2D pincells of different enrichment

Overall, the eigenvalue comparison suggests a good agreement of the nTF and Serpent2 libraries since it remains in acceptable levels (< 200 pcm) (see Section 2.7.3) for all models. With P0, nTF overestimates the eigenvalue in all cases, except the Gd pins and the 1.3% enriched fuel. The difference is increasing with enrichment, except for the 4.0% pin. On the other hand, the effect of resonance self-shielding is obvious on the Gd pincells, even when using 10 radial subdivisions. nTF underestimates the eigenvalue in comparison to Serpent2, in contradiction to the pincells without Gd. This is a prime example of error cancellation. When P2 is used nTF overestimates the eigenvalue for all pincells. The difference is increased; however, it follows the same trend as observed for P0, increasing with enrichment. Again the Gd pins present a lower discrepancy in comparison to the pins without Gd, nonetheless the difference between the discrepancies (with and without Gd) is decreased.

3.2.1.2 Assembly models

The assembly models studied in this section correspond to two X2 fresh fuel assemblies described in the benchmark specifications. As illustrated in Fig. 3.2, one assembly is built with a single type of low enrichment fuel (1.3%) and the other (4.0% inside) contains a ring of different enrichment pins at the outer boundary (3.6%), together with several Gd pins (3.3% with 5.0% Gd) close to the center. These specific models were selected to illustrate the effect

of MOC transport for various “levels” of heterogeneity in the lattice. Both assemblies are simulated at 600 K, with all material compositions corresponding to the X2 critical state. The P0 transport corrected scattering treatment is used. It must be pointed out, that the outer diameter of the central guide tube is larger than the pincell size in nTF and it cannot be modeled according to the specifications. Thus, the diameter is decreased both in the nTF models of the two assemblies and in Serpent2 (see also Section 3.2.3.1). Fig. 3.3 presents the relative difference of the normalized power, $[(\text{Nor.POW}_{\text{Serpent2}} - \text{Nor.POW}_{\text{nTF}}) / \text{Nor.POW}_{\text{Serpent2}}]$, on the pin level for the 2D assembly. The uncertainty of the Serpent2 calculations remains $< 0.03\%$ for the pin power and 2 pcm for the eigenvalue (6,000 active batches and 140 inactive batches of 500,000 histories each). The difference of the eigenvalue, $[\text{keff}_{\text{Serpent2}} - \text{keff}_{\text{nTF}}]$, for the 2D assembly calculations is respectively 59 pcm and 25 pcm, remaining in acceptable levels. The effect of the 2D calculation on the eigenvalue is not consistent with the pincell results. nTF underestimates the eigenvalue for the 2D assemblies, where the maximum absolute eigenvalue difference corresponds to the low enrichment assembly, in contradiction to what was presented up to this point. For the 13AU assembly (1.3% enriched fuel), the relative power difference remains $< 0.2\%$ with RMS of 0.06%. The effect of heterogeneous transport from the MOC calculation is minimal. The heterogeneous 390GO assembly presents higher discrepancies with a maximum at 0.33% and RMS at 0.08%. The RMS is very close to that of the homogeneous assembly since the maximum discrepancies appear only for the Gd pins. For both cases nTF presents a tendency to flatten the power profile, overestimating the power at the edge and underestimating it in the center of the assembly. This is a common occurrence with MOC codes [102] and is studied further in the next sections of this chapter for the full core. It is clear that the flux dip of the Gd pins has an effect on the nTF pin power prediction, however there is still very good agreement with Serpent2. The heterogeneous 390GO assembly is simulated also with 4 subdivisions in fuel pins and 7 subdivisions in the Gd pins to study the effect of a coarser mesh. The pin power discrepancies (maximum and RMS) of the Gd pins remain the same. The eigenvalue difference increases by 10 pcm.

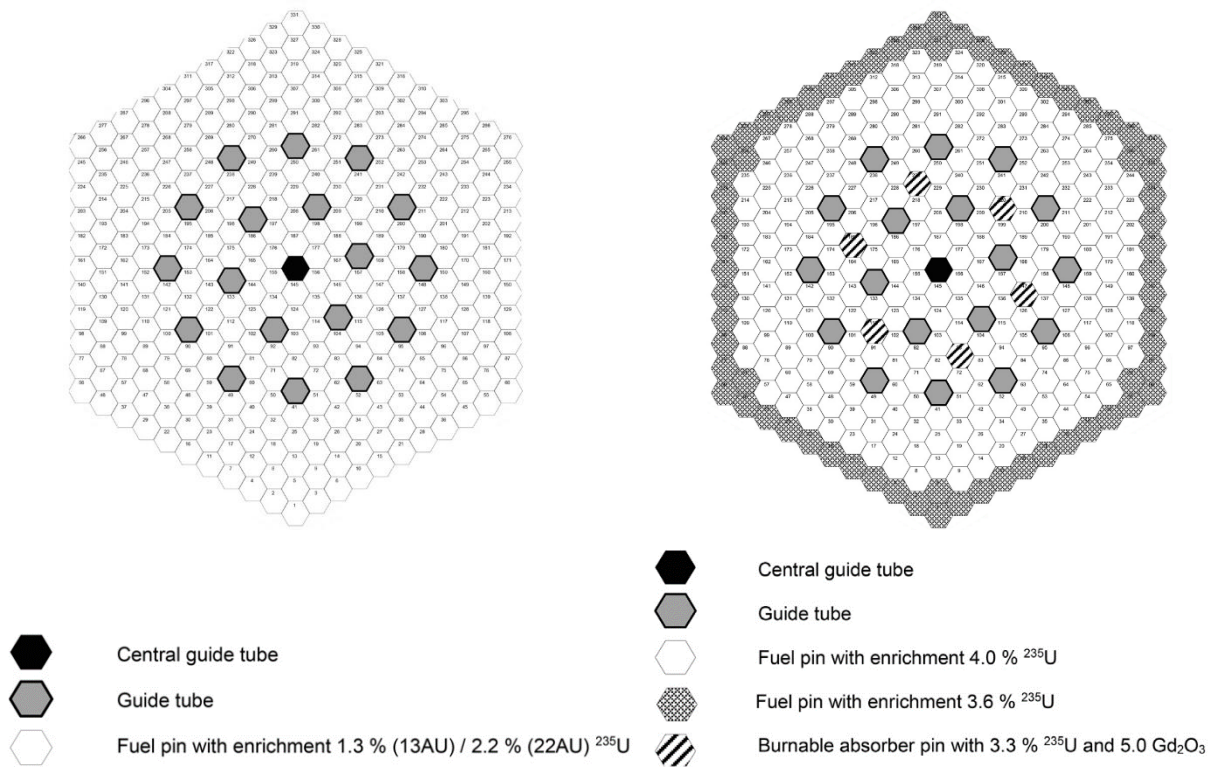


Figure 3.2. Pin layout of X2 fuel assembly 13AU (left) and 390GO (right)

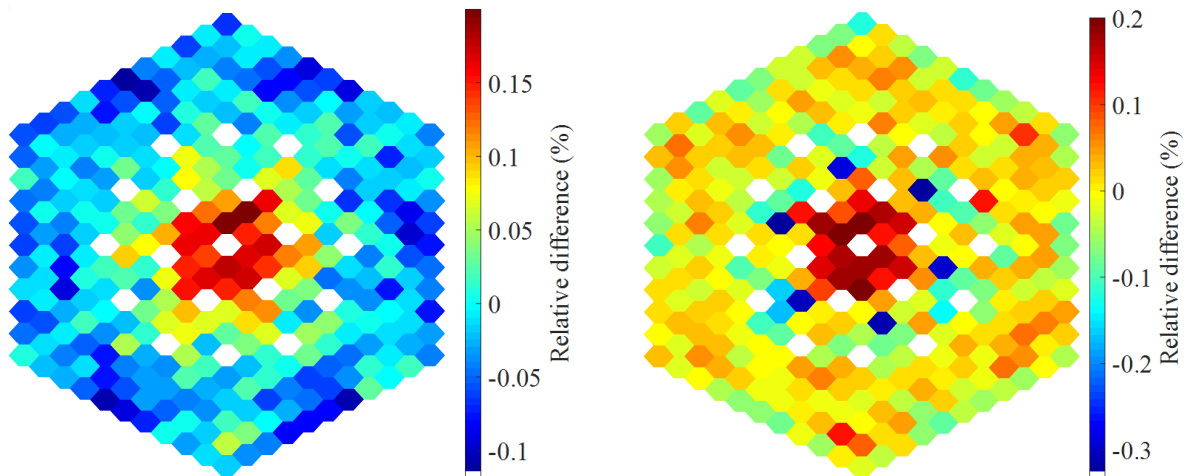


Figure 3.3. Relative pin power difference of nTF vs Serpent2 for the X2 fuel assembly 13AU (left) and 390GO (right)

Finally, in order to study the effect of the 1D MOC axial solver the two assemblies are modeled in 3D. The same pin layout, as depicted in Fig. 3.2, is extended to 3.55 m, the height of the active core for the X2 benchmark. A coolant bottom and top reflector of 17.75 cm is added to reduce the axial leakage due to the void boundary conditions (22 axial nodes in total). The uncertainty of the Serpent2 calculations remains $< 0.08\%$ for the axial power profile and 4 pcm for the eigenvalue. For the 3D 13AU assembly, the maximum relative power difference,

$[(\text{Nor.Pow.Serpent2} - \text{Nor.Pow.nTF}) / \text{Nor.Pow.Serpent2}]$, in the axial profile is 0.37% and the RMS 0.23%. The difference in the eigenvalue, $[\text{keff}_{\text{Serpent2}} - \text{keff}_{\text{nTF}}]$, is 40 pcm. Similarly, the 390GO 3D assembly has a maximum relative power difference of 0.36% and RMS of 0.15% and a difference in the eigenvalue of -2 pcm. The axial solver seems to have some effect on the power distribution; however, it is independent of the assembly heterogeneity and it remains at an acceptable level. The maximum absolute eigenvalue difference corresponds to the low enrichment 3D assembly, following the trend observed for the 2D assembly models. However for both 3D assemblies the difference is decreased in comparison to the 2D cases, which can be attributed to the axial solver.

Overall, the comparison of nTF vs Serpent2 for small VVER configurations proved the capacity of the code to deal with computational features, which can be sources of inaccuracy in deterministic transport codes. The effect of some said features (e.g. flux dip of Gd pins) is observed in the nTF results and can be expected to emerge in the calculations that follow. However, the corresponding discrepancies are small enough to verify that nTF is capable to handle basic functions of simulating hexagonal fuel elements.

3.2.2 Verification with a 2D full core model with a heavy reflector

In order to gradually increase the level of complexity, this section is focused on the modeling of a simplified 2D core. As it was mentioned in Chapter 2, the NURESIM-SP1 benchmark framework includes 2D core problems for the VVER-1000, which allow code-to-code comparison. Specifically, NURESIM-SP1 V1000-2D-C1-tr [96] is based on a simplified 2D VVER-1000 core model with heterogeneous UOX-fuel loading and a heavy reflector. The relevant picture from Chapter 2 is reproduced in this section to facilitate the reading (see Fig. 3.4). The simplified 2D model is ideal to study the performance of nTF on the modeling of the full active core, without the presence of problematic geometries (e.g. corner stiffeners) that can be sources of discrepancies. All such structural elements are removed from the model or homogenized. Thus, the only heterogeneities on the active core originate from the fuel assembly distribution (see Fig. 3.4). Another important feature of the VVER, is the heavy reflector. Concerning multi-physics calculations, the impact of the heavy reflector model on the accuracy of global and local parameters is very strong for the neutronic analysis [103]. It can be attributed to the structure of the reflector, which contains localized moderator-rich cavities. This complex geometry poses an issue for deterministic codes [104]. High-resolution

solvers especially, must reproduce the effect of the reflector as realistically as possible, in order to grasp the local flux and power distribution accurately everywhere in the active core. The heavy reflector (see Fig. 3.4) described in the V1000-2D-C1-tr benchmark, although excluding some very modeling-demanding features (groove region), is characteristic of a VVER-1000. The bias introduced by relevant modeling approximations on the calculation of local and global quantities can be quantified with this benchmark. This will allow the determination of an effective way to model the heavy reflector with nTF before attempting to simulate real 3D VVER geometries.

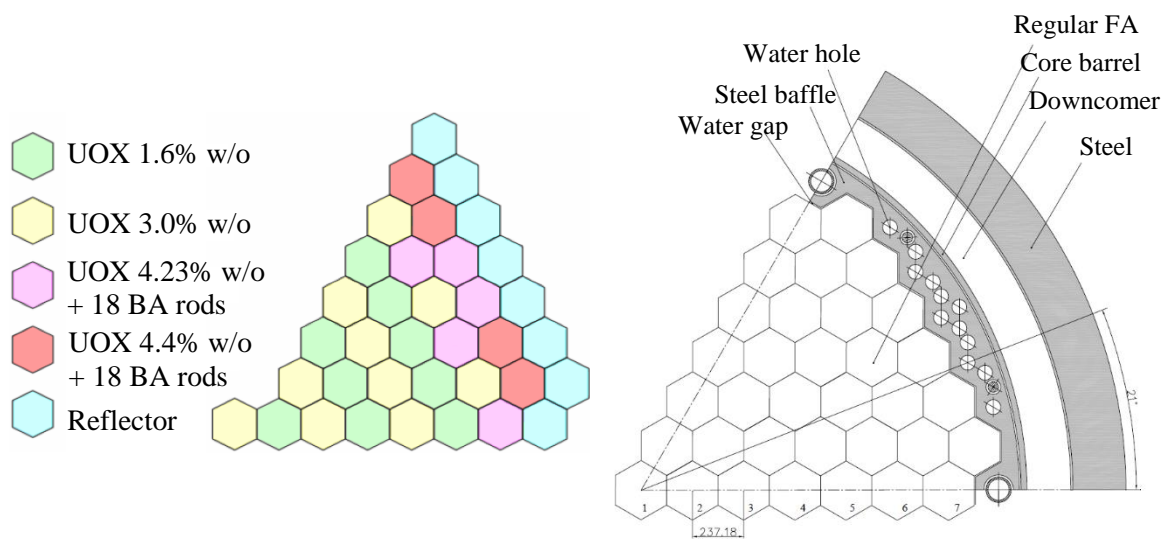


Figure 3.4 (Fig. 2.10) Left: The symmetric fresh fuel loading of exercise V1000-2D-C1-tr. Right: Technical drawing of the heavy reflector of the VVER-1000 core as specified in the benchmark

The benchmark specifications includes reference solutions for the fresh fuel HZP state, provided by a lattice and a Monte Carlo code. However, the libraries used by both codes do not match the nTF libraries. In order to remove the impact of the different cross-section libraries, the benchmark is simulated with Serpent2. The full VVER-1000 core with the heavy reflector, as specified in the V1000-2D-C1-tr benchmark, is modeled explicitly. The geometry of the active core is modeled explicitly also in nTF. However, several modifications are necessary in the code in order to reproduce some of the structural elements of the heavy reflector. Originally, the code allowed only the definition of assemblies, of specific size, which consist of the pincell lattice and a surrounding gap. The gap size and material could vary, however not in the same assembly. Thus, structures like the water holes or the water gap surrounding the active core could not be replicated accurately. In the course of this study, the code was extended by SNU to allow the modeling of circular orifices, like the water holes or the water gap between the

steel buffer and the core barrel [66]. The pincells of the reflector assemblies are defined as homogeneous elements, filled with the metal of the heavy reflector (in this case steel). The location, material and dimensions of the orifices are specified in the nTF input. The code identifies the pincells in the reflector assemblies that correspond to the position of the orifices. If more than half the area of a pincell is contained in the orifice, then the pincell is filled with the material of the orifice (in this case moderator) (see Fig. 3.5). From this point on in the thesis, this modeling method will be referred to as the nTF reflector modeling approach. Up to this point, no actions were taken to model explicitly the water gap between the active core and the reflector. In order to study the impact of the heavy reflector on the neutronic behavior of the core and to verify the new relevant capacities added to nTF, two different modeling approaches are used. Firstly, the active core is modeled surrounded by two layers of homogeneous assemblies (model I). The inner assembly layer is homogenized steel and borated moderator, volume weighted to preserve atomic densities, accounting for the effect of the buffer and the core barrel zones. The outer layer is made of borated moderator, representing the downcomer (see Fig. 3.4). The second approach consists of a more refined modeling scheme involving homogeneous pincells (model II). The water gap surrounding the active core is modeled by surrounding the inner reflector assemblies with a coolant gap and simulating the pincells facing the active core as a homogeneous mixture of steel and water. The water holes, the downcomer and the water gap between the steel buffer and the core barrel are reproduced with homogeneous pincells of steel or water, according to the nTF reflector modeling approach. An example of this modeling approach is depicted in Fig. 3.5.

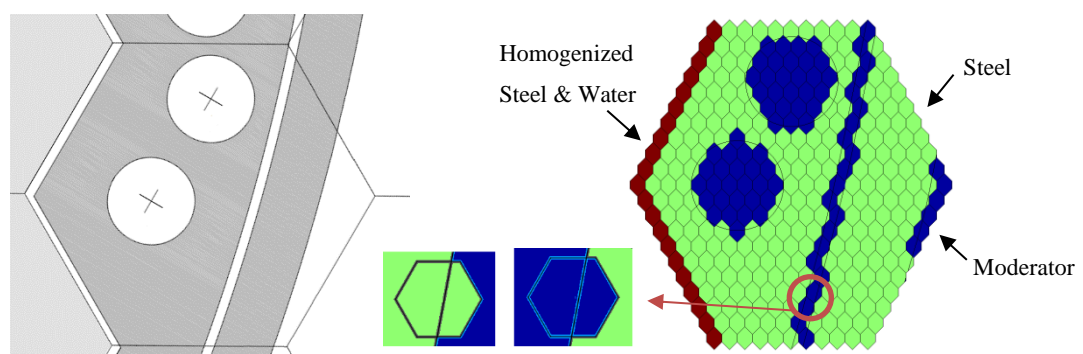


Figure 3.5. Left: A reflector section corresponding to one assembly, as specified in the benchmark specifications. Right: nTF model II of the same assembly with homogeneous pincells for the water gap

Fig. 3.6 depicts the relative difference of the normalized assembly power map of nTF, with the simplified (model I) and refined reflector model (model II), in comparison to Serpent2, $[(\text{Nor.POW.Serpent2} - \text{Nor.POW.nTF}) / \text{Nor.POW.Serpent2}]$ for $1/6^{\text{th}}$ of the VVER core. Also, the

difference of the eigenvalue is presented on the same figure, $[\text{keff}_{\text{Serpent2}} - \text{keff}_{\text{nTF}}]$. 4,000,000,000 particle histories are considered in Serpent2 (4,000 cycles x 1,000,000 particles) in order to achieve a 1σ uncertainty of 1 pcm for the eigenvalue and $< 0.06\%$ in the assembly power distribution. In order to ensure the convergence of the fission source (Shannon Entropy), 400 inactive cycles are used. For nTF the MOC tracks are set to a ray spacing of 0.05 cm; 24 azimuthal angles for the whole core and 4 polar levels are also considered. This configuration is adopted after consultation with SNU. At this point in the study, nTF is using P0 transport corrected total cross-section with an isotropic scattering source (see Section 2.3.2.2).

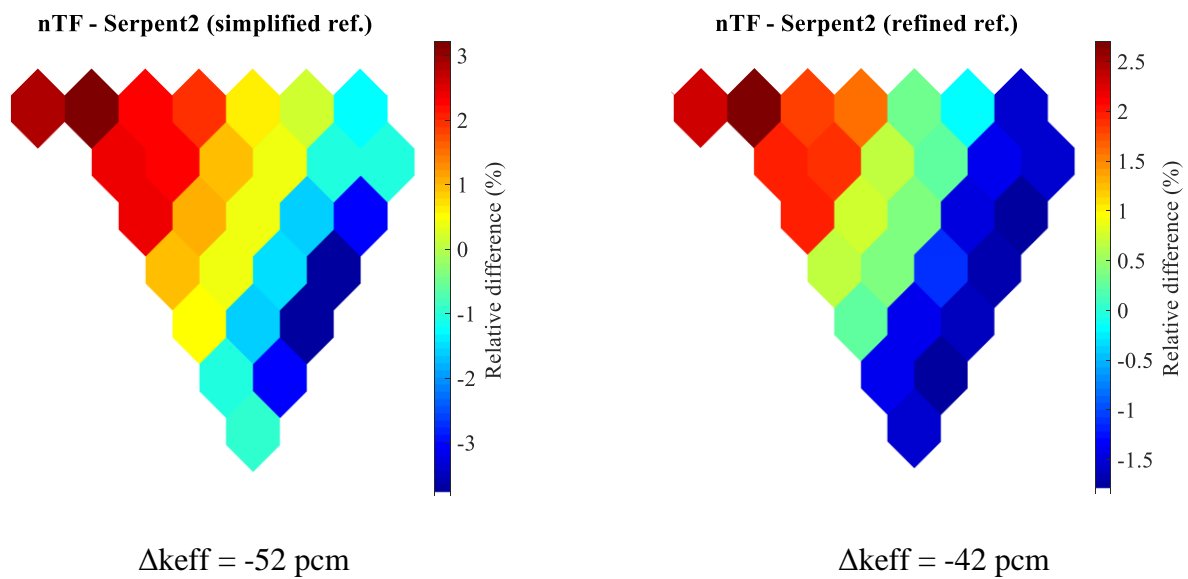


Figure 3.6. Relative assembly power difference and eigenvalue difference between nTF and Serpent2 for the case with a simplified [model I] (left) and a refined [model II] (right) reflector model in nTF

For both cases, nTF presents a relatively good agreement with Serpent2. Δkeff remains well below 200 pcm. Concerning the power maps, the highest discrepancies are present on the nTF solution with the simplified reflector (model I), reaching 3.8%, which is higher than the target accuracy, with a RMS difference of 2.0%. The relative assembly power difference decreases for the refined reflector (model II) solution together with the difference in the eigenvalue. The maximum is 2.7% and RMS reaches 1.5%. The two maps of Fig. 3.6 diverge not only in the magnitude of discrepancies but also the shape of the profile presents some differences. This can be attributed to the different reflector models.

At the assembly level, the nTF discrepancies with respect to the Serpent2 reference are small. However, the purpose of nTF as a high-resolution code is to predict the neutronic behavior of the core on a local scale, rather than with global parameters like the assembly

power. This can be especially challenging with a VVER-1000 due to the strong heterogeneity of the pin power distribution, created by the fuel load and the impact of the heavy reflector. Fig. 3.7 presents the normalized pin power distribution of 1/6th of the core as it is predicted by Serpent2. The layout of assemblies with different enrichment results in strong variations of the power profile and the flux of the pins close to the reflector is well below the average. In order to verify nTF and examine the validity of the modeling approximations for high-resolution VVER analysis, the pin power distribution of the 2D VVER-1000 core for the simulations, illustrated in Fig. 3.6, with simplified (model I) and refined reflector (model II) is compared with the solution of Serpent2. The Monte Carlo simulation (see also Fig. 3.7) is repeated with a higher number of particles (100,000 cycles x 1,000,000 particles) to achieve increased accuracy on the pin power prediction, allowing for an average 1σ uncertainty of 0.7% in the inner assemblies and 1.4% for the ones neighboring the reflector.

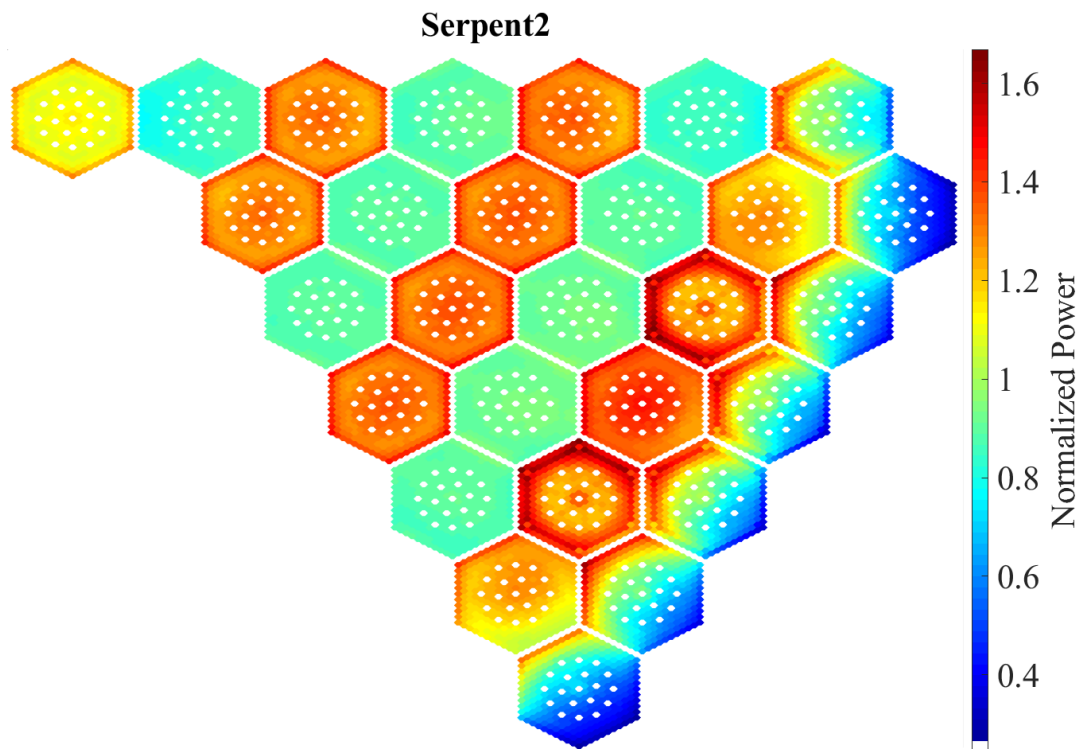


Figure 3.7. Normalized power for the VVER-1000 core as calculated by Serpent2

Despite the low discrepancies in the assembly power comparison, the cross-examination of the nTF high-resolution calculations on a local scale presents a very different outcome. The effect of the approximated reflector models is apparent on the comparison of the respective solutions with Serpent2. In the case of the simplified reflector, the pin power RMS is 2.1%, nonetheless the pin power difference increases significantly for the assemblies close to the

reflector, where it can reach ~8%. The refined reflector model allows overall lower differences in the pin power (1.9% RMS difference); nonetheless, there are strong discrepancies, up to ~10%, on the outer layer of pins neighboring the heavy reflector and specifically the homogenized water gap.

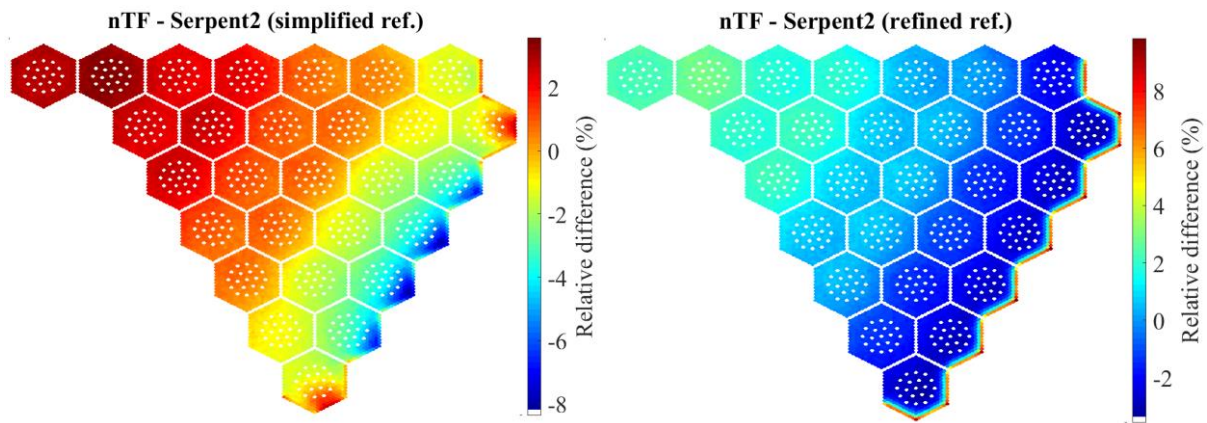


Figure 3.8. Relative pin power difference between nTF and Serpent2 for the case with a simplified [model I] (left) and a refined [model II] (right) reflector model in nTF

In general, the above power maps prove the sensitivity of the prediction for the core neutronic behavior to the modeling of the reflector. It is clear that the approximations involved affect strongly the region close to the reflector, but also have an impact to the overall power profile, introducing power tilts. This can be attributed to the structure of the reflector, combining water and steel in complex formations. The moderator-rich regions close to the active core have a strong effect on radial leakage, which cannot be simulated accurately by homogenized geometries, even if the size of the region appears relatively insignificant, like the water gap. The introduction of spatial approximations on the reflector models is a standard practice in the conventional approach (see Section 3.3.3). However, it is apparent that modeling approximations that are adequate for coarse mesh calculations [95] (see Fig. 3.6) cannot be used for high-resolution solutions (see Fig. 3.8). By examining the above figures, it becomes clear that when high-resolution tools are used for the prediction of local quantities, the heavy reflector should be modeled with detail, especially its moderator regions close to the active core. On that note, nTF modeling capabilities were extended by SNU to include the water gap surrounding the active core (model III) (see Fig. 3.9) [67]. The radial decomposition of a hexagonal assembly in nTF consists of a honeycomb mesh of fuel pins, surrounded by the water gap of the assembly subdivided in rectangular cells (see Fig. 2.5). Due to the structure of the computational mesh, nTF still fails to model explicitly the water gap corners. The corner is

approximated by a rectangular cell containing a mixture of homogenized moderator and steel, volume-weighted to match the real proportions of the region defined by the cell.

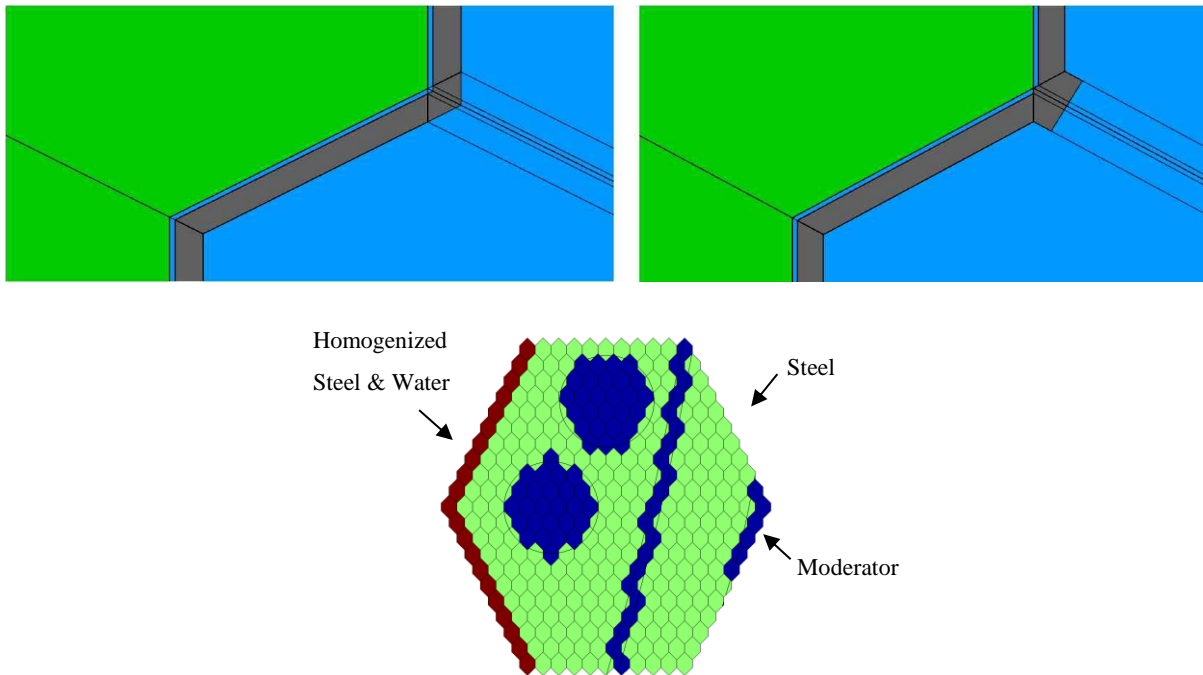


Figure 3.9. Exact geometry (top left) and nTF model III (top right) of the reflector water gap. nTF model II (bottom) with homogeneous pincells for the water gap

Fig. 3.10 depicts the relative difference on the normalized pin power distribution of nTF, with the semi-explicitly modeled water gap (model III), vs the Serpent2 solution. The RMS equals 1.6% and the maximum difference does not exceed 3.3%, even in the reflector neighboring regions where the relative power is very low (see Fig. 3.7). The difference in the eigenvalue of the two calculations drops to $\Delta k_{eff} = -38$ pcm. The low pin power relative difference, even in problematic regions, e.g. close to the reflector, and considering the heterogeneity of the fuel loading, is a statement of the performance of nTF when it comes to high-resolution VVER modeling. Both RMS and maximum pin power difference are higher than the target accuracy set in Section 2.7.3; however not significantly, especially taking into account the modeling approximations on the heavy reflector [102].

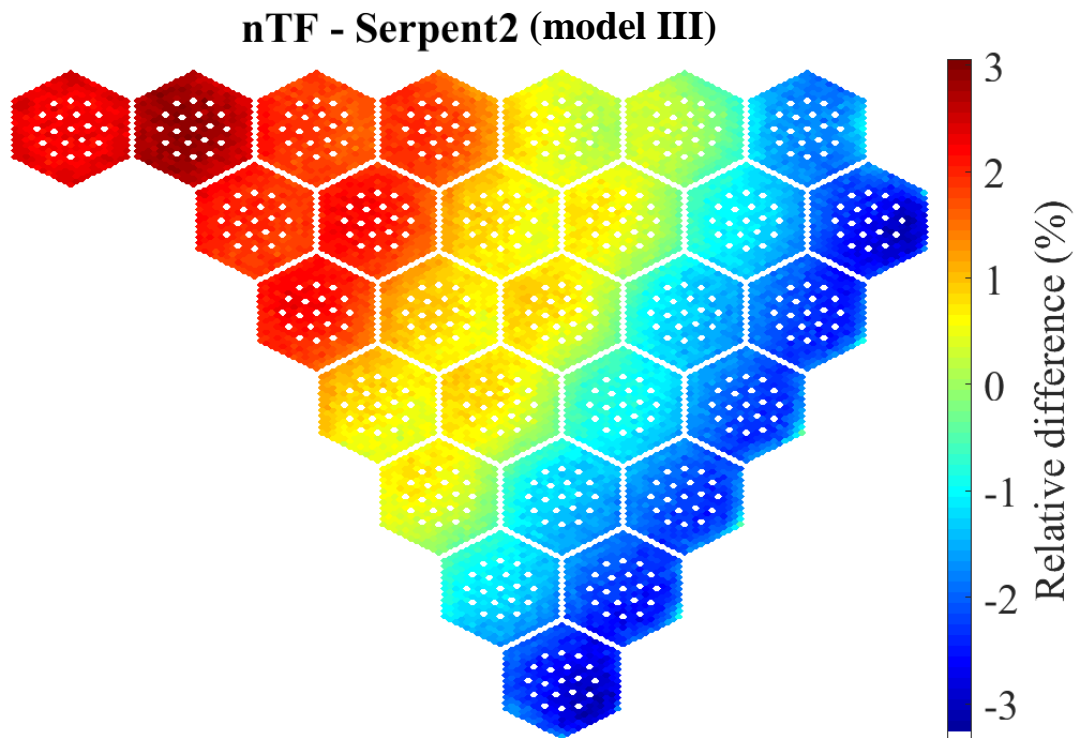


Figure 3.10. Relative pin power difference between nTF and Serpent2 for the case with a semi-explicitly modeled reflector water gap in nTF [model III]

Despite the good agreement of the calculations, a tilt in the pin power difference is also apparent. nTF underestimates the power in the center of the core in comparison to Serpent2 and overestimates it in the outer assemblies, flattening thus the power profile, following the trend observed in Section 3.2.1.2. The tilt is partially caused by the approximations involved in the nTF reflector modeling approach. CASMO5-VVER uses a similar approach for the modeling of heavy reflectors in full core models, which results also in power tilts [102]. In addition, unlike CASMO5-VVER, nTRACER uses one spectrum for the condensation of cross-sections that corresponds to the fuel region and not the reflector material. This means that the self-shielding in steel is not taken into account accurately, which could be a source of discrepancy. The tilt could also be partially attributed to the treatment of anisotropic scattering by the transport correction. In order to test this hypothesis, nTF was modified by SNU to include P2 anisotropic scattering (see Section 2.3.2.2). Fig. 3.11 presents the relative pin power difference for the nTF model III with P2 scattering vs Serpent2. All other parameters of the nTF calculation are identical. In the same figure, the pin power difference of nTF-P0 vs nTF-P2 is also presented. The color scale is the same for both plots.

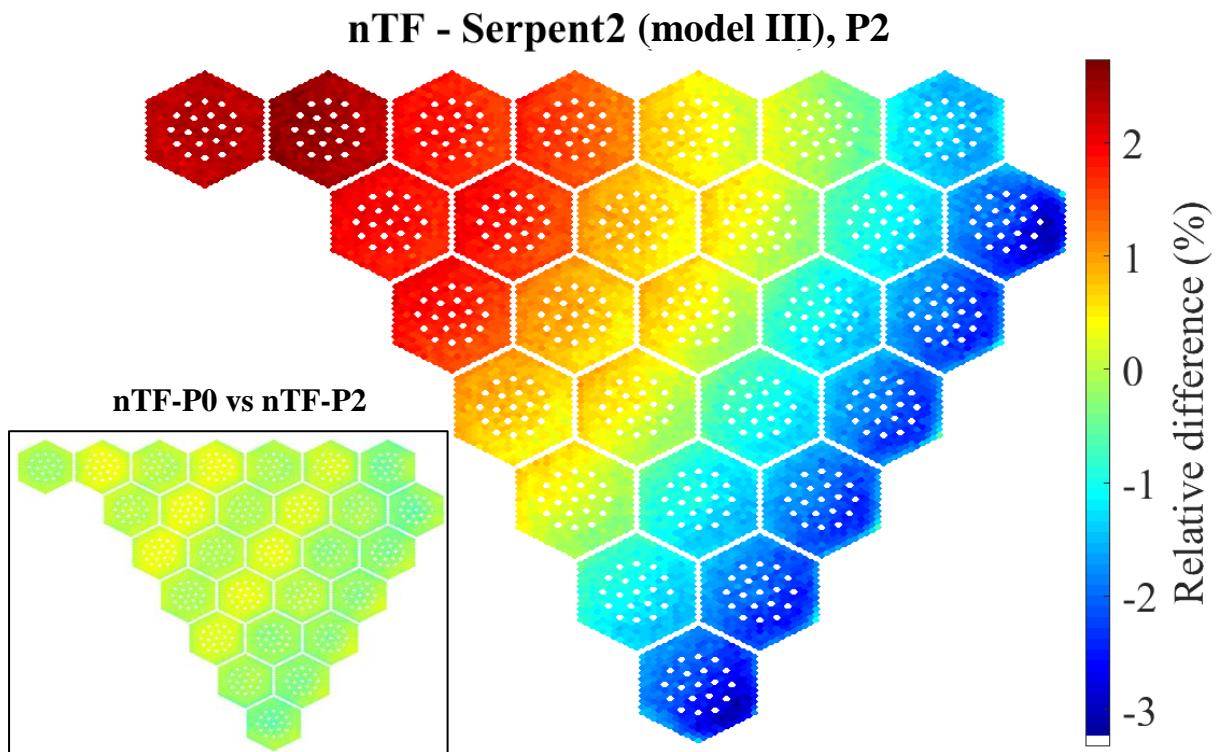


Figure 3.11. Relative pin power difference between nTF and Serpent2 for the case with a semi-explicitly modeled reflector water gap in nTF [model III] and P2 anisotropic scattering approximation

As is apparent in Fig. 3.11, the use of the P2 scattering approximation leads to reduction of the pin power discrepancies with respect to Serpent2; however not enough to reduce the tilt significantly. This finding is consistent with previous studies on the topic [45]. The pin power difference RMS equals 1.5% and the maximum reaches 3.2%. The subplot illustrates the effect of P2 on the nTF pin power map. The tilt becomes less pronounced and the profile of the difference is more smooth radially e.g. the discrepancies in the assemblies with peak power (see Fig. 3.7) are smaller and closer to the level of their neighboring assemblies. The pin power difference from the reference solution is decreased at a maximum of 0.6%. The difference of the eigenvalue is increased, Δk_{eff} equals -35 pcm. Besides the effect of the reflector model and P2, the tilt in the power profile is a common outcome when comparing MOC solvers with Monte Carlo codes [105], as it is observed also with the CASMO5-VVER verification (see Section 3.3.2). Even though P2 has a positive impact to the solution, the improvement is not enough to justify the resources required for such a calculation. It must be pointed out that even though the original model was only occupying 39% of the node memory, P2 is so computationally expensive that the ray-tracing scheme had to be switched to Group Major from Node Major (see Section 2.3.2.1) in order to fit in the cluster. This resulted in severe penalties

on the running time, increasing it from 3 hrs and 53 mins to 9 hrs and 42 mins (300 CPUs for both calculations).

In general, it is verified that nTF can simulate full core hexagonal geometries with the necessary detail required by a high-resolution neutronic tool. The modeling of the heavy reflector is always a challenging task for deterministic codes; however; the nTF geometry description capabilities are refined enough to offer an accurate modeling of the VVER-1000 heavy reflector. The calculations with the nTF model III not only prove the overall capability of the code to provide accurate predictions on a local scale, they also verify the MOC 2D transport calculation, specifically since the nTF and Serpent2 models are based on the same cross-section libraries and are built with the same predefined material compositions.

3.2.3 Verification with a 3D full core model and validation with experimental data

At this stage of the work, following the study and developments of the code, nTF is fit to be tested for a full VVER-1000 core. nTF models of actual 3D VVER cores have never been compared to measured data. This means that auxiliary modeling options (e.g. spacer grids) and refining numerical tools (e.g. relaxation methods), included in the Cartesian version of the code, are not yet available for VVER models. Besides the actual reproduction of complex geometric structures, the solver needs to build the appropriate computational grid to achieve the convergence of the solution. For an MOC code, like nTF, this includes the appropriate ray spacing, azimuthal and polar angles but also suitable subdivision of the different material regions in the cells, to produce accurate sub-pin predictions. Obviously, the finer the computational mesh becomes, the more expensive is the calculation. The successful use of the solver lies on the optimal balance between spatial resolution, modeling accuracy and computational cost. In the previous section, it became obvious that high-resolution codes can be inefficient with some geometry approximations, like homogenization of the heavy reflector. Thus, despite the complexity of the geometry, some structural elements need to be modeled explicitly, in order to successfully predict local parameters. This has a double impact on the simulation. Firstly, in order to model the complex structural element the code builds more cells on the same region. An example is the modeling of the reflector water gap (see Fig. 3.9) which, when homogenized, was reproduced by a single row of inter-assembly gap cells, whereas the semi-explicit model is built by two rows of cells, one row of water and one of steel, increasing the number of regions. At the same time, as the region is subdivided and smaller cells emerge,

the mesh required to achieve convergence must also become finer. The ray tracing of the MOC calculation must be dense enough so that each cell is traversed by at least one ray. The simulation of a real core requires many elements to be modeled explicitly. The mesh must also be fine enough to achieve the convergence of a 3D model with millions of cells. This makes the calculation computationally expensive.

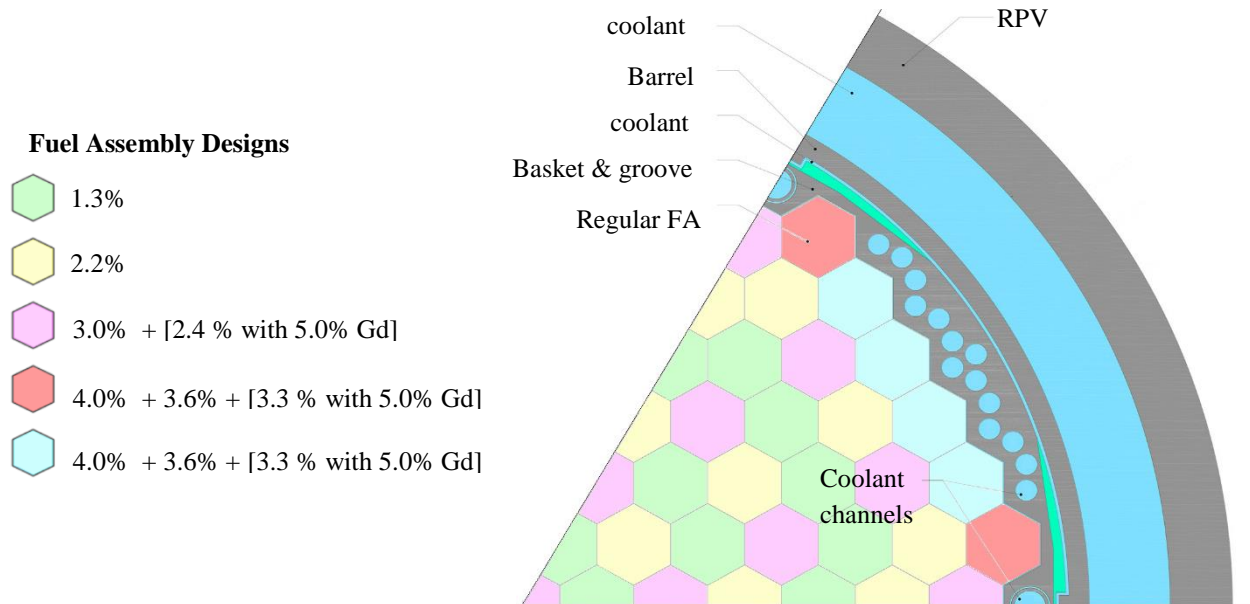


Figure 3.12. (Fig. 2.11) Fuel designs, core layout and Serpent2 model of the heavy reflector for the X2 benchmark

The goal of this work is to optimize the nTF model of a full VVER-1000 core in order to provide accurate high-resolution predictions with minimized computational costs. The X2 benchmark [98] is chosen for this analysis. The benchmark model is based on a real VVER-1000, incorporating all elements which were excluded from NURESIM-SP1 V1000-2D-C1-tr for the sake of simplicity in the code-to-code comparison. The core layout and the model of the heavy reflector is copied in this section from Chapter 2 to facilitate the reader (see Fig. 3.12). The additional modeling requirements challenge further the capabilities of nTF, especially considering the intended time optimization and memory limits.

3.2.3.1 X2 model of nTF

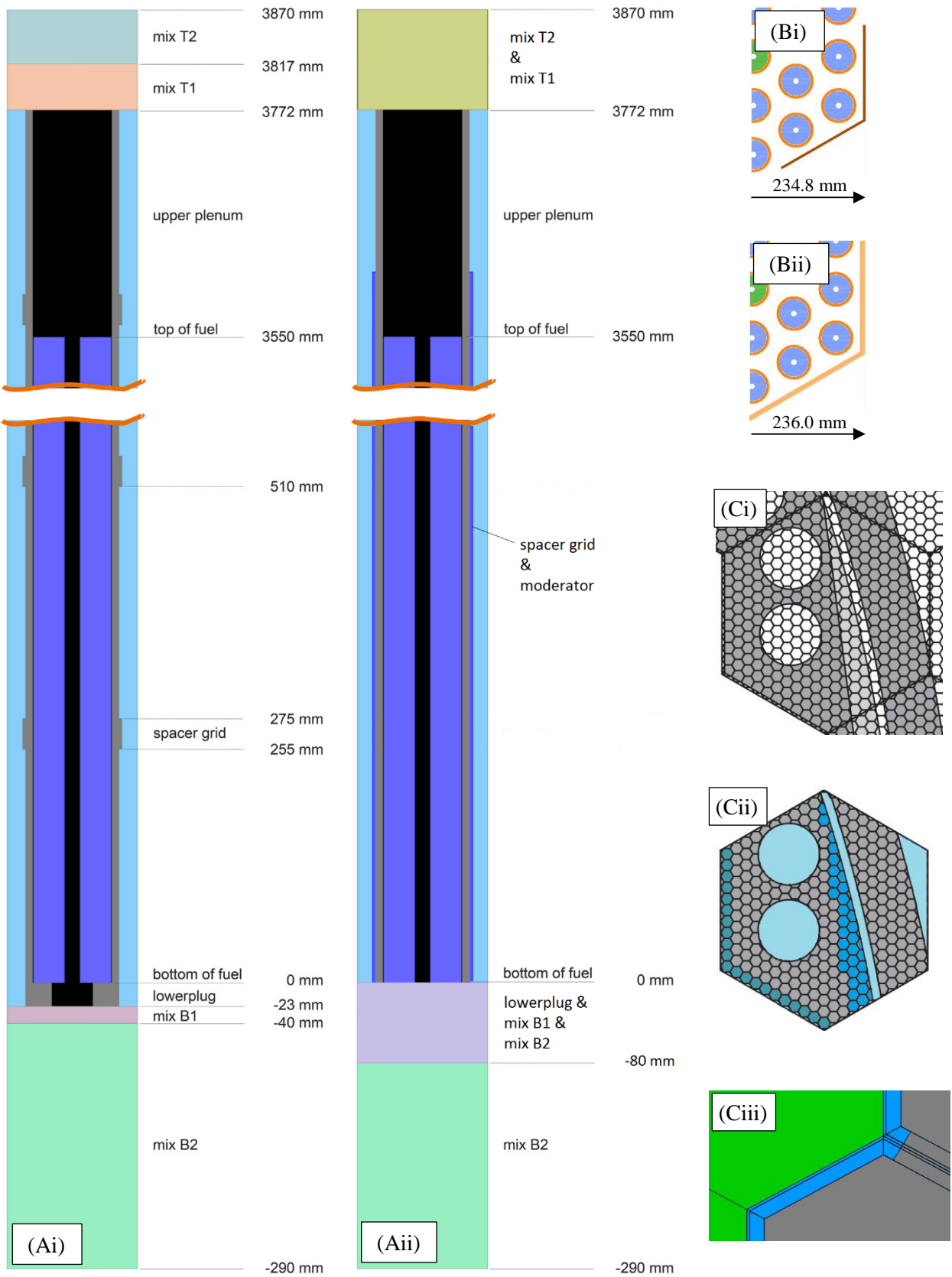
Despite the development of the code illustrated in the previous section, several approximations are still necessary to model the X2 HZP full core with nTF. The aim is to study the current performance of nTF in modeling a real VVER-1000 core with the use of approximations for “problematic” structures, together with the impact of those approximations on global and local parameters. Subsequently, if necessary, the code will be modified or

extended accordingly, to incorporate modeling elements that are crucial for the accuracy of the solution. Fig. 3.13 depicts all geometry approximations applied to the nTF model. Side (i) presents the X2 reference model built by Serpent2 and side (ii) the equivalent nTF approximation. Fig. 3.13.A.i & 3.13.A.ii illustrate respectively the axial layout of the fuel rod in Serpent2 and nTF. Fig. 3.13.B.i & 3.13.B.ii present the model of the corner stiffener in Serpent2 and nTF. Finally, Fig. 3.13.C.i & 3.13.C.ii depict details of the radial reflector, modeled explicitly in Serpent2 but only approximately in nTF. A few but important modeling options for the geometry and the computational methods used in nTF are listed below:

- In the reference model, spacer grids are approximated as added width to the cladding for their actual height (see Fig. 3.13.A.i). In nTF, the mass of all spacer grids is homogenized with the moderator mass of a water column, equal in radius to that of the spacer grids in the Serpent2 model, extending from the bottom of the fuel to the top of the last spacer grid in the upper plenum (see Fig. 3.13.A.ii). The purpose of this approximation is that axial decomposition of the 3D core with small nodes can cause instabilities in nTF [85].
- The benchmark specifications defines the axial top and bottom reflectors as mixtures of homogeneous materials of specific height (see Fig. 3.13.A.i). In this work, the top reflector is modeled as a single homogeneous region of equal width to the equivalent regions (T1 & T2) of the Serpent2 model (see Fig. 3.13.A.ii). The bottom reflector is divided in two segments. The lower segment is built with the same material (B2) suggested in the benchmark specifications. The top segment consists of a homogeneous mixture of the lower plenum, the 1st homogeneous region of the Serpent2 model (B1) and part of the 2nd homogeneous region of the reference model (B2) (see Fig. 3.13.A.ii). The further homogenization of the axial reflectors is necessary due to the small height of the different regions in the Serpent2 model.
- The radial decomposition of a hexagonal assembly in nTF consists of a honeycomb mesh of fuel pins, surrounded by the water gap of the assembly subdivided in rectangular cells (see Fig. 2.5). The latest version of nTF lacks the capacity to define assembly gap cells of different material; thus, the corner stiffeners of the active core (see Fig. 3.13.B.i) are not modeled explicitly. Instead, the mass of the corner stiffeners, of one assembly, are homogenized with the mass of the moderator in the water gap (see Fig. 3.13.B.ii).
- According to the benchmark specifications, the central guide tube has a radius of 0.65 cm. This exceeds the size of the pincell model (flat-to-flat 1.275 cm) and cannot be reproduced. The radius is reduced in the nTF model, in order to fit the central guide tube in a single pincell. A better approximation would be to reduce both the inner and outer diameter to

preserve the mass of cladding and coolant [102]. Nonetheless, the effect of the approximation on the power of the surrounding pins is no more than 0.2% in 2D.

- Concerning the heavy reflector (see Fig. 3.13.C.i), as illustrated in the previous section, the latest version of nTF allows the modeling of the water holes, the water liner between the core basket and barrel, and the downcomer with the nTF reflector modeling approach. The code was also extended, during this study, to allow for the semi-explicit modeling of the water gap between the active core and the basket [67]. This can be more computationally demanding; however, it was illustrated in Section 3.2.2 (see Fig. 3.8 & Fig. 3.10) that it is necessary for the accuracy of the solution. Both modeling options of homogenized cells (see Fig. 3.13.C.ii) and semi-explicit reproduction (see Fig. 3.13.C.iii) are studied in this work, in order to examine their impact on a 3D calculation. Finally, the homogeneous groove region defined in the reference model cannot be modeled explicitly by nTF. Alternatively, the groove is represented by homogeneous pincells that map approximately its shape in the reflector assemblies (see Fig. 3.13.C.ii).
- The X2 HZP nTF solution is produced with transport corrected P0 scattering. It will be also simulated with P2 scattering to study the effect on a 3D model.
- At this stage of the study, nTF cannot introduce a Control Rod (CR) into the model unless it is built explicitly. Thus, the size of the core axial layers are adjusted to allow the exact reproduction of the B₄C and DyTi layers of the CR. The axial mesh is differing from the Serpent2 model (20 layers x 17.75 cm). Nonetheless, this does not pose any obstacle for the comparison of the results and removes a possible source of discrepancy, which would be the homogenization of the CR material in partially rodded nodes.



3.2.3.2 Convergence Study

In this work the term “convergence” is used with a dual meaning. Firstly, it refers to the ability of the code to converge to a solution, meaning the calculation will actually finish after the user defined convergence criteria for the eigenvalue, fission source and flux residual are reached [10^{-6} , 10^{-5} , 10^{-5}]. Secondly, the solution is considered converged if by using a finer computational mesh the results are not changing significantly. The change is regarded as significant, if it is comparable to the discrepancy level expected when comparing the code results with the reference solution.

As it was mentioned before, the computational mesh of nTF is dependent on the MOC ray spacing, the number of azimuthal and polar angles, and also on the subdivisions of each material region in the pincell. There are some basic recommendations deriving from the study of deterministic codes (CASMO manual [90]), like a fuel pin should not be modeled with less than 3 subdivisions and a Gd pin with no less than 10, to accurately reproduce the flux profile within a fuel rod. In order to optimize the use of nTF, several mesh configurations are tested with a 2D X2 full core model, including all approximations of Fig. 3.13. It must be pointed out that some extra limitations are set later in the work by necessary modifications on the code, which do not correspond to the X2 model described in Section 3.2.3.1, but are still taken into account for the optimization of the mesh. However, all the numbers included in this section are produced with the X2 model described in Section 3.2.3.1. The reason for not using the final X2 model for convergence analysis is that the model of the above section is much more flexible in terms of computational complexity and allows examining several mesh configurations, which the final model cannot. This study is not performed in 3D, since the main factor affecting convergence, but also computational resources, are the MOC planar calculations. However, it should be taken into account that the axial solver requires a significant share of the node memory (<15%). The limitations in terms of resources set for the nTF standalone HZP calculations is the size of the cluster and that the running time should be ~4 hrs to be comparable with the time required by nTRACER to model a Cartesian PWR state-point [45].

1. Ray spacing: In the previous section the ray spacing used was 0.05 cm. In order to check convergence the ray spacing was decreased to 0.01 cm. This changed the assembly power distribution by a maximum of 0.04% and a RMS of 0.02%. The difference is below the 1σ uncertainty of the Serpent2 reference solution, < 0.1% [98] for an assembly layer and pin power. Also, the finer ray spacing increased the memory requirement by only 8.4%,

but also tripled the time of the calculation bringing it to ~3 hrs (all other parameters optimized). Normally, the right decision would be to keep the ray spacing at 0.05 cm. However, the final model of X2, which will be presented in later sections, cannot converge with a ray spacing of 0.05 cm. The cells of the model are too small resulting in computational instabilities. Given that the memory cost is manageable and that the calculation time is still within bounds the ray spacing was decreased to 0.01 cm.

2. Azimuthal angles: The option to use 24 azimuthal angles in total is very computationally heavy and maybe even unnecessary with such dense ray spacing. Firstly, the calculation does not fit in the cluster, but also it could be an overkill on time requirements. This is justified by the test of 18 azimuthal angles, which increases the running time of the 2D core to more than 5 hrs (all other parameters optimized). When 12 azimuthal angles are used the calculation lasts ~3 hrs (all other parameters optimized). Comparing the power distribution with the use of 12 and 18 azimuthal angles, the assembly power changes 0.09% at maximum with an RMS of 0.04%. Given that the maximum difference is approaching the uncertainty levels of Serpent2, the pin power distribution is also cross-compared for the 2 cases. The maximum pin power difference reaches 0.18% in few pins close to the Gd pins. This discrepancy can be considered minimal in comparison to the nTF results for 2D verification (see previous section), thus 12 azimuthal angles are selected for the HZP calculations.
3. Polar angles: After consultation with SNU the number of polar angles is fixed to 4. A trial is made with 8 polar angles, but the calculation results to computational instabilities.
4. Pincell region subdivisions: Following the observations of Section 3.2.1.2, the fuel pin is divided in 4 regions and the Gd pins in 7 regions. The CR pins are subdivided in 8 regions. All other pincell elements are meshed according to their size, trying to keep the thickness of each subdivision < 0.15 cm. In the final model, the mesh of the gap cells is dictated by the modeling of the corner stiffeners (introduced in the next section) and the reflector water gap, reaching a minimum of 0.01 cm. Using the approximated model, a calculation is performed with one less subdivision in the fuel pins, the Gd pins and the reflector homogenized cells (all other parameters optimized). The maximum assembly power difference from the calculation with the finer mesh is 0.07% and the RMS 0.02%. Again, the discrepancy remains below the Serpent2 uncertainty levels. However, the memory saved is only ~16% and the time is reduced by only ~12%. Given that the calculation with the finer mesh and all other parameters optimized occupies only 64% of the node memory, the finer mesh is selected for the HZP calculations.

To summarize, the nTF X2 model employs a ray spacing of 0.01 cm, with 12 azimuthal angles and 4 polar angles. The fuel pins are modeled with 4 radial subdivisions, except Gd pins that are modeled with 7. The CR pins are modeled with 8 radial subdivisions.

3.2.3.3 Verification of the nTF X2 HZP model with the benchmark reference solution

The Monte Carlo reference solution, included in the benchmark specifications, corresponds to the critical state of the reactor. For the critical conditions, the eigenvalue calculated by Serpent2 is equal to 1.00012 ± 0.00001 . The results of five independent Serpent2 runs, each simulating 48×10^9 neutron histories, are averaged. The standard deviation for the assembly and pin power values is $< 0.1\%$. The full core is simulated with both codes, however all results are provided for 1/6th core. Both codes do not take into account gamma smearing. nTF is initially used with the model described in Section 3.2.3.1. In this case, a single full core calculation requires 300 cpus (12 cpus x 25 axial layers) for 15,073 secs (~ 4 hrs and 11 mins) and 7.40 TB (88.2% of the total memory corresponding to 25 nodes). Fig. 3.14 illustrates the relative difference of the axially averaged normalized pin power map of nTF in comparison to Serpent2 $[(\text{Nor.Pow.}_{\text{Serpent2}} - \text{Nor.Pow.}_{\text{nTF}}) / \text{Nor.Pow.}_{\text{Serpent2}}]$. The axial relative power profile is also presented for both codes.

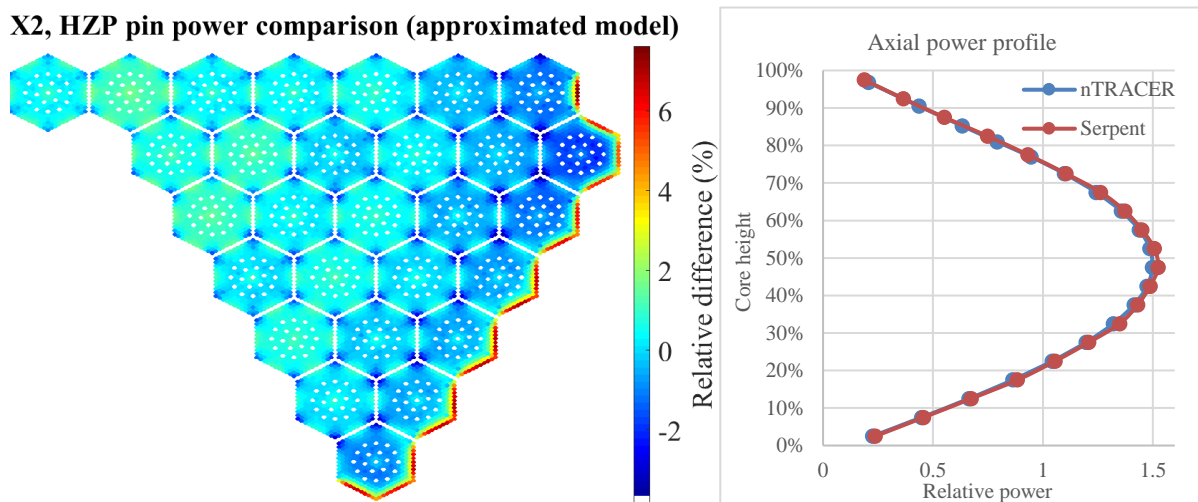


Figure 3.14. Relative pin power difference between nTF and Serpent2 (left) and axial relative power profile of both codes (right). All approximations are used in nTF

The eigenvalue difference between nTF and the reference solution, $[\text{keff}_{\text{Serpent2}} - \text{keff}_{\text{nTF}}]$, for the calculation involving all approximations, is -28 pcm, well below the target accuracy. Comparing the axial profiles of the two codes, it becomes apparent that the peak power is underestimated in nTF ($< 1.7\%$). The highest relative difference is found in the layer next to the bottom reflector ($\sim 5\%$). This can be attributed to different axial leakage, due to the

approximations applied to the nTF model, especially on the axial reflectors and the spacer grids. The map of the pin power difference produces its maximum at 7.6% on the pins neighboring the reflector. The corresponding RMS equals 1.1%. The distribution of the relative difference on the outer layer of pins is consistent with the one presented in Fig. 3.8, where the water gap surrounding the active core is also homogenized (see Fig. 3.13.C.ii) for the 2D calculation. In addition, it is apparent that the pin power at the corners of each assembly is overestimated by nTF due to the homogenization of the corner stiffeners (see Fig. 3.13.B.ii). Extra moderation at the corners of all the assemblies due to the coolant-steel mixture is creating anomalies to the power distribution.

The conclusions drawn from Fig. 3.14 are that the water gap of the reflector and the corner stiffeners should be modeled explicitly, in order to achieve accurate local predictions with nTF (see Section 2.7.3). The explicit modeling of the bottom reflector with the lower plug (see Fig. 3.13.A.i) would result in a thin axial layer of 2.3 cm thickness (lower plug), which would lead to computational instabilities [85]. At this stage of the study, nTF can only simulate one type of assembly containing the reflector water gap. In Section 3.2.2, the 2D heavy reflector model next to the core is built with a single type of homogeneous steel assembly containing the water gap. The water holes are applied to the model separately. In this case, the approximated model of the groove region (see Fig. 3.13.C.ii) requires the definition of several assemblies to map the shape accurately. Thus, nTF was extended by PSI to apply the water gap in different type of assemblies independently of their location in the core. In addition, the code was further extended by SNU to model the corner stiffeners. The model remains semi-explicit, since the new version of the code only allows to define an integer number of gap cells (see Fig. 2.5), starting from the assembly corners, with the corner stiffener material. This means that the length of the corner stiffener can only be approximated by a multiplier of the pincell size. Nonetheless, in this case there is very small difference between the actual length of the corner stiffener and the model.

The nTF calculation with the new model (final nTF X2 model) requires 15,256 secs (~4 hrs and 14 mins) with 300 cpus and the required memory is increased to 7.44 TB. The small increase in calculation time and memory corresponds to the new elements of the model. The map of the relative difference for the axially averaged normalized pin power of the new nTF calculation in comparison to Serpent2 $[(\text{Nor.Pow.Serpent2} - \text{Nor.Pow.nTF}) / \text{Nor.Pow.Serpent2}]$ is presented in Fig. 3.15. The maximum pin power difference drops to 3.4% and the RMS equals 1.5%. The eigenvalue difference, $[\text{keff}_{\text{Serpent2}} - \text{keff}_{\text{nTF}}]$, is increasing to -74 pcm. However, the

eigenvalue and the RMS are still in acceptable levels (see Section 2.7.3). The maximum pin power difference exceeds the target set in Section 2.7.3, but not significantly. The profile of the pin power difference presents the familiar MOC tilt [105], observed also in the 2D full core comparison (see Fig. 3.10). Nonetheless, in this map there is a stronger discrepancy at the edge of the assemblies next to the reflector, caused by the model of the corners of the water gap surrounding the active core (see Fig. 3.9). In addition, the pincells around the central guide tube exhibit stronger discrepancies than the surroundings. This is caused by the reduced central guide tube diameter, described in Section 3.2.3.1. Finally, it must be pointed out that the power of all Gd pins is overestimated by nTF, in accordance to what is observed in Section 3.2.1.2. In the outer region where nTF generally overestimates the power, the Gd pins appear to have a larger difference. Similarly, in the center where nTF underestimates the power, the Gd pins are not matching the profile of their surroundings and their difference is smaller. The axial power profile remains almost the same (maximum relative difference ~5% at the bottom of the core).

X2, HZP pin power comparison (final X2 model)

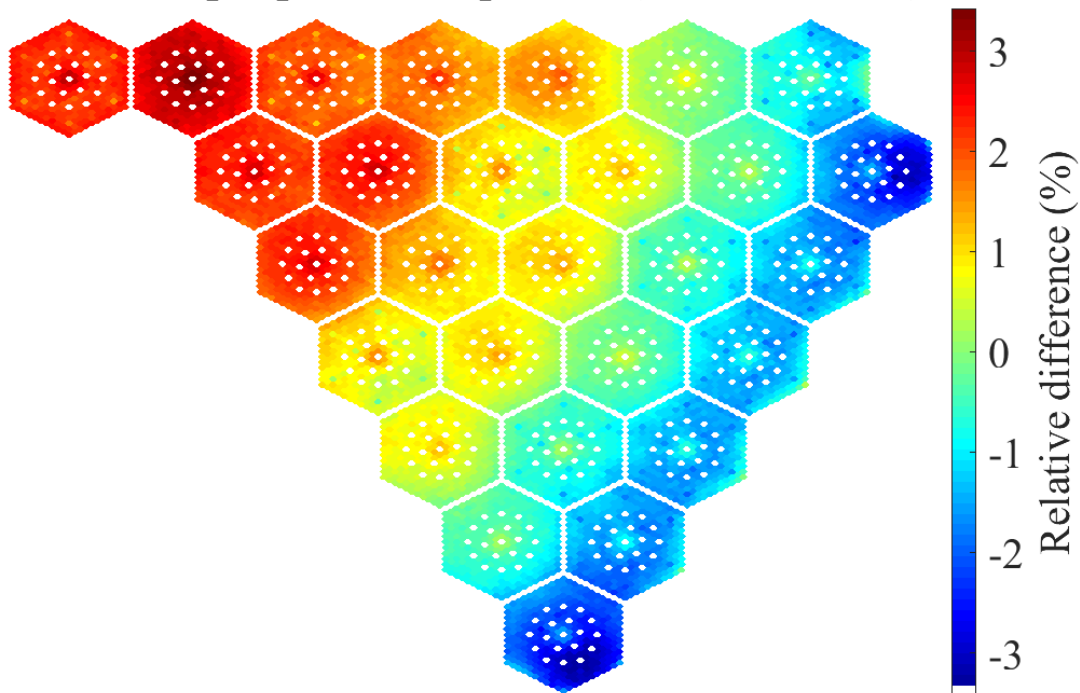


Figure 3.15. Relative pin power difference between the nTF HZP final X2 model and Serpent2

Despite the observed discrepancies, the final X2 model of nTF presents very good agreement with the reference solution on all accounts. In order to examine the axial evolution of the core power map, Fig. 3.16 illustrates the relative power difference for each assembly of the 1/6th core as a function of height, together with the relative difference of the axial profile at

the same height $[(\text{Nor.Pow.}_{\text{Serpent2}} - \text{Nor.Pow.}_{\text{nTF}}) / \text{Nor.Pow.}_{\text{Serpent2}}]$. The last few axial nodes of the nTF X2 model do not have the same thickness as the reference Serpent2 model thus the assembly power is compared up to ~ 2.6 m.

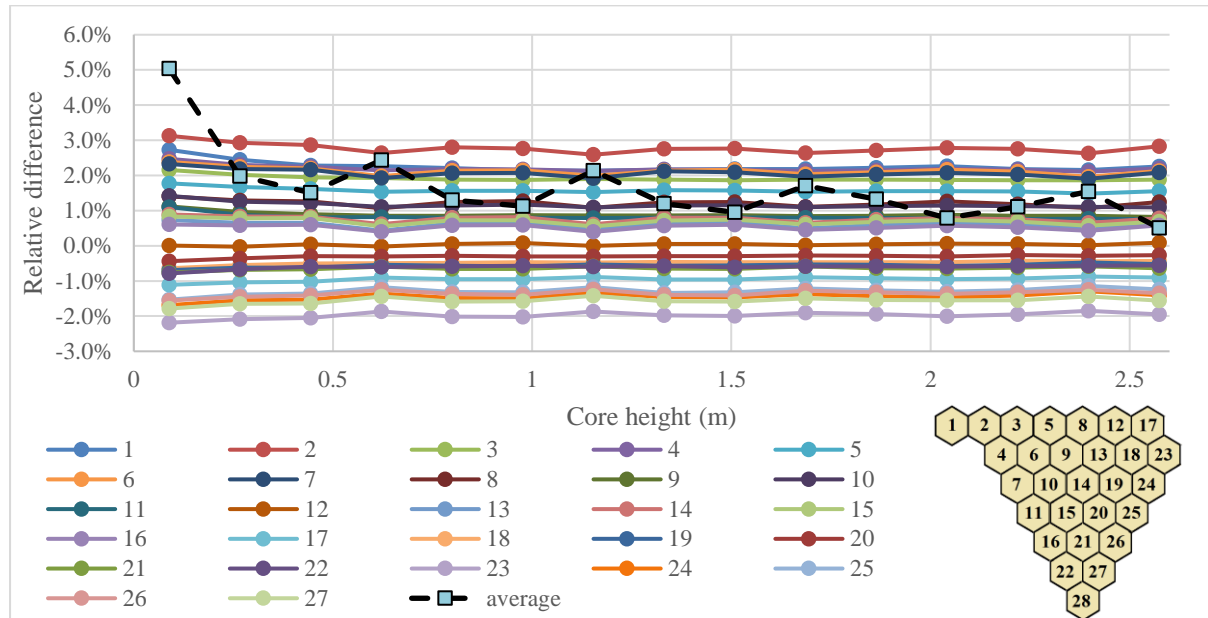


Figure 3.16. Relative assembly power difference between nTF and Serpent2 vs core height and relative difference of the axial power profile at the same level.

The relative difference of the assembly power ranges from -2.4% to 3.2%. It is apparent in Fig. 3.16 that for each assembly the difference remains almost steady throughout the height of the core, which means that the pin power difference (see Fig. 3.15) does not result from an error compensation due to axial averaging. For the sake of completeness, the calculation is repeated with P2 anisotropic scattering. Similarly to the 2D model, the corresponding memory requirements exceed the capacity of the node. Thus, the ray-tracing method is switched once more from Node Major to Group Major (see Section 2.3.2.1) to limit the memory consumption. As expected, the wall-time increases to ~ 21 hrs. Fig. 3.17 presents the distribution of the relative difference, $[(\text{Nor.Pow.}_{\text{Serpent2}} - \text{Nor.Pow.}_{\text{nTF}}) / \text{Nor.Pow.}_{\text{Serpent2}}]$, for the axially averaged normalized pin power vs the reference solution. In the same figure, the pin power difference of nTF-P0 vs nTF-P2 is also presented. The color scale is the same for both plots. The eigenvalue difference increases to -111 pcm. Also, the maximum pin power discrepancy increases to 3.6%. However, the RMS slightly drops to 1.4%. The subplot illustrates the effect of P2 on the nTF pin power map. It is obvious in Fig. 3.17 that the differences close to the reflector are generally smaller. Nonetheless, it must be pointed out that the discrepancies of the Gd pins are more pronounced in comparison to the surrounding profile. The RMS of the relative difference

between the nTF solution with P0 and P2 is 0.2%. Table 3.1 summarizes the results of the two calculations.

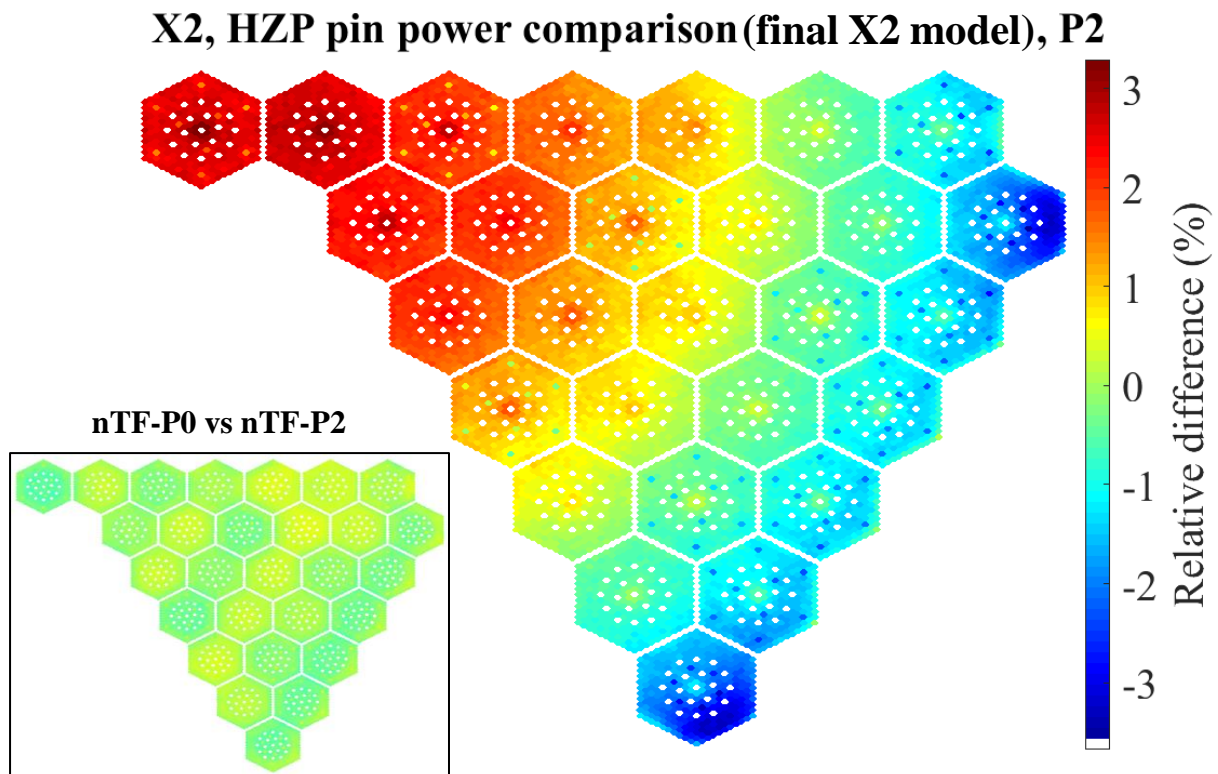


Figure 3.17. Relative pin power difference between the nTF HZP final X2 model with P2 anisotropic scattering and Serpent2

Scattering treatment	Δk_{eff} (pcm)	Max (%)	RMS (%)
P0	-74	3.4	1.5
P2	-111	3.6	1.4

Table 3.1. Pin power and eigenvalue difference of nTF vs Serpent2 for the X2 3D core

3.2.3.4 Validation of the nTF X2 HZP model with experimental data

At this stage, the nTF HZP model is optimized and verified, allowing the study to proceed with the validation of said model and nTF against experimental data. As it was mentioned in Chapter 2, the X2 benchmark specifications contain measurements done during start-up tests: two temperature reactivity coefficients (TRC), the SCRAM worth with a “stuck” rod and the measurement of the differential worth (s-curve) for CR bank #10. Fig. 2.13, illustrating the position of the stuck rod in the core and the location of CR bank #10, is repeated to facilitate the reader (see Fig. 3.18).

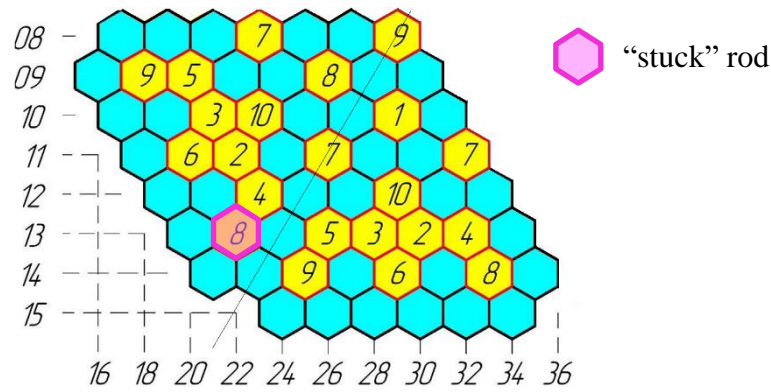


Figure 3.18. (Fig. 2.13) Positions of the control rod banks in the reactor core

Starting with the temperature reactivity coefficients, the different core states of the HZP experiments, described in Table 2.3, are modeled in nTF using the X2 model, optimized in the previous section, with the same calculation options as for the critical state. The full core is simulated for each case; hence, all calculation costs are similar to the ones described in the previous section. Table 3.2 presents the temperature reactivity coefficients as simulated by nTF, Serpent2 and measured. As described in the benchmark specifications, the reactivity coefficients are calculated as a reactivity difference between two corresponding calculations: $[\Delta\rho = 1/k_{eff2} - 1/k_{eff1}]$, where k_{eff1} and k_{eff2} are the eigenvalues of the two reactor states before and after the perturbation respectively. Concerning the reactivity coefficients, for the first TRC the nTF calculation is within 1σ of the measured value and 2σ of the Serpent2 result. For the second TRC, nTF underestimates the value more than 2σ in comparison to both measured and simulated data. In both cases, nTF under-predicts the reactivity change due to the isothermal change in reactor temperature. In order to study these discrepancies, the eigenvalues of the Serpent2 calculations for the four TRC points were obtained by the benchmark team and compared with the corresponding nTF solutions $[keff_{Serpent2} - keff_{nTF}]$. As depicted in Table 3.2, the eigenvalues predicted by nTF are in good agreement with the Monte Carlo results. Such discrepancies prove the capacity of nTF to model the VVER core in different operational states. The inconsistency on the TRC values is caused by the small temperature difference between operational points. Specifically, the difference of $\Delta keff$ between the two points of each TRC is only 2 or 3 pcm. However, when divided by the temperature difference between TRC points (~ 4.5 °C), the minor 3 pcm discrepancy can shift the TRC value more than 0.67 pcm/°C, which is larger than the uncertainty of the experiment and the Serpent2 calculation.

HZP test	CB (g/kg)	Tin (°C)	Experiment	Serpent2	nTF	$k_{eff}^{Serpent2} - k_{eff}^{nTF}$ (pcm)
TRC1, point 1	7.05	276.4	-5.39 ± 0.54 pcm/°C	-5.60 ± 0.3 pcm/°C	-5.26 pcm/°C	-94
TRC1, point 2	7.05	280.6				-96
TRC2, point 1	5.7	275.7	-14.67 ± 0.15 pcm/°C	-14.63 ± 0.3 pcm/°C	-13.94 pcm/°C	-103
TRC2, point 2	5.7	280.2				-106

Table 3.2. Temperature reactivity coefficients simulated and experimentally measured

The worth of CR #10 is measured starting with the rod fully inserted (0%) while all other rods are out (100%). The stepwise extraction of CR #10 is compensated by adjusting the boron concentration. Temperature and pressure remain the same. There is no experimental uncertainty associated to these measurements in the benchmark specifications. The uncertainty of Serpent2 reaches a maximum of 4 pcm for integral rod worth and ranges from 0.2-0.4 pcm/% for differential rod worth (pcm/% means pcm per 1% of insertion, the same unit as the differential worth). Fig. 3.19 illustrates the experimental s-curve ($s\Delta\rho$) and the predictions of Serpent2 and nTF, together with the differential worth ($d\rho/dh$) of CR #10 as a function of end-of-step position.

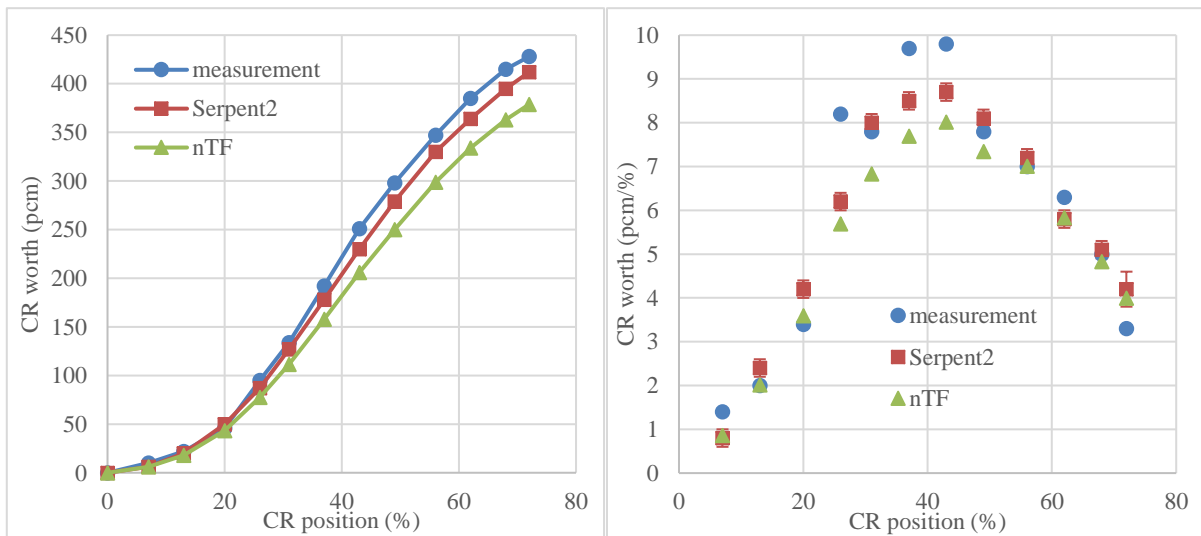


Figure 3.19. S-curve and differential rod worth for CR #10

The comparison of nTF with the experimental and calculated differential worth demonstrates a good overall agreement except for few points in the central part, where the Serpent2 results are significantly lower than the measurement; nTF is even lower. At the same time, the measured data points do not fit into the expected smooth curve, which suggests a large experimental uncertainty as is stated in the benchmark specifications. The specifications also

mention that apart from measurement uncertainties, the possible reason for deviation can be the specified density of the CR materials, which can be bigger in reality. The maximum discrepancy of differential rod worth of nTF from the measurement is 2.0 pcm/% and from Serpent2 1.2 pcm/%, which surpasses the 2σ uncertainty in Serpent2. The total CR worth, as it is calculated by the s-curve, is underestimated by 50 pcm by nTF in comparison to the measurement and 33 pcm in comparison to Serpent2. This is respectively $\sim 11\%$ and 8% of the total CR worth, which according to the utility perspective is above the limit when nTF is compared to the measurement ($>10\%$) (see Section 2.7.3). In order to get a better understanding of the discrepancy, a 2D model of the assembly with CR bank #10 (left pin layout on Fig. 3.3 but with 2.2% enrichment) is simulated in nTF and Serpent2, rodDED and unrodDED, with P0 & P2. The results are summarized in Table 3.3, $[\Delta k_{\text{eff,Serpent2}} - \Delta k_{\text{eff,nTF}}]$. nTF underestimates significantly the rod worth with P0, for both B₄C and DyTi. When P2 is used the discrepancy is reduced to acceptable levels. The underestimation of the rod worth agrees with what is observed in Fig. 3.19. The total CR worth of bank #10 is also calculated with the P2 approximation for the scattering source. However, there is no significant improvement to the solution (underestimation of 48 pcm from the measurement and 31 pcm from Serpent2).

case	$\Delta k_{\text{eff, P0}}$ (pcm)	$\Delta k_{\text{eff, P2}}$ (pcm)
UnrodDED	44	-20
RodDED, B ₄ C	-230	42
RodDED, DyTi	-286	-140

Table 3.3. Eigenvalue difference of nTF from Serpent2 for the 2D assembly model of CR bank #10

According to the benchmark specifications, the SCRAM worth with the “stuck” rod and the full SCRAM worth was measured as follows: “*First, from the nearly critical state all control rods, except the chosen “stuck” cluster, were dropped to the lowest position. The worth of SCRAM with one cluster “stuck” was measured. Second, after about 1 min the “stuck” rod was dropped down and the full SCRAM worth was measured.*” [98]. The measured values and the calculated ones by Serpent2 and nTF are presented in Table 3.4. The nTF SCRAM worth is closer to the experiment than the Serpent2 values. In the 1st case, nTF overestimates the reactivity by 6.7%, exceeding the 1σ uncertainty of the experiment, and in the 2nd case by 5.4%, remaining within 1σ . From the utility perspective this is acceptable since both differences are less than 10% (see Section 2.7.3). The results of nTF are closer to the Serpent2 prediction than the experiment, nonetheless far from the 1σ uncertainty of the Monte Carlo code (~ 180 pcm). According to the benchmark specifications, the systematic deviation between predicted and

experimental values of SCRAM worth is a known issue for VVER-1000 units [106] due to the applied measurement technic [107]. In addition, the experiment was performed in a dynamic way, whereas the calculations are static, which can also cause discrepancies (for more information refer to the benchmark specifications [98]). The SCRAM cases are also attempted with P2 treatment for the anisotropic scattering. However, the calculations cannot converge.

experiment	measurement (pcm)	Serpent2 (pcm)	nTF (pcm)
SCRAM, “stuck” rod	5230 ± 310	5750 ± 2	5582
Full SCRAM	7000 ± 430	7570 ± 1	7381

Table 3.4. Experimentally measured and calculated SCRAM worth

3.3 Neutronic analysis with the conventional approach

Even though PARCS has been verified and validated extensively for VVER geometries, CASMO5-VVER is a relatively new module of CASMO5; thus, it has not been used broadly yet. Since the level of development of the two solvers is different for hexagonal geometries, they are studied and verified separately before simulating together the X2 HZP critical case. The goal is to obtain an independent assessment of the two codes. This is important since PARCS has never been used with CASMO5-VVER cross-sections for VVER analysis, outside LRT. The work performed in LRT for the development of the CASMO5-VVER/PARCS code system surpasses this thesis. The LRT VVER project includes two internships [102], [108], one of which was supervised by the author of the present thesis [108]. Part of the analysis presented in the following sections was performed on the framework of the two internships and is referenced as such.

3.3.1 Verification of PARCS with 2D full core models

In order to assess the performance of PARCS without the use of a lattice code, exercise V1000-2D-C1 from the relevant NURESIM-SP1 benchmark is selected. This exercise involves a 2D HZP unrodded full core calculation with zero axial buckling for nodal solvers, which was already used in Section 3.2.2. For the sake of conciseness, the detailed analysis conducted for the verification of PARCS with this benchmark is presented in the Appendix. The outcome of this work is that the two-group cross-sections defined in the specifications [95] are not compatible with PARCS, specifically the discontinuity factors for the reflector assemblies. For this reason, two-group cross-sections are generated with Serpent2 for exercise V1000-2D-C1. Serpent2 has been used in the past to generate cross-sections for PARCS VVER models [109].

This work is part of [108]. The 2D core is simulated explicitly with Serpent2, to provide a reference solution for comparison, based on the V1000-2D-C1-tr [96] specifications. The two-group cross-sections and ADFs are computed by single assembly models with reflective boundary conditions for the active core. The transport correction card is used in Serpent2 [108]. The modeling of a VVER heavy reflector and the cross-section generation presents a significant challenge for conventional code systems [104]. Owing to its 30° symmetry, the neutronic parameters can be calculated by the five different Serpent2 models, illustrated on Fig. 3.20. Each region is represented as a rectangle extending from the boundary of the assembly, to the downcomer. Reflective boundary conditions are set on all surfaces except on the eastern boundary, where vacuum condition is used. The neutron source is modeled by the neighboring fuel assembly of the corresponding reflector region. In the nodal calculation, the ADF corresponding to the fuel-reflector boundary is assigned to all the reflector assembly surfaces in contact with fuel in the hexagonal geometry. All the other surfaces are assigned unity ADFs. This is acceptable since the discontinuity factor is most important near the fuel, because of the strong flux gradient between the fuel and the reflector.

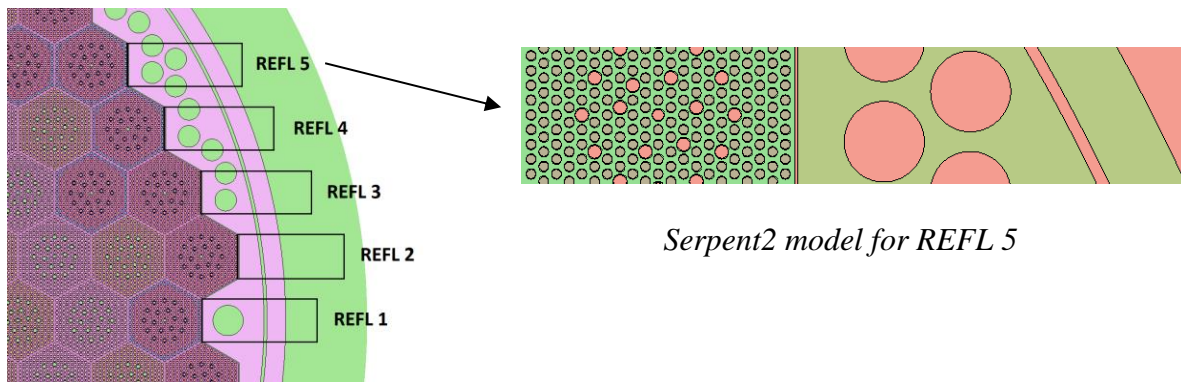


Figure 3.20. Reflector models used for two-group cross-section generation with Serpent2 [108]

Fig. 3.21 presents the relative difference of the assembly power between Serpent2/PARCS and the Serpent2 reference solution. The difference in eigenvalue is 69 pcm and the maximum power map discrepancy reaches 3.6% with RMS of 1.2%. The highest relative difference corresponds to assemblies which are close to the reflectors. The reflectors are expected to introduce discrepancies due to the modeling approximations. However, in general there is good agreement between the two codes.

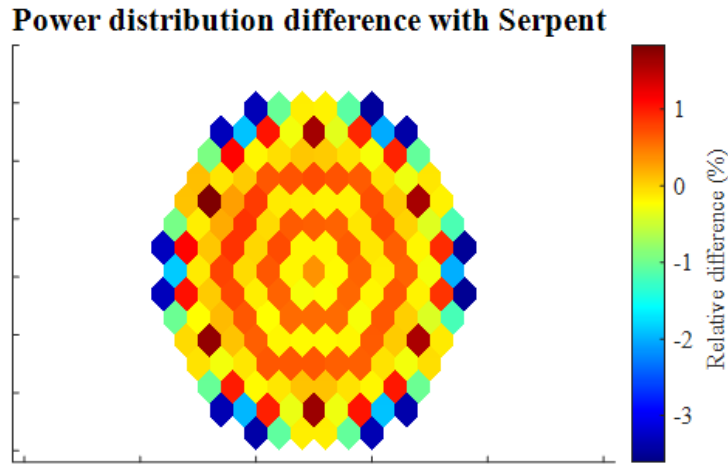


Figure 3.21. Relative difference of the assembly power map calculated by Serpent2/PARCS vs the Serpent2 reference solution for exercise V1000-2D-C1 [108]

3.3.2 Verification of CASMO5-VVER for 2D geometries

The verification of CASMO5-VVER is discussed in detail in [102]. This section repeats the major outcomes of the study conducted by Jaerim Jang during her internship within LRT, and adds some observations concerning the treatment of anisotropic scattering. Considering that CASMO5-VVER is also a MOC transport code, the outcome of this verification can be cross-examined with the observations made in the previous sections for nTF, concerning basic functions like the accuracy of control rod models. The work presented in [102] is focused on the OECD benchmark Rostov-2 [63]. The benchmark is based on a VVER-1000 core with a very similar configuration to X2. Fig. 3.22 illustrates the different assembly types of Rostov-2 for which CASMO5-VVER is verified. As a first step, the lattice code is used to calculate the eigenvalue of rodded and unrodded assemblies of uniform enrichment without Gd. The unrodded 2D assembly models are simulated for HZP, where fuel and moderator temperature are 600 K, and Hot Full Power where the fuel is simulated at 900 K and the moderator at 600 K with 1000 ppm boron concentration. Two types of CR are simulated, B_4C and $Dy_2O_3-TiO_2$ in HFP. Figure 3.23 presents the comparison of CASMO5-VVER multiplication factors vs Serpent2. Two CASMO5-VVER solutions are provided with different Pn-scattering orders: P0 and P3, $[k_{eff}^{CASMO5-VVER} - k_{eff}^{Serpent2}]$.

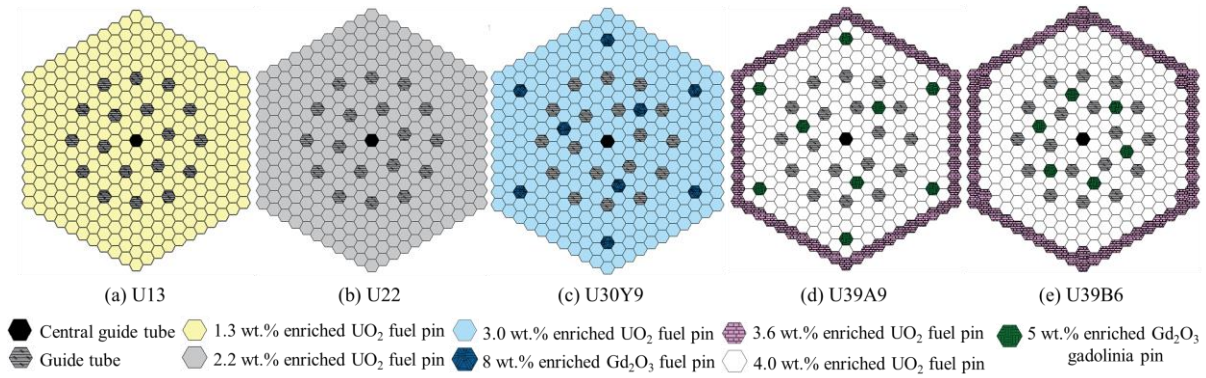


Figure 3.22. Radial layouts of Rostov-2 assemblies [102]

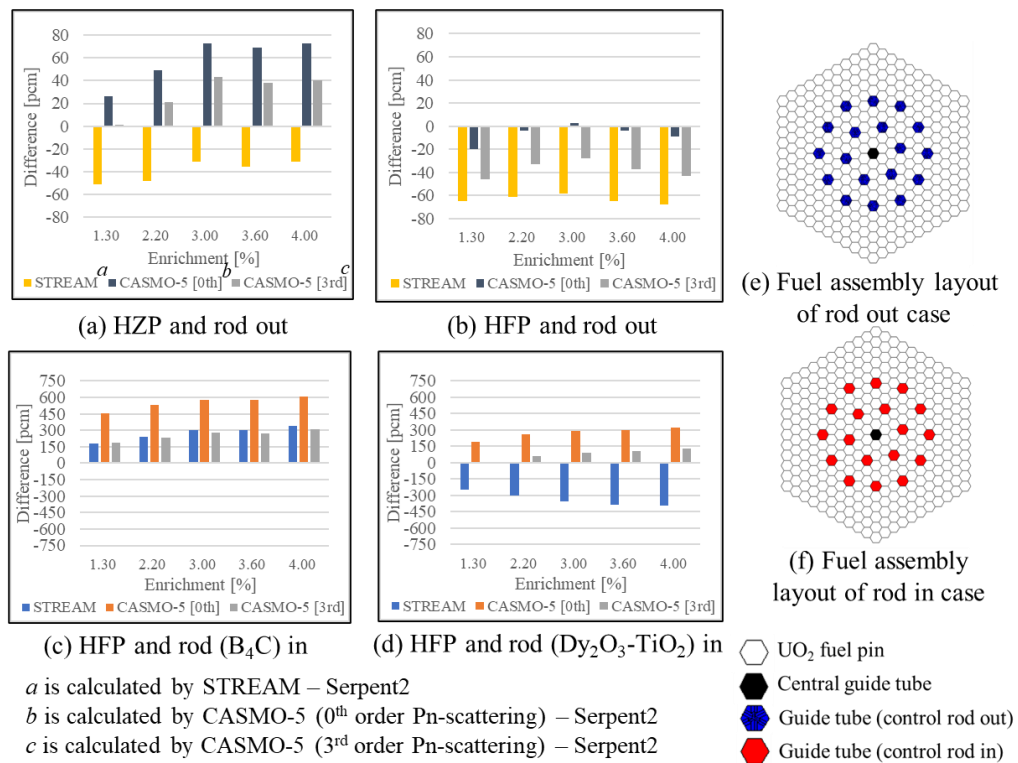


Figure 3.23. Eigenvalue comparison between CASMO5-VVER and Serpent2 for rodded and unrodded assemblies with P0 and P3 scattering treatment [102]

The CASMO5-VVER discrepancies remain within the target accuracy (< 200 pcm) for unrodded HZP and HFP with P0 transport corrected and P3. CASMO5-VVER overestimates the eigenvalue increasingly with enrichment at HZP conditions. The rodded cases present similar behavior to what is discussed in Section 3.2.3.4 for nTF. The lattice code overestimates the eigenvalue significantly (max ~ 600 pcm for B_4C and ~ 300 pcm for $Dy_2O_3-TiO_2$) when P0 transport corrected is used. This discrepancy is decreased to acceptable levels with the P3 scattering treatment. CASMO5-VVER is also compared with Serpent2 for two-group cross-section generation for Rostov-2 assemblies U22 and U39A9 (see Fig. 3.22). Fig. 3.24 depicts

the relative difference of the diffusion coefficient (D), absorption cross-section ($\Sigma\alpha$), down-scattering ($\Sigma_{S1\rightarrow2}$) and nu-fission ($\nu\Sigma f$) for the two groups calculated by CASMO5-VVER vs Serpent2 as a function of burnup $[(X_{S_{CASMO5-VVER}} - X_{S_{Serpent2}}) / X_{S_{CASMO5-VVER}}]$.

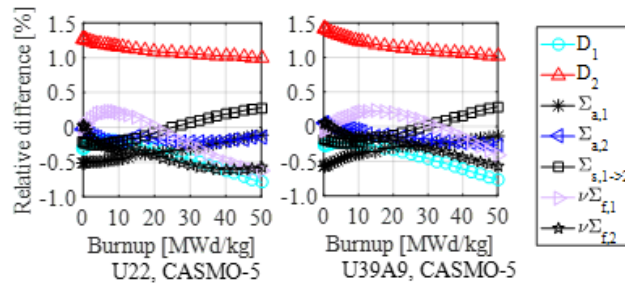


Figure 3.24. Two-group cross-section comparison of CASMO5-VVER vs Serpent2 [102]

The differences remain below 1.0% for both assemblies for all cross-sections except the diffusion coefficient of the thermal group, which reaches a maximum of 1.5% at 0 MWd/kg. This behavior has been observed in previous studies for PWR lattices [110]. The low levels of discrepancy verify CASMO5-VVER and justify its use as a lattice code in the LRT conventional core solver. In Section 3.2, the effect of anisotropic scattering treatment on the pin power distribution is discussed for nTF. In order to study the effect of the scattering treatment with another MOC code and verify CASMO5-VVER for full core calculations, Rostov-2 is modeled in 2D with P0, P3 and P5 approximations for the anisotropic scattering. The results are compared with a Serpent2 calculation (100000 batches \times 1000000 histories, 1000 inactive cycles). The reflector model in Serpent2 is built, following the approximations of CASMO5-VVER, with homogenized pins of water and steel, preserving the real volume of the corresponding material in the actual reflector. Fig. 3.25 illustrates the approximated reflector model and the Rostov-2 core layout. The goal of using an approximated reflector model is to remove the bias introduced in CASMO5-VVER and quantify the effect of the scattering treatment. Fig. 3.26 illustrates the relative difference of the pin power distribution as calculated by CASMO5-VVER vs Serpent2, $[(Nor.Pow.Serpent2 - Nor.Pow.CASMO5-VVER) / Nor.Pow.Serpent2]$. The pin power uncertainty reaches 0.3% in Serpent2 and the eigenvalue uncertainty 1 pcm. Table 3.5 presents the eigenvalue difference, $[keff_{Serpent2} - keff_{CASMO5-VVER}]$, and maximum relative pin power difference together with the RMS.

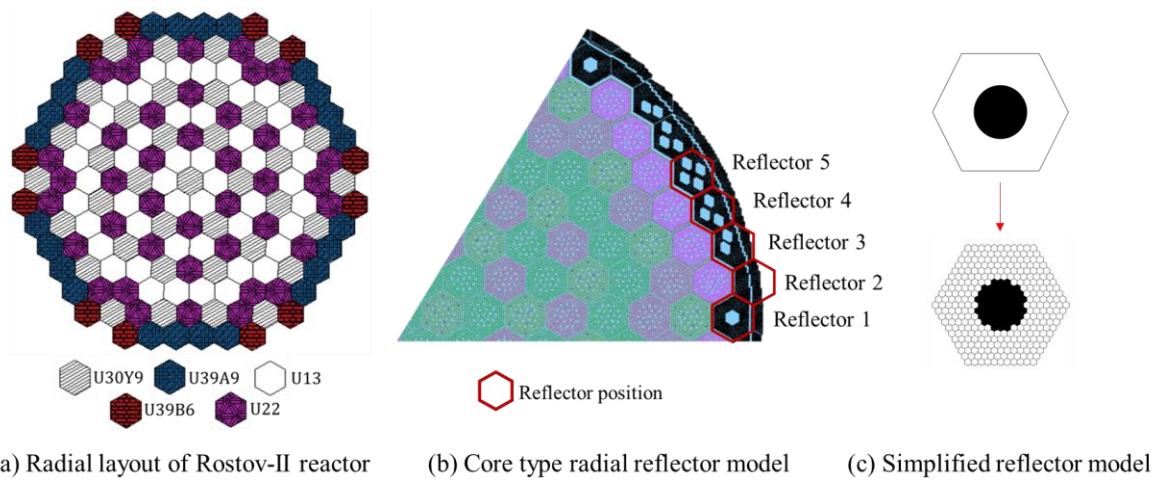


Figure 3.25. Rostov-2 core layout and CASMO5-VVER reflector model [102]

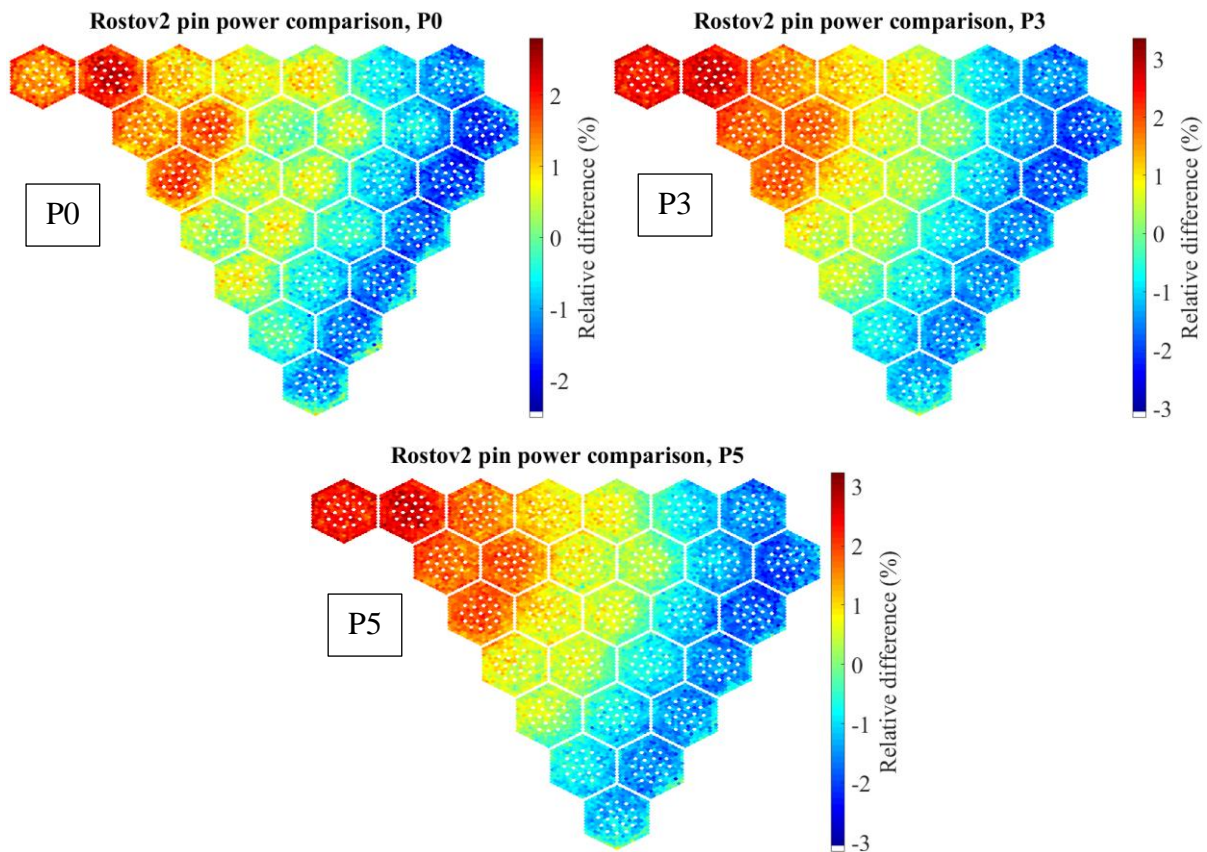


Figure 3.26. Relative difference of the normalized pin power as calculated by CASMO5-VVER with P0, P3 and P5 scattering treatment vs Serpent2

Scattering treatment	Δk_{eff} (pcm)	Max (%)	RMS (%)
P0	-59	2.8	1.0
P3	-29	3.6	1.4
P5	-28	3.2	1.3

Table 3.5. Pin power and eigenvalue difference of CASMO5-VVER vs Serpent2 for 2D Rostov-2

The discrepancies presented between CASMO5-VVER and Serpent2 remain in acceptable levels for all 2D full core cases; however, the maximum difference is higher than the target accuracy with P3 and P5. When the order of the scattering treatment is increased, the eigenvalue difference is decreased significantly. Nonetheless, the opposite occurs with pin power. This is not the case for the 2D verification of nTF (section 3.2.2), even though similar behavior is observed in the 3D full core comparison. Nonetheless, both MOC solvers present a tilt in the pin power distribution, where the relative power is underestimated in the center of the core and overestimated in the edge, making the overall radial profile more flat. This tilt can be accentuated by the approximated modeling of the heavy reflector (more information in [102]). However, Fig. 3.26 proves that the heavy reflector is not the only source of the tilt, since the model of the heavy reflector is identical in CASMO5-VVER and Serpent2. In addition, both for nTF and CASMO5-VVER this effect is not eliminated when the order of the scattering treatment is increased, which verifies the conclusion that the tilt is an inherent feature of MOC deterministic codes.

3.3.3 Verification of the CASMO5-VVER/PARCS code system with a real 3D VVER-1000 core model

In the framework of the LRT VVER project, the CASMO5-VVER/PARCS code system is studied extensively with different VVER-1000 benchmarks (V1000-2D-C1-tr [108], Rostov-2 [102]). Nonetheless, this thesis presents only the verification of the code system with the X2 benchmark [98], following the development of the high-resolution multi-physics core solver. The two-group neutronic data are generated by single assembly calculations and not the 2D full core model. The core layout and the model of the heavy reflector are presented in Fig. 3.12 (see Fig. 2.11). All fuel assemblies are modeled explicitly in CASMO5-VVER for the X2 critical state. The corner stiffeners are simulated, similarly with nTF, as gap cells; thus, can only extend to an integer of pincell boundaries. In addition, the outer diameter of the central guide tube is limited by the size of the pincell. The standard CASMO5 computational mesh is used for the MOC calculation with transport corrected P0 scattering and the resonance upscattering model. The ADFs are post-processed and altered in the CASMO5-VVER output file to match the GenPMAX required input for hexagonal geometries. Each ADF is defined as the average surface flux divided by the average flux of the assembly for that energy group. As it was discussed before, the generation of cross-sections for reflector assemblies in hexagonal geometry can be a complicated task [104], where several approximations need to be introduced,

resulting in discrepancies. In Section 3.3.1, it was illustrated that Serpent2 allows explicit modeling of the specific reflector regions, selected for the generation of cross-sections. However, in CASMO5-VVER the same reflector regions are modeled as successive slabs of different materials (1D reflector models). This is a common practice for VVERs and Cartesian geometry [111], [112]. The thickness of the slabs is calculated by preserving the average dimension of the structural element on the horizontal axis. The total volume and atomic density, of the different materials included in one slab is preserved. A single ADF is produced for each reflector model in the fuel-reflector interface, which is assigned to all fuel-neighboring surfaces of the reflector assembly in the PARCS calculation. Fig. 3.27 displays a comparison between the Serpent2 and CASMO5-VVER model for reflector REFL3.



Figure 3.27. Heavy reflector assembly model (REFLE3) in Serpent2 (left) and CASMO5-VVER (right)

In order to optimize the cross-sections for the X2 critical case, several modeling options are studied with CASMO5-VVER. Initially, the corner stiffeners are excluded from the calculation to assess their impact in the solution. Also, the CASMO5 critical spectrum correction (see Section 2.5.2.4) is tested for the fuel assemblies. Fig. 3.28 presents the relative difference of the normalized assembly power profile, $[(\text{Nor.POW}_{\text{Ref}} - \text{Nor.POW}_{\text{CASMO5-VVER/PARCS}}) / \text{Nor.POW}_{\text{Ref}}]$, between CASMO5-VVER/PARCS and the Serpent2 reference solution for X2 without corner stiffeners, with corner stiffeners and with the addition of the CASMO5 critical spectrum correction. The maps of assembly power difference with and without corner stiffeners are built with the same color scale. The same figure also illustrates the relative difference of the axial power profile for all cases. All calculations with PARCS are performed as criticality searches. Thus, instead of comparing eigenvalues, the difference in boron concentration is included in the figure $[\text{BC}_{\text{Ref}} - \text{BC}_{\text{CASMO5-VVER/PARCS}}]$.

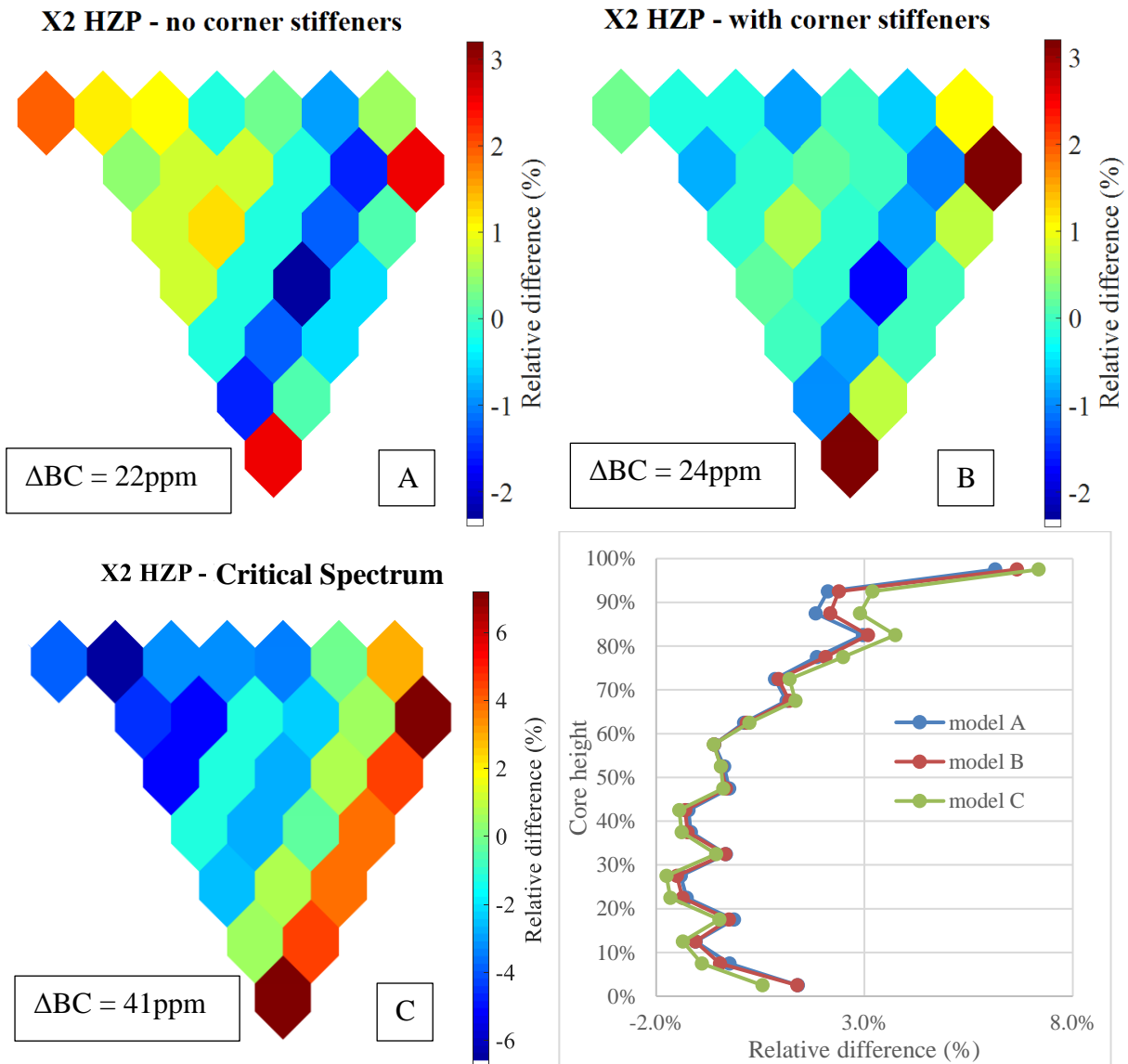


Figure 3.28. Relative difference of the assembly power and difference in BC between CASMO5-VVER/PARCS and the X2 reference solution for model (A) without corner stiffeners, (B) with corner stiffeners and (C) with the CASMO5 critical spectrum correction

Several conclusions can be drawn by Fig. 3.28. Firstly, the modeling of the corner stiffeners has a strong impact in the PARCS solution. Even though the maximum difference increases from 2.5% to 3.2%, the RMS decreases slightly from 1.1% to 1.0%. The profile of the relative assembly power difference is also flatter in comparison to solution (A). The higher discrepancy for solution (B) is presented in the assemblies next to the reflector. A possible explanation is the incapability of CASMO5 to model corner stiffeners for the Cartesian reflector models (see Fig. 3.27), thus excluding them, from the fuel-reflector interface. The impact on the reflector cross-sections, especially on ADFs, changes the power profile. The maximum discrepancy for the axial profile is also found close to the reflector for both cases

(6% for model A, 6.7% for model B). The irregular shape of the relative difference of the axial profile (dips) can be attributed to the explicit modeling of spacer grids in the reference solution. The axial nodes where there is a steep decrease in the relative difference do not contain spacer grids. In general, the discrepancies of the axial profile are higher after 72.5% of the height. This can be attributed to the modeling of the control rod, which is inserted up to 76% of the height for the X2 critical case, with a single material instead of both B₄C and DyTi [102]. The case with the corner stiffener results in a higher RMS also for the axial profile (1.9% for model A, 2.0% for model B). Despite their discrepancies, both cases (A) and (B) verify the capacity of the code system to model a 3D full core VVER-1000 (see Section 2.7.3). On the other hand, the same is not true when the CASMO5 critical spectrum correction is included, in terms of power map and BC. The maximum difference increases to 7.2% and the RMS equals 3.7%. Also for the axial profile the maximum difference increases to 7.2% and the RMS to 2.3%. Obviously, the CASMO5 spectrum correction is not improving the solution when combined with PARCS. As it was mentioned in Section 2.5.2.1, this is expected since CASMO5 is optimized for SIMULATE3, which is doing its own leakage correction. Thus, the leakage correction is not used for the rest of this work. Table 3.6 summarizes the results of the calculations.

		Model A	Model B	Model C
Assembly power	RMS	1.1%	1.0%	7.2%
	Max	2.5%	3.2%	3.7%
Axial power	RMS	1.9%	2.0%	7.2%
	Max	6.0%	6.7%	2.3%
Boron concentration		22 ppm	24 ppm	41 ppm

Table 3.6. Assembly power, axial profile and boron concentration difference of CASMO5-VVER/PARCS vs Serpent2 for the X2 3D full core models A, B and C

The verification of CASMO5-VVER and PARCS presented in this section suggests that both solvers, even though never used together for hexagonal geometries, are suitable for the development of a conventional code system for the safety analysis of VVERs. The sensitivity study on the scattering order performed with CASMO5-VVER supports the findings of Sections 3.2.2 and 3.2.3, by exhibiting behaviors that are common for both MOC solvers. The optimization and verification of the conventional code system for the X2 benchmark allows

the use of CASMO5-VVER/PARCS for further analysis on VVERs and finally cross-comparison with the capabilities of the high-resolution core solver.

3.4 Major outcomes of the work presented in this chapter

- The optimized nTF 3D full core model is verified and validated for steady state neutronic analysis. The verification and validation of the nTF for an actual VVER-1000 core proves that deterministic codes can achieve high-resolution predictions of equivalent accuracy with Monte Carlo codes but with a better spatial resolution.
- Different modeling options are tested and the impact of approximations is quantified, specifically for the heavy reflector, which is always a problematic region for VVERs, and the modeling of corner stiffeners. By examining Fig. 3.28 and the results of the conventional neutronic solver, it becomes apparent that the strict modeling requirements are only relevant to high-resolution predictions. The neutronic calculation can include several strong approximations (e.g. reflector is modeled as a homogeneous material of steel and water) without presenting discrepancies beyond the acceptable levels on the coarse mesh. However, high-resolution solvers must allow very limited approximations to achieve target accuracy in local predictions.
- The assumption of transport corrected isotropic scattering (P0) is shown to have a negligible effect on the performance of MOC solvers compared to P2, P3 or P5 approximations of the scattering source; as it has been observed before [45].
- CASMO5-VVER and PARCS are also verified, separately and together for steady state neutronic analysis.
- Finally, the leakage correction of CASMO5-VVER, is shown to be inaccurate when used with PARCS.

Chapter 4

Multi-Physics Analysis of the Hot Full Power State

«Γενηθήτω φῶς»

4.1 Objective

The development of a high fidelity multi-physics core solver requires the use of a high-resolution neutronic code, together with a thermal-hydraulic (T/H) code capable of analysis on a similar level of detail. If the intended neutronic solver can achieve sub-pin predictions, then the coupled T/H solution should provide sub-channel level feedback and sub-pin level temperature information. Otherwise, the potential of the solvers is diminished. Obviously, in order to accomplish the coupling between codes of such high-resolution and decrease computational costs, some approximations are necessary. However, as it is proven also in Chapter 3, the introduction of many spatial approximations in high-resolution calculations (homogenization of areas instead of an explicit modeling) can be a significant source of discrepancy for local quantities, even if the global parameters are predicted accurately. This chapter also illustrates that in spite of the simple T/H phenomena occurring in a VVER, a sub-channel code is still necessary to capture the local T/H behavior in the core. Nonetheless, there are difficulties in modeling a full 3D core with a T/H high-resolution solver. Considering that a single VVER assembly consists of ($\sim 660 \times \# \text{ axial layers}$) sub-channels and ($\sim 331 \times \# \text{ temperature rings} \times \# \text{ axial layers}$) fuel pin mesh points, the number of unknowns in the problem for a full core model is significant. Due to the size of the model and the geometry modeling flexibility of T/H sub-channel codes (required for the modeling of experimental facilities), the production of the full core model can be even more challenging than for the

neutronic code. The necessary approximations to ease the computational and modeling burden must be analyzed in detail and validated.

Besides the effectiveness of the selected T/H code in high-resolution analysis, the methods used to couple the different elements of the multi-physics solver are very important as they can introduce additional sources of error. For high-resolution solvers, only coupling schemes that allow the simultaneous execution of both codes can be efficient in terms of data exchange and computational costs. When external coupling is applied, the two solvers are executed in standalone mode independently several times. Initially, the neutronic solver calculates the power distribution with a T/H feedback guess. The resulting power distribution profile is subsequently fed, usually by an external wrapper, to the T/H solver which provides feedback. The neutronic code is executed again to calculate a new power distribution using the result of the T/H solver, again through an external wrapper. This sequence is repeated until both the neutronic and T/H solution are converged. Even though external coupling can be simpler to implement, the time required by high-resolution tools to converge for a single state point and the amount of data that needs to be transferred between the codes make it an unsuitable choice for novel solvers. Internal coupling allows the merging of the functions calculating the neutronic and T/H solutions into one algorithm, where both solvers progress simultaneously towards convergence. Nowadays, the evolution of computing clusters and computational methods is facilitating the development of such coupling schemes. However, an internal coupling scheme still poses significantly more challenges in terms of code development and technical realization. On the coding side, the main issues are the correct exchange of data on the fly, the appropriate treatment of inconsistencies in the neutronic and T/H meshes (e.g., gap cells are modeled differently) (see Section 4.2.2) and the production of consistent models (e.g. consistent geometry and consistent boundary conditions) for neutronics and T/Hs according to the needs of each calculation. The technical aspect includes the potentiality of the different codes for common compilation and the availability of a server suitable for this type of calculation. In addition, a major factor that impacts the code development and the technical configuration of a coupled code system is the joint parallelization of the relevant solvers. Important differences in parallelization schemes can result in severe computational penalties, in time and memory, or in extreme cases render the whole task impossible (e.g. for large models, if one of the two solvers cannot be parallelized then the memory requirements of the corresponding model must be covered by a single computational node).

All these aspects can pose serious challenges in the development and use of coupled code systems, especially if the specific solvers are not created with the intention to be used together. In this chapter, the development of the LRT multi-physics core solver [113], [114], with nTF and CTF, for the analysis of full core VVER configurations is described in detail. As it was mentioned before, CTF has been validated for coarse mesh full core VVER models [29] and for high-resolution simulations of single VVER assemblies [68]. However, it has never been used before for high-resolution full core VVER calculations, which makes the production of such a model challenging, especially because parallelized calculations are required with CTF. As it was mentioned in Chapter 1, this work does not include a standalone verification of CTF. The detailed verification of the T/H code was not considered a priority since in VVER normal operation the neutronic phenomena are the key factor for core behavior. Nonetheless, a more thorough study of CTF standalone would be beneficial for the next stages of this work, as it would allow a better understanding of the biases introduced by the T/H feedback to the full core solution. The novel multi-physics code system is verified versus a solver of similar capabilities, Serpent2/SUBCHANFLOW, for a full VVER-1000 core. In addition, nTF/CTF is compared with nTF and a simple 1D-TH solver embedded in nTF (see Section 2.3.7). The purpose is to study the performance of a simplified computationally inexpensive T/H solver vs a sub-channel code for full core analysis. It must be pointed out that the 1D-TH solver, initially available only for Cartesian geometries, has been expanded in the course of this study for hexagonal geometries. The performance of PARCS with its embedded simplified T/H solver for Hot Full Power (HFP) VVER analysis is also briefly presented in this chapter, to study the effects of T/H feedback in a conventional solver.

4.2 Development of the nTF/CTF core solver

As it was mentioned before, nTRACER has been coupled with CTF in the past for steady state analysis of Cartesian geometries [69]. The coupled code system involved older versions of the codes. The resulting core solver, even though studied extensively at the time by the developers, is not used anymore and was never updated with the latest versions of the codes. SNU is developing its own sub-channel code ESCOT [49], with axial domain decomposition like nTRACER. Normally for Cartesian geometries, the CTF developers provide a pre-processor, which simplifies the use of CTF by automatizing the full core model generation; however, such a pre-processor is not available for hexagonal geometries. Despite all the issues listed above, the existing outdated coupling interface in nTRACER is used as a basis for the

development of the nTF/CTF coupling scheme. CTF includes its own coupling interface for neutronic solvers, which follows the evolution of the code. The automatic generation of inputs for single VVER assemblies with specific geometry and operating conditions for standalone CTF calculations was initiated in the study described in [68] by Karlsruhe Institut für Technologie (KIT). The relevant script provided by KIT is employed as a guide in this work for the geometry description of VVER configurations in CTF (see Section 4.2.3).

4.2.1 Internal coupling scheme

In order to present in detail the development of the LRT core solver for VVERs, the algorithm of coupled nTRACER/CTF execution is described in this section and presented in Fig. 4.1 in the form it used to function during [69] & [48]. The coupled code system used an internal coupling scheme with CTF compiled and linked as a dynamic library. The coupling interface was introduced in nTRACER specifically for data exchange with CTF. In this arrangement, nTRACER functioned as a master code, which called pre-existing CTF subroutines through the coupling interface, to perform the T/H calculation when necessary. nTRACER provided the basic geometric description and boundary conditions of the T/H model to CTF, through the relevant pre-processor, as well as the pin power distribution whenever CTF was executed to provide feedback (feedback iteration). CTF returned the moderator temperature and density for each pincell. The fuel rod temperature was calculated by the fuel conduction model embedded in nTRACER. CTF was called iteratively by nTRACER until the volume-averaged fuel temperature, calculated by nTRACER, was converged for each pin.

In the new coupling scheme of nTF/CTF, nTF remains the master code, with CTF compiled and linked as a library, optimizing the communication time. Fig. 4.1 presents the new high-resolution solver in transposition to the old capabilities. Fig. 4.2 illustrates the flowchart of the coupled code system from the perspective of the neutronic code. nTF is modified to function as the equivalent of a CTF pre-processor for hexagonal geometries. It creates directly the CTF input according to the neutronic model including some basic T/H parameters provided to nTF as input. At each T/H feedback iteration, nTF calls CTF as a subroutine, providing the detailed pin power distribution. After CTF is executed to convergence (quasi-static simulation convergence criteria [*private communication with NCSU*]), it returns the moderator temperature and density for each pincell (pin averaged), as well as the temperature profile for the fuel rod (fuel, gap and cladding). Some of the CTF subroutines employed in the data exchange are part of the official CTF coupling interface and others are fully introduced in the

framework of this work. nTF uses the new T/H parameters to update the cross-sections with the subgroup method and then proceeds to the planar MOC and CMFD calculations. Since the neutronic solution requires a tighter convergence (10^{-6} for the eigenvalue) than the T/H solution (10^{-4} on volume-averaged fuel temperature [private communication with SNU]), due to the different sensitivity of the solutions on the relevant parameters, feedback is not required for every outer iteration of nTF. After reaching convergence of the T/H solution, the changes in the power distribution are assumed not to affect the T/H feedback significantly. Subsequently, the neutronic calculation proceeds without feedback until the neutronic solution is converged.

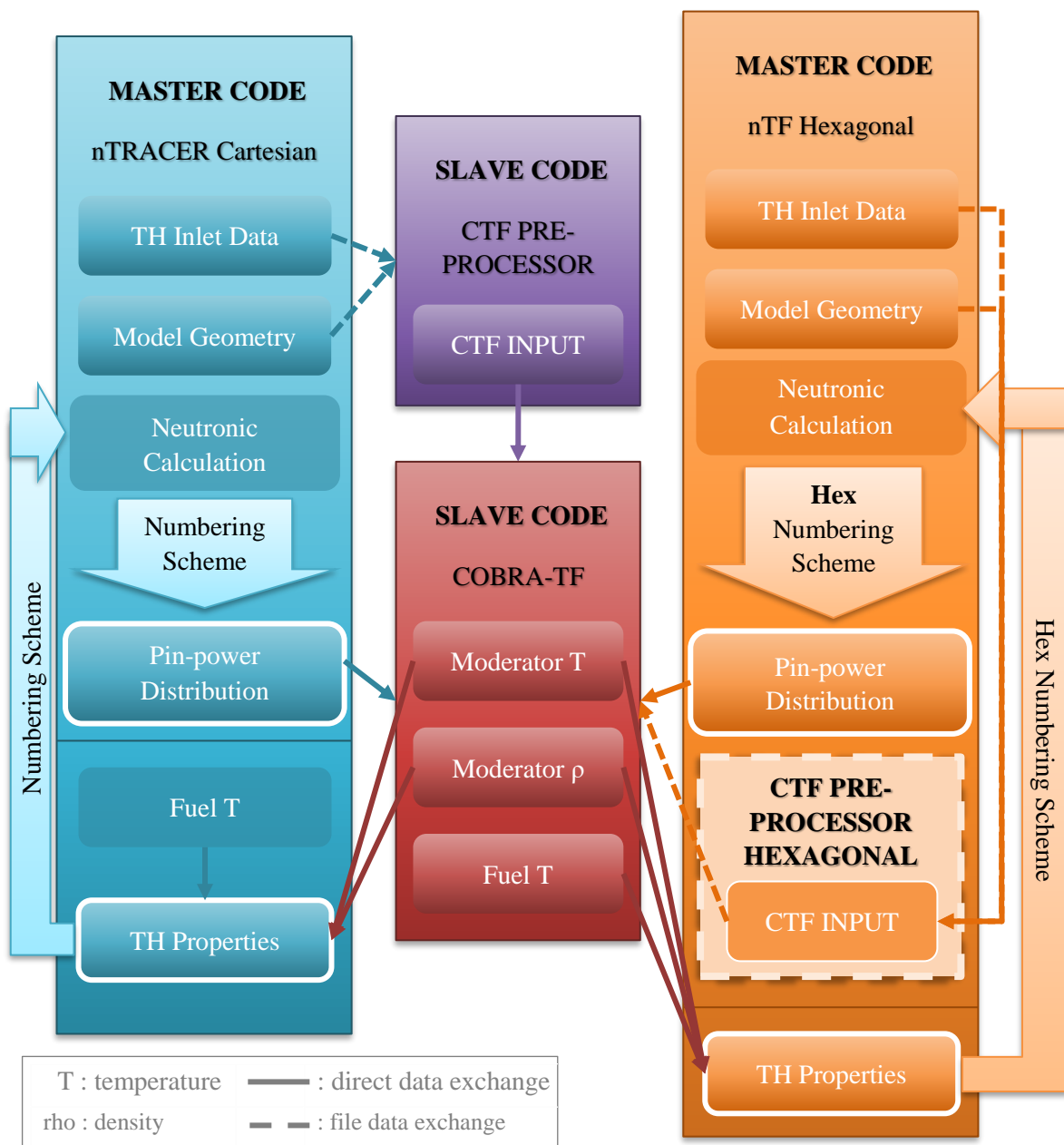


Figure 4.1. Structure of the nTRACER/CTF & of the nTF/CTF coupled code system

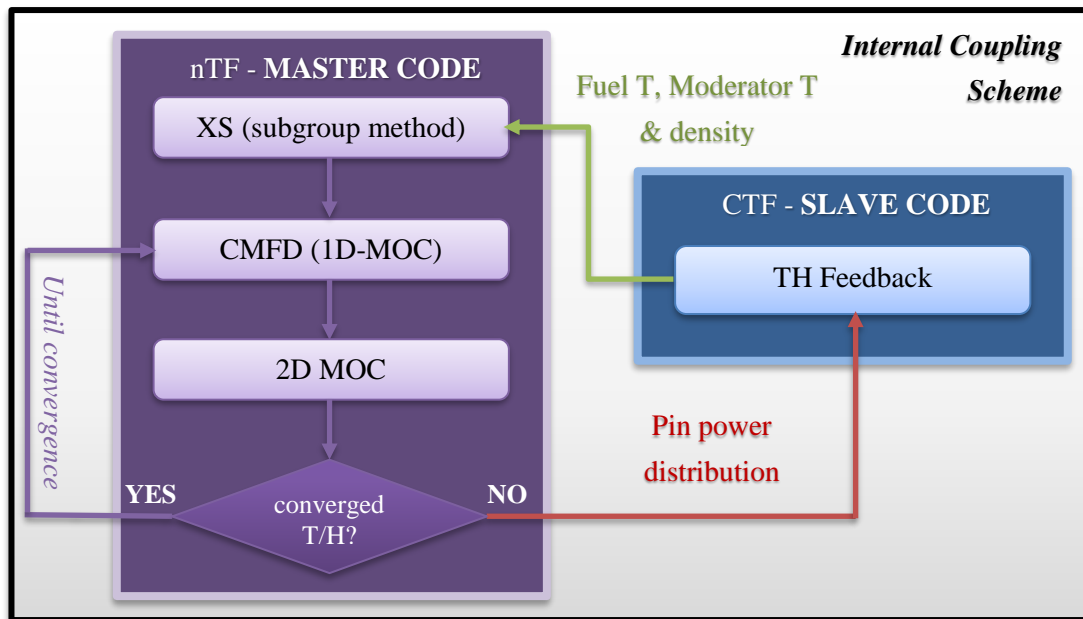


Figure 4.2. Internal coupling scheme for the nTF/CTF multi-physics core solver

4.2.2 Domain Decomposition

nTF and CTF use different meshes for the 3D domain decomposition in hexagonal geometry. The basic radial decomposition for the two codes is presented in Fig. 4.3, together with the superimposition of the respective meshes. The smallest structural element for the nTF models is the pincell, which consists of a fuel rod segment surrounded by coolant. The pincell is divided radially in several regions (FXRs) of equal volume with spatially flat cross-sections, which are defined by a unique set of parameters (e.g. temperature) for each FXR region (see also Section 2.3.2). As can be seen in Fig. 4.3, the shape of the pincell depends on its position in the fuel assembly. This irregularity is particular for hexagonal assemblies due to their geometry. The inter-assembly water gap is modeled by individual water cells. Axially, the solution domain is divided into several layers on a coarse mesh, since VVER cores are radially more heterogeneous than axially. As it was mentioned also in Section 2.4.2, CTF decomposes the domain into an array of channels, which are delimited by fuel rods and the open gaps, defined on the vertical planes crossing the centers of neighboring rods. For the treatment of hexagonal geometry, CTF combines the use of triangular channels in the assembly and square channels at the assembly boundary, which include the inter-assembly gap. Axially, the mesh is the same as in nTF. The methodology used by CTF allows the modeling of any possible configuration of fuel rods and assemblies, as long as the neighboring channels are defined in the input data.

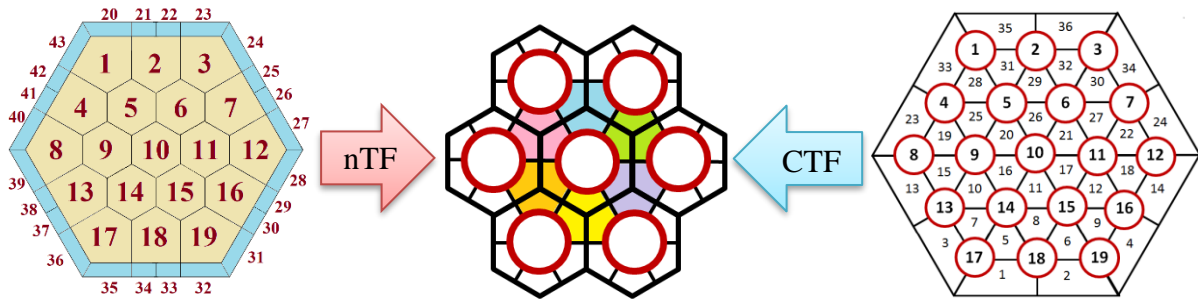


Figure 4.3. Domain Decomposition in nTF and CTF and superimposition of the meshes

For the coupled code system, the temperature profile of each fuel pin (fuel, gap and cladding) is transferred to nTF for the cross-section generation (see Section 4.2.4). The water density and temperature in the pincell, which is transferred to nTF, is calculated by averaging the corresponding parameters of the neighboring channels, according to the fraction of the wetted perimeter of the pin that corresponds to each channel (see Fig. 4.3). This means that all the FXR regions of the moderator in a pincell have the same water density and temperature. The inter-assembly gap cells are assigned the water temperature and density of the neighboring pincell (energy conservation).

The numbering scheme of the computational cells in nTF (see Fig. 4.3) is fixed in the solver and follows the sequence of the assemblies for a multi-assembly model (see Fig. 4.4). In CTF, the numbering scheme of pins and water channels can be defined by the user and has no effect on the calculation, as long as the sub-channels and fuel rods neighboring an element are defined correctly. In order to facilitate the flow of the algorithm for full core models, the standard CTF numbering format is altered [68]. The labeling of the fuel rods follows the sequence of the nTF pincells, without taking into account gap cells. The numbering of the sub-channels starts from the bottom to the left and is independent of the assembly formation in multi-assembly models (see Fig. 4.4). Fig. 4.4 provides examples of the nTF and the corresponding CTF hexagonal numbering scheme for the core solver, illustrating a mini-core of seven assemblies. In Cartesian geometry, the cells at the edge of neighboring assemblies, with no fuel rod in between, are merged into one sub-channel. In this work for hexagonal geometries, the meshing follows the borders of the assembly (see Fig. 4.4). This choice was discussed with the CTF developers in NCSU and is deemed an appropriate possible alternative, especially since it simplifies the introduction of corner stiffeners or assembly shrouds, both typical of VVERs, in the T/H model. As long as a gap is defined between the border cells in the input, the exchange of momentum, mass and energy is allowed (see Section 2.4.2).

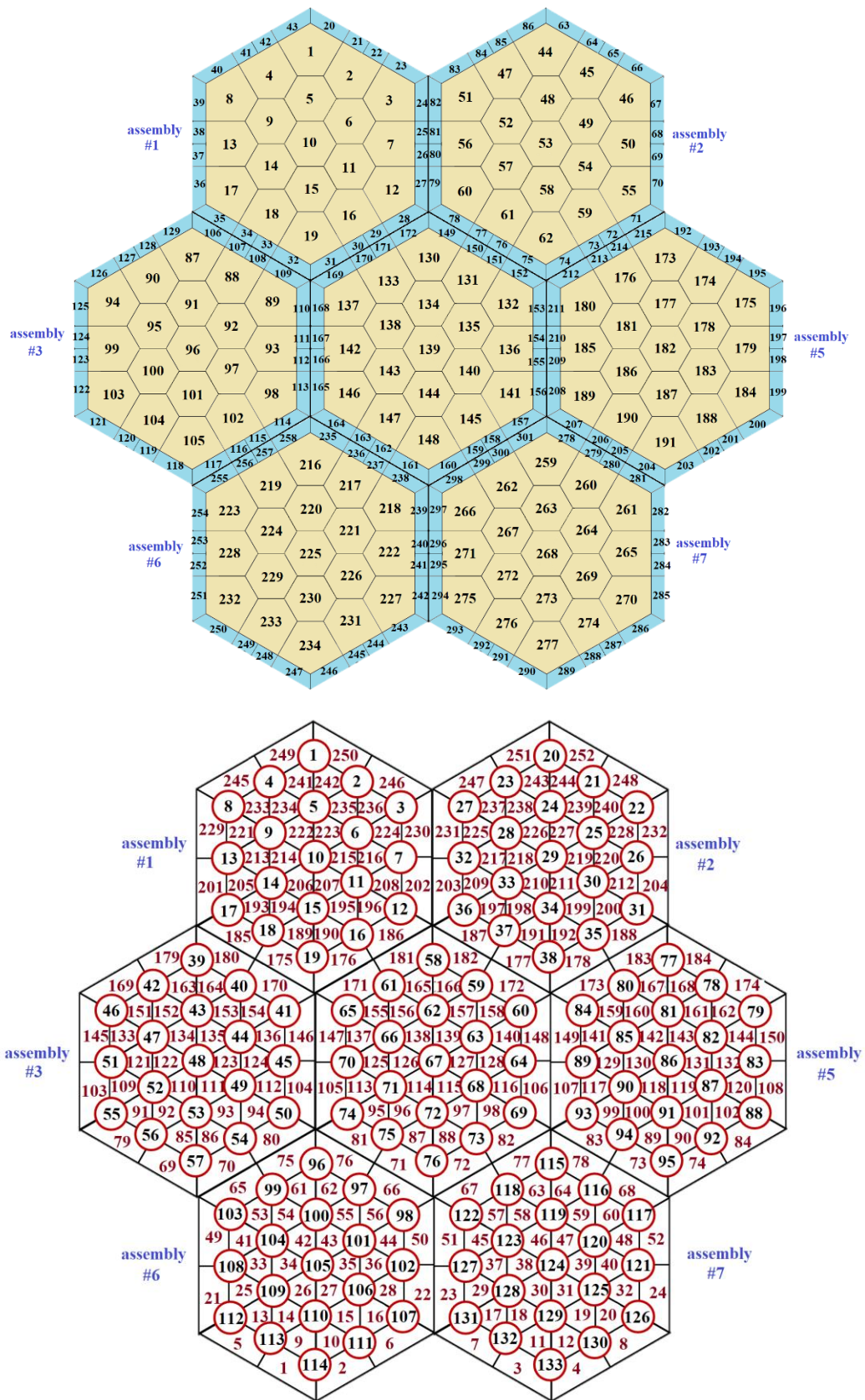


Figure 4.4. Numbering scheme of computational cells for a hexagonal geometry mini-core in nTF (top) and CTF (bottom)

In the course of this thesis, all data exchange subroutines existing in the outdated nTRACER coupling interface are updated to function for hexagonal full core models. The modifications include geometry dependent functions, which are extended to match the architecture of the VVER fuel assembly. This is necessary due to the differences in the mesh used by the codes for Cartesian and hexagonal geometry. One of the main modifications is the introduction of a new subroutine linking the different fuel rod numbering schemes used in the neutronic and the T/H code, following the pattern presented in Fig. 4.4. Moreover, due to the difference in the modeling of the inter-assembly water gap in Cartesian and hexagonal geometries, a new subroutine for water-gap treatment is necessary. Finally, all data exchange subroutines from nTF to CTF and vice-versa, are updated to follow the hexagonal numbering scheme.

4.2.3 CTF pre-processor for hexagonal geometries in nTF

As it was mentioned in the previous section, the nTRACER/CTF code system used the CTF pre-processor to create the CTF input for Cartesian geometries. This included an additional independent executable in the coupling (see Fig. 4.1). In the nTF/CTF coupling scheme a new subroutine is included in nTF, which has the equivalent function to the Cartesian pre-processor, for hexagonal geometries. This subroutine creates the CTF input directly, without the use of an additional executable or an external file, simplifying thus the execution of the coupled code system. The neutronic geometry model is used as a base for the T/H input. The nTF hexagonal pre-processor allows the production of CTF models of equivalent size and configuration as their neutronic counter-parts. There is not any limitation on the number of pins per assembly or the number of assemblies in a core model. However, at this point, the nTF hexagonal pre-processor cannot handle the symmetry options of nTF and requires the modeling of the full geometry. Besides fuel rods, the treatment of guide tubes (GTs) and axial reflectors is also included. A GT is modeled explicitly with CTF, whereas the axial reflector is defined as an additional axial layer of the fuel rods with zero power. This approximation is applied after consultation with SNU and is considered sufficient for now. Radial reflectors and spacer grids are not modeled by the LRT core solver. Heavy radial reflectors have no direct T/H effect on the active core besides confining the coolant flow with the core barrel. Radial heat conduction is neglected [*private communication with X2 benchmark team to be consistent with the Serpent2/SUBCHANFLOW model*]. All relevant neutronic effects are reflected to the T/H calculation by the power distribution. The 3 mm water gap surrounding the active core is also

neglected from the T/H model [private communication with X2 benchmark team to be consistent with the Serpent2/SUBCHANFLOW model]. The effects of spacer grids (pressure drop, flow mixing) are neglected in the T/H model but considered in an ad-hoc manner in the neutronic solution (see Section 3.2.3.1). Besides the geometry of the CTF model, all other T/H parameters are also imported from nTF. This includes material properties (e.g. gap thermal conductivity), boundary and operational conditions (e.g. exit pressure and assembly inlet mass flow) and finally computational options (e.g. convergence criteria). In this work, the core mass flow is subdivided equally between the assemblies. Some of the parameters (e.g. gap thermal conductivity) are defined in the nTF source and can only be changed by modifying the code. An initial guess of the power distribution is also provided in the CTF input by nTF. It corresponds to the result of the first CMFD iteration and, although not necessary (initial guess can be 1.0), it is included in order to accelerate the convergence of the T/H solution.

4.2.4 Introduction of the CTF fuel pin temperature profile to the coupled code system

The nTRACER/CTF coupling scheme, created for Cartesian geometries, required only the moderator temperature and density for each pincell as T/H feedback from CTF. The temperature profile of the fuel pin, the gap and the cladding was calculated by the fuel conduction solver of nTRACER for each pincell. However, in a high-resolution coupled code system the temperature of the fuel rod materials should be provided by the T/H code, since the models and equations used for the fuel conduction by CTF allow higher accuracy than the simplified solver included in nTF (1D-TH).

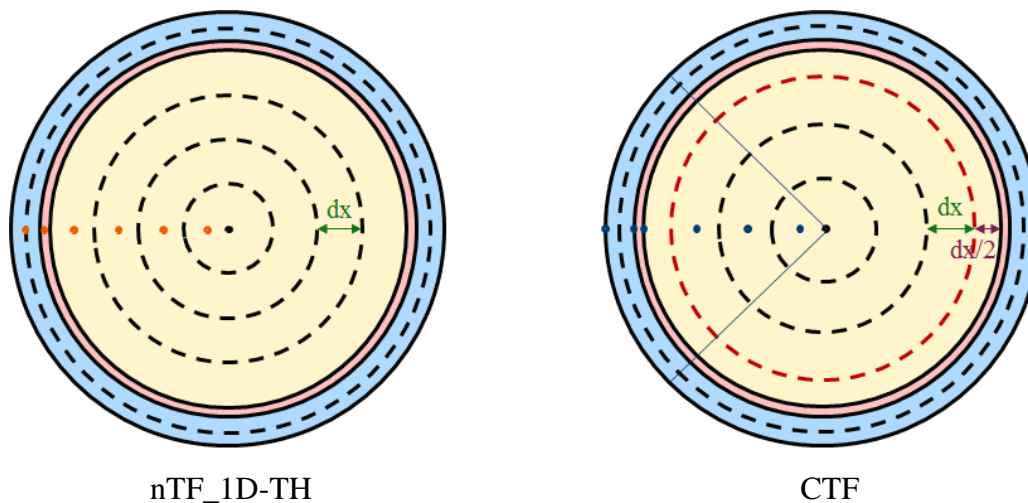


Figure 4.5. Radial discretization of the fuel pin in nTF_1D-TH and CTF for the fuel conduction solver

The discretization of the fuel rod in nTF_1D-TH and CTF for the solution of the conduction equation is presented in Fig. 4.5, where the calculation points of the temperature are identified for the two codes. nTF_1D-TH divides the fuel pin in equispaced nodes. The fuel temperature is initially calculated on the surface of the nodes and subsequently on the fuel node center with interpolation (see Section 2.3.7). The T/H nodes in the fuel pin differ from the FXRs used in the neutronic calculation. The corresponding FXR temperature is calculated as the volume-averaged value of the T/H nodes or segments of the nodes contained in the FXR. The cladding is divided in two nodes. The cladding temperature used for the cross-section generation is the volume-averaged value of the two nodes. The gap temperature is defined as the mean value of the temperature at the fuel outer surface and the inner surface of the cladding. CTF on the other hand, further discretizes the T/H radial nodes in azimuthal segments and defines the fuel temperature at the center of the segment for all inner subdivisions and at the surface of the fuel pin for the last node, which has half the width of the inner nodes (see Section 2.4.4). The cladding is divided in two nodes and the temperature is defined at the inner and outer surface. The gap conductance is defined in the CTF input and remains constant throughout the core, since the gap size is also kept constant, as thermal expansion is not taken into account. The gap temperature is not calculated by CTF. Finally, VVER fuel pins usually have a hole in the center to accommodate material evolution during irradiation. In CTF the hole can be modeled explicitly, whereas the T/H discretization of nTF can only be applied to solid fuel.

In order to use the CTF fuel temperature in nTF, the neutronic code is modified on the course of this thesis to apply the CTF fuel pin discretization when coupled to CTF. In addition, nTF is modified to model the hole of the VVER fuel pin or solid fuel, according to the geometry description of the fuel pins in the input, with CTF and 1D-TH. In the neutronic calculation, the temperature for the FXR regions is not changing azimuthally. A subroutine is added in CTF to calculate the azimuthal average of the temperature for each radial node and transfer the data to nTF. The pin surface temperature is used for the outer T/H node. In general, the fuel conduction calculation requires a large number of T/H nodes for the calculation of the fuel temperature profile (~10), larger than the number of FXRs used (~4). Thus, the use of the surface temperature rather than the node average has a small impact in the cross-section generation. The nTF data extraction subroutine is updated to receive the radial temperature profile by CTF for each pin and the volume-averaged fuel temperature. The cladding temperature is defined as the volume average of the surface temperatures provided by CTF. Finally, the gap temperature

is calculated in nTF as the mean of the temperatures at the fuel outer surface and the cladding inner surface.

4.2.5 Parallelization

Both nTF (MPI + OpenMP) and CTF (MPI) are capable of parallel simulations (see Section 2.2). This is an important feature for high-resolution solvers intended to perform full core analysis, since the memory requirements (see Section 2.4.3) are forbidding the use of a single computational node, especially when symmetry simplifications are not taken advantage of. The main obstacle for parallelization is the different domain decomposition approaches of the two codes: in nTF, it is applied axially (one MPI per axial plane) but radially in CTF (MPIs are distributed among sub-channels, e.g. one per assembly or a group of assemblies). It was one of the reasons that SNU abandoned the nTRACER/CTF core solver and developed their own sub-channel T/H code [49], which follows the domain decomposition of nTRACER. However, the recent evolution of CTF and the availability of a computationally flexible and powerful cluster like Merlin6 (see Section 2.2) at PSI allowed the development of a double domain decomposition parallelization scheme, which is employed in the nTF/CTF multi-physics core solver for full core analysis.

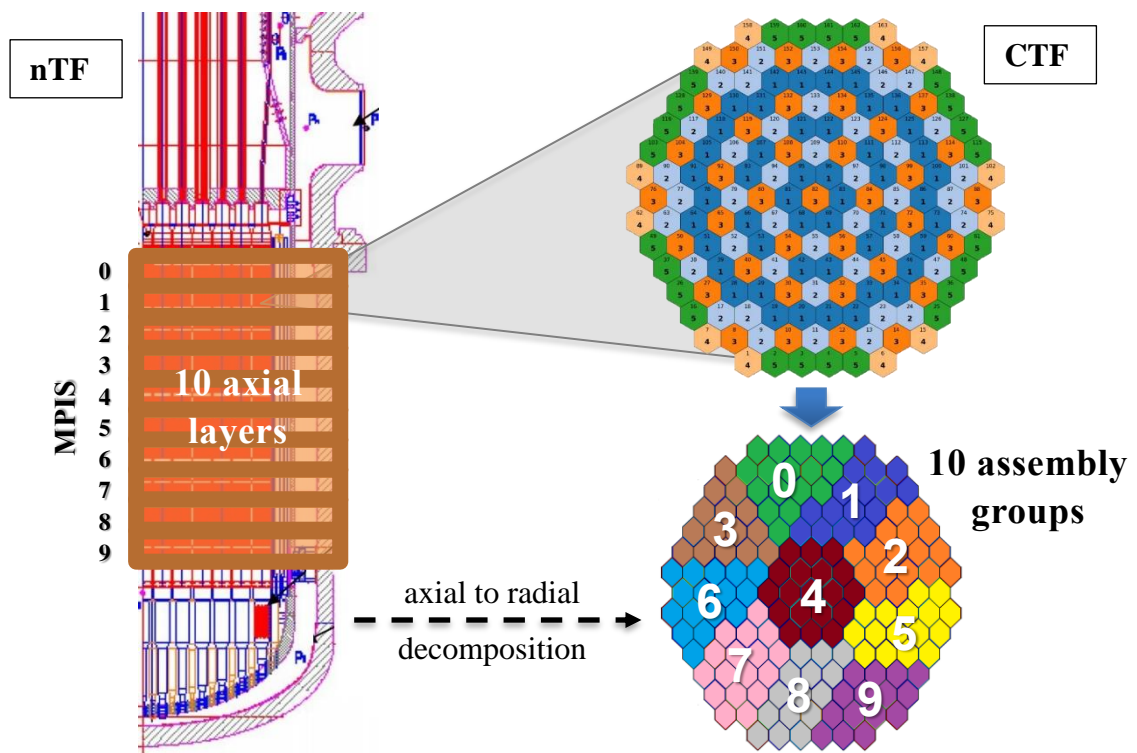


Figure 4.6. Double domain decomposition parallelization scheme of nTF/CTF

For the LRT coupled code system, since nTF is the master code, the computational resources are allocated according to the requirements set by the nTF axial domain decomposition. The easier and more cost effective option is the use of the same resources, as they are assigned in MPI tasks by nTF, for the T/H calculation. CTF allows radial parallelization on groups of assemblies. The user has full freedom to select which assemblies are grouped together, as long as the CTF input is cataloging the corresponding sub-channels belonging to each MPI. Thus, the multi-assembly model can be subdivided in smaller clusters of different configurations, allowing a full core model to be radially subdivided to as many assembly groups as the number of available MPIs, at maximum. The double decomposition parallelization scheme is illustrated in Fig. 4.6. The grouping of neighboring assemblies to form clusters simplifies the calculation, as the communication time between MPIs is reduced. The reason is that the amount of data exchanged between MPI “x” and the other MPIs is dependent on the number of the inter-channel connections (gaps) at the assembly edges, the assemblies assigned to MPI “x”, which are connected with the rest of the core that is assigned to other MPIs. The number of assembly groups in CTF can be smaller than the number of available MPIs for specific cases (small models).

The allocation of resources from nTF to CTF is developed in an nTF subroutine and is based on the MPI libraries. The goal is to achieve flexibility of the CTF radial decomposition according to the needs of each calculation. To that end, all nTF assigned MPIs are separated in two groups with their own communicator, generated from the global communicator. One group consists of the MPIs that perform the T/H calculation and the other group of the remaining MPIs, which remain idle during CTF execution. The different MPIs that perform the T/H calculation are assigned to the user-defined radial subdivisions of the T/H multi-assembly model by the CTF input. Once the T/H calculation is done and the data exchange completed, then the new temperature and density distributions are communicated to all MPIs in nTF. The new T/H conditions are assigned to the FXRs of each axial layer by the corresponding MPI.

The existing nTRACER/CTF coupling interface contained some preliminary steps for the parallelization of small configurations. However, the handling of the computational resources in the nTF/CTF coupled code system, for small configurations or full core models, is exclusively developed on the framework of this thesis. All pre-existing subroutines are replaced by new functions, which either follow a user-defined radial decomposition map or assign each MPI to one assembly, as long as the number of assemblies is lower than the number of MPI tasks. The user-defined radial decomposition map for CTF is introduced as an additional input

card in nTF, following the concept employed in MPACT [115]. The map assigns to all active core assemblies an MPI ID, which is used by nTF to build the equivalent parallelization scheme in the CTF input. According to the number of MPIs defined in the nTF input, the code separates the MPIs which are used or not for the T/H calculation. The subroutine for the broadcasting of information to all MPIs is updated to match the new hexagonal numbering scheme; and to include the temperature profile of the pin. The CTF source is also modified to allow the initialization of its parallel execution through nTF. All the other required functions were already developed for parallel execution.

4.2.6 Capabilities and coupled compilation of the nTF and CTF versions used for the LRT multi-physics core solver.

At the time of this study, CTF has never been used at PSI in parallel for any other core configuration than PWRs. After a private consultation with the development team of NCSU, CTF v4.0 is revealed as the first code version to perform parallel calculations independently of the model geometry. CTF v4.0 is extensively different from the version used for the development of the nTRACER/CTF core solver. Several subroutines used in the coupling with nTF are modified or fully replaced and variables are organized as larger group objects. Thus, further development is necessary to take into account the new structure of CTF in nTF. In addition, the compiling modules used by CTF v4.0 are not matching the configuration used until now for nTF. For this work, the neutronic code is extended to GNU compilers with MPICH libraries by SNU. In addition, CTF v4.0 requires specific LAPACK and PETSc libraries. The compilation of the libraries and the codes with specific modules that allow their coupled execution was achieved only on the LCLRS machines and Merlin6 cluster (see Section 2.2). The modules used for the common compilation are listed in Table 4.1. The execution of the LRT core solver was not accomplished in CSCS, due to lack of the necessary memory resources for full core modeling and because the common compilation of the codes could not be achieved in the cluster environment.

Modules used for the compilation of nTF/CTF	1) cmake/3.15.5	4) openssl/1.0.2r	7) intel/17.4
	2) gcc/5.5.0	5) TclTk/8.6.9	
	3) mpich/3.2.1	6) Python/2.7.16	

Table 4.1. Modules used for the compilation of nTF/CTF in LCLRS and Merlin6

Considering nTF, the code is under intense development, so no official version number was defined. The latest source used for this work includes all the modifications described in Chapter 3 for the modeling of real VVER cores. The nTF T/H module includes several subroutines that are common for the coupled code system and the 1D-TH solver. In order to accommodate all the features imposed by the new coupling, several modifications and restructuring are necessary to include both options of T/H feedback. In addition, the need to model homogenized regions of moderator and steel, where the water density and boron concentration is adjusted according to the T/H feedback, required the addition of new features in the neutronic code. It must be pointed out that from this point on, the two-group acceleration technique, employed on the CMFD formulation (see Section 2.3.3) is no longer used in this work. When the acceleration is applied with feedback (CTF or 1D-TH) the radial power profile of nTF becomes strongly asymmetric for symmetric models. The issue was not resolved due to lack of time. In order to assess the impact of deactivating the two-group acceleration to the convergence of the solution, a mini-core built by 7 X2 13AU assemblies (see Fig. 3.2), is simulated in 3D Hot Zero Power (HZP) with nTF/CTF, with as tight convergence criteria as possible to avoid instabilities in the calculations [$2 \cdot 10^{-7}$ 10^{-6} 10^{-6}]. The mini-core is chosen in order to ensure the full convergence of the solution, which could not be achieved for full core models due to their complexity and computational needs. In addition, the radial asymmetry is not present for HZP. The axial reflectors of the mini-core are built according to the nTF X2 model (see Section 3.2.3.1). The converged solution is compared with two calculations with the same model, using the convergence criteria employed for full core analysis [10^{-6} 10^{-5} 10^{-5}], with and without acceleration. The RMS difference of the axial profiles from the converged solution is 0.1% and 0.5% respectively. This is not significant considering the range of discrepancies in the axial profile (see Section 3.2.3.3). The assembly and pin power differences are insignificant. It must be pointed out that for a full core model the discrepancies should increase. Deactivating the two-group acceleration of the CMFD formulation does not affect the accuracy of the solution for the mini-core model; however, it increases the calculation time of the full core HFP simulation more than 35%.

The development of the coupled code solver involves extended changes in the source of both codes, especially nTF. Moreover, CTF is applied for the first time to full core high-resolution modeling of hexagonal geometry, what is more, in parallel. Finally, several simplifications are adopted for the T/H model, adding to the necessary approximations

employed by the neutronic code. In order to use the LRT core solver for steady state and, subsequently, cycle analysis the above approximations and their impact on the accuracy of the high-resolution predictions are studied in the following sections.

4.3 Comparison of the nTF/CTF core solver with the Serpent2/SUBCHANFLOW high-resolution multi-physics code system

The next step of this study is the comparison of the LRT core solver with a code system of equivalent fidelity and resolution in neutronics and T/H, Serpent2/SUBCHANFLOW (see Section 2.6). The results were provided by the Helmholtz-Zentrum Dresden-Rossendorf (HZDR). Such analysis is performed using the HFP state of the X2 benchmark. The Serpent2 X2 model built for the HFP state, is the same as the HZP model described in [98], except that all control rod banks are fully extracted. The associated T/H model of SUBCHANFLOW (SCF) is built and provided by KIT [64]. The reference solution is generated similarly with [98], by performing three independent runs of the coupled code system and averaging the results. Each of the three independent simulations is executed with 4×10^9 histories in Serpent2. As discussed in Section 2.6.2, SCF is a sub-channel T/H code, using a similar computational methodology with CTF. On the other hand, nTF and Serpent2 employ completely different methods to generate the neutronic solution. A major difference is the handling of the fuel temperature in the two neutronic solvers. As it was described in Section 4.2.4 of this chapter, CTF provides a fuel temperature profile for each pin, which is then volume-averaged to match the several FXRs of nTF for the specific pin. On the other hand, Serpent2 receives a single temperature from SCF for each pin. This temperature can be the volume average or the Doppler fuel temperature ($0.3 \times T_{\text{center}} + 0.7 \times T_{\text{surface}}$). Besides the exchange of data between the codes, the two multi-physics solvers can differ in several aspects, as, for example, the correlations used for material properties. Before proceeding with the comparison of the solvers for the full VVER-1000 core, basic functions of the codes, relevant to the simulation of the HFP state, are cross-compared in order to pinpoint inconsistencies. Subsequently, the X2 HFP solutions of two code systems are compared on a global and local scale.

4.3.1 Study of basic functions of the coupled code systems for HFP calculations

The objective of this section is to identify differences in the computational methodology of the two multi-physics code systems, which have an impact on HFP analysis, and quantify

that impact when possible. The handling of Doppler treatment or moderator dilution by the neutronic code library affects the results of HFP calculations. In order to assess the nTRACER library in that respect, nTF and Serpent2 standalone simulations of simple VVER configurations, like 2D pincells and single assemblies, are cross-compared. Finally, the correlations used by the T/H codes for the definition of material properties are also compared.

4.3.1.1 nTF vs Serpent2 for simple VVER configurations

In Section 3.2.1.1, it is observed that the 2D pincell with 3.6% w/o enrichment presents the largest eigenvalue difference when nTF is compared with Serpent2 for the HZP state. Thus, the same enrichment is chosen to extend the 2D pincell comparison to moderator density and fuel temperature variations. Fig. 4.7a depicts the eigenvalue difference between nTF and Serpent2, $[k_{eff_{Serpent2}} - k_{eff_{nTF}}]$, as a function of the moderator density. Temperature is stable at 600 K and the boron concentration is adjusted according to the density variation to always match 1207 ppm. Fig. 4.7b presents the effect of the Doppler treatment, on the pincell model. The moderator density and temperature are kept stable at 0.7629 g/cc and 600 K respectively. All nTF calculations employ P0 transport corrected scattering treatment. The uncertainty for all Serpent2 calculations is ~ 5 pcm.

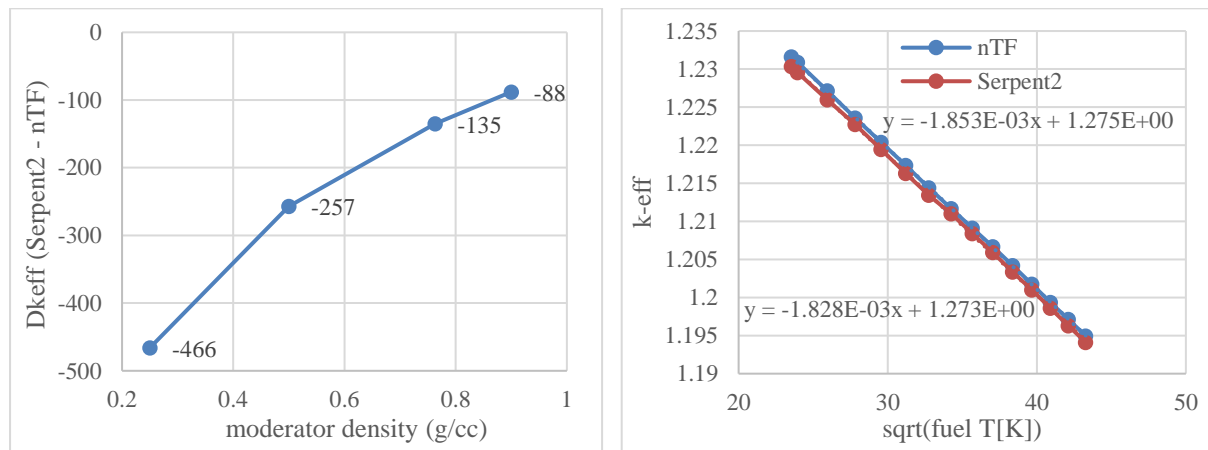


Figure 4.7. Eigenvalue difference of nTF vs Serpent2 as a function of moderator density (a) and eigenvalue of the same codes as a function of fuel temperature (b) for a 3.6% w/o pincell

In Fig. 4.7a, nTF is overestimating the eigenvalue in all cases. The cases where the pincell is simulated in no normal operating conditions, like very low moderator density (0.25 g/cc, 0.5 g/cc), nTF is presenting large discrepancies. These conditions will never apply to normal operation of a pressurized water core. In addition, taking into account that the nTRACER library is optimized for the Korean OPR1000 operating conditions [private communication with SNU], these discrepancies can be expected. In all other calculation points, the eigenvalue

difference remains in acceptable levels. In Fig. 4.7b, the difference between nTF and Serpent2 is decreasing as fuel temperature increases. This is attributed to the nTF library Doppler treatment. The effect can be quantified by the difference in the slope of the linear fit illustrating the eigenvalue as a function of the square root of the fuel temperature, which is $[(\text{Slope}_{\text{Serpent2}} - \text{Slope}_{\text{nTF}}) / \text{Slope}_{\text{Serpent2}}]$. This difference equals 1.4% which is not significant.

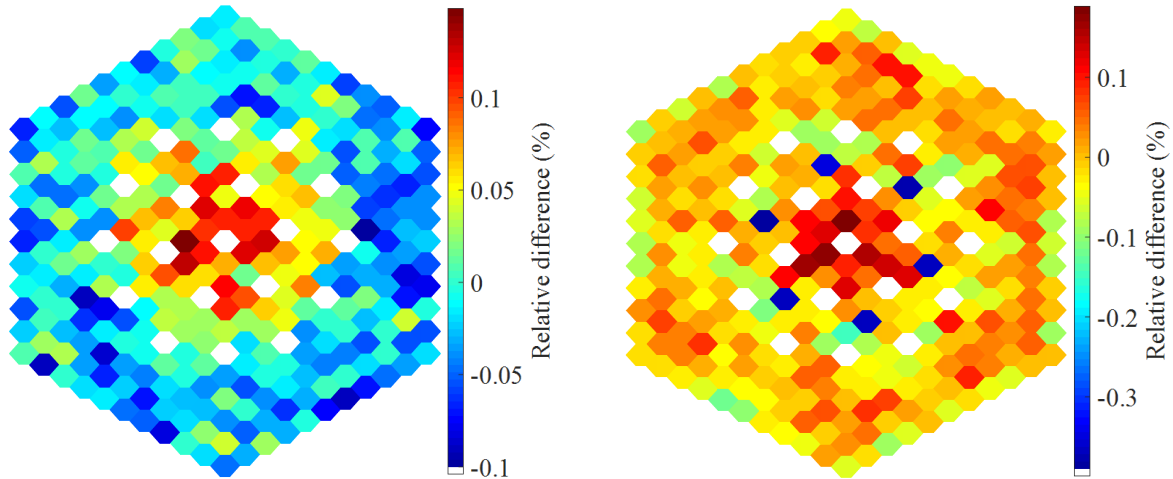


Figure 4.8. Relative pin power difference of nTF vs Serpent2 for the X2 fuel assembly 13AU (left) and 390GO (right) for HFP

The assembly models studied in this section correspond to the two X2 fresh fuel assemblies presented in Section 3.2.1.2 (see Fig. 3.3). As described in Chapter 3, one assembly is built with a single type of low enrichment fuel and the other contains a ring of high enrichment pins at the outer boundary, together with several Gd pins close to the center. The fuel temperature for both assemblies is set at 900 K. All other materials are simulated at 600 K. Fig. 4.8 presents the relative difference of the normalized power, $[(\text{Nor.Pow}_{\text{Serpent2}} - \text{Nor.Pow}_{\text{nTF}}) / \text{Nor.Pow}_{\text{Serpent2}}]$, on the pin level for the 2D assembly. The uncertainty of the Serpent2 calculations remains $< 0.03\%$ for the pin power and 2 pcm for the eigenvalue. The difference of the eigenvalue, $[\text{keff}_{\text{Serpent2}} - \text{keff}_{\text{nTF}}]$, for the 2D assembly calculations is respectively 73 pcm and 45 pcm. Comparing the eigenvalue differences with the corresponding ones for the HZP case (59 pcm and 25 pcm respectively), it becomes clear that the definition of a different fuel temperature (600 K for HZP) has some effect on the calculation. Besides the eigenvalues, for the 13AU assembly the relative power difference remains $< 0.15\%$ with a RMS of 0.04%. The heterogeneous 390GO assembly presents higher discrepancies with a maximum at 0.39%, again for the Gd pins, and the RMS equals 0.05%. The pin power difference is similar to what is observed in Chapter 3. However, the discrepancies (maximum and RMS) are smaller for both assemblies for HFP than HZP, which can be attributed to the optimization of the library

for OPR1000 (the operating conditions of the reactor should be closer to the HFP case rather than HZP).

4.3.1.2 Comparison of material properties correlations in CTF & SCF

The use of specific correlations for the calculation of material properties can have a significant impact on the solution. When comparing solvers that use different correlations then the results can diverge. Specifically in the T/H model, the main parameters that affect the results are the fuel-to-cladding gap conductance and the heat capacity and thermal conductivity of the fuel and the cladding. In order to eliminate possible sources of discrepancy when comparing nTF/CTF vs Serpent2/SCF for the full VVER-1000 core, the above-mentioned parameters are compared for the two solvers:

- Gap conductance: Normally the gap conductance varies over the core, since the gap size is changing with temperature and exposure as the fuel and the cladding expand. Both CTF and SCF are capable of simulating variations in gap conductance. However, in order to verify the nTF/CTF coupling scheme for a simple model that will allow the quantification of possible discrepancies in the LRT solver, the gap conductance is set constant at $10,000 \text{ W}/(\text{m}^2 \cdot \text{K})$ for both T/H solvers.
- Fuel specific heat capacity: The fuel heat capacity for 95% theoretical fuel density is calculated in both T/H codes according to the correlations available in MATPRO – 11 [116].
- Fuel thermal conductivity: CTF defines the fuel thermal conductivity, for 95% theoretical fuel density, according to the correlations of MATPRO – 11 [116]. SCF on the other hand uses the model of code FRAPCON – 4 [117]. Fig. 4.9 shows the thermal conductivity as a function of temperature, as it is defined in the two codes. Taking into account that the maximum fuel temperature calculated by CTF in the X2 HFP full core is 1,668 K, the two curves are almost identical for a large part of the core temperature range diverging at 1,668 K by ~3%.
- Cladding specific heat capacity: The Zircaloy heat capacity is defined in CTF according to the relevant table in MATPRO – 11 [116] and in SCF according to MATPRO – 9 [118]. Fig. 4.10 (left) illustrates the cladding heat capacity as a function of temperature. The maximum difference in the range of cladding temperature, as calculated by nTF/CTF, for the X2 HFP is ~4%.
- Cladding thermal conductivity: The Zircaloy thermal conductivity is also defined in CTF according to the relevant table in MATPRO – 11 [116] and in SCF according to MATPRO – 9 [118]. Fig. 4.10 (right) illustrates the cladding thermal conductivity as a function of

temperature. The maximum difference in the range of cladding temperature, as calculated by nTF/CTF , for the X2 HFP is $\sim 3\%$.

The difference in material properties between CTF and SCF appears not large enough to result in major discrepancies. However, since CTF allows user-defined material properties the effect of different correlations is studied further in the next section.

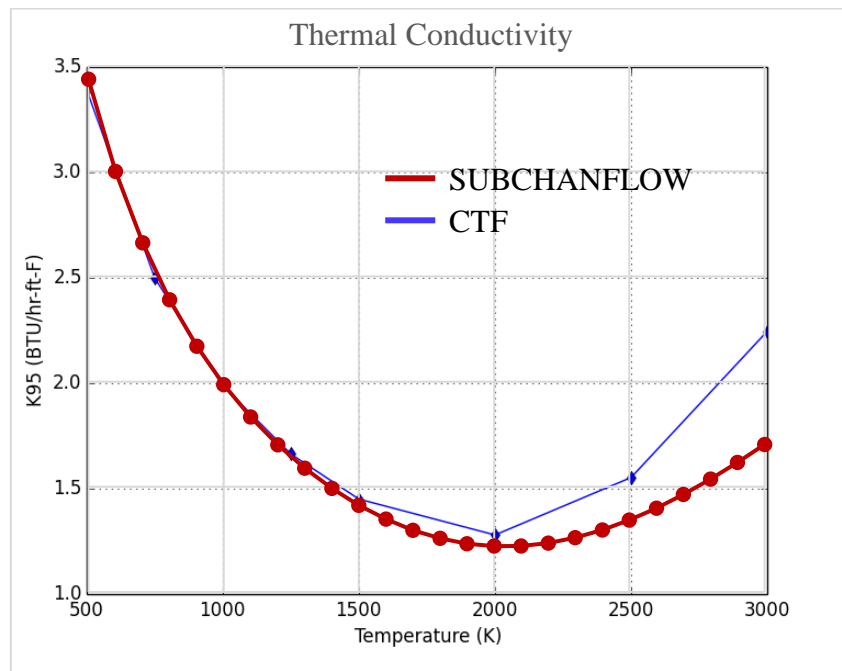


Figure 4.9. Fuel thermal conductivity defined by CTF and SCF as a function of temperature

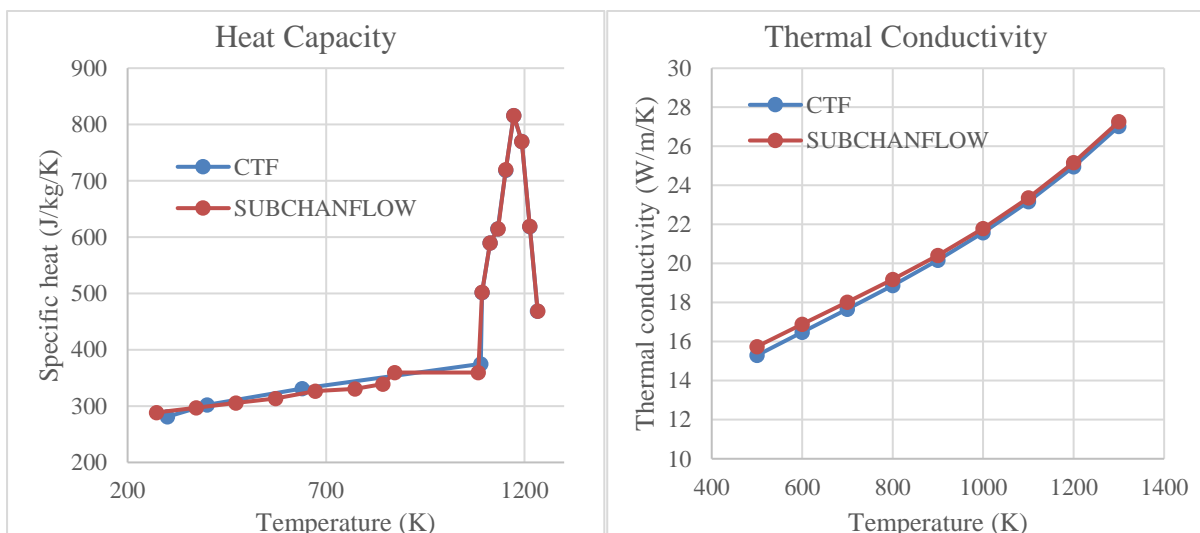


Figure 4.10. Zircaloy specific heat capacity (left) and thermal conductivity (right) defined by CTF and SCF as a function of temperature

4.3.2 VVER full core comparison

Having a better understanding of some basic differences in the two solvers, this stage of the study can focus on the verification of nTF/CTF with Serpent2/SCF for the full core HFP case. As it was mentioned in Chapter 2, the X2 benchmark includes several stages, one of which is HFP [119]. The core inlet temperature is 287 °C and the outlet pressure 157 bar. The total power produced is 3000 MW and the coolant flow in the active core is 109.8 kg/s per assembly. Both multi-physics tools perform a critical boron search for these operating conditions. The nTF model validated for HZP is used in this study. The core is fully unrodded. Spacer grids and corner stiffeners are not taken into account in the T/H model. The Serpent2/SCF model for X2 HFP [97] is adjusted to match some key features of the nTF/CTF model, in order to remove sources of discrepancy in the solution. As it was demonstrated in the previous sections and in Chapter 2, there are some differences in the methods and correlations used by the two coupled code systems. Some inconsistencies cannot be addressed directly. However, the introduction of a single fuel pin temperature instead of a profile as T/H feedback and the different material correlations can be reproduced by nTF/CTF. The effect of these discrepancies is quantified in this section. Nonetheless, as a first step, all material properties and data exchange are defined in the two solvers with the default options. Serpent2/SCF also simulates the full core (360°), introducing the Doppler temperature of each fuel pin as feedback.

Fig. 4.11 presents the relative difference of the normalized axially averaged pin power distribution for 1/6th of the core, $[(\text{Nor.Pow.}_{\text{Serpent2/SCF}} - \text{Nor.Pow.}_{\text{nTF/CTF}}) / \text{Nor.Pow.}_{\text{Serpent2/SCF}}]$. The difference of the calculated critical boron $[\text{BC}_{\text{Serpent2/SCF}} - \text{BC}_{\text{nTF/CTF}}]$ is -2 ppm; the maximum pin power difference does not exceed 2.9% and the RMS equals 0.8%. The target accuracy requirements defined in Section 2.7.3 are satisfied. The tilt that is observed in the HZP case (see Fig. 3.15) is not apparent in the pin power difference of the HFP. The T/H effects have a strong impact in the power distribution, averaging out partially the tilt of the standalone simulation. The effect of the central guide tube, which is modeled with a reduced outer diameter (see Section 3.2.3.1), is apparent in the pin power difference similarly to Fig. 3.15. In Fig. 4.11, the pin power difference is presenting a similar spatial pattern inside most of the assemblies. Serpent2/SCF is predicting a more peaked power profile inside the assemblies. The source of this discrepancy cannot be identified directly. It can be attributed to the different formulations and methods used by the two T/H solvers (e.g. cross-flow), but also to the tendency of the

MOC neutronic code to smoothen the heterogeneities in the radial power profile (see Chapter 3 & Fig. 4.8). Fig. 4.12 illustrates the axial power profile for both calculation schemes and their relative difference.

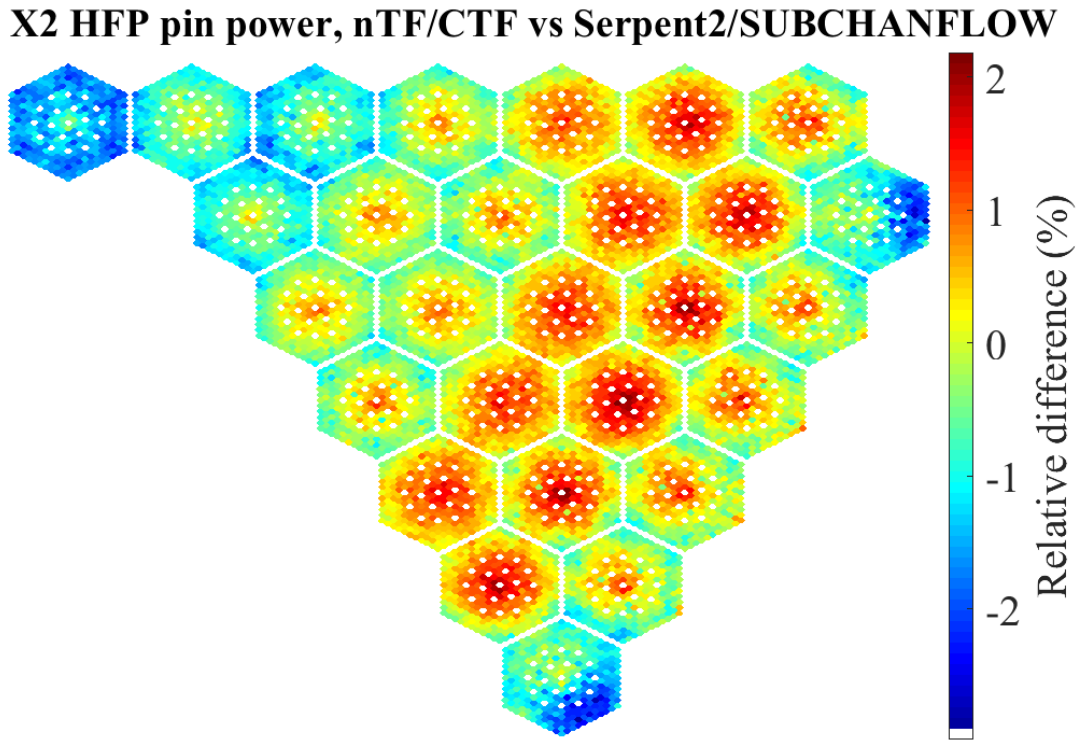


Figure 4.11. Relative pin power difference between nTF/CTF and Serpent2/SCF for the X2 HFP state

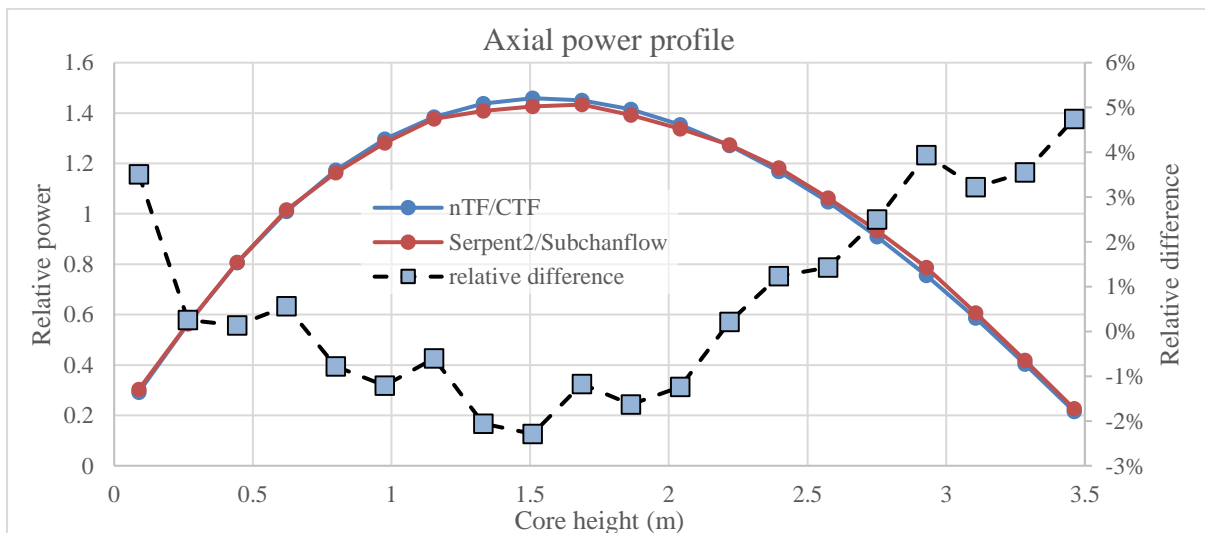


Figure 4.12. Axial relative power profile and its relative difference between nTF/CTF and Serpent2/SCF for the X2 HFP state

The level of differences for the axial profile is similar to what is observed for the HZP comparison. The irregular shape of the relative difference (dips) can be attributed to the explicit

modeling of spacer grids in the Serpent2/SCF. The axial nodes where there is a steep decrease in the relative difference do not contain spacer grids. The maximum difference ($< 5\%$) is observed on the nodes neighboring the top axial reflector, where the power is the lowest. Unlike HZP, nTF/CTF is overestimating the peak power in the HFP case ($\sim 2.3\%$). In addition, nTF/CTF predicts the power peak lower in core height. In order to examine the axial evolution of the core power map, Fig. 4.13 illustrates the relative power difference for each assembly of the $1/6^{\text{th}}$ core as a function of height, together with the relative difference of the axial profile at the same height. The radial profiles of the assembly power difference at the bottom and top of the core are also illustrated.

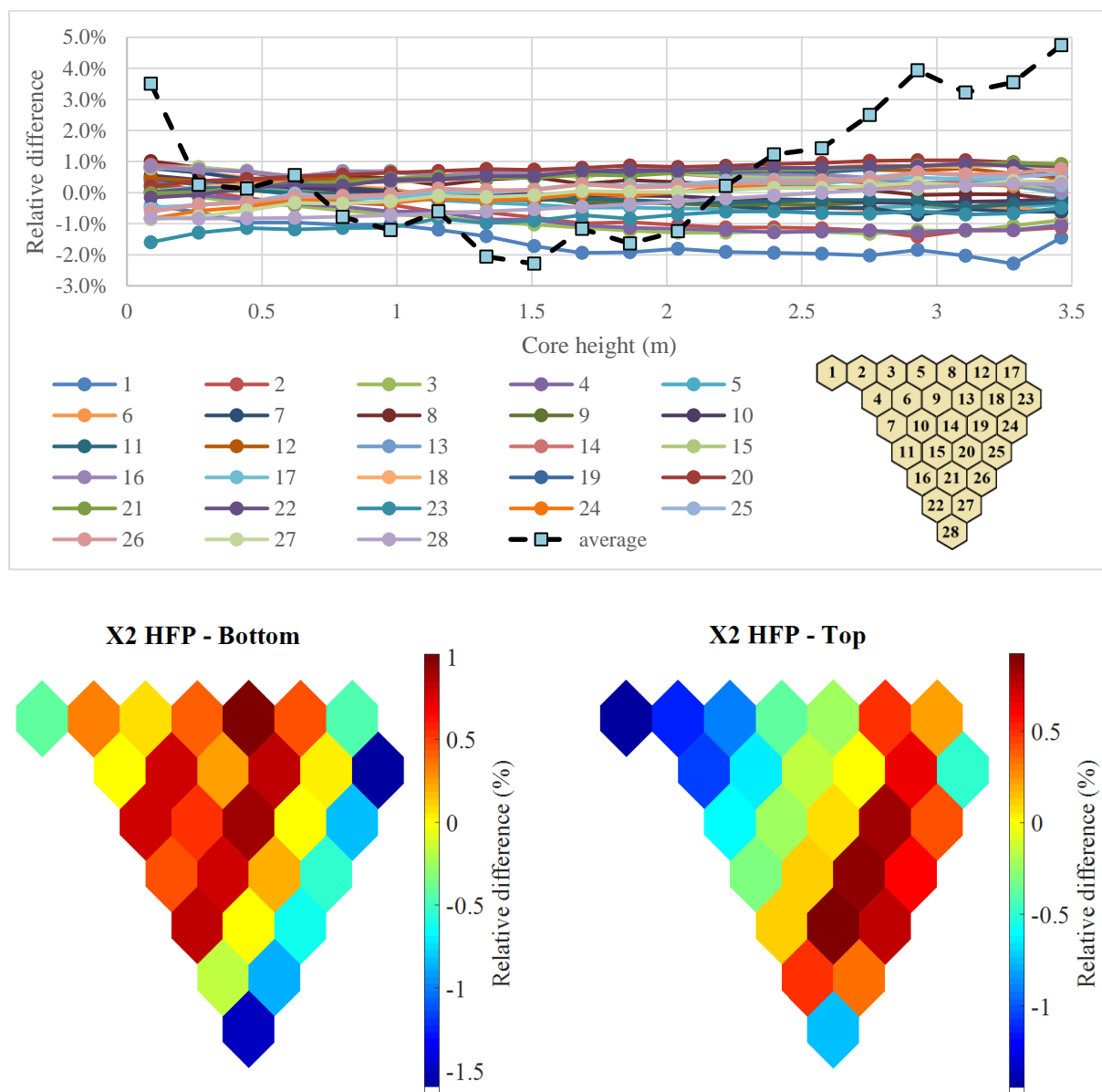


Figure 4.13. Relative assembly power difference between nTF/CTF and Serpent2/SCF vs core height and relative difference of the axial power profile at the same level

The relative difference for the assembly power reaches a maximum absolute value of 2.3% close to the top of the core. Besides assembly 1, which is in the center of the core, the relative difference of all other assemblies lies between -1.4% and 1%. It is apparent on Fig. 4.13 that the sign of the difference remains the same throughout the height of the active core for some assemblies, whereas it changes for others. This means that the small pin power differences, reported in Fig. 4.11, are partly the result of compensation due to axial averaging. The shape of the power profile difference at the bottom is not the same as in the top of the core, where nTF overestimates the power in the center creating a tilt in the distribution. This change can be attributed to the T/H feedback. In general, the assembly power difference remains within the accuracy requirements defined in Section 2.7.3.

Before commenting on the discrepancies of the power prediction, it is beneficial to also compare the temperature profiles of the two solvers, since the neutronic and T/H effects are intertwined for multi-physics solvers. Fig. 4.14 presents the difference in the calculated coolant temperature, $[\text{Cool.Tem.Serpnet2/SCF} - \text{Cool.Tem.nTF/CTF}]$, as a function of height together with the axial power profile. The maximum temperature difference reaches 0.3 K and the RMS is 0.19 K. At the bottom half of the core, nTF/CTF predicts a lower coolant temperature until the height where nTF/CTF begins to underestimate the power in comparison to Serpent2/SCF. This can be related to the shape of the power profile. nTF/CTF predicts a more peaked power profile. The lower coolant temperature on the bottom of the core results in more moderation, which creates the stronger power peak. Then the top of the core is less moderated, by comparison, thus the power is lower. Similarly, the radial profile of the assembly power at the top of the core is more peaked than the Serpent2/SCF solution, predicting higher power in the center of the core and lower close to the reflector. In addition, as was observed in Chapter 3, nTF tends to underestimate the power at the bottom of the core, which could in turn affect the coolant temperature. The outlet temperature is not identical in the two solutions, which can be possibly attributed to the different modeling of axial conduction. Further investigation is required, nonetheless the discrepancy is not significant. Concerning the fuel temperature predictions, the two code systems are compared in terms of Doppler temperature, since it is the feedback fuel temperature for Serpent2/SCF. Serpent2/SCF is calculating the Doppler temperature using the temperatures of the inner and outer fuel surface. On the other hand, as it is discussed in Sections 4.2.4 and 2.4.4, CTF calculates the fuel temperature only in the center of the radial nodes, except for the outer surface. Given that the thickness of the innermost radial node in nTF/CTF is 0.4 mm and that the slope of the temperature profile of the fuel pin is close to 0 at

the center (see Fig. 4.15), the center temperature of the innermost radial node (see Fig. 4.5) is used for the calculation of the Doppler temperature in nTF/CTF. Fig. 4.16 presents the difference in the Doppler fuel temperature, $[\text{Fuel.Tem.}_{\text{Serpent2/SCF}} - \text{Fuel.Tem.}_{\text{nTF/CTF}}]$, as a function of height, together with the difference of the coolant temperature and the power profile at the same height. nTF underestimates the Doppler temperature for the whole core height. The maximum difference is 12 K and the RMS 7.7 K, which accounts to about 20 pcm difference in terms of eigenvalue. The shape of the profile is following the power difference. The discrepancy can be attributed to the different material properties (see Section 4.3.1.2). CTF is applying higher fuel thermal conductivity than SCF for high temperatures. In addition, the calculation of the Doppler temperature by the two coupled code systems with a different “center” temperature should have an impact on the profile. Nonetheless, it should not be significant. These assumptions are tested in Section 4.3.2.1.

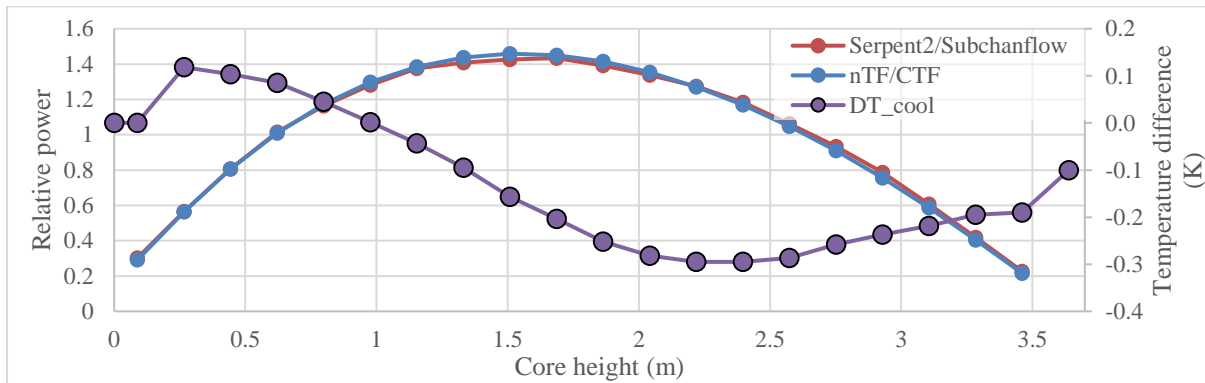


Figure 4.14. Axial relative power profile of both codes and absolute coolant temperature difference between nTF/CTF and Serpent2/SCF as a function of height

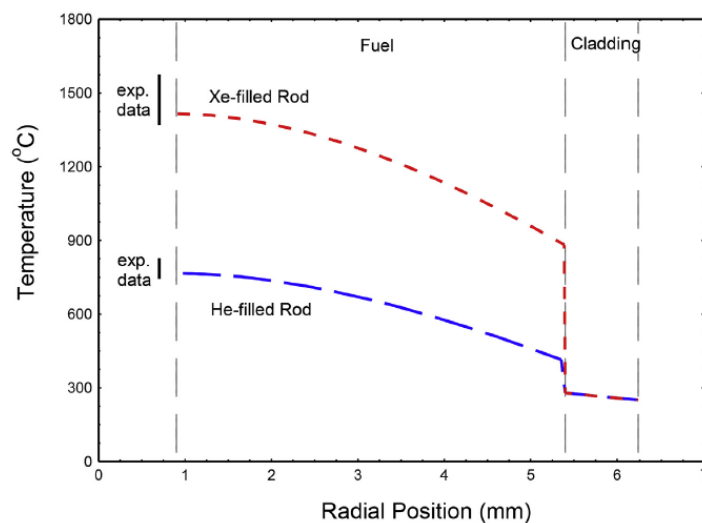


Figure 4.15. Typical radial temperature distribution in a LWR fuel rod measured experimentally [120]

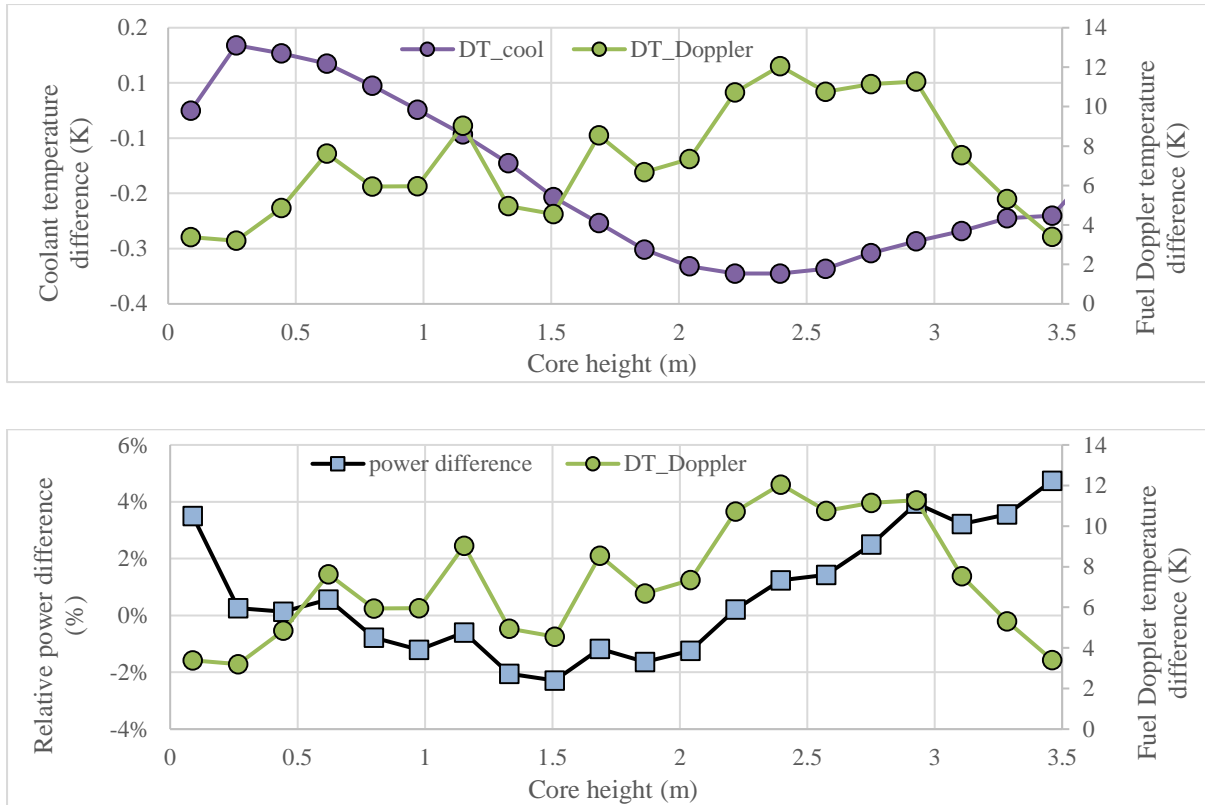


Figure 4.16. Absolute coolant temperature difference and absolute fuel Doppler temperature difference (top) and relative axial power difference and absolute fuel Doppler temperature difference (bottom) between nTF/CTF and Serpent2/SCF as a function of height

One major advantage of nTF/CTF is its capability for sub-pin predictions, whereas coupled code systems based on Monte Carlo codes, like Serpent2/SCF, are limited to pin-wise coupling (due to the enormous computational cost of obtaining statistically converged power estimates within the fuel rod). SCF, like CTF, is calculating the temperature profile for each pin, even though the T/H feedback provided for the Serpent2 neutronic calculation is a pin-wise distribution of fuel temperature (Doppler). In order to study the performance of nTF/CTF for sub-pin predictions, the fuel temperature at the center (innermost node center) and outer surface of a selected pin is compared with the inner and outer surface temperature of the same pin as predicted by Serpent2/SCF. The selected pin experiences zero axially averaged pin power difference in the comparison presented in Fig. 4.11. This selection ensures that the two coupled code systems are compared only in terms of sub-pin temperature predictions, removing other causes of discrepancy. Fig. 4.17 presents the absolute temperature difference, $[\text{Fuel.Tem.}_{\text{Serpent2/SCF}} - \text{Fuel.Tem.}_{\text{nTF/CTF}}]$, between the coupled code systems and the location of the selected pin in the core. The average over the height uncertainty (1σ) is 0.9 K for the outer surface temperature of the pin and 4.7 K for the inner surface temperature. The maximum difference of the fuel surface temperature is -7.1 K and the RMS is 3.9 K, which shows good

agreement of the two code systems. The maximum difference of the center temperature is 62.2 K and the RMS is 38.5 K. Similarly to the core average Doppler temperature (see Fig. 4.16), nTF/CTF underestimates the center temperature for the whole height of the pin. The difference is lower at the bottom and the top of the core where the power is lower (and the surface temperature difference is also low). This can be attributed to the different material properties.

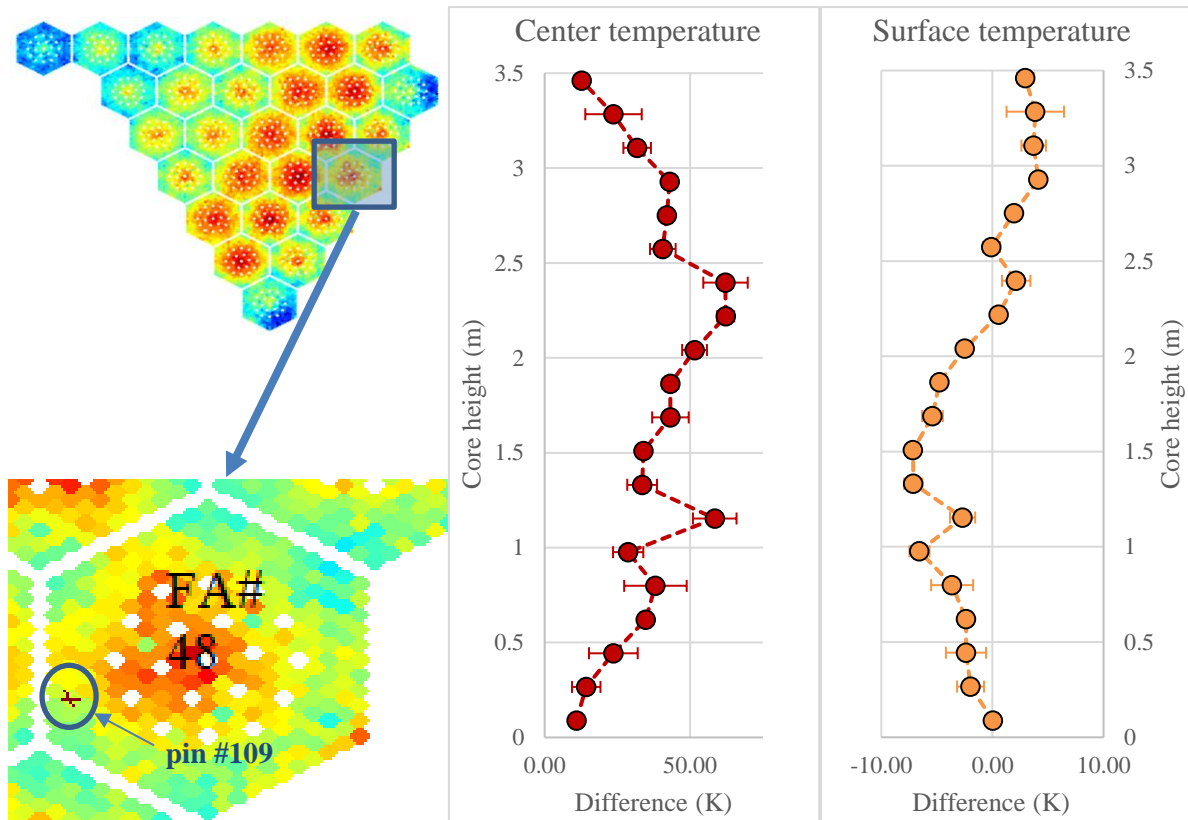


Figure 4.17. Location of the selected pin in the core (left). Absolute center and surface temperature difference between nTF/CTF and Serpent2/SCF for the selected pin (right)

4.3.2.1 Comparison of the nTF/CTF X2 model with Serpent2/SCF with the same material properties

In order to study further the discrepancies that are observed in the comparison of nTF/CTF with Serpent2/SCF for the X2 HFP full core model, the same case is simulated by the novel LRT core solver using the SCF material properties (see Section 4.3.1.2). The fuel and cladding heat capacity and thermal conductivity are inputted in CTF as functions of temperature. Fig. 4.18 illustrates the axial power profiles of nTF/CTF and Serpent2/SCF together with their relative difference, $[(\text{Pow}_{\text{Serpent2/SCF}} - \text{Pow}_{\text{nTF/CTF}}) / \text{Pow}_{\text{Serpent2/SCF}}]$, as a function of height. Fig. 4.19 presents the axial profiles of the radially averaged Doppler temperature, together with

their absolute difference, $[\text{Fuel.Tem.}_{\text{Serpent2/SCF}} - \text{Fuel.Tem.}_{\text{nTF/CTF}}]$, as a function of height. In both figures, the corresponding difference curves from the calculation with the CTF material properties are also included (see Fig. 4.12 & Fig. 4.16).

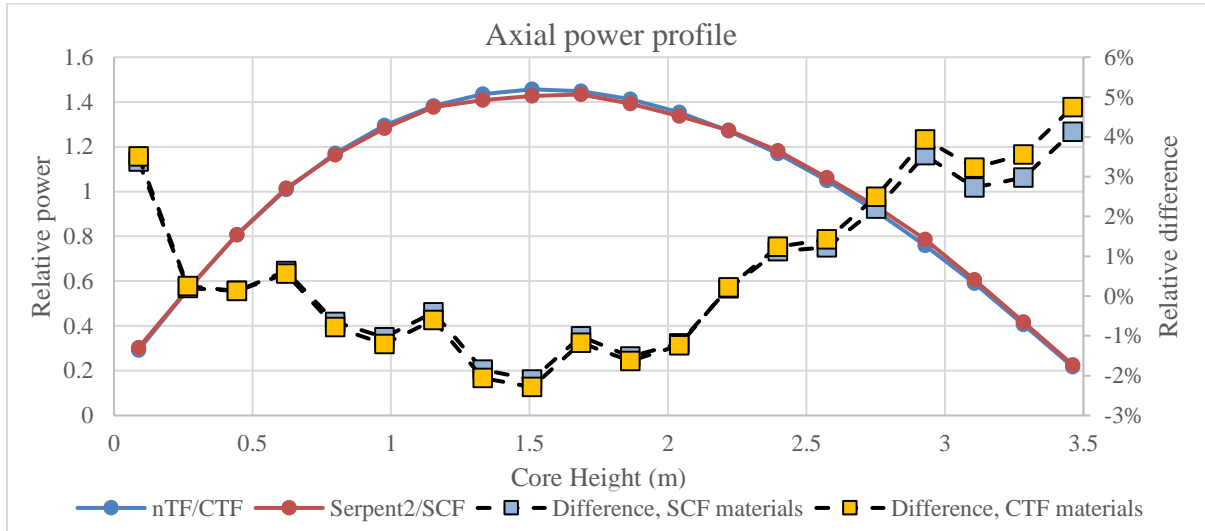


Figure 4.18. Axial relative power profile its relative difference between nTF/CTF and Serpent2/SCF for the X2 HFP state with SCF & CTF material properties

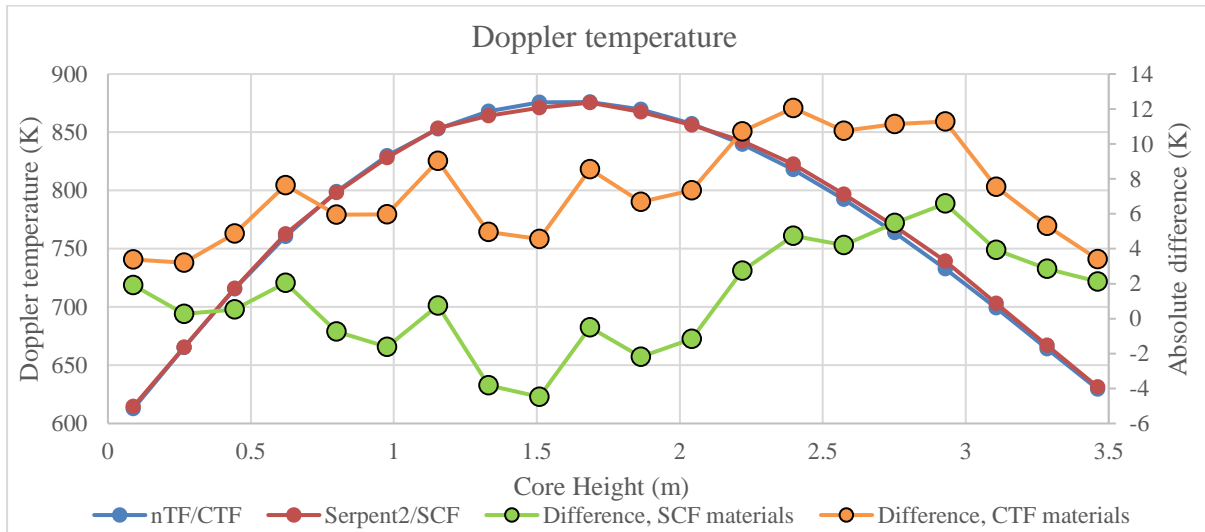


Figure 4.19. Axial Doppler temperature profile and its absolute difference between nTF/CTF and Serpent2/SCF for the X2 HFP state with SCF & CTF material properties

By examining Fig. 4.18 & Fig. 4.19, it becomes apparent that the use of the SCF material properties in nTF/CTF is improving the agreement of the coupled code systems, especially for the fuel temperature. The difference of the calculated critical boron, $[\text{BC}_{\text{Serpent2/SCF}} - \text{BC}_{\text{nTF/CTF}}]$, is 1 ppm. The maximum relative difference at the top of the core is decreased from 4.7% to 4.1% and the RMS from 2.2% to 2.0%. nTF/CTF is still predicting the peak power in a lower

height than Serpent2/SCF. The pin power difference remains at the same levels (max < 3%, RMS equals 0.8%). The agreement of the axial profile of the coolant temperature is also slightly improved, with the maximum temperature difference dropping at 0.27 K. The change in the material properties does not have such a big impact on the other results as it has for the fuel temperature. The maximum difference of the radially averaged Doppler temperature is reduced to -6.6 K from 12.1 K and the RMS to 3.2 K from 7.7 K. In Fig. 4.19, the evolution of the Doppler temperature difference as a function of height, for the solution with the SCF material properties in CTF, is almost identical to the corresponding power profile difference. nTF/CTF overestimates and underestimates the fuel temperature, in comparison to Serpent2/SCF, for the same axial nodes where it overestimates and underestimates the power. The good agreement of the fuel temperature when SCF material properties are used by nTF/CTF, also verifies the assumption that the calculation of the center temperature in different locations of the inner fuel node for each pin by nTF/CTF (center of inner node) and Serpent2/SCF (inner surface) has not a significant effect in the solution. This analysis confirms also the conclusions drawn when comparing the fuel temperature in the selected fuel pin (see Fig. 4.17), stating that the difference is caused by inconsistent material properties.

4.3.2.2 Comparison of the nTF/CTF X2 model with Serpent2/SCF with Doppler fuel temperature feedback in both coupled code systems

The X2 HFP state is also simulated with nTF/CTF using a pin-wise fuel temperature distribution as feedback, like Serpent2/SCF, instead of a temperature profile for each pin. CTF is providing the temperature of the outer fuel surface and the temperature at the center of the innermost radial node for each pin to nTF. nTF is calculating the Doppler temperature for each pin and uses it to all the FXRs of the pin. The agreement of the two coupled code systems is deteriorating. The axial power profile of nTF/CTF becomes more peaked, diverging further from the Serpent2/SCF solution. The maximum difference at the top of the core is increasing to 6.8% and the RMS to 3.1%. The boron difference is also increasing to -17 ppm. The discrepancies of the coolant temperature increase (maximum difference is 0.37 K). This can be attributed to the fact that nTF is built to calculate cross-sections with fuel temperature profiles for HFP simulations (see Section 2.3.1) and not the Doppler temperature of the fuel pin.

The outcome of this work verifies the novel LRT core solver for full core multi-physics calculations. Despite the approximations used in the neutronic and T/H model, nTF/CTF

presents very good agreement with Serpent2/SCF. Further study is required to better understand some biases in the results, which was not conducted during this PhD, since the biggest part of the available time was dedicated to the development of the novel coupled code system. The verification of the models for VVER HFP analysis is the first step for the application of nTF/CTF to multi-physics cycle analysis.

4.4 Comparison of the nTF/CTF core solver with the nTF/1D-TH multi-physics tool

The next step in this work is the comparison of the coupled code system nTF/CTF vs the capacity of nTF as a multi-physics tool with its embedded 1D simplified T/H solver. The purpose is to examine if a multi-physics tool, consisting of a high-resolution neutronic code and a simplified T/H solver, is adequate to predict accurately global and local parameters for a full core, where the neutronic phenomena are dominating the core behavior and the T/H analysis involves single phase mostly upward flow (pressurized water). During the development of the LRT core solver, the 1D-TH tool of nTRACER is also extended to model VVER assemblies, including GTs and the axial reflector. In nTF, the moderator temperature in GT channels and in the water gap is defined as the average moderator temperature of the assembly (energy conservation). The temperature of the channels in the top reflector is the outlet temperature of the last active layer for each channel. All geometry relevant parameters, like the hydraulic diameter or the wetted perimeter, are extended to hexagonal geometries. Finally, the hole in the fuel pin is also taken into account. Initially, the two multi-physics solvers are compared for small configurations, in order to quantify the impact of the key approximations involved in the simplified 1D-TH solver, and subsequently, they are tested with a real VVER-1000, namely the HFP state of the X2 benchmark.

4.4.1 Mini-core models

For this study, a cluster of seven VVER-1000 assemblies is modeled with vacuum radial boundary conditions. The axial structure of the cluster and all operating conditions are the same as the X2 HFP model, except for the power, which was set to 50% to avoid the possibility of coolant boiling in the cluster (*Case 0*). This configuration is chosen since it maintains the geometry of the X2 model axially and simplifies the radial heterogeneity of the core, removing also the effect of the heavy reflector. The difference of the cluster axial power profile as predicted by both multi-physics tools is illustrated in Fig. 4.20 and the difference of coolant

temperature in Fig. 4.21. Fig. 4.22 presents the map of the axially averaged pin power difference between nTF/CTF and nTF/1D-TH. It must be pointed out that CTF takes into account the pressure matrix distribution for the calculation of water properties, whereas 1D-TH calculates all water properties at the core exit pressure. It must be also noted that the steam tables used by the two solvers are not consistent. nTF/CTF predicts the power peak lower in core height than nTF/1D-TH. In general, nTF/CTF is predicting higher power at the lower half of the core for approximately the first 2 m of the core height. The maximum power difference for the axial profile is ~13% and the RMS reaches 7.4%. Similarly, the maximum coolant temperature difference is ~1.4 K and the RMS ~0.9 K. In Fig. 4.22, nTF/CTF seems to predict a flatter power profile within each assembly. The maximum pin power difference is 0.74% and the RMS reaches 0.27%. Several tests are performed, the results of which are presented below.

- ✓ Case 1: The first step is to set the power to 0% (HZP with TH feedback) to verify that there are no major coding errors in the solvers and test if the water properties table differs significantly between nTF and CTF. The comparison of the relevant power distribution results in very low discrepancies (max 0.1%), which follow the same axial trend as *Case 0*. These differences can be attributed to the small pressure difference in the coolant between the top and bottom of the core (0.3 bar), taken into account in CTF.
- ✓ Case 2: The axial reflector is removed from the model to examine if the T/H model cannot reproduce its effect accurately. However, the discrepancies are not reduced.
- ✓ Case 3: The linear heat rate in both models is assigned a constant value, in order to verify that energy is preserved in both systems. The difference of the coolant temperature at the top of the active core is ~0 K, which verifies the methods used for the definition of the water gap and, in the case of the 1D-TH, GT water properties. When a reflector is added, the difference is no longer 0 at the top of the core, since CTF is modeling axial conduction in the reflector whereas 1D-TH is not (1D-TH overestimates the temperature at the last active node by 0.03 K).
- ✓ Case 4: In order to test the effect of radial coolant mixing, the inter-channel connections (gaps) (see Section 2.4.2) are removed from the CTF model. The relative difference for the axial power profile is presented also in Fig. 4.20. It is apparent that the results have better agreement, with the maximum power difference being reduced to ~10.5% with an RMS of ~6%. More importantly, the maximum coolant temperature difference decreases to 0.75 K with an RMS of 0.4 K (see Fig. 4.21). Fig. 4.22 presents the map of the axially averaged pin power difference between the two solvers also for this case. The maps of the pin power

difference with and without mixing are built with the same color scale. The discrepancies of the power profile are decreasing when mixing is not taken into account in CTF. The maximum difference drops to 0.35% and the RMS to 0.17%. The discrepancies in the pin power are not significant with or without the coolant mixing. Nonetheless, it can be assumed that in the full core, where there is stronger radial heterogeneity, the effect of the coolant mixing will be stronger. However, cross-flow is not the only source of discrepancies. The outer layer of pins in the assemblies experiences larger differences in comparison to their neighboring pins. This can be attributed to the method used by 1D-TH for the calculation of the inter-assembly gap temperature. Normally, the temperature of the inter-assembly gap is lower than the average assembly temperature that 1D-TH is using. This means that the moderator density in the nTF/CTF calculations is higher in the gap, resulting in a better moderation and a higher power for the border pins of the assembly. In order to examine this hypothesis, the difference of the pin coolant temperature for the middle of the core as calculated by nTF/CTF, with CTF not taking mixing into account, and nTF/1D-TH is presented in Fig. 4.23. nTF/1D-TH overestimates the temperature for all the pins at the borders of the assemblies. In addition, the temperatures of the GTs, which in 1D-TH are also assigned the average assembly temperature, present high discrepancies. Finally, there is a tilt in the difference, with nTF/CTF predicting higher coolant temperature towards the center. This can be attributed to the approach used by 1D-TH for mass flow distribution, where the total mass flow of the assembly, including gap cells and GTs, is subdivided among the fuel rods for the solution of the 1D energy balance equation in each fuel pin, to ensure energy conservation. Hence, the mass flow of the pin in 1D-TH is slightly larger than in CTF, resulting in lower coolant temperature. The temperature tilt results in nTF/CTF still predicting a flatter power profile when cross-flow is not taken into account.

- ✓ Case 5: Different material properties are employed in CTF and in the nTF 1D-TH solver for the fuel and cladding heat capacity and thermal conductivity [*private communication with SNU*]. In order to test their effect, a single pincell configuration is simulated (average pin power of a VVER-1000) using the nTF/CTF coupled system, but this time with the fuel temperature feedback provided by the fuel conduction model in nTF. Fig. 4.24 illustrates the pin temperature profile as it is calculated by CTF and the nTF conduction model, where the gap temperature is exactly the same. The fuel temperature profiles are diverging increasingly, reaching a maximum difference of 10 K at the center of the pin. This difference is not significant, nonetheless it can be amplified in pins with higher power.

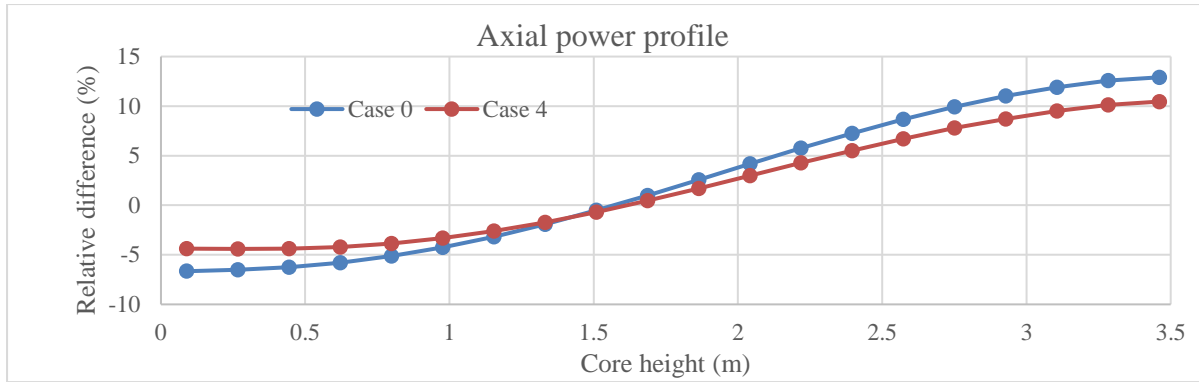


Figure 4.20. Relative difference of the axial power profile, $[(\text{Pow}_{\text{nTF/1D-TH}} - \text{Pow}_{\text{nTF/CTF}}) / \text{Pow}_{\text{nTF/1D-TH}}]$, between nTF/CTF and nTF/1D-TH for Case 0 & Case 4

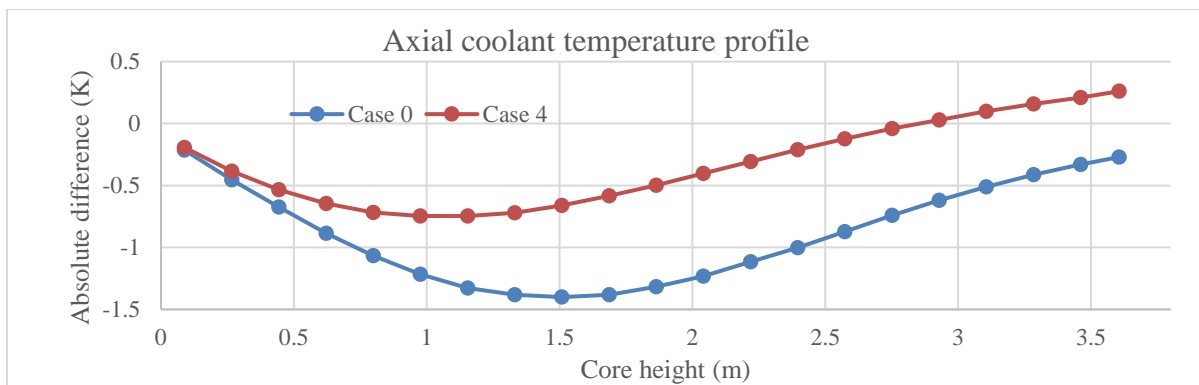


Figure 4.21. Absolute difference of the coolant temperature, $[\text{Cool.Tem}_{\text{nTF/1D-TH}} - \text{Cool.Tem}_{\text{nTF/CTF}}]$, between nTF/CTF and nTF/1D-TH for Case 0 & Case 4

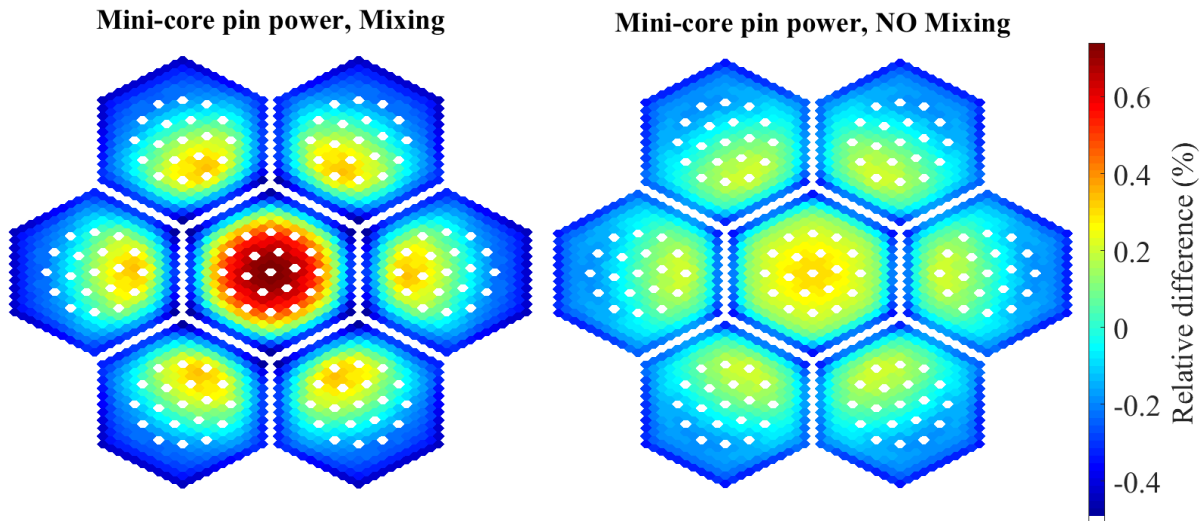


Figure 4.22. Relative difference of the pin power profile, $[(\text{Pow}_{\text{nTF/1D-TH}} - \text{Pow}_{\text{nTF/CTF}}) / \text{Pow}_{\text{nTF/1D-TH}}]$, between nTF/CTF and nTF/1D-TH for Case 0 & Case 4

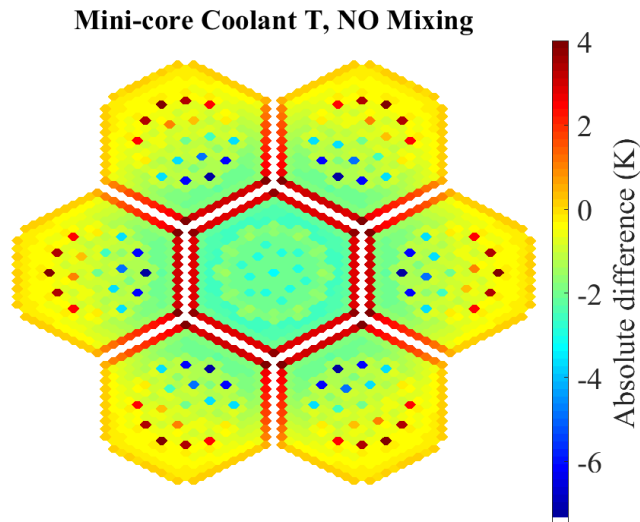


Figure 4.23. Absolute difference of the pin-wise coolant temperature at the mid-height of the mini-core, $[\text{Cool.Tem}_{\text{nTF/1D-TH}} - \text{Cool.Tem}_{\text{nTF/CTF}}]$, between nTF/CTF and nTF/1D-TH for *Case 4*

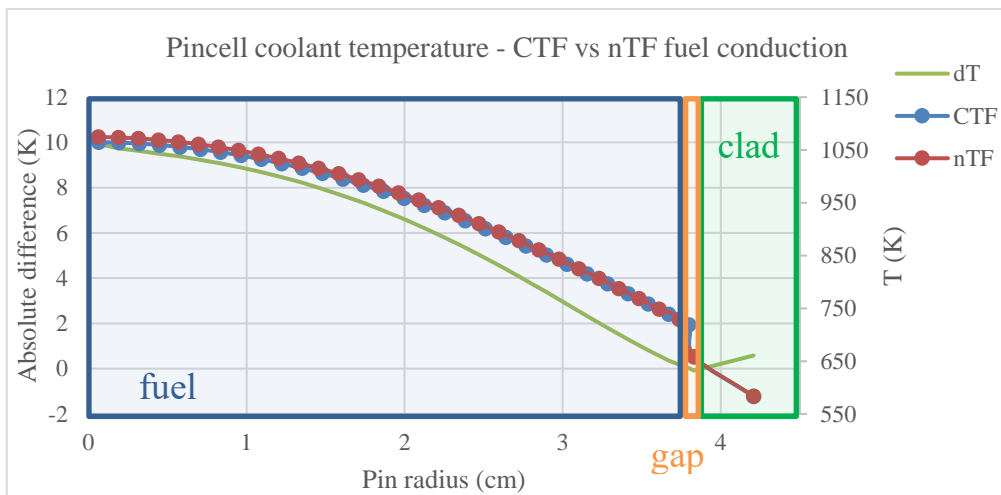


Figure 4.24. Temperature profile of a pincell calculated by CTF and the nTF fuel conduction model, starting with the same fuel gap temperature

4.4.2 VVER-1000 full core comparison

The comparison of nTF/CTF vs nTF/1D-TH for small configurations unveiled significant discrepancies. It is beneficial to extend this work to full core models, in order to study the capacity of the multi-physics tool with the simplified solver for real-sized geometries. To that end, the X2 HFP state is simulated by nTF/CTF and nTF/1D-TH. The core inlet temperature is 287 °C and the outlet pressure 157 bar. The total power produced is 3000 MW and the coolant flow in the active core is 109.8 kg/s per assembly. Both multi-physics tools perform a critical boron search for these operating conditions. CTF takes into account the pressure distribution for the calculation of water properties, whereas 1D-TH calculates all water properties at the

exit pressure. Both calculations are performed with the less memory, more time consuming Group Major scheme (see Section 2.3.2.1). Fig. 4.25 presents the relative difference of the axially averaged pin power distribution for 1/6th of the core, $[(\text{Pow}_{\text{nTF/1D-TH}} - \text{Pow}_{\text{nTF/CTF}}) / \text{Pow}_{\text{nTF/1D-TH}}]$. Fig. 4.26 illustrates the axial power profile for both calculation schemes and their relative difference.

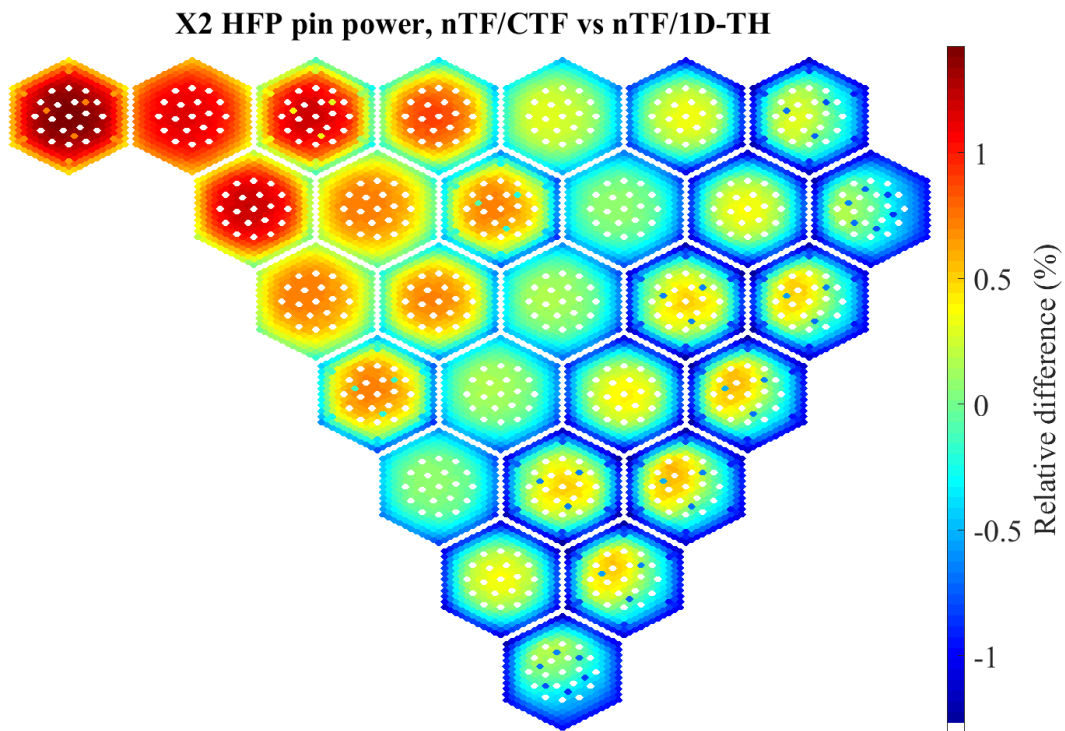


Figure 4.25. Relative pin power difference between nTF/CTF and nTF/1D-TH for the X2 HFP state

The difference of the calculated critical boron, $[\text{BC}_{\text{nTF/1D-TH}} - \text{BC}_{\text{nTF/CTF}}]$, is -21 ppm. This value translates roughly to 210 pcm of eigenvalue difference, which is significant considering the neutronic solver is the same in both calculation schemes. The maximum pin power difference does not exceed 1.3% and the RMS equals 0.6%. Nonetheless, the effect of 2D mixing in CTF and 1D-TH assigning the average assembly coolant temperature to the inter-assembly gap is apparent in the pin power map, since the nTF/CTF solver seems to predict a flatter power profile within each assembly, in accordance with the observations of Section 4.4.1. There is also a tilt in the power difference, similar to what is observed in Fig 4.22, with nTF/1D-TH generally overestimating the power in the center of the core, which can be attributed partially to the inter-assembly mixing of CTF and to the distribution of the total assembly mass flow among fuel pins in 1D-TH (see Section 4.4.1).

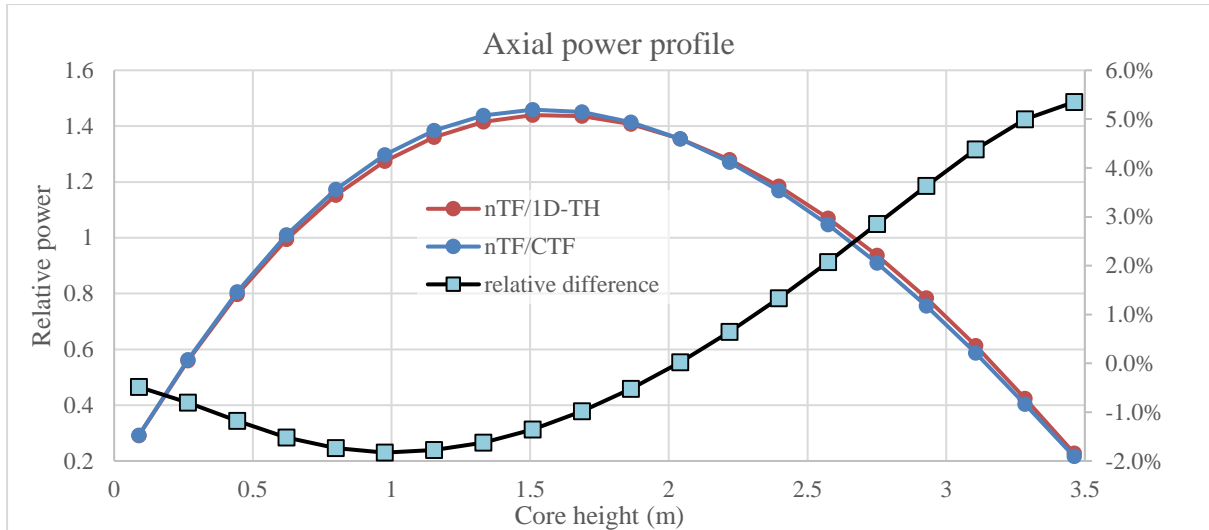


Figure 4.26. Axial relative power profile and its relative difference between nTF/CTF and nTF/1D-TH for the X2 HFP state

Despite the low pin power difference, the axial power profile shows higher discrepancies (maximum ~5.3% at the top and RMS equals 2%). nTF/CTF predicts the power peak lower in core height than nTF/1D-TH, similarly to Section 4.4.1. In order to examine the axial evolution of the core power map, Fig. 4.27 illustrates the relative power difference for each assembly of the 1/6th core as a function of height, together with the relative difference of the axial profile at the same height. In addition, the radial profiles of the assembly power difference at the bottom and top of the core are illustrated. The relative difference for the assembly power reaches 2% close to the bottom of the core, which is higher than the maximum difference for the axially averaged pin power; however, it remains in acceptable levels. It is apparent on Fig. 4.27 that the sign of the difference and the direction of the tilt is changing with the height, following the change in the axial power profile. Thus, the discrepancy for the pin power is compensated when averaging the power axially.

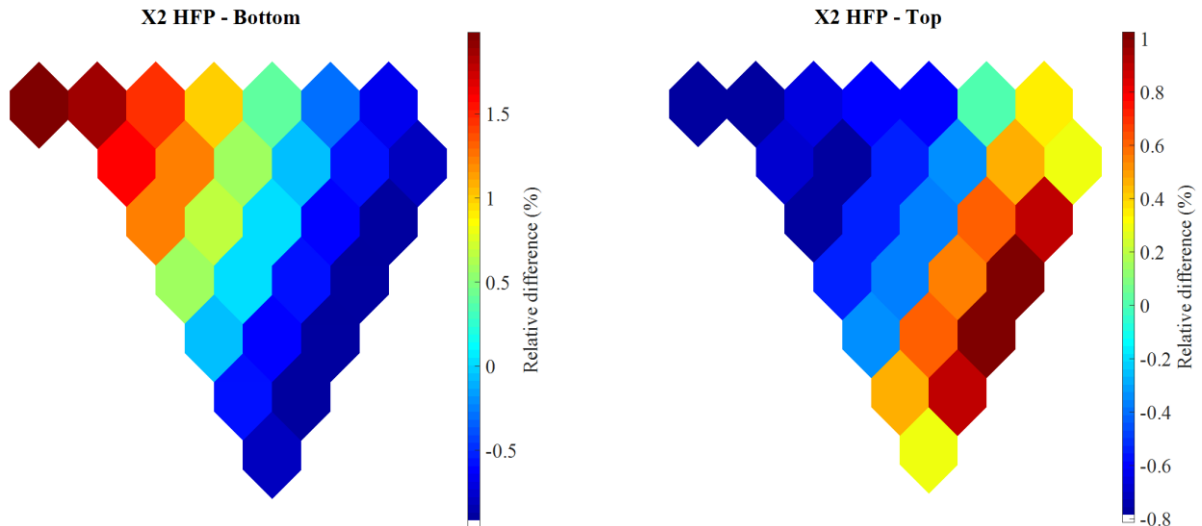
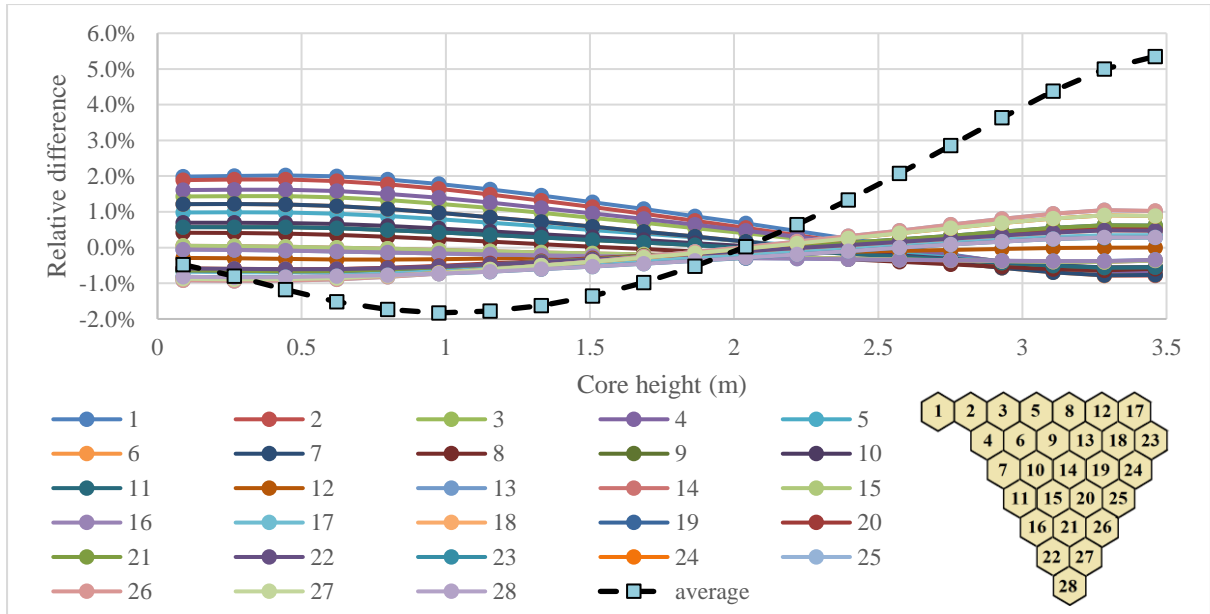


Figure 4.27. Relative assembly power difference between nTF/CTF and nTF/1D-TH vs core height and relative difference of the axial power profile at the same level.

Before drawing any conclusions on the performance of the multi-physics solver with the simplified T/H tool, it is beneficial to also compare the temperature profiles of the two solvers, since the neutronic and T/H effects are intertwined for multi-physics calculations. Fig. 4.28 presents the difference in the coolant temperature, $[\text{Cool.Tem.}_{\text{nTF/1D-TH}} - \text{Cool.Tem.}_{\text{nTF/CTF}}]$, as a function of height, together with the axial power profile. The maximum temperature difference reaches ~ 1.5 K approximately at the height that the power profiles of the two solvers coincide. Such a discrepancy is significant for T/H analysis. After that point, the temperature difference decreases with height as the nTF/1D-TH power profile overtakes the nTF/CTF axial relative power. At the top of the core, the temperature difference is not 0 K due to the presence

of the heavy reflector, as it was observed also for *Case 3* in Section 4.4.1. Fig. 4.29 presents the difference in the coolant temperature as a function of height together with the difference of the volume-averaged fuel temperature, $[\text{Fuel.Tem.}_{\text{nTF/1D-TH}} - \text{Fuel.Tem.}_{\text{nTF/CTF}}]$, for the same height. The maximum difference reaches ~ 96 K. The different material properties used in the two multi-physics solvers are partially responsible for the overestimation of the fuel temperature by nTF/1D-TH (see Fig. 4.24). The shape of the profile is a combination of the power difference and the coolant temperature difference since all these quantities are codependent.

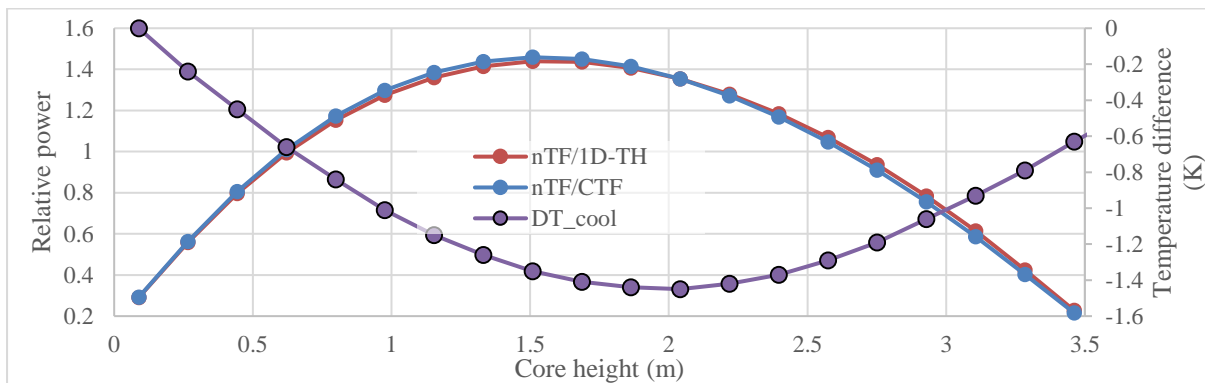


Figure 4.28. Axial relative power profile of both codes as a function of height and absolute coolant temperature difference between nTF/CTF and nTF/1D-TH.

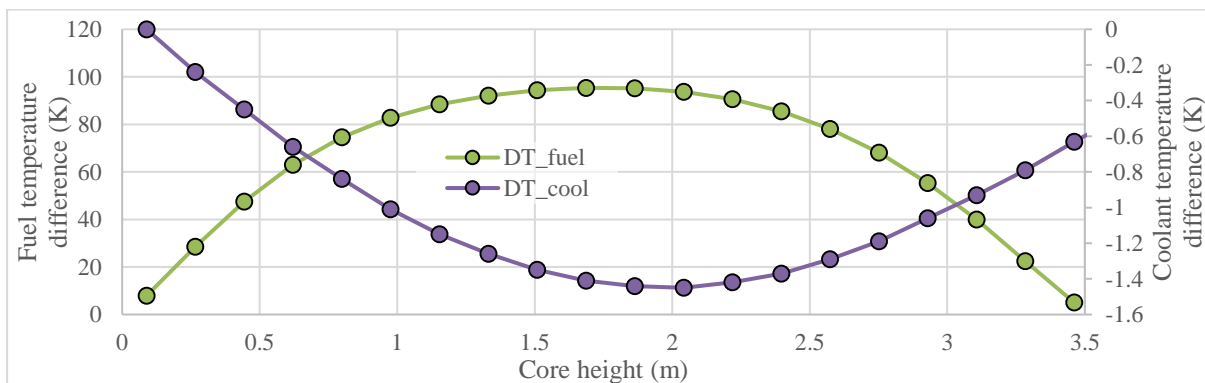


Figure 4.29. Absolute coolant temperature difference and absolute volume-averaged fuel temperature difference between nTF/CTF and nTF/1D-TH as a function of height.

The discrepancies observed in the power and temperature profiles between the two solvers are caused by the different methods used for the calculation of the T/H feedback and the material properties. The simplified 1D-TH solver does not prove as efficient as CTF in the modeling of the HFP full core. It must be pointed out, that the calculation scheme of the 1D-TH

solver can be improved (e.g. the distribution of mass flow in fuel pins). However, with the current state of the solver several trends emerge in the power and temperature comparison that lead to significant discrepancies (e.g. max 1.5 K coolant temperature difference), or compensate discrepancies, hiding the real magnitude of the difference (e.g. pin power). The computational cost of the 1D-TH solver is insignificant in comparison to CTF (< 1%). Nonetheless, given that in comparison to the neutronic calculation CTF consumes a small part of the resources (16% of calculation time & < 5% of the memory), the use of the sub-channel solver is the best choice for full core VVER analysis.

4.5 Multi-physics analysis with the conventional approach

In this study, as it is explained in Chapter 1, the conventional neutronic code system CASMO5-VVER/PARCS is not used coupled to an external T/H solver. The simplified internal 1D T/H solver of PARCS is considered sufficient to simulate the T/H feedback of the VVER-1000 core for HFP steady state and cycle analysis. Nonetheless, in order to quantify possible discrepancies due to the use of the simplified T/H solver, the X2 HFP state is simulated with CASMO5-VVER/PARCS and compared with the reference Serpent2/SCF solution. The models used for the cross-section generation in CASMO5-VVER and PARCS are the same as for the HZP case with corner stiffeners (see Fig. 3.28 B), updated for the HFP operating conditions. Both multi-physics tools perform a critical boron search for these operating conditions. Fig. 4.30 presents the relative difference of the normalized assembly power profile, $[(\text{Nor.POW}_{\text{Serpent2/SCF}} - \text{Nor.POW}_{\text{PARCS/1D-TH}}) / \text{Nor.POW}_{\text{Serpent2/SCF}}]$, between CASMO5-VVER/PARCS/1D-TH and the Serpent2/SCF solution for X2 HFP with corner stiffeners. At the same figure, the HZP comparison of CASMO5-VVER/PARCS vs the Serpent2 benchmark reference solution [98] is also presented. The relative difference color-bar is the same for both figures. Comparing the two plots, it is clear that the use of the simplified 1D T/H solver does not introduce any strong discrepancies in the solution. The maximum assembly power relative difference decreases from 3.2% for HZP to 2.9% for HFP. The RMS difference remains the same at 1%. The difference in boron concentration increases by 6 ppm. On the other hand, the maximum difference of the axial profile decreases to 3.7% from 6.7% and the RMS to 1.8% from 2.0%. The decrease of the maximum relative difference at the top of the core can be attributed to the fact that the X2 HFP model is unrodded, in contradiction to the HZP critical case (see Section 3.3.3).

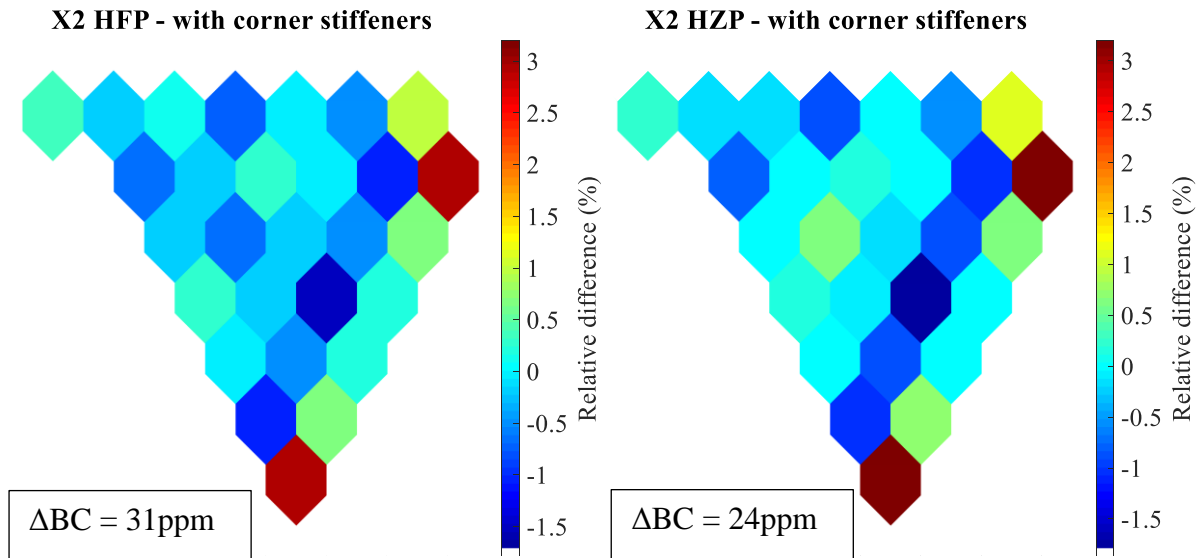


Figure 4.30. Relative difference of the assembly power and difference in BC between the CASMO5-VVER/PARCS X2 model with corner stiffeners and the reference solution for the HFP (left) and HZP (right) case.

The CASMO5-VVER/PARCS core solver seems to be adequate to predict global quantities for VVER-1000 analysis, even when the T/H feedback is provided by the simplified 1D T/H solver of PARCS.

4.6 Major Outcomes of the work presented in this chapter

- One of the biggest achievements of this thesis is the development of nTF/CTF for high-resolution coupled VVER full core calculations. As it was mentioned before, CTF has never been used for full core VVER simulations. nTF has also never been used with a T/H solver, internal or external, outside this work. The internal coupling of the two codes, even though it is partially based on existing subroutines, follows a completely different approach from what was attempted before for Cartesian geometry, allowing the introduction of sub-pin T/H fuel feedback by CTF. Most importantly though, the realization of multi-physics calculations with a sub-pin level resolution for 3D VVER full core analysis has not been done before (to the extent of the writer's knowledge).
- The CTF hexagonal pre-processor, embedded in nTF, is the only subprogram that can generate full core VVER models for CTF, besides the official CTF pre-processor, currently under development.

- HPC methods are required by both solvers (nTF and CTF), to achieve computationally intensive simulations, like VVER full core steady state analysis, in the available clusters at PSI. The novelty of the coupling methodology for the two solvers lays mainly in the double decomposition parallelization scheme, which minimizes the time and memory requirements of the multi-physics calculations; and allows fitting them in the Merlin6 cluster. It should be noted here, that such calculations are not possible on CSCS due to the memory requirements. It becomes clear that state-of-the-art HPC should be an integral part of all nuclear simulation tools, especially high-resolution solvers, since the time efficiency is a crucial factor for production and design calculations.
- nTF/CTF is verified with a coupled code system, Serpent2/SUBCHANFLOW, of similar accuracy but lower spatial resolution.
- nTF/CTF is also compared with nTF/1D-TH for the same full core model. The simplified 1D T/H solver of nTF introduces several significant biases in the solution, despite the relative simplicity of the T/H phenomena involved (single phase flow in steady state). These biases result in error cancellations (e.g. pin power) or in larger discrepancies (e.g. coolant temperature). The trends introduced by the 1D-TH solver in the X2 HFP model demonstrate that accurate multi-physics calculations cannot be achieved on a local scale unless both solvers employ equivalent levels of resolutions and approximations.
- Further proof of that are the results of the conventional computational route, which employs a simplified 1D T/H solver to simulate the same scenario as the high-resolution solver. The change in the discrepancies of the coarse mesh is minimal, in comparison to HZP results (Chapter 3). In the conventional LRT core solver, the use of a simplified 1D T/H solver is efficient, since the calculation is performed in the coarse mesh and the neutronic solution is also using a simplified approach.

Chapter 5

Multi-Physics Depletion Analysis

«Η δε μελέτη φύσεως αγαθά πλείονα δωρεΐται»

5.1 Objective

The major goal of this thesis is the development of a high-resolution high fidelity multi-physics core solver for cycle analysis of VVERs. The core solver that is illustrated in the previous chapters and is capable of steady state multi-physics high-resolution VVER simulations, is only part of the effort. The expansion of such a solver to cycle calculations presents further challenges, which are tackled in this chapter. As it was mentioned in Chapter 2, nTRACER includes depletion capabilities [121], [122], which have been verified for Cartesian geometries [45]. Besides the depletion solver used by the neutronic code, a cycle calculation requires the consecutive simulation of several state-points, or burnup (BU) steps, with varying operating conditions. The core solver should be able to adjust key parameters, like power level, according to the configuration of the new state-point, while retaining the information of local material composition and BU calculated in the previous step. This can be done on-the-fly or with restart files, performing each BU step as a separate calculation and storing the relevant information externally. Either method requires specific functionalities, like for example the variation of the flow level on-the-fly, which must be available in the neutronic and the thermal-hydraulic (T/H) code of the core solver. Additionally, when an internal coupling scheme is used, the master code should communicate all such variations to the slave code.

Besides, the capabilities of the codes the main difficulties in performing cycle analysis with high-resolution high fidelity multi-physics code systems are the computational requirements. As it was illustrated in previous chapters, full core VVER high-resolution

calculations are demanding in terms of computational resources and the parallelization scheme of the LRT core solver can operate only in specific configurations (one mpi task per computational node). Since a steady state calculation needs several hours for completion, cycle analysis can occupy the cluster for several days or weeks, depending on the number of burnup steps. On this aspect, the availability of the cluster is a deciding factor also on the method used for cycle analysis. When calculations are performed on-the-fly, the total time required for the cycle analysis can be shorter, since the code moves directly to one burnup step after another. However, the calculation cannot be interrupted until completion. This means that the computational resources required for cycle analysis will be unavailable to other users for a significant amount of time. Scientific servers like Merlin6 or CSCS do not allow multi-node calculations of the size of nTF/CTF for more than 24 hrs. On the other hand, when the solver uses restart files, the analysis is more flexible since the calculation can be interrupted between BU steps and continued at another point in time. Nonetheless, the total time required for such a calculation is larger when a restart file is used (see Section 5.2.2 & 5.4). Finally, the total amount of memory available is another parameter to be considered when high-resolution multi-physics tools are used for cycle analysis. The requirements of a depletion calculation are always higher in comparison to e.g. Hot Full Power (HFP) since more information needs to be stored for each FXR (more isotopes in material composition and BU information).

The issues illustrated in the previous paragraphs are studied and specific developments are made in the coupled code system to allow the simulation of the 1st cycle of the X2 benchmark. All the necessary modifications to the solver and the selected modeling options are discussed in detail, together with the results of the core solver, which are compared to experimental data. It must be pointed out that at this stage of the study, all comparisons refer to global parameters only (boron curve and assembly power). The reason is the lack of more high-resolution measurement data. Together with the high-resolution solver, also the conventional code system CASMO5-VVER/PARCS is employed for cycle analysis. The generation of the suitable cross-section matrix with a lattice code for depletion calculations requires additional parametrization with exposure (histories/trees) (see Section 2.5.1). The fact that the CASMO5-VVER built-in cross-section matrix is optimized to be used specifically with SIMULATE5 and not PARCS introduces additional complications. The steps required to simulate the 1st cycle of X2 with the conventional code system CASMO5-VVER/PARCS are described in detail and the results are compared to experimental data. Finally, one of the goals of this thesis is the comparison of the novel approach with the conventional tools used for analysis. In this chapter, the two coupled

code systems, CASMO5-VVER/PARCS and nTF/CTF, are compared in terms of accuracy for global parameters and computational requirements, in order to study the original assumption made in Chapter 1 that a high-resolution solver can be used as an audit tool for reactor analysis.

5.2 Cycle analysis with nTF/CTF

The depletion solver embedded in nTRACER can be used directly for hexagonal geometries, with few technical modifications, since the depletion calculation only depends on the geometry of the fuel pin and not the lattice. In addition, CTF is also equipped with models that take into account local BU in material properties and can simulate basic structural changes caused by depletion e.g. fuel swelling. In this work however, CTF is not taking into account the BU of the fuel rods, due to lack of time to develop the relevant data exchange subroutine that would inform CTF about the local BU of the nTF pincells. This issue should be addressed in the next stages of development of the LRT core solver. Similarly to previous chapters, the first step in extending the LRT core solver for cycle calculations is the assessment of the nTRACER depletion capability for small VVER configurations. Secondly, the cycle analysis calculation scheme of nTF/CTF is described together with all the relevant modifications to the code systems. The X2 nTF/CTF model for depletion calculations is presented as well, focusing on the approximations and modeling options which are necessary to achieve cycle analysis with the available computational resources. Finally, the outcome of the LRT core solver for the 1st cycle of X2 is compared with experimental data.

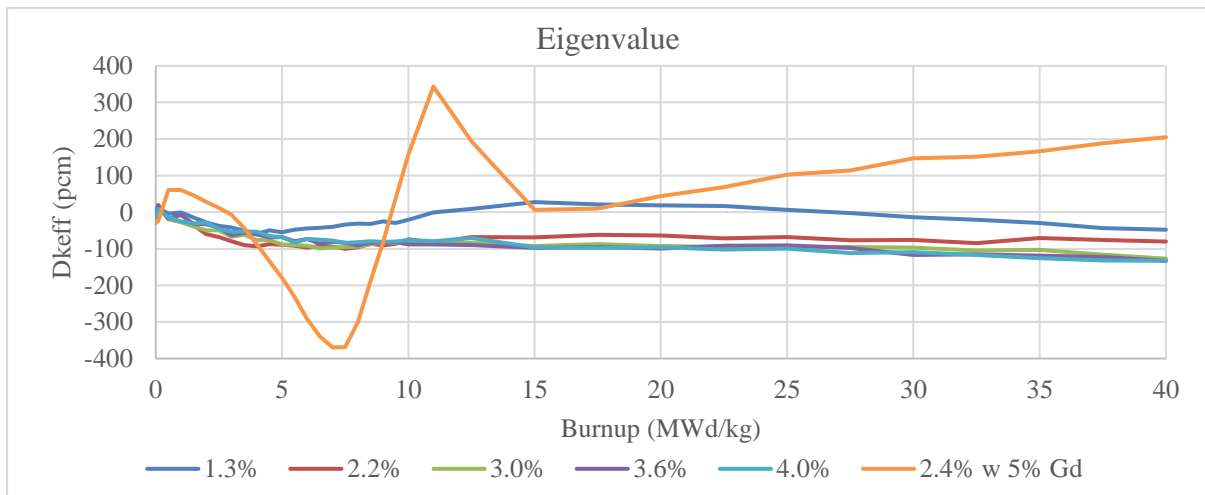
5.2.1 Assessment of the nTRACER depletion solver with Serpent2

In this section, nTRACER is used to simulate single 2D pincells of different enrichment from fresh fuel to 40 MWd/kg. The LCLRS machines are used. The results are compared with the outcome of Serpent2, which performed all calculations in CSCS. Normally in order to fully evaluate the nTRACER depletion library, the models should be depleted until ~70 MWd/kg (the BU at which LWR fuel is spent). Nonetheless, since the core exposure is around 13 MWd/kg at the end of the 1st cycle of X2 (with a maximum assembly-average burnup of 16.5 MWd/kg), this study focuses on a BU range that is relevant for the problem at hand. The geometry and variation of enrichment of the 2D pincells considered corresponds to the core loading of X2 for the 1st cycle of operation [98]. The fuel temperature is set to 900 K and all other elements at 600 K. All material compositions are defined according to the benchmark specifications, except of the moderator number density that is adjusted for 600 K. In order to

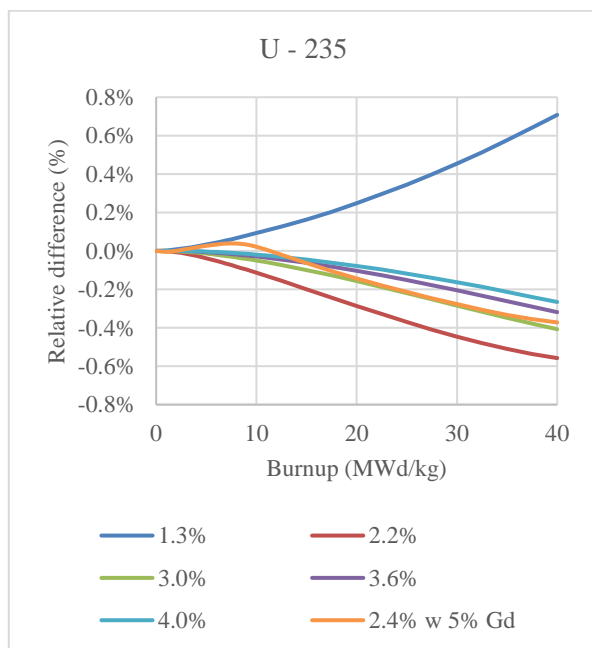
ensure flux level consistency between Serpent2 and nTF, the energy released per fission of key isotopes, e.g. U-235, Pu-239 and others, is defined in Serpent2 according to the values used in the nTRACER depletion library. The pincells are modeled with P2 scattering treatment in nTF. Fuel pins without Gd are sub-divided in 7 radial rings and Gd pins in 10 radial rings. Serpent2 is simulating 3,000 neutron batches \times 50,000 histories for every depletion step to achieve 1σ uncertainty of < 5 pcm. Fig. 5.1a presents the evolution of the eigenvalue difference between nTF and Serpent2, $[keff_{Serpent2} - keff_{nTF}]$, as a function of BU for different enrichments. Fig. 5.1b-e present the relative difference of the number density between nTF and Serpent2, $[(Num.Den._{Serpent2} - Num.Den._{nTF}) / Num.Den._{Serpent2}]$, for key isotopes as a function of BU.

Concerning the Gd pin, the difference in the eigenvalue reaches ~ 380 pcm, which is significant. The difference of the concentrations of Xe-135 and Sm-149 presents fluctuations, similarly with the eigenvalue difference. This signifies inconsistencies in the depletion of Gd. The concentrations of Pu-241 and U-235 present similar behavior as in the non-Gd pins. U-235 is overestimated by nTF, whereas Pu-241 presents good agreement with Serpnet2 as its concentration increases. Concerning the pincells without Gd, the evolution of the eigenvalue and isotope concentration is similar, except for the 1.3% enriched pin. For low BU, the eigenvalue difference between nTF and Serpent2 is smaller than 30 pcm and as exposure increases nTF overestimates keff by ~ 100 pcm for all pincells, except the one corresponding to the 1.3% enriched fuel. The isotopic density of Pu-241 is initially underestimated by nTF, when the concentration is very low, and gradually converges to 0%. The discrepancy of the isotopic concentration of U-235 is increasing with BU. All higher enrichment pins are overestimating U-235 concentration in nTF for higher exposures, whereas the 1.3% pin is underestimating it. The relative difference is significant at 40 MWd/kg. Concerning neutron absorbers, as Xe-135 concentration increases with BU, the difference for all higher enrichment pins is reaching $\sim -1\%$ at low exposure, Xe-135 being overestimated by nTF, and then drops to 0%. For the 1.3% pin, it converges to 0% for low BU and then increases to 1%. On the other hand, the concentration of Sm-149, another strong neutron absorber, is significantly underestimated in nTF, reaching $\sim 7\%$ at the end of the cycle. In order to get a better understanding of the results, more isotopes are compared for the 2.2% enrichment (see Fig. 5.2). The concentration of Pu-239 is compared between nTF and Serpent2. Serpent2 breeds more since the concentration of Pu-239 is increasingly larger in comparison to nTF. Nd-148 is also compared between the two codes. The concentration of Nd-148 is directly proportional to the number of fissions occurring [123]. Since the energy released per fission is

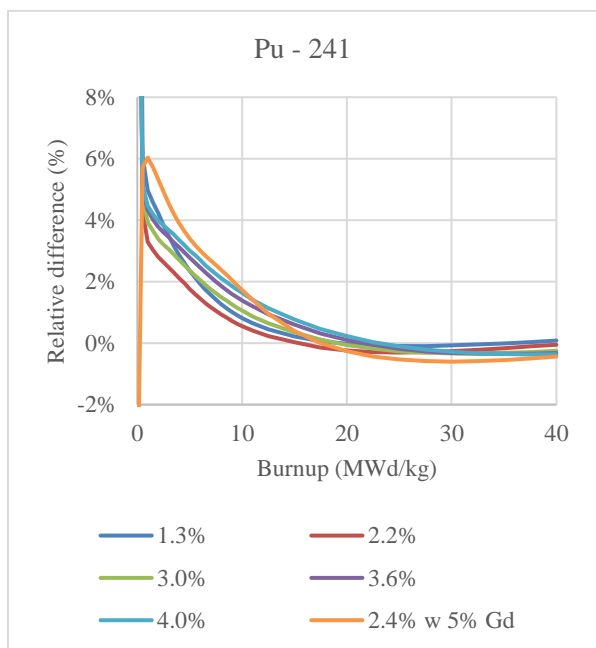
consistent in both codes, the divergence in the concentration of Nd-148, which at 40 MWd/kg reaches 1.6%, signifies that the production yield is different in the two codes. After communication with SNU, it was confirmed that there are differences in the depletion chain and production information of the nTRACER library in comparison to Serpent2, especially for Sm-149. A new depletion library is currently being produced in SNU with an updated depletion chain. Despite the discrepancies presented in Fig. 5.1 and Fig. 5.2, the eigenvalue difference for all pincells, except the Gd pin, remains within target accuracy throughout the cycle (see Section 2.7.3). Similar discrepancies of the eigenvalue are observed when the MOC code MPACT is compared with Serpent2 [124]. As such, it is reasonable to conclude that nTF can be used for cycle analysis.



(a)



(b)



(c)

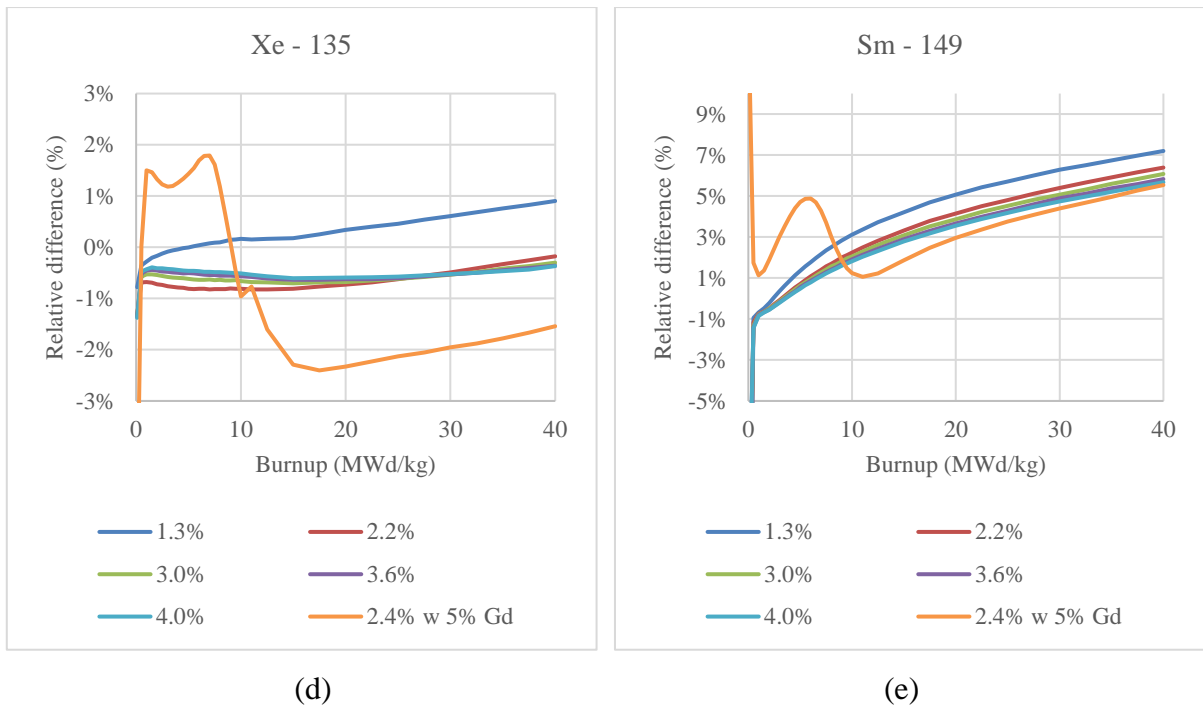


Figure 5.1. Eigenvalue difference (a) and relative difference of the number density of U-235 (b), Pu-241 (c), Xe-135 (d) and Sm-149 (e) between nTRACER and Serpent2 as a function of BU

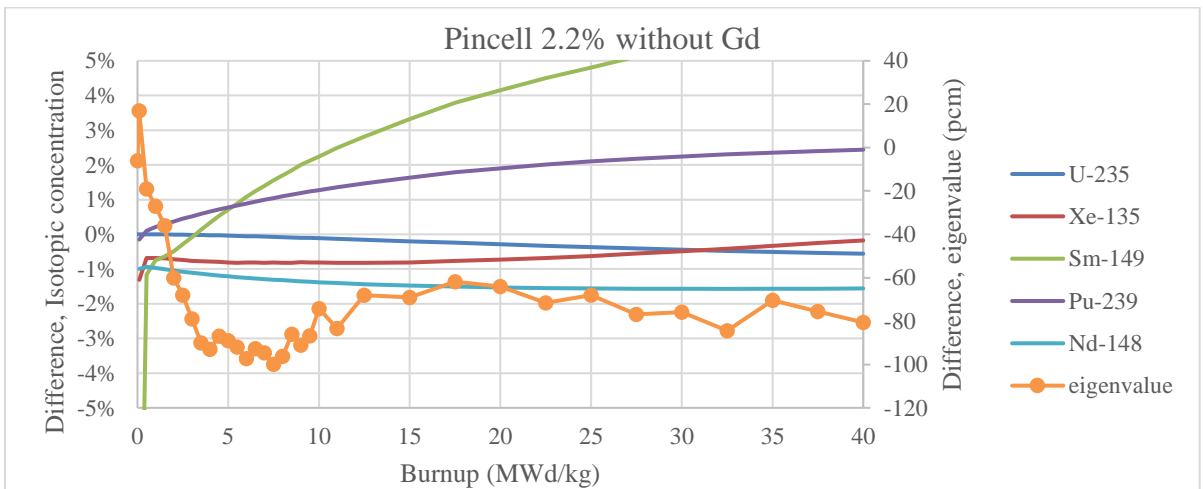


Figure 5.2. Eigenvalue difference and relative difference of the number density of important isotopes for the 2.2% pin between nTRACER and Serpent2 as a function of BU

5.2.2 nTF/CTF cycle analysis scheme

In order to use the LRT core solver for cycle analysis, a depletion calculation scheme needs to be developed, which optimizes the use of the available computational resources. Throughout this study, the LRT core solver is performing full core calculations on cluster Merlin6, since it is the only option that can cover the memory requirements (343 GB/node). Normally, Merlin6 cannot allow calculations the size of a VVER-1000 full core analysis to run for more than

24 hrs. Taking into account the time required even for a standalone nTF full core calculation (~4 hrs), 24 hrs are not enough to simulate a full operating cycle. In order to allow flexibility, the nTF/CTF cycle analysis scheme is based on the use of restart files. A single BU step (step k) can be simulated independently of the previous and next BU step, as long as a restart file is created after the completion of each BU step. In addition, the existence of restart files allows the simulation of the core condition between the original BU steps when that is necessary. A simulation that includes the use of restart files requires two state-point calculations per BU step. When the core solver is simulating burnup step k, the first state-point calculation is performed with the material composition of burnup step k-1 and the new operating conditions. Then, the second state-point calculation uses the resulting flux to deplete further the material composition to the designated exposure of step k, with the simplified predictor-corrector method (see Section 2.3.6). Fig. 5.3 presents the depletion calculation scheme of the LRT core solver. As it is described in Section 2.3.6, in the full predictor-corrector scheme, the corrector step is followed by a second transport calculation, with the averaged material composition of the predictor and the corrector. This step is omitted in the simplified predictor-corrector method. However, in the scheme presented in Fig. 5.3, the transport calculation with the averaged material properties of the predictor and the corrector of burnup step k-1 is actually performed as the first state-point of burnup step k, with the corresponding operating conditions. Thus, the depletion calculation scheme of the novel LRT core solver is functioning as a full predictor-corrector. In addition to the scheme presented in Fig. 5.3, the option for more than one BU steps to be executed on-the-fly sequentially in a single simulation (without restart files) is included in the coupled code system for models where the total depletion time is small, like assemblies or pincells (simplified predictor-corrector).

From a developer's point of view, the extension of the LRT core solver to cycle analysis required the addition of a capability to produce and use restart files in nTF. All necessary subroutines were available in nTRACER but for Cartesian geometries. Thus, it required only few modifications, e.g. print results according to the nTF format. However, other functions of the code system required a bigger effort. The necessary modifications to the code system are described in the following sections.

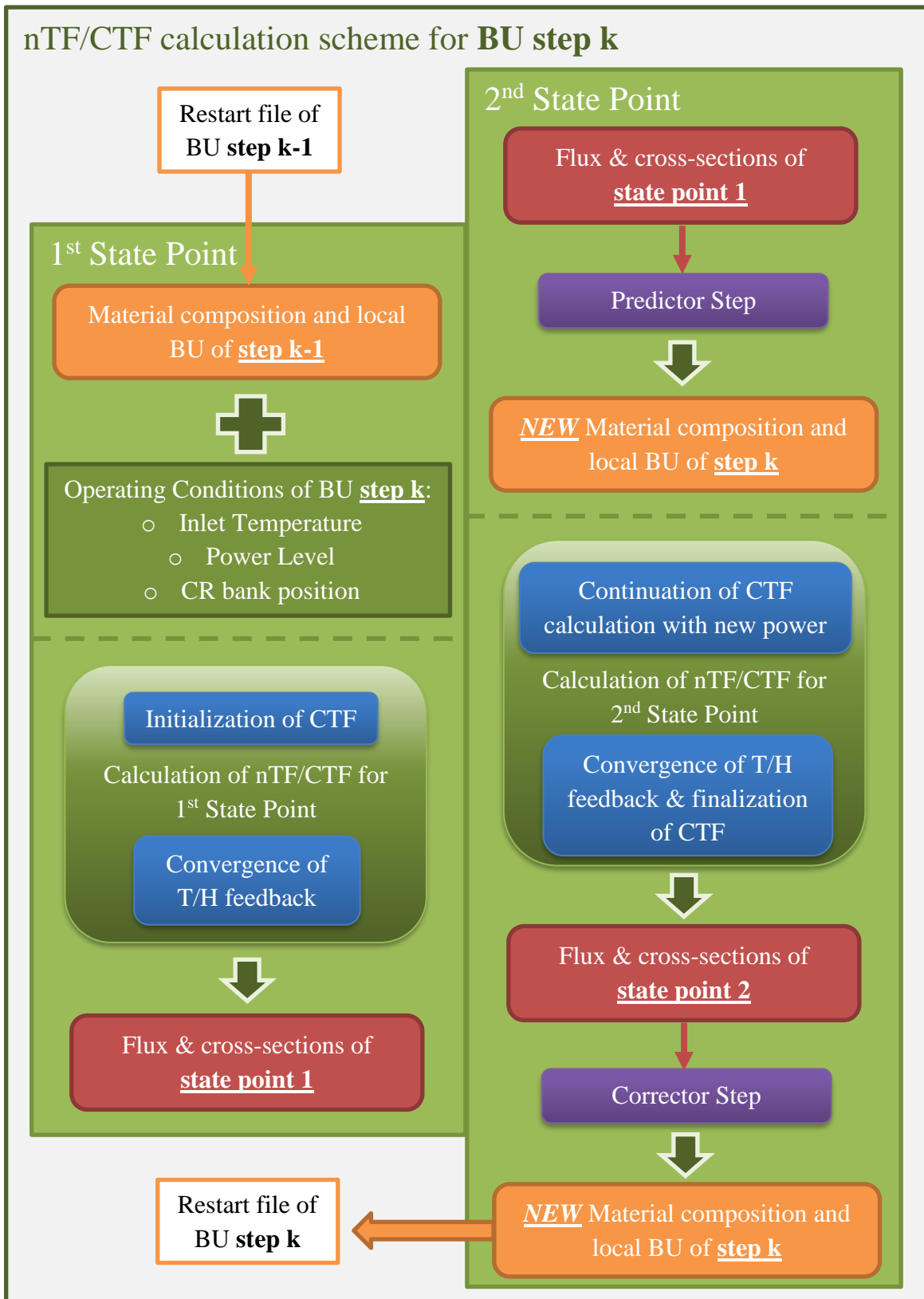


Figure 5.3. nTF/CTF depletion calculation scheme for BU step k

5.2.2.1 T/H feedback after the 1st state-point

In the HFP steady state calculation, CTF is finalized once the T/H solution is converged. Since nTF needs to perform two sequential calculations for each burnup step for full core models, CTF must be restarted for the second state-point. However, once CTF is finalized, all nTF functions related to computational resources distribution and initialization of the CTF executable would have to be repeated to restart CTF. This is time consuming. Another solution would be to not finalize CTF until the end of both state-points, introducing T/H feedback calculations before every MOC loop, even if the T/H solution is converged (see Fig. 4.2). However, this results in severe time penalties as additional CTF calculations, that are not required since the T/H solution is converged, can amount to hours of calculation time (see Section 4.2.1). In order to tackle this issue, a new input card is programmed in nTF that informs the modules handling CTF if depletion calculations are following and how many depletion state-points are simulated after the 1st state-point calculation (one for full core models, ≥ 1 for assembly or pincell models). Then, CTF is paused when the T/H solution is converged for one state-point and continues when the next state-point begins. This method simplifies the execution of the core solver since the resources are allocated once in the beginning of the calculation. It also decreases the total calculation time, since CTF begins the T/H feedback calculation of the second state-point with an informed initial guess, which is the T/H solution of the previous state-point. Given that for each BU step the power level, inlet temperature and mass flow are the same for both state-points, according to the scheme of Fig 5.3, CTF requires ~123 mins for the full core T/H solution of the 1st state-point and ~96 mins for the 2nd state-point.

5.2.2.2 Restart files for hexagonal geometry

nTRACER includes a subroutine that documents all necessary information for the FXRs of the neutronic model to an external file. The axial layers and assemblies are scanned sequentially from bottom to top and from left to right. For each pincell, the number of FXRs is catalogued and subsequently each FXR is described as fuel or non-fuel, depletable or not, in need or not of resonance treatment, containing or not Gd and finally moderator or non-moderator. In case an FXR is defined as fuel or depletable, the local BU, temperature and material composition is also included in the external file. The restart file is inputted in the next nTRACER calculation through an additional subroutine that can identify mismatches on the description of the FXRs in the file and the model of nTRACER. These subroutines were extended to hexagonal geometries. In nTF, the pincells are documented according to their

sequence in the global numbering scheme and not their position in the assembly. Currently, the flux cannot be stored in the restart files. If the scalar flux of the FSRs, contained in the FXR, and the angular flux at the boundary is available in the restart file, then the first state-point transport calculation of each burnup step (see Fig. 5.3) can be omitted. In that case, the nTF/CTF full core depletion scheme would become a series of simplified predictor-corrector calculations (see Section 2.3.6). Fig. 5.4 presents an example of the data stored in the restart file for a moderator FXR and a fuel FXR.

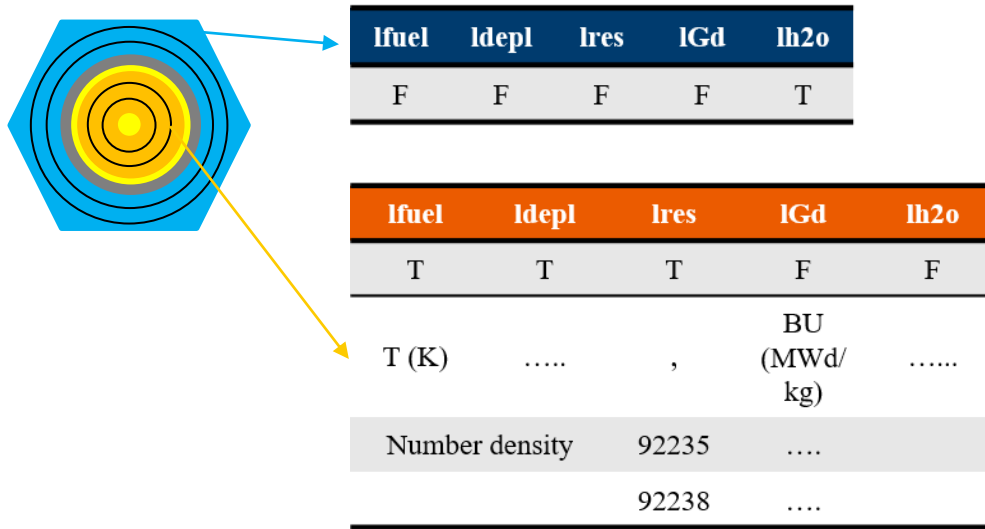


Figure 5.4. Data stored in the nTF restart file for a moderator FXR and a fuel FXR

5.2.2.3 Control rod insertion

Up to this point control rods (CR) are simulated explicitly in nTF by adjusting the size of the axial nodes to match the level of insertion and the change of materials in the rod (30 cm of B₄C and the rest Dy₂O₃·TiO₂). However, this is not possible when using restart files since the size of the nodes and the characteristics of FXRs should remain the same throughout the cycle analysis. Nonetheless, nTRACER includes a module for the movement of the CR bank in the core, for Cartesian geometry. The core is modeled unrodded and the CR banks are described separately in the input as an additional component. The position of the CRs is defined on the assembly layout for each bank and the configuration of the CR banks in the core is also described. Finally, the material of the CR for each bank is defined (one for each bank) together with the insertion height in the core. During this work, the CR module of nTRACER is extended to hexagonal geometries. The simulation of a CR requires the definition of a ghost cell with the geometric structure of the empty guide tube (GT) but with the material composition of the CR. Then, according to the insertion height, the part of the GT pin that contains the CR is replaced in the geometry model by the ghost cell or the properties are

volume-averaged if the rod is inserted partially in an axial node. The variables encompassing the geometry structure of the model in nTF are modified to include the CR ghost cell. In addition, all input subroutines reading the CR bank configurations or the positions of the different banks in the core are extended to hexagonal geometries. nTRACER includes a CR decussing method. However, this is not extended to nTF or used in this thesis. The simulation of the CR should be improved in the next stages of this study, allowing the modeling of two materials per bank and the decussing correction. Fig. 5.5 illustrates the model of a CR in nTF.

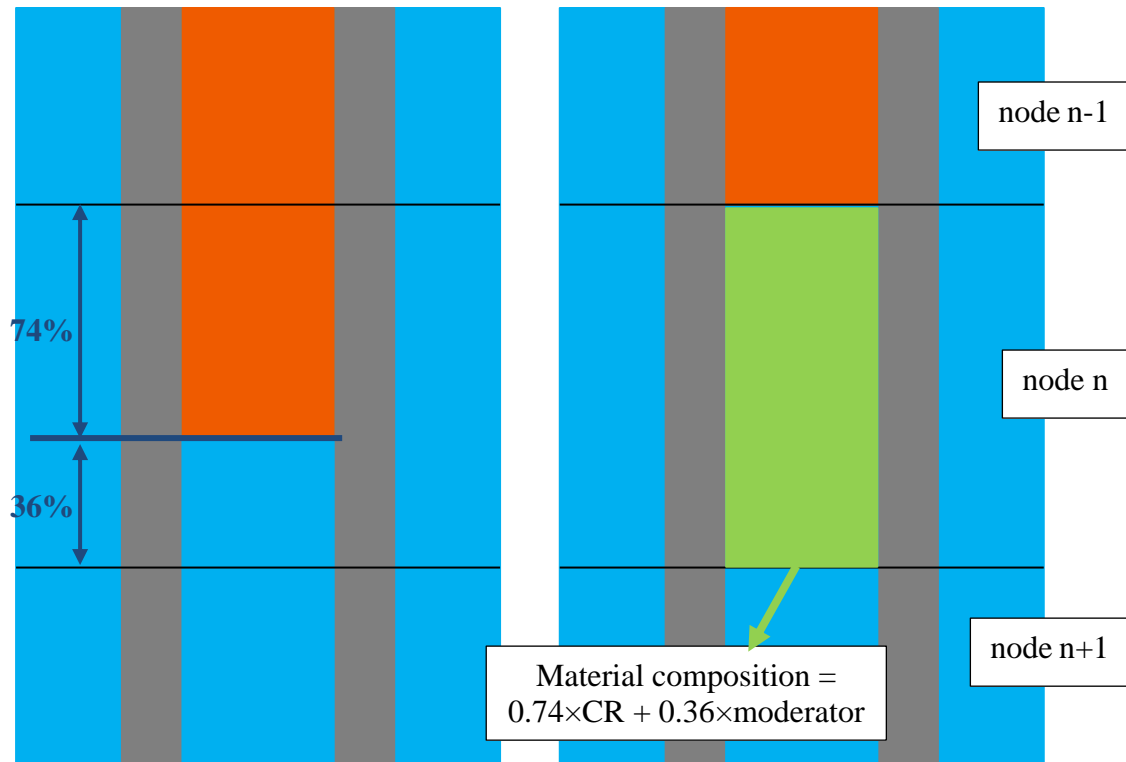


Figure 5.5. Real CR geometry (left) and nTF model (right)

5.2.3 The LRT core solver X2 model for cycle analysis

As it was mentioned in Chapter 2, one of the stages of the X2 benchmark is cycle analysis [97]. The Helmholtz-Zentrum Dresden-Rossendorf (HZDR) team updating the X2 benchmark has not yet published the updated power history and boron curve for the 1st X2 cycle of operation. However, they have provided to LRT all the data presented in this thesis. The core loading of the 1st X2 cycle is the same as the HFP state and the Hot Zero Power (HZP) state, presented in [98]. Fig. 5.6 illustrates the measured power history of X2 for the 1st cycle. HZDR has supplied LRT also with the history of the inlet temperature, rod position for CR bank #10 (see Fig. 2.13), boron concentration (BC), mass flow and axial offset. In addition, they provided a simplified power history, which is also presented in Fig. 5.6. The nominal power of X2 is 3000 MW [98]. It is apparent in this figure that both the measured and simplified power history

begin at 4.51 EFPDs and not the actual beginning of the cycle (see Section 2.7.2). This should not have a significant impact to the solution. In order to evaluate the use of the simplified history instead of the full power history for cycle analysis, the conventional LRT route is used to calculate the boron letdown curve with both (see Section 5.3.2 & Section 5.4). The RMS of the boron concentration of the points in the cycle that correspond to the BU steps of the simplified power history is the same in both calculations (with full and simplified power history). This means that the use of a simplified power history should not have an effect on the accuracy of the solution. The Merlin6 managing team agreed to grant LRT full access to 25 cluster nodes for 18 days in order to conduct the X2 cycle analysis with the high-resolution core solver.

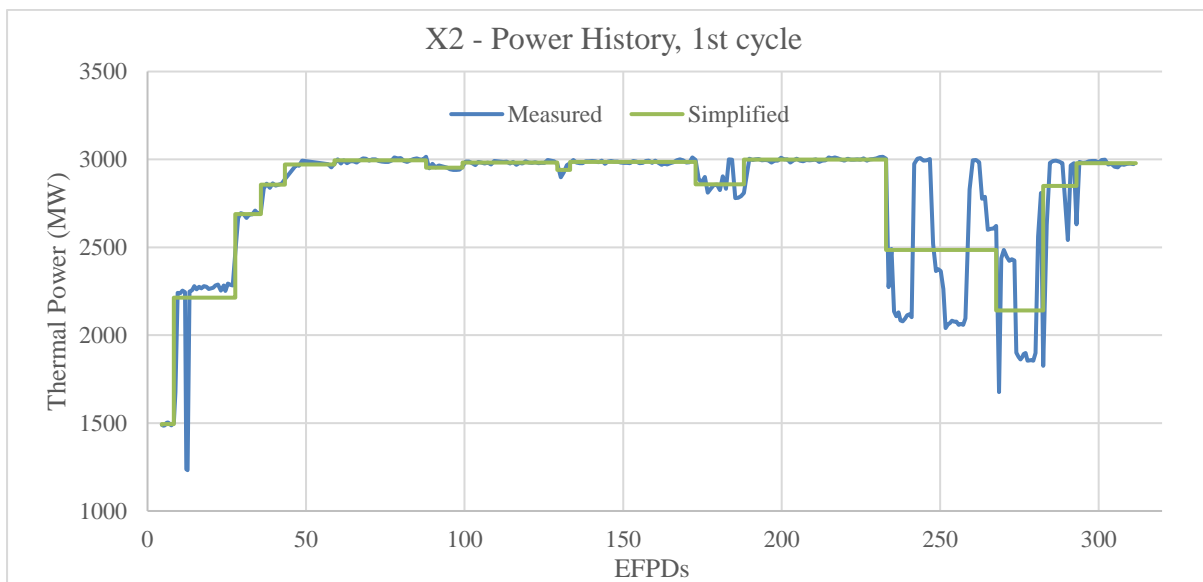


Figure 5.6. Measured and Simplified power history for the 1st cycle of X2 as a function of Effective Power Days (EFPDs)

The nTF/CTF X2 model for cycle analysis is based on the HFP model. In Chapter 4, it is discussed that the memory requirements of the model are too big to maintain the Node Major ray-tracing scheme used in the HZP case. Since the objective of the HFP study is to verify the nTF/CTF solver, the time penalties (~20 hrs per state-point) imposed by the Group Major ray-tracing scheme are acceptable. However, for cycle analysis, such penalties on the computational cost are not acceptable. For this reason, the Node Major scheme must be used. In order to achieve that, several changes in the model are necessary to decrease the memory requirements of the calculation. The modifications to the model are presented below together with the quantification of their effect on the accuracy of the solution. All effects concerning the neutronic solver are studied with HZP models unless specified otherwise:

- *Increase of the convergence criteria in nTF:* The convergence criteria for the neutronic solver are set to 1E-6 for the eigenvalue, 1E-5 for the fission source and 1E-5 for the residual for HZP and HFP calculations. In order to decrease the number of iterations the solver needs for convergence, the criteria of the source and residual are raised to 5E-5. The maximum effect on the axially averaged pin power of the X2 full core HFP model is 0.04% and the gain in terms of runtime (wall-time) with the multi-physics solver is 34%.
- *Decrease of the FXRs of all material regions in nTF:* In order to minimize memory requirements, the number of FXRs in all regions is decreased. Fuel regions are modeled by 3 rings not 4 and Gd with 6 FXRs not 7. The maximum effect on local pin power when decreasing the number of Gd FXRs is 0.03%. The memory requirements of the calculation are decreased by 5.2%. This is a small percentage of the overall memory requirements. Considering however the computational cost of the full core depletion calculations (see Section 5.2.4), such reduction is required to be able to carry out the calculation.
- *Switching off the MOC axial solver of nTF:* The axial solver requires 15% of the total calculation memory and 10% of the runtime. In order to decrease the memory requirements enough to employ the Node Major ray-tracing scheme, the MOC axial solver is turned off in nTF/CTF. Only the diffusion solver of the CMFD method is used in the axial direction. The effect on the solution is stronger than the previous approximations. Fig. 5.7 presents the axial power profile of the X2 HZP 1/6th core with the axial solver and without, and their relative difference. The average difference of the axial power profile is 0.7%; however, the difference increases next to the reflector regions, especially on the top of the core where the CR is inserted, reaching 5.8%. Nonetheless, it must be taken into account that the power is significantly lower next to the reflector. The effect on the axially averaged pin power is 0.25% on the rodded assembly.
- *Approximations in CTF:* As it was mentioned in the previous section, the local exposure distribution is not taken into account in CTF for the calculation of the material properties. Also, as in HFP, spacer grids are excluded from the T/H model. Finally the CR bank is not modeled in CTF, since it is inserted at maximum 25.6% during the whole cycle. Finally, the mass flow is kept steady during the whole cycle at 109.8 kg/s per assembly, since the variation of the total flow rate is not significant enough to alter this value. It must be pointed out that this is a strong approximation, since in a real VVER core the coolant flow is not the same in every assembly. As it was mentioned in Section 1.2, the modeling of the downcomer mixing has a significant impact on the accuracy of multi-physics calculations

(Kozloduy-6) [27]. However, there is not available information about the mass flow distribution at the core inlet for X2.

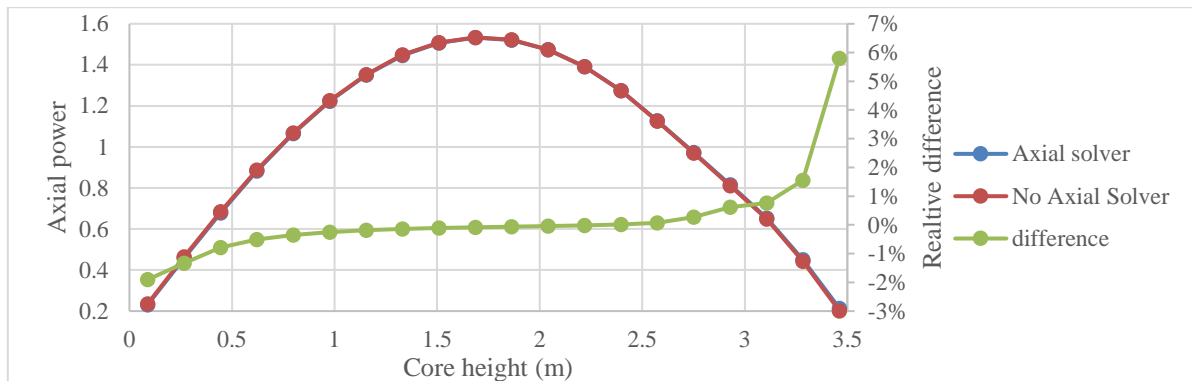


Figure 5.7. Axial power profile with and without the 1D MOC axial solver for X2 HZP 1/6th core and relative difference

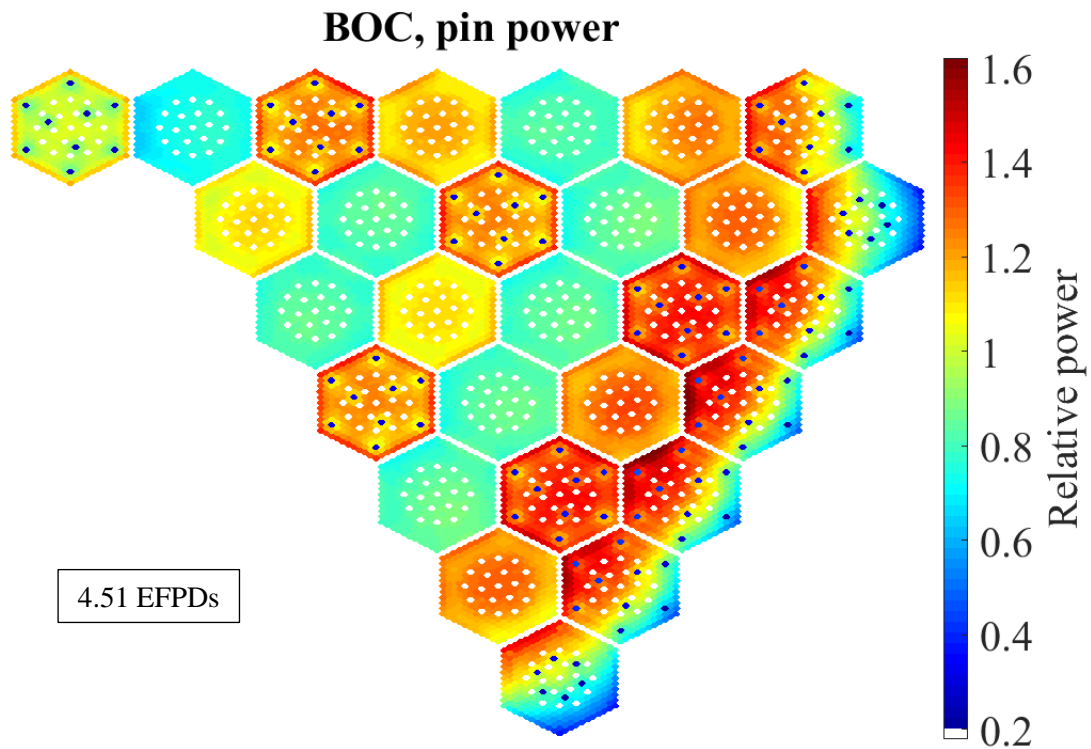
There is room for future work and improvement to the nTF/CTF cycle analysis scheme. Nonetheless, the current state of the high-resolution multi-physics core solver is adequate for the purpose of this thesis, to perform cycle analysis on a full core VVER model with the available computational resources and compare the outcome with coarse mesh experimental data and a conventional coupled code system.

5.2.4 Comparison of the nTF/CTF cycle analysis with experimental data

After all the modifications and approximations discussed in Sections 5.2.2 & 5.2.3 are applied to the nTF/CTF core solver, it requires ~16 – 21 hrs to simulate a BU step. The depletion solver needs 40 – 70 mins and the total memory use is 8.31 Tb, which corresponds to 99% of the available memory in 25 nodes. Due to time limitations, nTF/CTF performs the X2 cycle analysis with the simplified power history (see Fig. 5.6). The operating conditions for the 17 BU steps of the simplified history are presented in Table 5.1. The EFPDs refer to the end of the step. Fig. 5.8 presents the nTF/CTF axially averaged pin power maps at the beginning of cycle (BOC) – 1st step, middle of cycle (MOC) – 9th step and end of cycle (EOC) – 17th step. The same color bar is used for all maps.

Step #	EFPDs	Days	Th. Power (MW)	H10%	Tin (°C)	BU step (MWd/kg)	nTF/CTF BC (ppm)
1	4.51	9.08	1490.7	85.3	282.6	0.191748	898
2	8.33	16.75	1494	81.2	282.4	0.162412	895
3	27.68	42.98	2212.8	80.7	284.8	0.82269	835
4	35.72	51.95	2688.1	80.4	287.0	0.341831	803
5	43.31	59.92	2857.4	80.1	287.2	0.322698	784
6	58.97	75.73	2971.6	83.3	287.5	0.665805	750
7	87.86	104.66	2995.8	85.5	287.5	1.228295	680
8	99.4	116.39	2952.8	85.1	287.5	0.490638	668
9	129.22	146.38	2982.6	84.4	287.4	1.267835	586
10	133.3	150.54	2941	83.3	287.5	0.173466	586
11	172.9	190.33	2986	84.8	287.6	1.683644	453
12	188.14	206.32	2859.2	85.9	287.4	0.647948	417
13	232.89	251.08	2999.2	88.7	287.5	1.902603	250
14	267.69	293.08	2485.6	78.8	285.8	1.479566	164
15	282.54	313.89	2141.2	74.4	285.6	0.631367	136
16	293	324.91	2849.1	84.8	286.9	0.44472	40
17	311.74	343.78	2978.8	88.6	287.5	0.796755	0

Table 5.1. Operating conditions of the simplified cycle history simulated by nTF/CTF and the calculated boron concentration



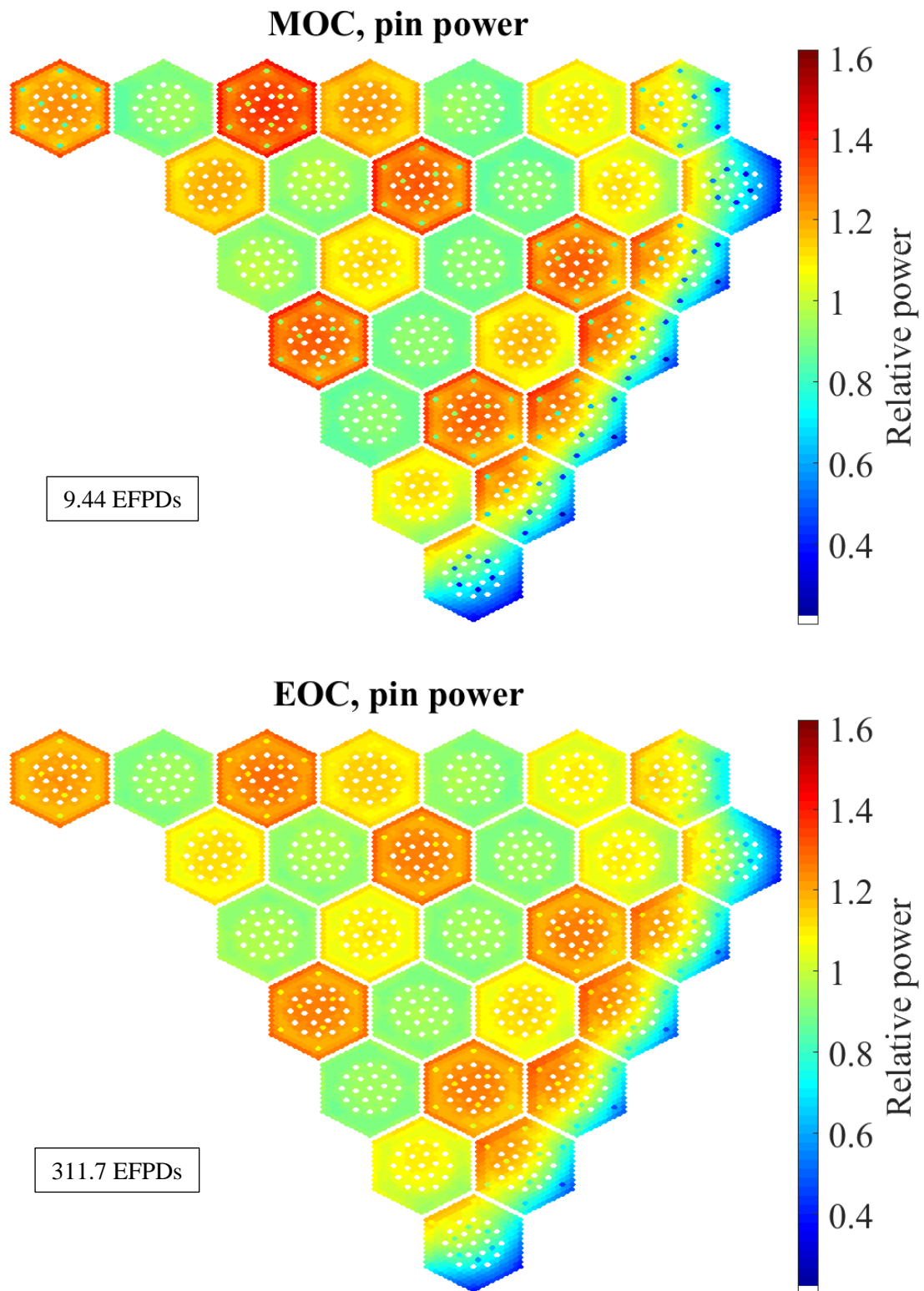


Figure 5.8. nTF/CTF relative pin power maps for the X2 BOC, MOC & EOC

When comparing the graphs of Fig. 5.8 it becomes apparent that the power profile becomes flatter with exposure. The fuel experiencing higher power is depleted faster, resulting in less radially heterogeneous flux distribution. Similarly, the neutron absorption in the Gd pins

becomes weaker as Gd is depleted. The assemblies neighboring the radial reflector present very strong power gradients. These will be a possible challenge to grasp with the conventional method. Fig. 5.9 illustrates the nTF/CTF calculated boron concentration as a function of BU and the measured boron letdown curve provided by the X2 benchmark team. The difference of the LRT core solver vs the measurements is also presented in the same figure ($[BC_{\text{measurement}} - BC_{\text{nTF/CTF}}]$, at the end of step). Fig. 5.10 illustrates the detailed and simplified power history, together with the difference of the LRT core solver from the measured values.

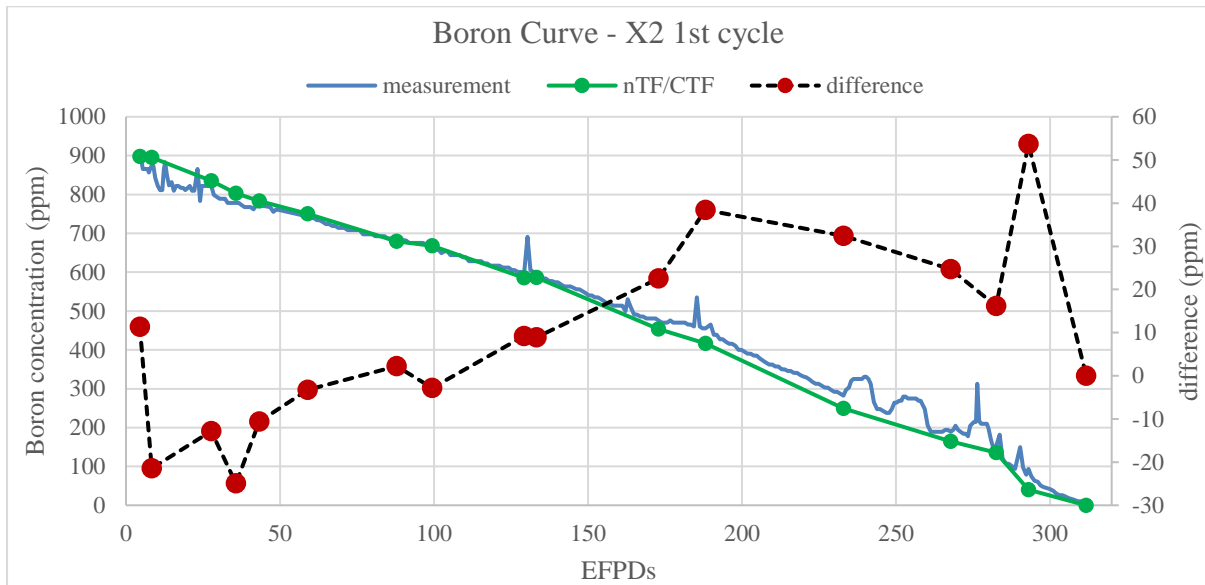


Figure 5.9. nTF/CTF calculated and measured boron curve for the 1st X2 cycle. The difference of the calculation vs the measurement is also presented

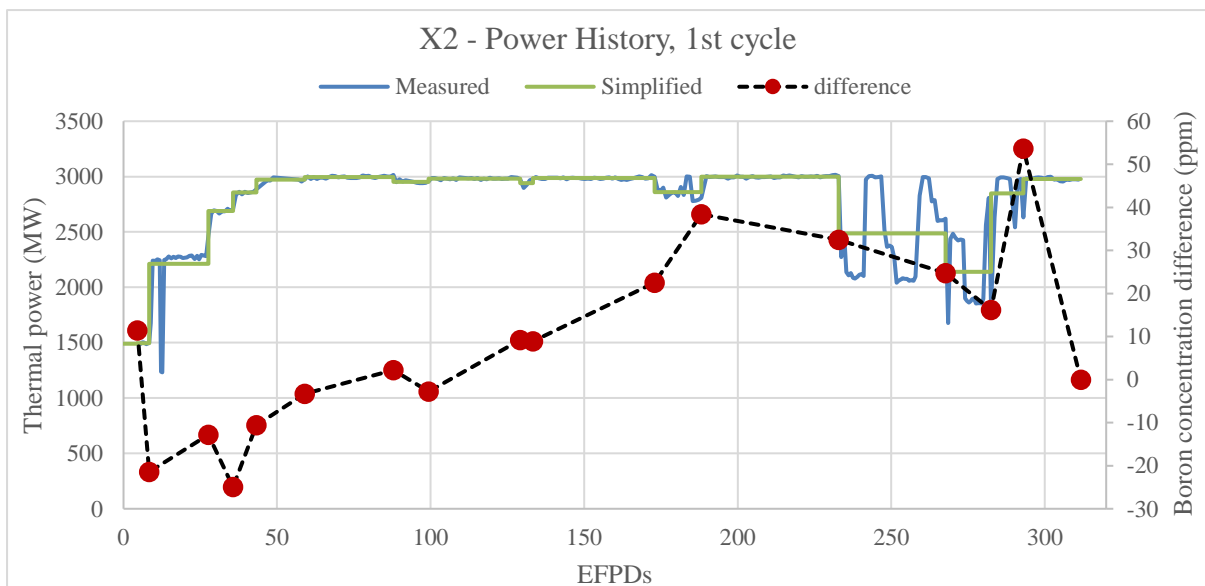


Figure 5.10. Measured and simplified power history for the 1st cycle of X2 as a function of EFPDs. The difference of the calculation vs the measurement is also presented.

The RMS difference between calculation and measurement in terms of boron concentration is 22 ppm, with a maximum of 54 ppm at the end of the cycle. When examining Fig. 5.10, it is apparent that nTF is overestimating the boron concentration from 4.51 EFPDs to 35.72 EFPDs and underestimating it from 172.9 EFPDs until 293 EFPDs. Both BU periods of higher discrepancy (steps 1-4 & steps 11-16) correspond to short term variations of the power level, which cannot be reproduced in detail by the simplified power history. Especially from 232 EFPDs to 293 EFPDs, the core power experiences strong fluctuations, which are modeled in nTF/CTF with the average power level. However, according to the calculations performed with the conventional LRT core solver (see Section 5.3.2 and Section 5.4), the use of the simplified power history should not have an effect on the accuracy of the solution. Further investigation is necessary. Nonetheless, from PWR utility perspective, the discrepancies are within acceptable limits throughout the curve (RMS < 32 ppm, max < 100 ppm) (see Section 2.7.3).

Besides the boron curve, the X2 benchmark team also provided three assembly power maps experimentally measured at specific points of the cycle (1st measurement: 29.8 EFPDs, 2nd measurement: 90.8 EFPDs & 3rd measurement: 208.7 EFPDs). The data consist of SPND readings at several locations in the active core and reconstructed power profiles based on the experimental readings. The thermal power of the reactor for each measurement point is also provided. Given that there is no specific information about the other operating conditions (e.g. inlet temperature) at the measurement time, the conditions of the power history step before the measurement are used. This assumption is valid since the difference between all measurement points and the previous BU step in the detailed power history is less than one EFPD. The LRT core solver simulates the three measurement points using the restart files of the previous BU step in the simplified curve. The operating conditions of the three measurement points and their BU difference from the previous step in the simplified curve are presented in Table 5.2. Fig. 5.11 illustrates the relative difference of the assembly power between nTF/CTF and the experimental data, and between nTF/CTF and the reconstructed data, $[(\text{Nor.Pow.}_{\text{ref}} - \text{Nor.Pow.}_{\text{nTF/CTF}}) / \text{Nor.Pow.}_{\text{nTF/ref}}]$, for the three measurement points. The maximum relative difference and the RMS of the nTF/CTF assembly power maps vs experimental and reconstructed data are also presented in Table 5.3.

Measurement point #	EFPD	Days	Restart file from step	Th. Power (MW)	H10%	Tin (°C)	BU step (MWd/kg)
1 st	29.8	45.9	3	2667	84.4	287.2	0.09
2 nd	90.8	108.1	7	2976	84.5	287.6	0.12
3 rd	208.7	227.4	12	3000	88.9	287.5	0.87

Table 5.2. Operating conditions of the three measurement points

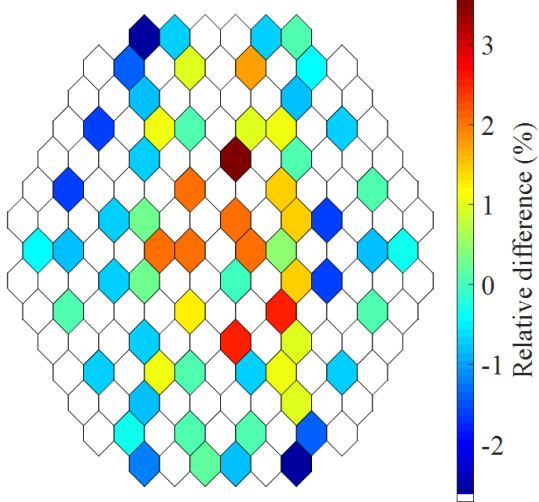
Measurement point #	nTF/CTF vs measured data		nTF/CTF vs reconstructed data	
	max (%)	rms (%)	max (%)	rms (%)
1 st : 29.8 EFPDs	3.57	1.29	3.17	1.27
2 nd : 90.8 EFPDs	3.29	1.14	2.28	0.82
3 rd : 208.7 EFPDs	2.72	1.01	2.47	0.94

Table 5.3. Maximum relative difference and RMS of nTF/CTF vs experimental and reconstructed data for the three measurement points

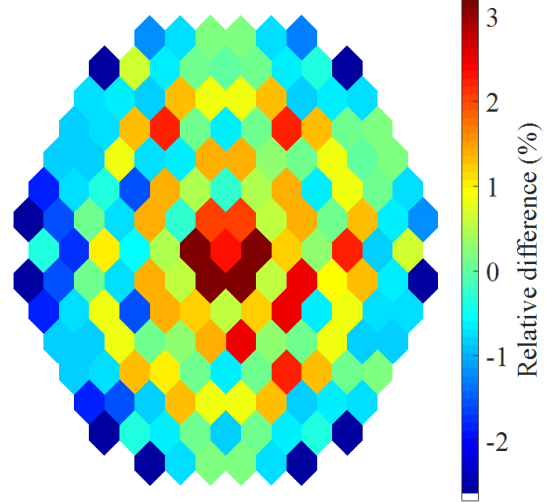
As it is mentioned in Section 2.7.2, there is not any measurement uncertainty associated with the experimental data, just a general requirement that the in-core monitoring system measures power distribution within 5% accuracy. However, there is no specific information as to how this requirement is applied. Also from the utility perspective, the maximum difference between code prediction and measurement for axially averaged power should be 5% (see Section 2.7.3). Given that the maximum assembly power difference in nTF does not exceed 3.6%, it can be concluded that the LRT core solver solution lies well within the uncertainty limit for all measurement points in the core. By examining Fig. 5.11 and Table 5.2, it becomes apparent that the relative difference decreases with BU, as expected since the power profile becomes more homogeneous. nTF/CTF has better agreement with the reconstructed data, especially in terms of maximum difference. In general though, the RMS is smaller than 1.3%, which shows good agreement with experimental data and the reconstructed solution.

Despite the modeling approximations employed in nTF/CTF, the novel core solver is capable of simulating the 1st cycle of X2 within the accuracy limits set by the utilities. The discrepancies in the boron curve remain in low levels throughout the cycle. The comparison of nTF/CTF with experimental data validates the accuracy of the coupled code system for the prediction of global parameters, for which there is available data. However, the main benefit of using nTF/CTF is to obtain sub-pin predictions throughout the cycle. Fig. 5.12 demonstrates the sub-pin normalized power profiles of three selected pins from an assembly neighboring the radial reflector, where the strongest power gradients are observed, at the mid-height of the core.

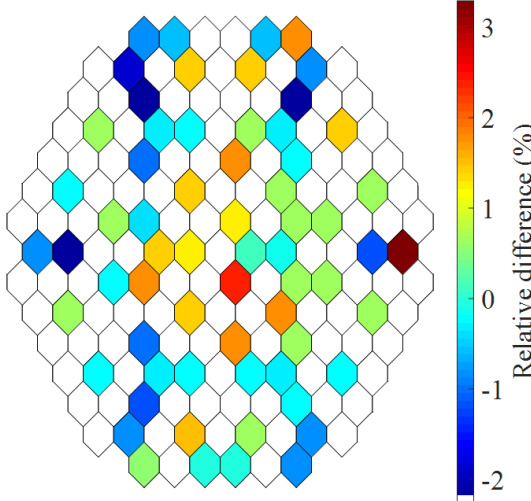
X2 1st point, nTF/CTF vs measured data



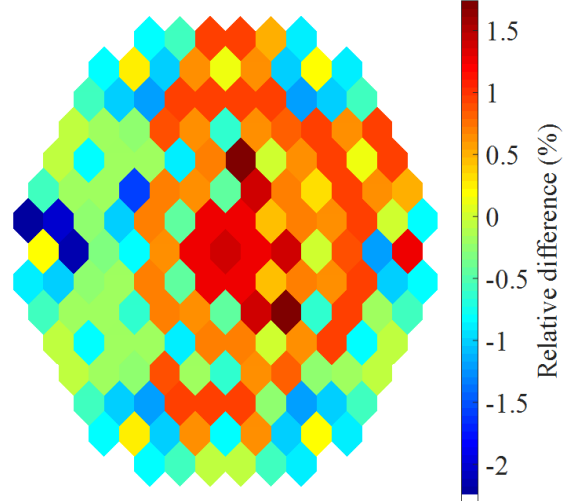
X2 1st point, nTF/CTF vs reconstructed data



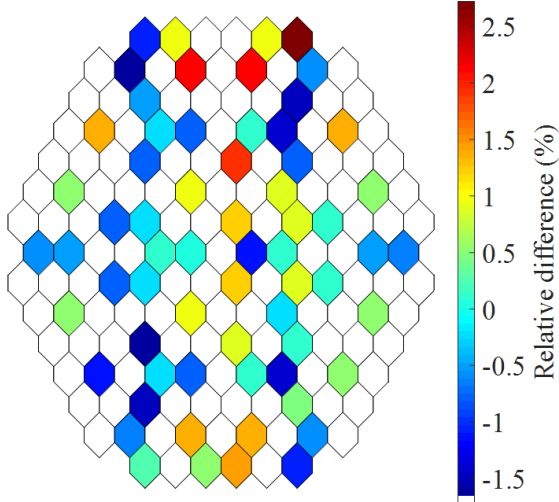
X2 2nd point, nTF/CTF vs measured data



X2 2nd point, nTF/CTF vs reconstructed data



X2 3rd point, nTF/CTF vs measured data



X2 3rd point, nTF/CTF vs reconstructed data

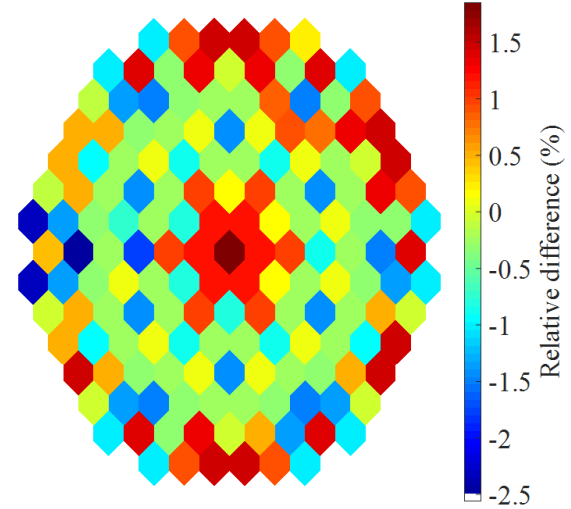


Figure 5.11. Comparison of the nTF/CTF assembly power vs experimental and reconstructed data for the three measurement points (1st: 29.8 EFPDs, 2nd: 90.8 EFPDs & 3rd: 208.7 EFPDs)

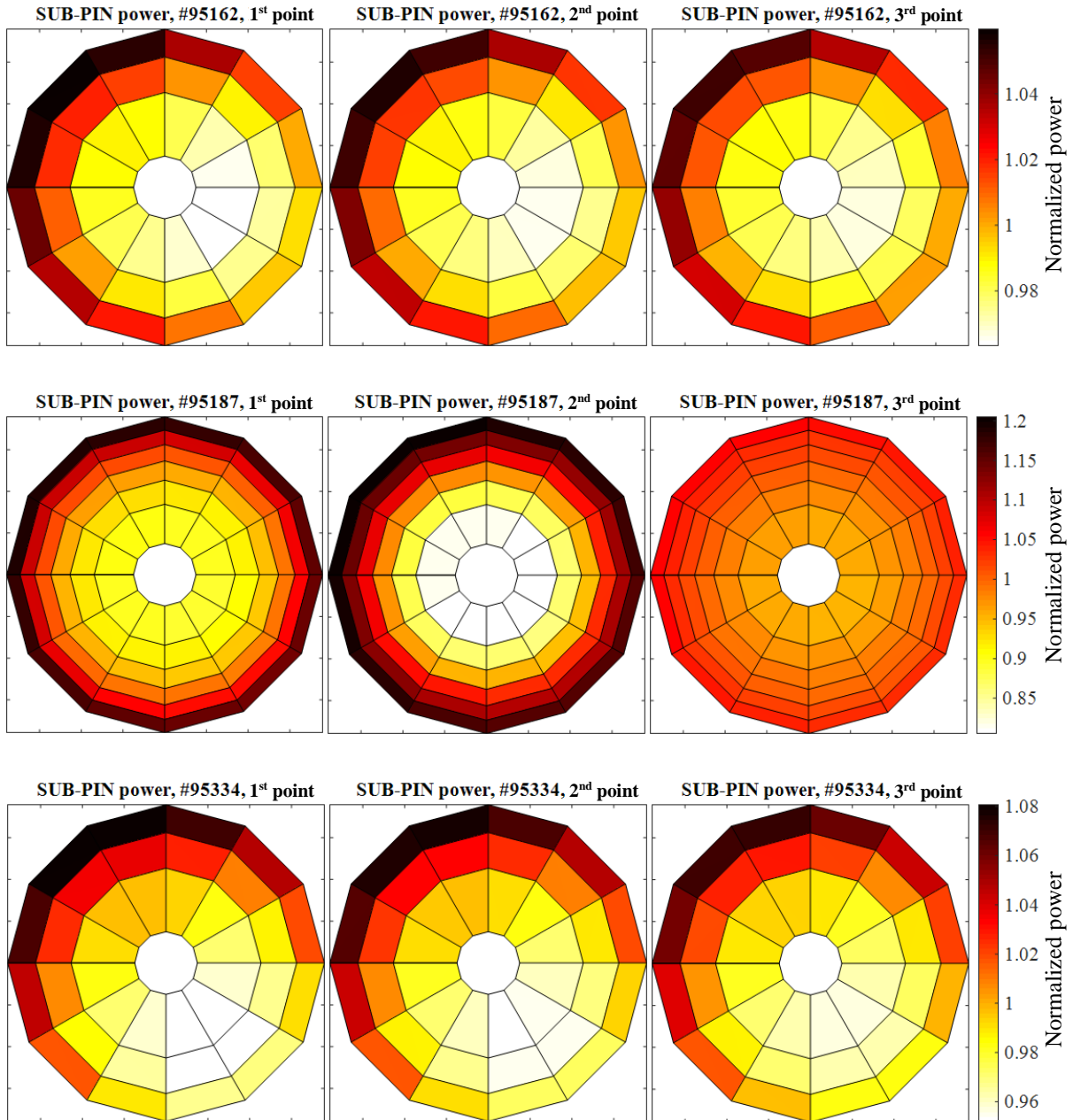
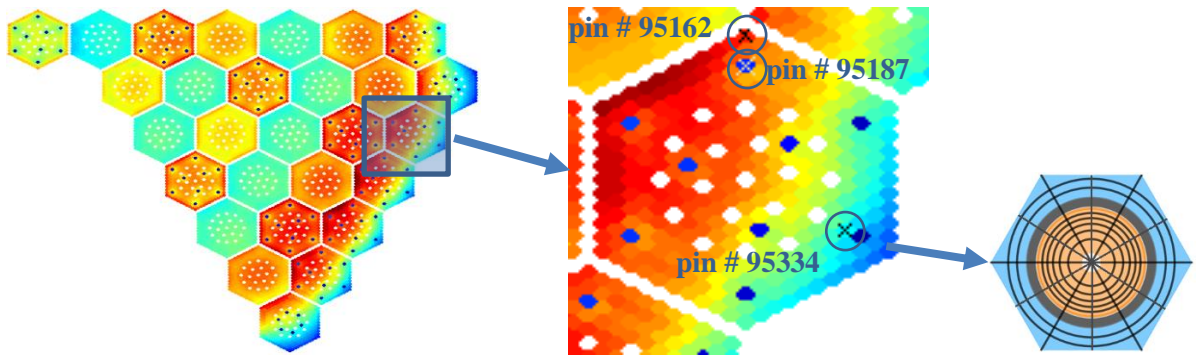


Figure 5.12. Sub-pin power profiles of selected pins at mid-core height for the three measurement points (1st: 29.8 EFPDs, 2nd: 90.8 EFPDs & 3rd: 208.7 EFPDs)

In Fig. 5.12, the location of the selected pins in the core is also presented. Pin # 95162 (3.6% w/o) is at the top of the assembly and experiences high power. Pin # 95187 is a Gd pin (3.3% w 5% Gd). Pin # 95334 (4.0% w/o) is located at the lower power region next to a Gd pin. Each pin is illustrated with a single color bar for the three measurement points (1st: 29.8 EFPDs, 2nd: 90.8 EFPDs & 3rd: 208.7 EFPDs) of the X2 cycle. All pins present higher power at the top left corner following the power gradient within the assembly. Especially for pin # 95334 this gradient is more pronounced, since it is neighboring a Gd pin. In pin # 95162 and pin # 95334, the power profile is gradually becoming less steep with BU. The effect is stronger for pin # 95162, since it experiences higher power. These two pins are modeled with 3 radial subdivisions so the flattening of the profile is not as clear as for pin # 95187. The Gd pin is modeled with 6 subdivisions. The power profile is steeper at 90.8 EFPDs, when Gd is mostly depleted on the outer rings, creating a strong flux gradient in the center of the pin. At 208.7 EFPDs, Gd is fully depleted, thus the profile becomes significantly less peaked. Fig. 5.12 demonstrates the capability of the novel LRT core solver to extract sub-pin level information for cycle depletion of VVERs.

5.3 Cycle analysis with CASMO5-VVER/PARCS

One additional goal of this thesis is the development of a conventional code system for VVER cycle analysis. On the framework of the LRT VVER project, CASMO5-VVER has been verified for assembly depletion calculations against Serpent2 [102]. In this work, in addition to the HZP and HFP steady state, CASMO5-VVER is used to generate cross-sections for PARCS for the analysis of the 1st X2 cycle. The main challenge to the simulation of the full cycle is the production of a cross-section library with CASMO5-VVER which can encompass the range of the X2 operating conditions and corresponding BU. The structure of the CASMO5-VVER library used for X2 is presented in this chapter, together with the outcome of the conventional code system for the 1st cycle of X2, which is compared with experimental data.

5.3.1 CASMO5-VVER case matrix for cycle analysis

As described in Section 2.5.1, the development of an appropriate case-matrix for cycle analysis should be detailed enough that the nodal code can extract cross-sections for all state-points of the power history, without extrapolation outside the range of the parameters for which the library was produced. CASMO uses built-in case-matrices, which are optimized for SIMULATE3 and SIMULATE5. However, private consultation with the PARCS developers

in the University of Michigan (UM) revealed that GenPMAXS may not fully support the CASMO built-in matrices for PWR calculations. A larger case-matrix, which includes more branches and histories, is required when doing coupled calculation (steady state and depletion) with CASMO-GenPMAXS-PARCS. UM provided LRT with the corresponding CASMO case-matrix, used for PWR cycle analysis by the PARCS developers. The structure of the history trees and the operating conditions of the branches of the UM case-matrix are presented in Table 5.4. The branches cross-sections are calculated for the exposures listed on the table.

Tree #	History tree				Branches			
	HCR	HTMO	HBC	HTF	CR	TMO	BC	TF
1	OUT	580	500	900	OUT	580	0.01	541
2	OUT	540	500	900	IN	600	500	900
3	OUT	620	500	900	540	620	2000	1800
4	OUT	580	0.01	900	560			
5	OUT	580	2000	900	Exposure (MWd/kg): 0.0, 0.1, 0.5, 1, 2, 4, 6, 8, 10, 11, 15, 20, 25, 30, 40			
6	IN	580	500	900				

Table 5.4 (see Table 2.2). Structure of the history trees and operating conditions of the branches used in the UM case-matrix. TMO: moderator temperature, TF: fuel temperature, H: history

The structure of the UM case-matrix ensures that no calculation point exists where two operating conditions need to be changed simultaneously from the history tree or the previous branch calculation. This is a requirement of GenPMAXS since it rearranges the branches of each tree without taking into account their sequence in the lattice calculation. Several trees are built with varying boron concentration and moderator temperature. The reason is that these parameters have a stronger effect on the cross-sections as history variables. For example, the BU of an assembly with lower moderator density translates to harder flux, which results in larger build-up of Pu. If the cross-section library is not including trees with low moderator densities then the nodal code cannot incorporate this effect accurately.

5.3.2 Comparison of the CASMO5-VVER/PARCS cycle analysis with experimental data

The X2 models built with CASMO5-VVER and PARCS for the HZP and HFP calculations are used also for cycle analysis (see Section 3.3.3). The case-matrix described in Table 5.4 is employed for the fuel assemblies and the reflector models in CASMO5-VVER. It must be noted that reflector assemblies do not undergo depletion; nonetheless, their impact to the active core changes according to the boron concentration, moderator density and fuel temperature of the neighboring assembly. CASMO5-VVER/PARCS uses the detailed power history (see

Fig. 5.6) to generate the boron curve for the 1st cycle of X2. In order to examine the performance of the code system with the CASMO built-in case matrix, a second cross-section library is generated using CASMO5-VVER, with the exact same models but with the built-in case-matrix instead of the UM case-matrix. However, GenPMAXS cannot process the CASMO5-VVER outputs to generate the cross-section files for PARCS (PMAXS, see Section 2.5.3) with the built-in case-matrix. Fig. 5.13 illustrates the boron curve for the 1st cycle of X2 calculated with the UM case matrix, together with the difference of the boron concentration from measured data, $[BC_{\text{measurement}} - BC_{\text{CASMO5-VVER/PARCS}}]$, as a function of BU. The CASMO5 leakage correction is not used for the cross-section generation, as it is not suitable to be used with PARCS (see Section 2.5.2.1 & Section 3.3.3).

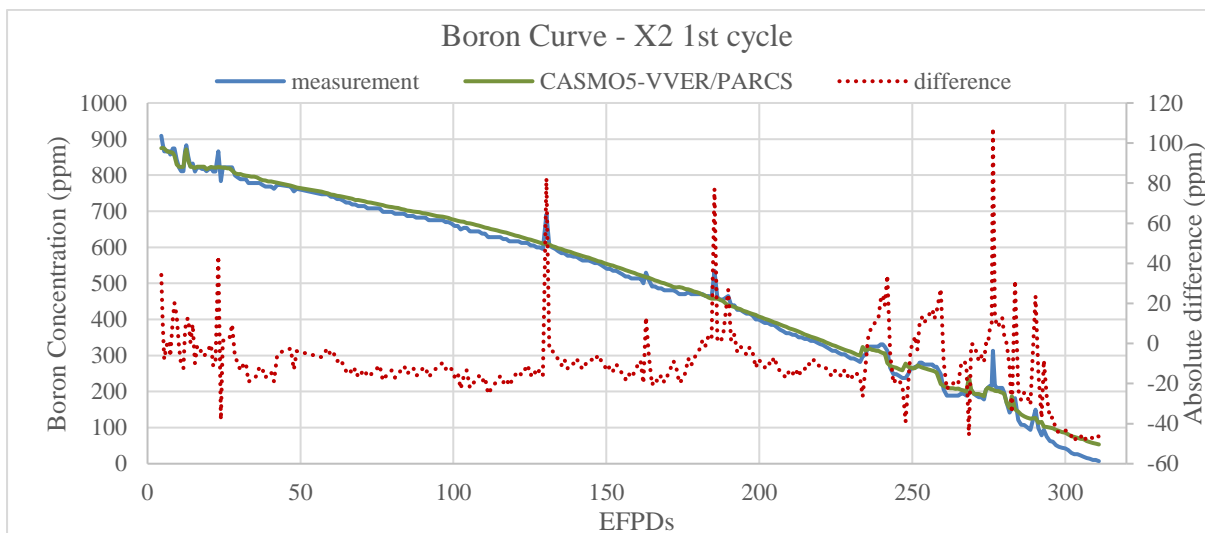


Figure 5.13. Boron letdown curve for the 1st cycle of X2 measured and calculated by CASMO5-VVER/PARCS with the UM case-matrix as a function of BU. The difference of the calculation vs the measurement is also presented

The coupled code system overestimates the boron concentration after ~27 EFPDs. Additionally, the three spikes in boron concentration at 130 EFPDs, 186 EFPDs and 276 EFPDs are not reproduced. During the 1st X2 cycle, the reactor was shut down several times for a few days. During that time, the core was filled with high-borated water and Xe was decaying. Normally, after the restart of the reactor, it takes some time for Xe to get to equilibrium. Hence, the short boron peaks correspond to the restart of the reactor after full shutdown. These shutdowns are not taken into account in the CASMO5-VVER/PARCS calculation, which justifies the relevant discrepancies in the boron letdown curve. The shape of the predicted boron curve follows the measured data, except after 233 EFPDs when the core experiences power fluctuations and the discrepancies become increasingly larger. Despite the

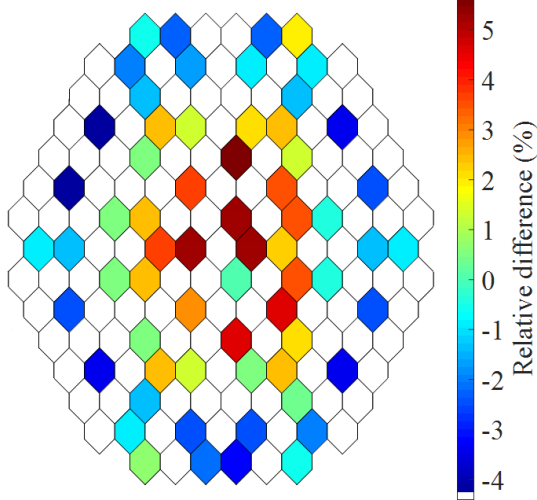
higher discrepancies at the end of cycle, reaching a maximum of 46 ppm, the difference in boron concentration remains below 100 ppm throughout the calculation with a RMS of 20 ppm; which is below target accuracy (see Section 2.7.3). This validates the boron curve predicted by the CASMO5-VVER/PARCS coupled code system, when a case-matrix tailored made for PARCS is used. The experimental power maps provided by the X2 benchmark team for three measurement points (1st: 29.8 EFPDs, 2nd: 90.8 EFPDs & 3rd: 208.7 EFPDs) are reproduced also with CASMO5-VVER/PARCS. Table 5.5 presents the maximum difference and the RMS of the coupled code system vs experimental and reconstructed data for all measurement points. Fig. 5.14 presents the detailed comparison of the power maps.

Measurement point #	CASMO5-VVER/PARCS vs measured data		CASMO5-VVER/PARCS vs reconstructed data	
	max (%)	rms (%)	max (%)	rms (%)
1st : 29.8 EFPDs	5.64	2.64	6.30	2.66
2nd : 90.8 EFPDs	4.58	2.30	3.89	2.11
3rd : 208.7 EFPDs	4.21	1.71	3.09	1.65

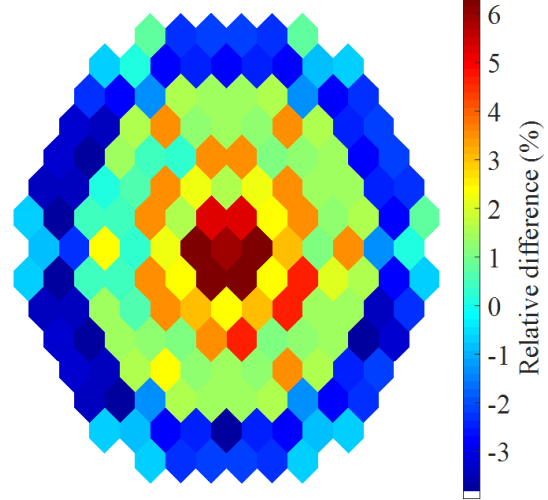
Table 5.5. Maximum relative difference and RMS of CASMO5-VVER/PARCS vs experimental and reconstructed data for the three measurement points

The power map of the coupled code system presents higher discrepancies for the first measurement point than for the other two. The maximum difference of the assembly power exceeds the 5% accuracy limit of the utility, and the RMS is higher than the acceptable value set for PWRs (see Section 2.7.3). There seems to be a tilt in the power profile difference for all cases, which is stronger for the 29.8 EFPDs when the power distribution is more heterogeneous. This behavior is more pronounced than what is observed for the HZP and HFP comparisons with Serpent2. It can be attributed to the approximate modeling of the reflector assemblies (see Fig. 3.27) and to the fact that no leakage correction is used for this calculation. The maximum assembly power discrepancy decreases to acceptable levels for the maps of 90.8 EFPDs and 208.7 EFPDs. However, the RMS remains above the utility limit (1.5%).

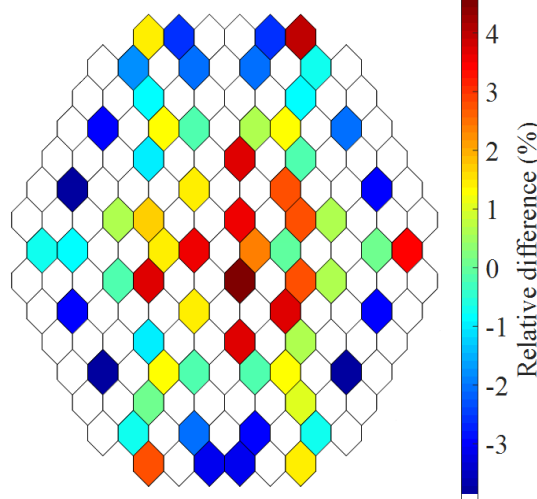
X2 1st point, CASMO-HEX/PARCS vs measured data



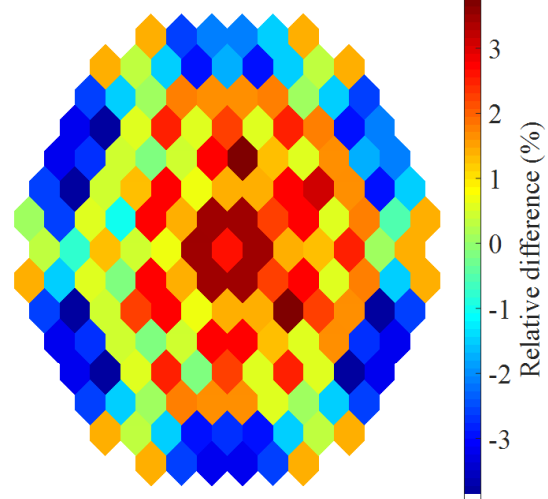
X2 1st point, CASMO-HEX/PARCS vs reconstructed data



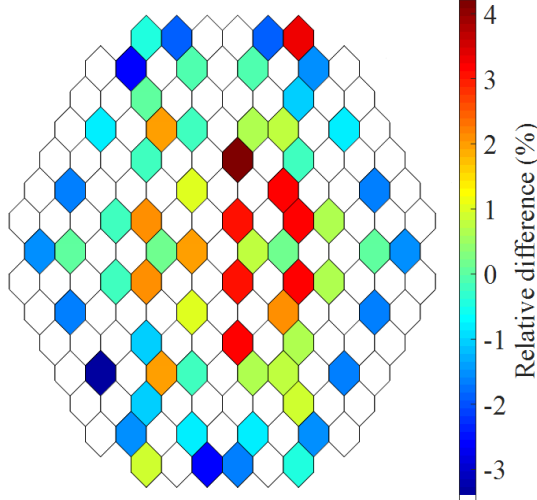
X2 2nd point, CASMO-HEX/PARCS vs measured data



X2 2nd point, CASMO-HEX/PARCS vs reconstructed data



X2 3rd point, CASMO-HEX/PARCS vs measured data



X2 3rd point, CASMO-HEX/PARCS vs reconstructed data

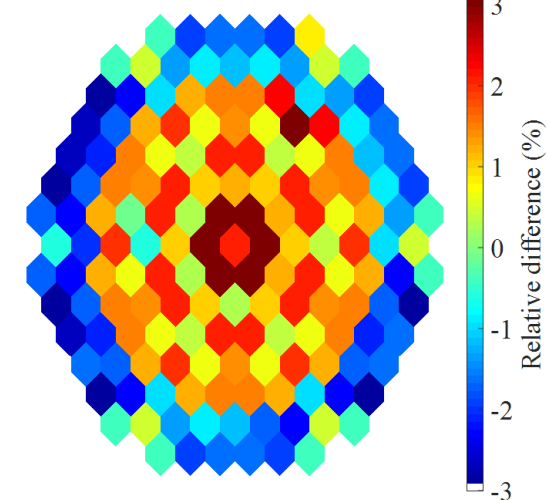


Figure 5.14. Comparison of the CASMO5-VVER/PARCS assembly power vs experimental and reconstructed data for the three measurement points (1st: 29.8 EFPDs, 2nd: 90.8 EFPDs & 3rd: 208.7 EFPDs)

The conventional coupled code system demonstrates good agreement with the measured boron curve, when the appropriate case matrix is used. However, the comparison of the assembly power maps with experimental data exceeds the acceptable accuracy limits set by the utilities. The use of an appropriate leakage correction in CASMO5-VVER, which can be employed with PARCS, could remove part of the discrepancy. In addition, more refined modeling of the reflector would improve the accuracy of the solution for the cycle measurement points, but also for the HZP and HFP case [102]. These improvements require further study of the solvers and the production of the relevant cross-section libraries with GenPMAXS, which is not attempted in this thesis due to lack of time.

5.4 Comparison of the novel and conventional LRT solver for VVER-1000 cycle analysis

As it was mentioned in the Introduction, a goal of this thesis is to study the performance of the novel high-resolution multi-physics code system nTF/CTF as a cycle analysis tool and compare it with a conventional solver like CASMO5-VVER/PARCS. At this point in the study, the two solvers can be compared only in terms of computational resources and global parameters. Even though PARCS can reconstruct the pin power profiles for Cartesian geometries, this functionality is not available yet for VVERs but is under development. However, it is obvious that in any case the conventional solver cannot reproduce the resolution of the novel approach, neither in terms of sub-pin fluxes nor in local T/H information. In this work, the comparison of the two solvers aims to quantify the extra computational cost, which is necessary to acquire the high-resolution information, and discuss the accuracy of the solvers on parameters that are relevant for cycle analysis. A more in-depth and systematic comparison (e.g. on local assembly power for HZP, HFP and cycle analysis) would allow a better understanding of the biases introduced by the approximations involved in the conventional approach. However, this would require the systematic comparison of CASMO5-VVER with nTF (see Section 3.3.2, CASMO5-VVER vs Serpent2) and the use of PARCS with cross-sections produced by nTF, in order to evaluate separately the effects of the lattice and the nodal code. This study is not part of the PhD.

In order to cross-compare the same models, CASMO5-VVER/PARCS is used to simulate the X2 boron letdown curve with the simplified power history (see Fig. 5.6). Fig. 5.15 illustrates the boron concentration as a function of BU calculated by both solvers. The same figure presents the difference in boron concentration from the measurement, $[BC_{\text{measurement}} -$

BC_{solver}], for both solutions. The conventional core solver is mostly overestimating the boron concentration throughout the cycle, similarly to what is observed with the detailed boron letdown curve (see Fig. 5.13). However, the discrepancies are lower at BOC & EOC in comparison to the novel solver, reaching a maximum of 44 ppm at the last BU step and an RMS of 19 ppm. The maximum difference in the calculation of nTF/CTF is 53 ppm and the RMS equals 22 ppm.

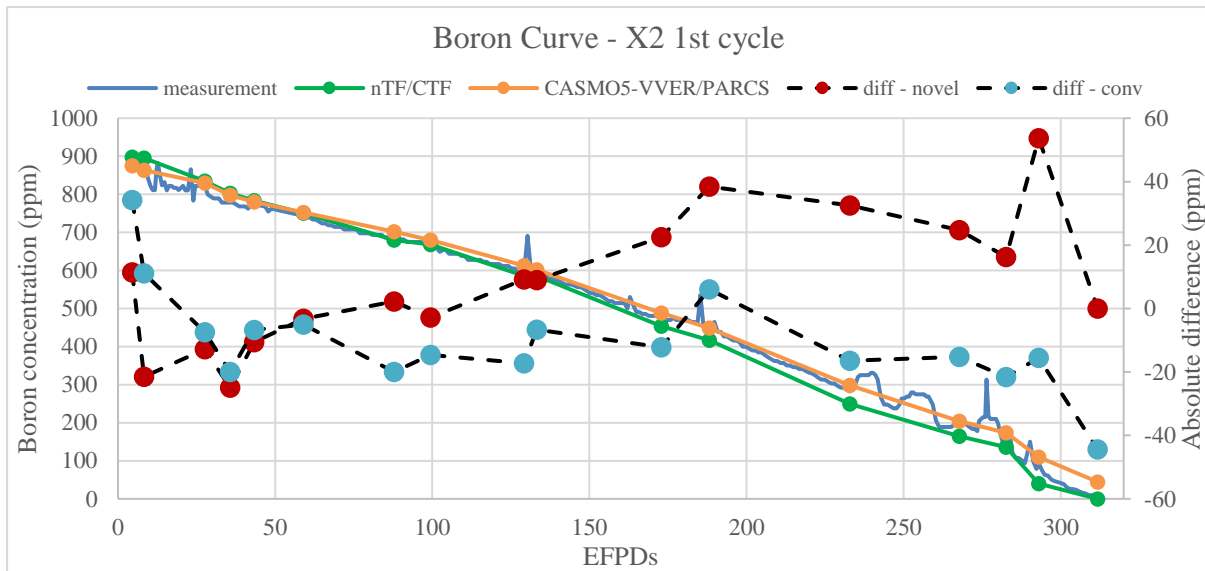


Figure 5.15. Boron letdown curve measured and calculated by nTF/CTF and CASMO5-VVER/PARCS with the absolute difference as a function of EFPDs

The two coupled code systems are also compared in terms of axial offset (AO). The experimental data of the 1st X2 cycle include AO measurements; however, not accompanied by uncertainty. The formula for the calculation of AO is $AO = \frac{P_T - P_B}{P_T + P_B}$ (%), where P_T is the power at the top half of the core and P_B at the bottom half. Fig. 5.16 presents the AO as calculated by nTF/CTF and CASMO5-VVER/PARCS together with the measurement as a function of BU. Both coupled code systems are diverging significantly from the measured data until 133 EFPDs. The maximum discrepancy for both curves from the measurement is presented at the first step and reaches 4.2% for nTF/CTF and 4.9% for CASMO5-VVER/PARCS. After this point, nTF/CTF is presenting very good agreement with the measured data, until 293 EFPDs when it starts diverging again. The AO calculated by CASMO5-VVER/PARCS is diverging also after 133 EFPDs, except for specific points (188 EFPDs, 293 EFPDs). The RMS for nTF/CTF equals 2.3% and for CASMO5-VVER/PARCS 2.6%. In general, nTF/CTF seems to have a better agreement with the measured values than CASMO5-VVER/PARCS, however both solvers are above target accuracy (see

Section 2.7.3). On the other hand, they experience a good agreement with each other. The maximum difference of AO calculated by nTF/CTF vs CASMO5-VVER/PARCS is 2.9% and the RMS is 1.3%, which is very close to target accuracy (see Section 2.7.3). Given that the two solvers present a relatively good agreement, their discrepancies with the measurements might be attributed to physical phenomena (e.g. chemistry related) not captured by the models.

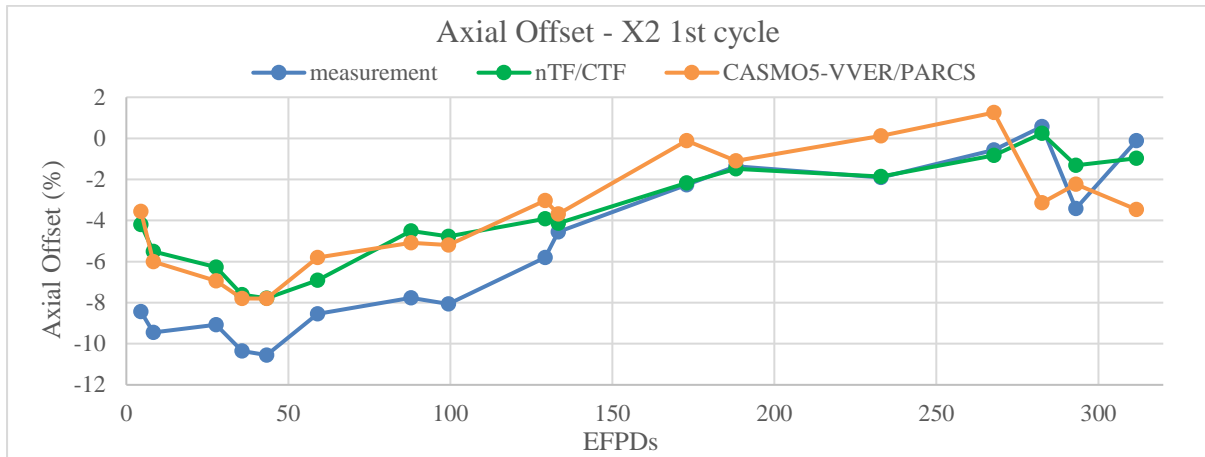


Figure 5.16. Axial offset measured and calculated by nTF/CTF and CASMO5-VVER/PARCS as a function of EFPDs

For core-averaged parameters like the boron let-down curve or the AO, the overall level of discrepancy is similar in both solvers. However, things change when examining their performance simulating the assembly power maps for the SPND measurement points (see Figs 5.11 & 5.14). The results of the comparisons are summarized in Table 5.6. When examining the corresponding graphs and the table below, it becomes apparent that nTF/CTF has a better agreement with both experimental and reconstructed data than the conventional approach. In addition, the novel solver does not present any tilts in the profile of the power difference, unlike CASMO5-VVER/PARCS.

Measurement point #	nTF/CTF vs measured data		nTF/CTF vs reconstructed data		CASMO5-VVER/PARCS vs measured data		CASMO5-VVER/PARCS vs reconstructed data	
	max (%)	rms (%)	max (%)	rms (%)	max (%)	rms (%)	max (%)	rms (%)
1 st : 29.8 EFPDs	3.57	1.29	3.17	1.27	5.64	2.64	6.30	2.66
2 nd : 90.8 EFPDs	3.29	1.14	2.28	0.82	4.58	2.30	3.89	2.11
3 rd : 208.7 EFPDs	2.72	1.01	2.47	0.94	4.21	1.71	3.09	1.65

Table 5.6. Maximum relative difference and RMS of nTF/CTF and CASMO5-VVER/PARCS vs experimental and reconstructed data for the three measurement points

Concerning computational costs, Table 5.7 summarizes the time requirements for both code systems. The total calculation time of the conventional solver consists of the time required by the lattice code to generate the cross-sections, assuming that each assembly type is handled simultaneously; and the calculation of the simplified boron letdown curve by the nodal solver. The time required by GenPMAXS to build the cross-section library is not taken into account since it amounts to a few seconds. The PARCS simulation is performed in serial, since the code cannot be parallelized, and that is reflected in the CPU time. The 6 cpus are used by CASMO5-VVER for the five fuel assembly calculations and for all the reflector models. Each CASMO5-VVER calculation is also executed in serial. It must be pointed out that this is not the most efficient way to use CASMO5-VVER. The lattice code can be executed in parallel; however, this was not possible with the available executable in the LCLRS machines. In addition, as it is described in Section 5.3.1, the case-matrix used for the generation of the X2 cross-section library is larger than the built-in case-matrix of CASMO5, to meet the requirements of PARCS. If CASMO5-VVER would be used with SIMULATE5, the built-in matrix would be sufficient for the X2 cycle analysis. Hence, the time requirements of the conventional approach that are presented in Table 5.7 are higher in comparison to what would be the typical computational cost of a cycle calculation with conventional solvers. The novel solver is using 12 cpus for each mpi; however, due to the large memory requirements it blocks the whole node, or 36 cpus. This is taken in to account in the CPU time calculation.

LRT solver	Wall time (hrs)	CPUs	CPU time (hrs)
nTF/CTF	325	300	292500
CASMO5-VVER/PARCS	68	6	403

Table 5.7. Computational time requirement of the LRT solvers for the simulation of the 1st X2 cycle

In terms of actual calculation time, the conventional approach is faster than the novel solver, as expected. It must be pointed out that the cross-section generation of specific assemblies is not repeated for every subsequent cycle calculation. In that case, only PARCS needs to be executed, which requires only 1 CPU hour for the simplified curve. The time required to produce the simplified boron curve with nTF/CTF is not forbidding for the use of the LRT core solver as an audit tool for cycle analysis. However, the cost of such a calculation is enormous; 300 cpus and 8.31 TB of memory need to be occupied for 325 hrs. The requirements of the high-resolution solver are significantly larger than what has been used up to now for cycle analysis. Nonetheless, it must be taken into account that nTF/CTF can be further optimized (see Conclusions & Future Work). Given the evolution in computing

systems, that made powerful servers available for high-resolution multi-physics calculations [8], it is reasonable to claim that a novel solver like nTF/CTF can be used as an audit tool for the core follow calculation and possibly safety analysis of VVERs.

5.5 Major Outcomes of the work presented in this chapter

- This chapter is dedicated to the development of both the novel and conventional computational route for VVER cycle analysis, achieving the desired outcome of the PhD. The flexibility of the high-resolution solvers and further modifications allowed the calculation of a full cycle boron letdown curve on Merlin6. The high-resolution coupled code system is validated with coarse mesh experimental data, achieving acceptable accuracy according to utility criteria. The capabilities of the coupled code system for sub-pin predictions on a full core model are showcased for the 1st cycle of X2.
- The conventional computational route, simulating the detailed power history, is validated with the same data, without the same success, especially when considering the experimental power maps.
- The sensitivity of the CASMO5-VVER/PARCS code system to the definition of the appropriate case-matrix proves that the level of approximations involved in the conventional approach makes the code system susceptible to errors, except if the user is an expert user.
- The computational cost of the high-resolution core solver is larger than the requirements of the conventional approach. However, not so large to make its use as an audit tool impractical, especially considering the improvements listed in this thesis that could reduce its cost.

Conclusions & Future Work

In recent years, the nuclear industry has moved towards the establishment of Best Estimate Plus Uncertainty (BEPU) safety limits for NPPs. The development of high-resolution high fidelity computational tools is a step forward to that direction. The goal of this PhD is the development of a novel multi-physics high fidelity core solver, capable of sub-pin level resolution, that is computationally cost-effective to be used as an audit tool for steady state and cycle depletion calculations. In addition, a conventional computational route is produced to serve as a measure of comparison to the capabilities and costs of the novel core solver. The development of both routes in parallel allows a better understanding of the corresponding methodology and the approximations involved in either approach.

Chapter 1 describes the motivation of this work and sets the specific research goals. The benefits of high-resolution high fidelity codes for core analysis are discussed. The production of information with few approximations provides a detailed representation of the core behavior, revealing problematic regions, which can be sources of fuel rod failure, and should in principle allow a more accurate estimation of the operational conditions in the core. Hence, the use of novel computational tools can help remove some of the conservatism and reduce the safety margins while guaranteeing the same level of safety. Despite the evolution of novel solvers for LWRs of Cartesian geometry, Chapter 1 demonstrates that there are no multi-physics tools of equivalent capabilities (sub-pin level resolution) for VVERs, to the extent of the writer's knowledge. Given the current expansion of VVER technology, there is a clear need for the development of refined multi-physics simulation tools capable of providing high fidelity high-resolution VVER full core analysis. This PhD aims at developing such a tool based on the neutronic code nTF and the sub-channel code CTF. Both solvers have been verified and validated for Cartesian PWRs and contain capabilities for hexagonal geometry modeling, which have not been used yet for full core high-resolution analysis. In order to compare the novel LRT core solver with a conventional tool, the development of a CASMO5-VVER/PARCS model for cycle analysis is also set as a goal for this thesis. Even though the nodal code PARCS has been verified and validated for VVERs, it has never been used with cross-sections generated by CASMO5-VVER since the expansion of the lattice code for

hexagonal geometries is relatively new. However, the two codes have been used at LRT for Cartesian geometries, for example for BWR cycle analysis.

Chapter 2 presents the methodology of the codes that are used in this PhD to build the novel and conventional LRT solver. In addition, the computational tools that are employed for the verification of the two LRT core solvers, Serpent2 and SCF, are also described. Finally, the benchmarks used in the thesis for verification and validation are presented together with the target accuracies, set by codes of similar capabilities for verification or by the utilities for validation.

Chapter 3 is focused on the appropriate modeling of a VVER core with a deterministic neutronic code to achieve accuracy on the local scale. Different modeling options are tested and the impact of approximations is quantified, specifically for the heavy reflector, which is always a problematic region for VVERs, the treatment of anisotropic scattering and the modeling of corner stiffeners. The optimized nTF 3D full core model is verified and validated for steady state neutronic analysis. The verification and validation of nTF for a real VVER-1000 core proves that deterministic codes can achieve high-resolution predictions of equivalent accuracy with Monte Carlo codes, but with a better spatial resolution. By examining the results of the conventional neutronic solver (see Fig. 3.28), it becomes apparent that strict modeling requirements are only relevant to high-resolution predictions. The neutronic calculation can include several strong approximations (e.g. reflector is modeled as a homogeneous material of steel and water) without presenting discrepancies beyond the acceptable levels on the coarse mesh. The use of coarse homogenization is one of the factors that define conservative safety limits. On the other hand, high-resolution solvers must allow very limited approximations to achieve target accuracy in local predictions, as it is demonstrated in Chapter 3. As a side note, in this chapter the assumption of transport corrected isotropic scattering (P0) is shown to have a negligible effect on the performance of MOC solvers compared to P2, P3 or P5 approximations of the scattering source; as it has been observed before [45]. Finally, the leakage correction of CASMO5-VVER, is shown to be inaccurate when used with PARCS.

One of the biggest achievements of this thesis is the development of nTF/CTF for high-resolution coupled VVER full core calculations. As it was mentioned before, CTF has never been used for full core VVER simulations. The CTF hexagonal pre-processor, embedded in nTF, is the only subprogram that can generate full core VVER models for CTF, besides the

official CTF pre-processor, currently under development for hexagonal geometries. nTF has also never been used with a T/H solver, internal or external, outside of this work. Most importantly though, in general, the realization of multi-physics calculations with a sub-pin level resolution for 3D VVER full core analysis has not been achieved before (to the extent of the writer's knowledge). The tight coupling of the two codes, even though it is partially based on existing subroutines, follows a different approach from what was attempted before for Cartesian geometry, allowing the introduction of sub-pin T/H feedback by CTF. nTF/CTF is verified with a coupled code system (Serpent2/SUBCHANFLOW) of similar accuracy but lower spatial resolution. High Performance Computing (HPC) methods are required by both solvers (nTF and CTF), to achieve such computationally intensive simulations (VVER full core steady state and depletion analysis) in the available clusters at PSI. The novelty of the coupling methodology for the two solvers lays mainly in the double decomposition parallelization scheme, which minimizes the time and memory requirements of the multi-physics calculations and allows fitting them in the Merlin6 cluster. It should be noted here, that such calculations are not possible on CSCS due to the memory requirements. It becomes clear that state-of-the-art HPC should be an integral part of all nuclear simulation tools, especially high-resolution solvers, since time efficiency is a crucial factor for production and design calculations. In Chapter 4, nTF/CTF is also compared with nTF/1D-TH for the same full core model. The simplified 1D T/H solver of nTF introduces several significant biases in the solution, despite the relative simplicity of the T/H phenomena involved (single phase flow in steady state). These biases result in error cancellations (e.g. pin power) or in larger discrepancies (e.g. coolant temperature). The trends introduced by the 1D-TH solver in the X2 HFP model demonstrate that accurate multi-physics calculations cannot be achieved on a local scale unless both solvers employ equivalent levels of resolutions and approximations. Further proof of that are the results of the conventional computational route, which employs a simplified 1D T/H solver to simulate the same scenario as the high-resolution solver. The change in the discrepancies of the coarse mesh is minimal in comparison to HZP results (Chapter 3). In the conventional LRT core solver, the use of a simplified 1D T/H solver is efficient, since the calculation is performed in the coarse mesh and the neutronic solution is also using a simplified approach.

The final chapter is dedicated to the development of both the novel and conventional computational route for VVER cycle analysis, achieving the desired outcome of the PhD. The flexibility of the high-resolution solver and further modifications allowed the calculation of a full cycle boron letdown curve on Merlin6. The high-resolution coupled code system is

validated with coarse mesh experimental data, achieving acceptable accuracy according to utility criteria. The conventional computational route, simulating the detailed power history, is validated with the same data, without the same success, especially when considering the experimental power maps. The sensitivity of the CASMO5-VVER/PARCS to the definition of the appropriate case-matrix proves that the level of approximations involved in the conventional approach makes the coupled code system susceptible to errors, if the user is not an expert user. The computational cost of the high-resolution core solver is larger than the requirements of the conventional approach. However, not so large that makes its use as an audit tool impractical, especially considering the improvements listed in this thesis that could reduce its cost significantly. The capabilities of the coupled code system for sub-pin predictions on a full core model are showcased for the 1st cycle of X2. The novelty and contribution of this PhD to the nuclear community is the proof that simulation tools, which can assist the nuclear industry to achieve a more sustainable future for VVERs by moving towards BEPU, can be developed and introduced to the utilities.

This thesis is the first major outcome of the LRT VVER project. It consists of the first steps in the establishment of both a novel and a conventional computational route for safety analysis of VVERs. As a first step, there is room for improvements, even before considering extending the core solvers to transient analysis.

❖ Firstly, the high-resolution core solver should be able to take advantage of problem symmetries, including 120° symmetry, which would be the case for X2, for HZP and HFP calculations. Currently, nTF can handle 60° symmetric cases. However, since symmetry could not be applied in this study, the coupling and the hexagonal pre-processor can only handle full core models. The use of the coupled code system, or even nTF alone, taking advantage of symmetry in the model, would decrease the computational requirements for the calculations. A state-point calculation of the X2 model but with 60° symmetry and the simplified 1D-TH solver embedded in nTF requires 3 hrs and <1 TB of memory in CSCS. Considering that CTF requires ~16% of the calculation time and very little memory (< 5%) for one full core calculation, the efficiency of the solver can increase significantly if the 120° symmetry option is introduced in nTF, even if the CTF calculation is performed with the full core model.

❖ Several modeling aspects should be tested with CTF that were not included in this work due to the lack of time, like the introduction of spacer grids and corner stiffeners or the modeling of the control rods. Finally, as it was mentioned in Section 4.2.2, the default approach in Cartesian geometry to model the inter-assembly gap is through the use of common sub-

channels between assemblies; the approach taken by the present work is to separate them per assembly. The effect on the solution of the different meshing options for the inter-assembly gap should be studied for full core VVER analysis.

❖ Concerning nTF specifically, several improvements are desirable. The issues of the acceleration scheme when T/H feedback is used should be resolved. The use of the acceleration on the CMFD formulation will reduce significantly the time required for cycle analysis. The control rod module should be expanded to two-material models and a control rod decussing treatment should be implemented. In addition, the introduction of a better approximation for spacer grids could be beneficial. Finally, the restart files should be expanded to include the FSR scalar flux and the angular flux at the boundaries, allowing the option of a simplified predictor-corrector scheme for the nTF/CTF cycle depletion. The computational time required for cycle analysis will be reduced by almost 50% with this option. However, the accuracy of the solution will also be affected.

❖ Merlin6 will soon introduce new computational nodes with higher memory capacity [*private communication with Merlin6 support team*]. When more memory is available, the nTF/CTF core solver could be improved for cycle analysis. The finer mesh of the X2 nTF model, used for HZP analysis, can be employed. The CTF model should be enhanced to take into account local fuel exposure during cycle calculations. In addition all approximations introduced in Chapter 5, like the use of just diffusion (CMFD) instead of a transport axial solver, should be eliminated to achieve better accuracy.

❖ Finally, the high-resolution coupled code system should be compared against measurements relevant to validate the sub-pin level information produced by the simulation tool; if such measurements are one day possible in VVERs.

❖ The conventional coupled code system follows the standard two-step approach, thus not many modifications are required to enhance its current capabilities. The major source of discrepancies in the calculations of CASMO5-VVER/PARCS is the modeling of the reflectors. Better reflector models should be tested to quantify the improvement on accuracy. Soon the University of Michigan will introduce pin-reconstruction for hexagonal geometries to PARCS, which should be tested with the LRT conventional solver. In addition, a leakage correction treatment in PARCS that can be applied together with the CASMO5-VVER cross-section library should be introduced.

Appendix

In order to assess the performance of PARCS without the use of a lattice code, exercise V1000-2D-C1 from the relevant NURESIM-SP1 benchmark [95] is selected. This exercise involves a 2D HZP unrodded full core calculation with zero axial buckling for nodal solvers. The core loading and the heavy reflector correspond to Fig. 3.5, excluding the BA rods on the outer layers of assemblies. As it was mentioned in Chapter 2, the benchmark specifications includes homogenized collapsed two-group diffusion parameters produced by MARIKO, based on a HELIOS 23-group cross-section library. These parameters include homogenized diffusion coefficients, cross-sections and discontinuity factors for fuel and reflector assemblies. The two-group diffusion reference solution by DYN3D is produced with these cross-sections. MARIKO also produces a heterogeneous transport reference solution. The same pre-generated two-group diffusion cross-sections are used by PARCS in this study. Fig. A.I presents the relative difference of the normalized assembly power map of PARCS in comparison to MARIKO, and PARCS in comparison to DYN3D $[(\text{Nor.POW}_{\text{Ref}} - \text{Nor.POW}_{\text{PARCS}}) / \text{Nor.POW}_{\text{Ref}}]$ for the unrodded symmetric fresh fuel loading.

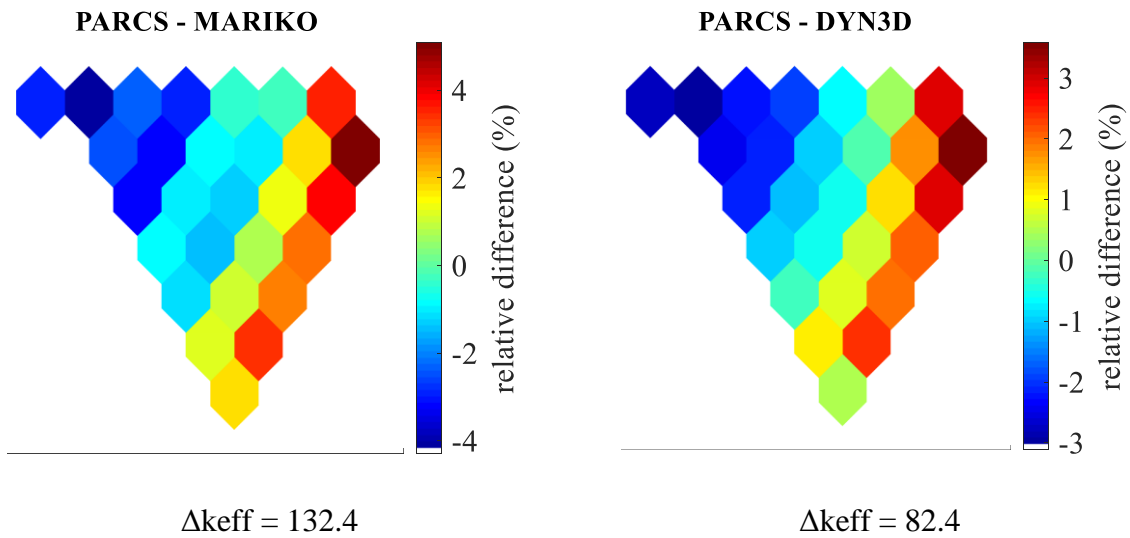


Figure A.1. Relative assembly power and eigenvalue difference between PARCS and Mariko, PARCS and DYN3D for the unrodded symmetric fresh fuel loading

The difference in terms of eigenvalues $[\text{keff}_{\text{Ref}} - \text{keff}_{\text{PARCS}}]$ remains $< 200\text{pcm}$ in both cases. However, there is a better agreement of PARCS with DYN3D, both in terms of reactivity

and power distribution. The maximum power discrepancy in the comparison of PARCS with the transport solution exceeds 5% and $RMS = 2.43\%$. The PARCS vs DYN3D assembly map reaches 3.59% and $RMS = 1.83\%$. The discrepancies observed between the solutions of the two diffusion codes, even though smaller than with the transport solution, signify discrepancies, given that both nodal solvers use the same cross-sections and their computational methods are similar. In addition, the PARCS solution presents strong asymmetry and there is a tilt in the relative power difference, both with MARIKO and DYN3D. This behavior calls for a more detailed study, which should focus on the reflector assemblies. Fig. 3.21 presents the relative difference in the power distribution between PARCS and DYN3D for the unrodded symmetric core with unity discontinuity factors in the reflector assemblies.

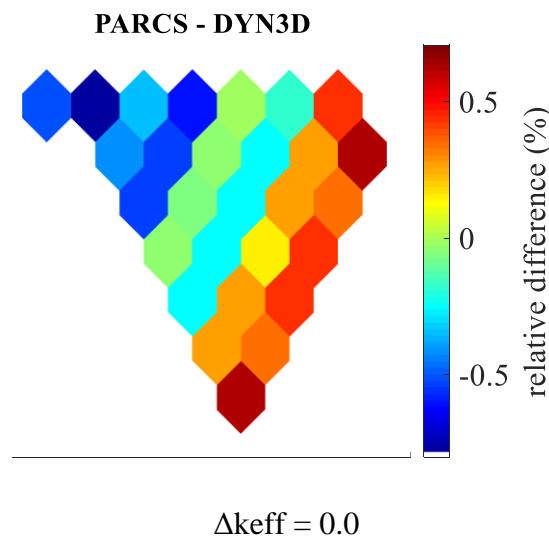


Figure A.2. Relative power difference and Δk_{eff} between PARCS and DYN3D for the unrodded symmetric fresh fuel loading with unity discontinuity factors in the reflector

Fig. A.2 indicates that when the discontinuity factors for the reflector surfaces (RDFs) are set to unity, there is a good agreement (max relative power difference 0.78%, $RMS = 0.39\%$) between PARCS and DYN3D. The conclusion is therefore that the magnitude of the RDFs specified in the benchmark, reaching 7.3 in some surfaces, is leading PARCS to asymmetric solutions. When the two highest values of the RDFs are replaced by unity factors, the asymmetry disappears. The definition of discontinuity factors is the same in PARCS and DYN3D, hence this can be attributed to the differences in the solvers used by the two codes. Despite the good agreement, there is still a tilt in the relative power difference, indicating inconsistencies in the leakage calculation between the two codes. This can be attributed to the different methodologies used in the two solvers.

Bibliography

- [1] F. D’Auria, “Best Estimate Plus Uncertainty (BEPU): Status and perspectives,” *Nucl. Eng. Des.*, vol. 352, no. November 2018, p. 110190, 2019.
- [2] A. Petruzzi, M. Cherubini, M. Lanfredini, and D. De Luca, “The Best-Estimate Plus Uncertainty (BEPU) challenge in the licensing of current generation of reactors,” *IYCE 2015 - Proc. 2015 5th Int. Youth Conf. Energy*, pp. 1–13, 2015.
- [3] M. Hursin, “Experiments for Validation and Enhancements of higher REsolution Simulation Tools (EVEREST),” 2021.
- [4] I. Clifford, M. Pecchia, R. Mukin, C. Cozzo, H. Ferroukhi, and A. Gorzel, “Studies on the effects of local power peaking on heat transfer under dryout conditions in BWRs,” *Ann. Nucl. Energy*, vol. 130, pp. 440–451, 2019.
- [5] S. Canepa, M. Krack, H. Ferroukhi, and A. Pautz, “SCALABILITY BENCHMARKING METHODOLOGY FOR HYBRID PARALLEL CORE CALCULATIONS WITH THE CODE nTRACER,” in *Joint International Conference on Mathematics and Computation*, 2015, pp. 1–13.
- [6] M. Avramova, A. Abarca, J. Hou, and K. Ivanov, “Innovations in Multi-Physics Methods Development, Validation, and Uncertainty Quantification,” *J. Nucl. Eng.*, vol. 2, no. 1, pp. 44–56, 2021.
- [7] IAEA, “Opportunities for Cogeneration with Nuclear Energy. IAEA Nuclear Energy Series No. NP-T-4.1,” 2017.
- [8] M. García *et al.*, “Validation of Serpent-SUBCHANFLOW-TRANSURANUS pin-by-pin burnup calculations using experimental data from the Temelín II VVER-1000 reactor,” *Nucl. Eng. Technol.*, vol. 53, no. 10, pp. 3133–3150, 2021.
- [9] Y. Y. Azmy, “NODAL INTEGRAL METHODS FOR THE NEUTRON * Managed by Martin Marietta Energy Systems , Inc ., under contract DE-AC05- DIFFUSION EQUATION *.”

- [10] G. Hegyi, A. Keresztúri, C. Maráczy, G. Hordósy, and E. Temesvári, “Simulation of start-up measurements with the KIKO3D code and its application for determining the scram rod worth uncertainty in the VVER-440 reactor,” *Ann. Nucl. Energy*, vol. 38, no. 2–3, pp. 694–704, 2011.
- [11] S. Kliem, Y. Kozmenkov, T. Höhne, and U. Rohde, “Analyses of the V1000CT-1 benchmark with the DYN3D/ATHLET and DYN3D/RELAP coupled code systems including a coolant mixing model validated against CFD calculations,” *Prog. Nucl. Energy*, vol. 48, no. 8, pp. 830–848, 2006.
- [12] E. Syrjälähti and A. Hämäläinen, “HEXTRAN-SMABRE calculation of the VVER-1000 coolant transient-1 benchmark,” *Prog. Nucl. Energy*, vol. 48, no. 8, pp. 849–864, 2006.
- [13] B. D. Ivanov, S. Aniel, P. Siltanen, E. Royer, and K. N. Ivanov, “Impact of cross-section generation procedures on the simulation of the VVER-1000 pump startup experiment in the OECD/DOE/CEA V1000CT benchmark by coupled 3D thermal-hydraulics/neutron kinetics models,” *Prog. Nucl. Energy*, vol. 48, no. 8, pp. 746–763, 2006.
- [14] L. Thilagam, C. Sunil Sunny, V. Jagannathan, and K. V. Subbaiah, “A VVER-1000 LEU and MOX assembly computational benchmark analysis using the lattice burnup code EXCEL,” *Ann. Nucl. Energy*, vol. 36, no. 4, pp. 505–519, 2009.
- [15] L. Thilagam, V. Jagannathan, C. Sunil sunny, and K. V. Subbaiah, “VVER-1000 MOX Core Computational Benchmark analysis using indigenous codes EXCEL, TRIHEX-FA and HEXPIN,” *Ann. Nucl. Energy*, vol. 36, no. 10, pp. 1502–1515, 2009.
- [16] J. A. Lozano, J. Jiménez, N. García-Herranz, and J. M. Aragonés, “Extension of the analytic nodal diffusion solver ANDES to triangular-Z geometry and coupling with COBRA-IIIc for hexagonal core analysis,” *Ann. Nucl. Energy*, vol. 37, no. 3, pp. 380–388, 2010.
- [17] N. Poursalehi, A. Zolfaghari, and A. Minucmehr, “Three-dimensional high order nodal code, ACNECH, for the neutronic modeling of hexagonal-z geometry,” *Ann. Nucl. Energy*, vol. 68, pp. 172–182, 2014.
- [18] A. Ramakrishna, V. Jagannathan, and R. P. Jain, “Analysis of regularly perturbed lattices and reaction rate distributions from TIC experiments for X7 lattices,” *Ann. Nucl.*

- Energy*, vol. 38, no. 7, pp. 1623–1644, 2011.
- [19] M. Horváth, I. Pós, and S. P. Szabó, “VVER-440 BENCHMARK WITH C-PORCA,” in *29th Symposium of AER on VVER Reactor Physics and Reactor Safety*, 2019.
- [20] A. A. Aleshin, A. P. Lazarenko, and M. J. Tomilov, “THE CURRENT STATUS OF THE KASKAD SOFTWARE PACKAGE,” in *29th Symposium of AER on VVER Reactor Physics and Reactor Safety*, 2019.
- [21] N. Soshitov, M. Tomilov, and I. Yasnopolskaya, “Validation results of the BIPR-8A code, the new module of the software package KASKAD,” *Kerntechnik*, vol. 85, no. 4, 2021.
- [22] Y. Kozmenkov, S. Kliem, and U. Rohde, “Validation and verification of the coupled neutron kinetic/thermal hydraulic system code DYN3D/ATHLET,” *Ann. Nucl. Energy*, vol. 84, pp. 153–165, 2015.
- [23] N. Kolev, N. Petrov, B. Ivanov, and K. Ivanov, “Simulation of the VVER-1000 pump start-up experiment of the OECD V1000CT benchmark with CATHARE and TRAC-PF1,” *Prog. Nucl. Energy*, vol. 48, no. 8, pp. 922–936, 2006.
- [24] A. Bousbia Salah, J. Vedovi, F. D’Auria, G. Galassi, and K. Ivanov, “Analysis of the VVER1000 coolant trip benchmark using the coupled RELAP5/PARCS code,” *Prog. Nucl. Energy*, vol. 48, no. 8, pp. 806–819, 2006.
- [25] B. D. Ivanov *et al.*, “OECD/DOE/CEA VVER-1000 coolant transient (V1000CT) benchmark - A consistent approach for assessing coupled codes for RIA analysis,” *Prog. Nucl. Energy*, vol. 48, no. 8, pp. 728–745, 2006.
- [26] O. Nuclear and E. Agency, *VVER-1000 Coolant Transient Benchmark Phase I (V1000CT-1) Volume 3 : Summary Results of Exercise 2 on Coupled 3-D Kinetics / Core Thermal-hydraulics*, vol. 5, no. 6201. 2007.
- [27] E. Royer, “VVER-1000 COOLANT TRANSIENT BENCHMARK Phase 2 (V1000CT-2),” vol. 2, 2010.
- [28] B. Ivanov, K. Ivanov, and E. Popov, “TRACE/PARCS calculations of exercises 1 and 2 of the V1000CT-2 benchmark,” in *PHYSOR-2006 - American Nuclear Society’s Topical Meeting on Reactor Physics*, 2006, vol. 2006, no. December 2014.

- [29] I. Spasov, P. Ivanov, and N. Kolev, “Simulation of a rod ejection transient in VVER-1000 with COBAYA4-CTF,” *Comptes Rendus L’Academie Bulg. des Sci.*, vol. 71, no. 3, pp. 325–334, 2018.
- [30] S. Aniel-Buchheit, “Simulation of the VVER-1000 pump start-up experiment in the OECD/DOE/CEA V1000CT benchmark by the FLICA4/CRONOS2 coupled code system,” *Prog. Nucl. Energy*, vol. 48, no. 8, pp. 773–789, 2006.
- [31] I. Spasov *et al.*, “Best-estimate simulation of a VVER MSLB core transient using the NURESIM platform codes,” *Nucl. Eng. Des.*, vol. 321, pp. 26–37, 2017.
- [32] W. Jaeger, V. H. S. Espinoza, and W. Lischke, “Safety Related Investigations of the VVER-1000 Reactor Type by the Coupled Code System TRACE/PARCS,” *J. Power Energy Syst.*, vol. 2, no. 2, pp. 648–661, 2008.
- [33] S. P. Nikonov, K. Velkov, and A. Pautz, “Detailed Modeling of Kalinin-3 Npp Vver-1000 Reactor Pressure Vessel By the Coupled System Code Athlet/Bipr-Vver,” *Int. Conf. Math. Comput. Methods Appl. to Nucl. Sci. Eng.*, no. December 2016, 2011.
- [34] V. A. Tereshonok, S. P. Nikonov, M. P. Lizorkin, K. Velkov, A. Pautz, and K. Ivanov, “KALININ-3 COOLANT TRANSIENT BENCHMARK – SWITCHING-OFF OF ONE OF THE FOUR OPERATING MAIN CIRCULATION PUMPS AT SPECIFICATION- First Edition,” 2008.
- [35] B. Chanaron, “Overview of the NURES SAFE European Project,” *Nucl. Eng. Des.*, vol. 321, pp. 1–7, 2017.
- [36] B. Chanaron *et al.*, “Advanced multi-physics simulation for reactor safety in the framework of the NURES SAFE project,” *Ann. Nucl. Energy*, vol. 84, pp. 166–177, 2015.
- [37] V. H. Sanchez-Espinoza, L. Mercatali, J. Leppänen, E. Hoogenboom, R. Vocka, and J. Dufek, “The McSAFE project - High-performance Monte Carlo based methods for safety demonstration: From proof of concept to industry applications,” *Int. Conf. Phys. React. Transit. to a Scalable Nucl. Futur. PHYSOR 2020*, vol. 2020-March, no. February, pp. 943–950, 2020.
- [38] D. B. Kothe, “CASL: The Consortium for Advanced Simulation of Light Water Reactors,” 2010.

- [39] P. J. Turinsky and D. B. Kothe, “Modeling and simulation challenges pursued by the Consortium for Advanced Simulation of Light Water Reactors (CASL),” *J. Comput. Phys.*, vol. 313, pp. 367–376, 2016.
- [40] R. A. Lefebvre, B. R. Langley, M. L. Baird, and J. P. Lefebvre, *NEAMS Workbench Status and Capabilities*. 2019.
- [41] C. J. Permann *et al.*, “MOOSE: Enabling massively parallel multiphysics simulation,” *SoftwareX*, vol. 11, p. 100430, 2020.
- [42] P. Suk, O. Chvála, G. I. Maldonado, and J. Frýbort, “Simulation of a NuScale core design with the CASL VERA code,” *Nucl. Eng. Des.*, vol. 371, no. October 2020, 2021.
- [43] J. P. Gorton, B. S. Collins, A. J. Wysocki, and N. R. Brown, “Assessment of CASL VERA for BWR analysis and application to accident tolerant SiC/SiC channel box,” *Nucl. Eng. Des.*, vol. 365, no. April, p. 110732, 2020.
- [44] Y. S. Jung, C. B. Shim, C. H. Lim, and H. G. Joo, “Practical numerical reactor employing direct whole core neutron transport and subchannel thermal/hydraulic solvers,” *Ann. Nucl. Energy*, vol. 62, pp. 357–374, 2013.
- [45] M. Ryu, Y. S. Jung, H. H. Cho, and H. G. Joo, “Solution of the BEAVRS benchmark using the nTRACER direct whole core calculation code,” *J. Nucl. Sci. Technol.*, vol. 52, no. 7–8, pp. 961–969, 2015.
- [46] A. Vasiliev *et al.*, “Cross-verification of SUHAM-TD and nTracer reactivity insertion transient solutions without materials homogenization approximation using OECD/NEA C5G7-TD benchmark,” *Ann. Nucl. Energy*, vol. 134, pp. 235–243, 2019.
- [47] J. Kang, M. Ryu, S. Jae, H. Kim, and H. G. Joo, “Direct whole core modeling and simulation of the SPERT III E-Core experiments by nTRACER,” *Prog. Nucl. Energy*, vol. 139, no. June, p. 103824, 2021.
- [48] J. Lee, H. G. Joo, Y. Perin, and K. Velkov, “nTRACER/COBRA-TF Coupling and Initial Assessment,” in *Proceedings of the KNS 2015 spring meeting Primary*, 2015, no. 47023042.
- [49] F. Alberto, L. Jaejin, and J. Han, “nTRACER/ESCOT Initial Coupling and Assessment,” *Trans. Korean Nucl. Soc. Virtual Spring Meet.*, no. December, pp. 2–5, 2020.

- [50] S. Palmtag and A. Godfrey, “VERA common input user manual,” 2015.
- [51] K. J. Connolly and F. Rahnema, “The COMET method in 3-D hexagonal geometry,” in *PHYSOR 2012: Conference on Advances in Reactor Physics - Linking Research, Industry, and Education*, 2012.
- [52] R. Ferrer, J. Hykes, and J. Rhodes, “Development of CASMO5 for VVER-1000/ 1200 analysis and preliminary validation using critical experiments,” *Kerntechnik*, vol. 84, no. 4, pp. 214–227, 2019.
- [53] F. Setiawan, M. Lemaire, and D. Lee, “Analysis of VVER-1000 mock-up criticality experiments with nuclear data library ENDF/B-VIII.0 and Monte Carlo code MCS,” *Nucl. Eng. Technol.*, vol. 53, no. 1, pp. 1–18, 2021.
- [54] N. Hafez, H. Shahbunder, E. Amin, S. A. Elfiki, and A. Abdel-Latif, “Study on criticality and reactivity coefficients of VVER-1200 reactor,” *Prog. Nucl. Energy*, vol. 131, no. December 2020, 2021.
- [55] S. B. F. Faghihi, *, S.M. Mirvakili, S. Safaei, “Neutronics and sub-channel thermal-hydraulics analysis of the Iranian VVER-1000 fuel bundle,” *Prog. Nucl. Energy J.*, no. 87, pp. 39–46, 2016.
- [56] I. Panka, G. Hegyi, A. Keresztúri, C. Maráczy, and E. Temesvári, “Hot channel calculation methodologies in case of VVER-1000/1200 reactors,” *Kerntechnik*, vol. 83, no. 4, 2018.
- [57] Y. Perin, S. Nikonov, R. Henry, I. Pasichnyk, and K. Velkov, “Comparative thermohydraulic analyses of VVER 1000 active core for two different construction types of assemblies,” *Kerntechnik*, vol. 84, no. 4, 2019.
- [58] R. Henry, Y. Périn, K. Velkov, and S. P. Nikonov, “3-D Coupled simulation of a VVER 1000 with PARCS/ATHLET,” *Int. Conf. Phys. React. Transit. to a Scalable Nucl. Futur. PHYSOR 2020*, vol. 2020-March, pp. 1025–1032, 2020.
- [59] A. I. Sinegribova and M. A. Uvakin, “VVER TRANSIENT SIMULATION RESULTS ANALYSIS FOR MAIN STEAM LINE BREAK ACCIDENT USING FUEL ASSEMBLY PIN-BY-PIN MODEL BY KORSAR/GP CODE,” in *29th Symposium of AER on VVER Reactor Physics and Reactor Safety*, 2019.

- [60] V. Doleček, L. Vyskočil, and V. Železný, “SIMULATION OF CROSSFLOWS IN A MIXED CORE OF VVER REACTOR WITH SUBCHANNEL CODE AND CFD CODE,” in *29th Symposium of AER on VVER Reactor Physics and Reactor Safety*, 2019.
- [61] M. Calleja, V. Sanchez, J. Jimenez, U. Imke, R. Stieglitz, and R. Macián, “Coupling of COBAYA3/SUBCHANFLOW inside the NURESIM platform and validation using selected benchmarks,” *Ann. Nucl. Energy*, vol. 71, pp. 145–158, 2014.
- [62] Y. Bilodid, E. Fridman, and T. Lötsch, “X2 VVER-1000 benchmark revision: Fresh HZP core state and the reference Monte Carlo solution,” *Ann. Nucl. Energy*, vol. 144, p. 107558, 2020.
- [63] M. Avramova, K. Ivanov, K. Velkov, and E. Al., “Benchmark on reactivity compensation with diluted boron by stepwise insertion of control rod cluster into the VVER-1000 core Specifications and Support Data,” 2018.
- [64] M. García *et al.*, “A subchannel coarsening method for Serpent2-SUBCHANFLOW applied to a full-core VVER problem,” in *International Conference on Physics of Reactors: Transition to a Scalable Nuclear Future, PHYSOR 2020*, 2020, vol. 2020-March, pp. 1049–1056.
- [65] F. Faghihi, S. M. Mirvakili, S. Safaei, and S. Bagheri, “Neutronics and sub-channel thermal-hydraulics analysis of the Iranian VVER-1000 fuel bundle,” *Prog. Nucl. Energy*, vol. 87, pp. 39–46, 2016.
- [66] S. Kim and H. G. Joo, “Calculation of ‘Full-Core’ VVER-440 Benchmark by nTRACER,” in *27th Symposium of AER on VVER Reactor Physics and Reactor Safety*, 2017.
- [67] S. Kim and H. G. Joo, “nTRACER Solutions of the Two-Dimensional VVER Benchmark Problems,” in *Transactions of the Korean Nuclear Society Virtual Spring Meeting*, 2020.
- [68] J. Jimenez, “Testing of SUBCHANFLOW and COBRA-TF models for a VVER fuel assembly,” 2015.
- [69] Y. Perin, “Development of a Multi-Physics, Multi-Scale simulation tool for LWR safety analysis,” TECHNISCHE UNIVERSITÄT MÜNCHEN, 2016.

- [70] R. Mukin, I. Clifford, H. Ferroukhi, and M. Seidl, “Thermal hydraulic analysis of PWR Assembly bowing using subchannel Code Cobra-TF,” *17th Int. Top. Meet. Nucl. React. Therm. Hydraul. NURETH 2017*, vol. 2017-Septe, 2017.
- [71] T. J. Downar *et al.*, “PARCS: Purdue advanced reactor core simulator,” in *Proceedings of the PHYSOR 2002 - International Conference on the New Frontiers of Nuclear Technology: Reactor Physics, Safety and High-Performance Computing - The ANS 2002 RPD Topical Meeting*, 2002, no. May 2014.
- [72] M. Ruščák and G. Mazzini, “Parcs/Trace Coupling Methodology for Rod Ejection on Vver 1000 Reactor,” *Acta Polytech. CTU Proc.*, vol. 4, p. 80, 2016.
- [73] J. Vojackova, F. Novotny, and K. Katovsky, “Safety analyses of reactor VVER 1000,” *Energy Procedia*, vol. 127, no. 2016, pp. 352–359, 2017.
- [74] M. Hursin *et al.*, “Development and validation of a TRACE/PARCS core model of Leibstadt Kernkraftwerk cycle 19,” *Ann. Nucl. Energy*, vol. 101, pp. 559–575, 2017.
- [75] D. Black, “Inside HPC,” 2021. [Online]. Available: <http://insidehpc.com/2015/09/cray-scales-fluent-to-129000-compute-cores/>.
- [76] R. Rabenseifner, “Introduction to the Message Passing Interface (MPI).” High-Performance Computing-Center Stuttgart (HLRS), 2020.
- [77] J. Y. Cho, K. S. Kim, H. J. Shim, J. S. Song, C. C. Lee, and H. G. Joo, “Whole core transport calculation employing hexagonal modular ray tracing and CMFD formulation,” *J. Nucl. Sci. Technol.*, vol. 45, no. 8, pp. 740–751, 2008.
- [78] N. Choi and H. G. Joo, “Stability enhancement of planar transport solution based whole-core calculation employing augmented axial method of characteristics,” *Ann. Nucl. Energy*, vol. 143, p. 107440, 2020.
- [79] S. Jae and H. G. Joo, “Evaluation of a New Group Structure for nTRACER Based on HELIOS 47 Group Structure and Extended Resonance Range for 20w % Uranium and MOX Fuels,” in *Transactions of the Korean Nuclear Society Virtual Spring Meeting*, 2020, no. 2, pp. 1–4.
- [80] H. S. Park, “Resonance Treatment Innovations for Efficiency and Accuracy Enhancement in Direct Whole Core Calculations of Water-Cooled Power Reactors,”

- Seoul National University, Reactor Physics Laboratory (SNURPL), 2018.
- [81] S. Choi, A. Khassenov, and D. Lee, “Resonance self-shielding method using resonance interference factor library for practical lattice physics computations of LWRs,” *J. Nucl. Sci. Technol.*, vol. 53, no. 8, pp. 1142–1154, 2016.
- [82] J. Han-gyu, “Method of Characteristics for Solution of PDE Solution along Characteristics Line MOC for Boltzmann Equation.” 2011.
- [83] M. Ryu, Y. S. Jung, C. H. Lim, and H. G. Joo, “Incorporation of Anisotropic Scattering in nTRACER,” in *Transactions of the Korean Nuclear Society Autumn Meeting*, 2014, no. 1.
- [84] K. S. Kim and M. D. Dehart, “Unstructured partial- and net-current based coarse mesh finite difference acceleration applied to the extended step characteristics method in NEWT,” *Ann. Nucl. Energy*, vol. 38, no. 2–3, pp. 527–534, 2011.
- [85] B. W. Kelley, “An Investigation of 2D/1D Approximations to the 3D Boltzmann Transport Equation,” *Michigan Univ.*, pp. 1–137, 2015.
- [86] A. M. . Graham, B. S. . Collins, and T. Downar, “Improvement of the 2D/1D Method in MPACT Using the Subplane Scheme,” in *M&C 2017 - International Conference on Mathematics & Computational Methods Applied to Nuclear Science & Engineering, April 16-20, 2017*, 2017.
- [87] R. K. Salko and M. N. Avramova, “COBRA-TF Subchannel Code (CTF) Theory Manual,” 2015.
- [88] S. Patankar, *Numerical heat transfer and fluid flow: Computational methods in mechanics and thermal science*. 1980.
- [89] D. S. Trent and J. R. Welty, *A summary of numerical methods for solving transient heat conduction problems*, Bulletin,. Oregon State University, Engineering Experiment Station: U.S. Environmental Protection Agency, 1974.
- [90] Studsvik, “CASMO5, A FUEL ASSEMBLY BURNUP PROGRAM,” 2019.
- [91] J. Y. Cho, H. G. Joo, B.-O. Cho, and S. Q. Zee, “Hexagonal Cmfd Formulation Employing Triangle-Based Polynomial Expansion Nodal Kernel,” in *International*

- Conference on Mathematics and Computational Methods Applied to Nuclear Science and Engineering*, 2001, no. September, pp. 1–15.
- [92] E. Woodcock, T. Murphy, P. Hemmings, and S. Longworth, “Techniques used in the GEM code for Monte Carlo neutronics calculation,” *Proc. Conf. Appl. Comput. Methods to React. ANL-7050*, no. 3, pp. 557–579, 1965.
- [93] J. Leppanen, “Serpent – a Continuous-energy Monte Carlo Reactor Physics Burnup Calculation Code,” *Tech. Res. Cent. Finl.*, p. 157, 2011.
- [94] U. Imke and V. H. Sanchez, “Validation of the subchannel code SUBCHANFLOW using the NUPEC PWR tests (PSBT),” *Sci. Technol. Nucl. Install.*, vol. 2012, 2012.
- [95] P. Petkov and S. Mittag, “Specifications, reference solutions and DYN3D solutions of the NURESIM-SP1 Benchmarks V1000-2D-C1, V1000-2D-C2 and V1000-2D-C3,” *Nuresim Milestone 19a1*, vol. 516560, pp. 1–51, 2007.
- [96] G. Todorova, N. P. Kolev, N. Petrov, P. Bellier, and S. Santandrea, “Solution of VVER mathematical benchmarks (I): V1000-2D-C1-tr by APOLLO2 MOC,” *Milestone 19b2*, vol. 516560, no. I, pp. 1–32, 2007.
- [97] T. Lötsch *et al.*, “The X2 benchmark for VVER-1000 reactor calculations. Overview and current status.,” in *Proceedings of the 26th AER Symposium on VVER Reactor Physics and Reactor Safety, Helsinki, Finland*, 2016, no. March.
- [98] Y. Bilodid, E. Fridman, and T. Lötsch, “X2 VVER-1000 benchmark revision: Fresh HZP core state and the reference Monte Carlo solution,” *Ann. Nucl. Energy*, vol. 144, p. 107558, 2020.
- [99] K. S. Kim *et al.*, “Development of the V4.2m5 and V5.0m0 Multigroup Cross Section Libraries for MPACT for PWR and BWR, Rev. 0,” 2017.
- [100] Tractabel, “WPEC Subgroup 46 Activity on ‘ Target Accuracy Requirements (TAR)’ Core physics validation.” 2021.
- [101] T. Bahadir and E. L. Georgieva, “‘ FULLCORE ’ and ‘ MIDICORE ’ VVER-1000 Benchmark Evaluations with Studsvik ’ s CMS5-VVER Codes,” in *Conference: 28th Symposium of AER on VVER Reactor Physics and Reactor Safety*, 2018.

- [102] D. Jang, Jaerim ; Hursin, Mathieu; Leea, Woonghee; Pautz, Andreas ; Papadionysiou, Marianna ; Vasiliev, Alexander ; Leea, “Analysis of Rostov-II benchmark using conventional two-step code systems,” 2021.
- [103] A. Sargeni, K. W. Burn, and G. B. Bruna, “The impact of heavy reflectors on power distribution perturbations in large PWR reactor cores,” *Ann. Nucl. Energy*, vol. 94, pp. 566–575, 2016.
- [104] P. T. Petkov and S. Mittag, “VVER-1000 radial reflector modeling by diffusion nodes,” *Prog. Nucl. Energy*, vol. 48, no. 8, pp. 764–772, 2006.
- [105] G. Gunow, B. Forget, and K. Smith, “Full core 3D simulation of the BEAVRS benchmark with OpenMOC,” *Ann. Nucl. Energy*, vol. 134, pp. 299–304, 2019.
- [106] A. Bikeev, M. Kalugin, A. Shcherenko, and D. Shkarovsky, “Simulation of VVER-1000 startup physics tests using the MCU Monte Carlo code,” *Ann. Nucl. Energy*, vol. 117, pp. 60–66, 2018.
- [107] D. V. Afanasiev, A. A. Pinegin, V. I. Orlov, and E. V. Tolmasova, “THE PRACTICE OF CONSIDERING REACTIVITY SPATIAL EFFECTS WHEN MEASURING EMERGRNCY PROTECTION EFFICIENCY IN VVER REACTORS,” in *24th Symposium of AER on VVER Reactor Physics and Reactor Safety*, 2014.
- [108] P. Lartaud, “Verification of the conventional approach for full core calculations on hexagonal geometries,” 2020.
- [109] S. Bznuni, A. Amirjanyan, N. Baghdasaryan, and J. Ramsey, “Comparative Analysis of Wwer-440 Reactor Core With Parcs / Helios and Parcs / Serpent Codes,” *Int. Conf. Top. Issues Nucl. Install. Saf.*, pp. 127–133, 2017.
- [110] B. R. Herman, B. Forget, K. Smith, and B. N. Aviles, “Improved diffusion coefficients generated from Monte Carlo codes,” *Int. Conf. Math. Comput. Methods Appl. to Nucl. Sci. Eng. M C 2013*, vol. 4, pp. 2947–2961, 2013.
- [111] K. I. Usheva, S. A. Kuten, A. A. Khruschinsky, and L. F. Babichev, “Generation of XS library for the reflector of VVER reactor core using Monte Carlo code Serpent,” *J. Phys. Conf. Ser.*, vol. 781, no. 1, 2017.
- [112] R. N. Bratton, M. Avramova, and K. Ivanov, “Oecd/nea benchmark for uncertainty

- analysis in modeling (UAM) for LWRS - summary and discussion of neutronics cases (PHASE I),” *Nucl. Eng. Technol.*, vol. 46, no. 3, pp. 313–342, 2014.
- [113] M. Papadionysiou, K. Seongchan, M. Hursin, A. Vasiliev, A. Pautz, and H. G. Joo, “Coupling of nTRACER to COBRA-TF for High-Fidelity Analysis of VVERs,” *Physor 2020 Transit. to a Scalable Nucl. Futur.*, 2020.
- [114] M. Papadionysiou *et al.*, “Coupling of COBRA-TF to nTRACER for Full Core High-Fidelity Analysis of VVERs,” in *International Conference on Physics of Reactors: Transition to a Scalable Nuclear Future, PHYSOR 2020*, 2022, vol. 2022-May, pp. 170–177.
- [115] T. Downar, “MPACT Theory Manual Version 2.2.0,” 2016.
- [116] D. L. Hagrman, G. A. Reyman, and R. E. Mason, “MATPRO - version 11, tree-nureg-1280, rev 1,” 1980.
- [117] K. J. Geelhood, W. G. Luscher, P. A. Raynaud, and I. E. Porter, “Frapcon-4.0: A Computer Code for the Calculation of Steady-State, Thermal-Mechanical Behavior of Oxide Fuel Rods for High Burnup September,” 2015.
- [118] P. E. MacDonald and L. B. Thompson, “MATPRO - version 9, tree-nureg-1005,” 1976.
- [119] T. Loetsch, V. Khalimonchuk, and A. Kuchin, “Proposal of a benchmark for core burnup calculations for a VVER-1000 reactor core,” in *19th AER Symposium on VVER Reactor Physics and Reactor Safety*, 2009, vol. 0801504, pp. 53–109.
- [120] P. Van Uffelen, J. Hales, W. Li, G. Rossiter, and R. Williamson, “A review of fuel performance modelling,” *J. Nucl. Mater.*, vol. 516, no. April, pp. 373–412, 2019.
- [121] Y. S. Jung, S. W. Park, and H. G. Joo, “Implementation and verification of quadratic depletion method in direct whole core calculation code nTRACER,” in *Korean Nuclear Society Spring Meeting*, 2012, no. 5, pp. 212–213.
- [122] N. Choi, H. Park, H. G. Lee, S. Jae, S. Jeon, and H. G. Joo, “Recent capability and performance enhancements of the whole-core transport code nTRACER,” *Int. Conf. Phys. React. Transit. to a Scalable Nucl. Futur. PHYSOR 2020*, vol. 2020-March, pp. 1195–1206, 2020.

- [123] B. F. Rider, C. P. Ruiz, J. P. Peterson Jr., and F. R. Smith, "Determination of Neodymium-148 in Irradiated Uranium and Plutonium as a Measure of Burnup," 1967.
- [124] K. S. Kim, C. A. Gentry, A. T. Godfrey, Y. Liu, and S. Palmtag, "Development of the multigroup cross section library for the CASL neutronics simulator MPACT: Verification," *Ann. Nucl. Energy*, vol. 132, pp. 1–23, 2019.

Curriculum Vitae

Education

- 2018-2022 : **Nuclear Engineering PhD**, Paul Scherrer Institut (PSI)
Title : “Multi-Physics Modeling of VVERs with High Fidelity High-Resolution Codes”
- 2015-2017 : **Nuclear Engineering MSc**, ETHZ (Swiss Federal Institute of Technology in Zurich) & EPFL (Swiss Federal Institute of Technology in Lausanne), *Graduation grade* : **5.68/6**
Diploma thesis : “Monte Carlo simulation of a scintillation detector for spent fuel characterization in a hot cell”
- 2009-2015 : **Integrated Bachelor in Mechanical Engineering with MSc in Energy Engineering**, School of Mechanical Engineering, National Technical University of Athens (NTUA), *Graduation grade* : **8.63/10**
Diploma thesis : “Study of the response of a germanium detector with the use of experimental methods and Monte-Carlo simulation techniques”

Professional experience

- **Part time** working in the Laboratory for Reactor Physics (LRS) of EPFL for 8 months
- *July 2016 – September 2016*, Three months **internship** in NAGRA (National Cooperative for the Disposal of Radioactive Waste), Switzerland
- *February 2017*, One month **internship** in NAGRA (National Cooperative for the Disposal of Radioactive Waste), Switzerland
- *May 2019 – August 2019*, Three months **internship** in Seoul National University Reactor Physics Laboratory as a PhD fellow, South Korea

Training Courses

- ❖ *September 2012* - Association of Greek Women Engineers
"The role of biomass in energy production-Applications"
- ❖ *5-8 November 2012* - Mentor Hellas Greece, "Introduction to Matlab and Programming Techniques"
- ❖ *31 March -12 April 2014* – Intensive Course MANTRA 2014, Education and Culture DG in cooperation with universities: Alma Mater Studiorum Università di Bologna and Università degli Studi di Catania, Italy "Medical Applications of Nuclear Technologies and Radiation"
- ❖ *10 October 2014 - 26 March 2015* – Postgraduate Educational Course (PGEC) on radiation protection and the safety of radiation sources, International Atomic Energy Agency (IAEA),
Thesis: “Atmospheric transport and dispersion of radioactivity, following a major nuclear accident: Use and validation of EEA HYSPLIT model for the case of the Fukushima Dai-chi nuclear accident.”

- ❖ *18 – 21 June 2018* – Training Course: Fundamentals of reactor kinetics and theory of small space-time dependent fluctuations in nuclear reactors, Chalmers University of Technology, Gothenburg, Sweden.
- ❖ *22 – 31 August 2018* – “Maximizing the Benefits of Experiments for the Simulation, Design and Analysis of Reactors”, 24th session of the Frédéric Joliot/Otto Hahn (FJOH) Summer School, Karlsruhe Institute of Technology and the Nuclear Energy Division of CEA Cadarache.
- ❖ *10 – 14 February 2020* – “Short Courses on Modelling and Computation of Multiphase Flows”, 37th session, Swiss Federal Institute of Technology (ETHZ), Switzerland.
- ❖ *12 – 16 October 2020* – Parallel Programming Workshop (MPI, OpenMP and Advanced Topics), High Performance Computing Center Stuttgart (HLRS).
- ❖ *19 – 30 July 2021* – “Holistic Innovation: Integrating methods, experiments and people to advance nuclear technology”, MeV Summer School, USA.

Publications

- “*Monte Carlo simulation of a scintillation detector for spent fuel characterization in a hot cell*”, Papadionysiou M. *et al.*, Nuclear Engineering and Design 332 (2018) 119–126
- “*Assessment of nTRACER and PARCS Performance for VVER Configurations*”, Papadionysiou M. *et al.*, Nuclear Science and Engineering, 194(11) (2020) 1056-1066.
- “*Assessment of nTRACER and PARCS Performance for VVER Configurations*”, Papadionysiou M. *et al.*, Int. Conf. Math. Comput. Methods Appl. to Nucl. Sci. Eng. (M&C 2019), pp. 700–709, 2019.
- “*Coupling of nTRACER to COBRA-TF for high-fidelity analysis of VVERs*”, Papadionysiou M. *et al.*, Proceedings of the PHYSOR 2020 (p. 1285 (8 pp.)).
- “*Validation of the High-Resolution Code nTRACER against VVER-1000 Hot Zero Power Measurements*”, Papadionysiou M. *et al.*, Int. Conf. Math. Comput. Methods Appl. to Nucl. Sci. Eng. (M&C 2021).
- “*Coupling of COBRA-TF to nTRACER for full core high-fidelity analysis of VVERs*”, Papadionysiou M. *et al.*, Proceedings of the PHYSOR 2022.

Scholarships & Awards

- ✓ **Scholarship** of Pateras Foundation *October 2015 – July 2017*
- ✓ **Award** for best presentation, American Nuclear Society Student Conference, *April 2017*
- ✓ **Award** for best summary, American Nuclear Society Student Conference, *April 2017*
- ✓ **Award** for best PhD work (2nd year), Nuclear Energy Systems Division PhD Day, PSI, *2019*
- ✓ **Award** for best PhD work (4th year), Nuclear Energy Systems Division PhD Day, PSI, *2021*

Involvement in National Programms

- ✦ *Summer 2004*: Volunteering to the Olympic Games of Athens

